distribution around the machine was found. The enhancement at the injection port could be attributed to $\underline{D} + D$ reactions between shine through particles and adsorbed deuterium gas at the beam dump.

Furthermore, the total neutron production was calculated and compared with the measurements. A homogeneous plasma cross-section with 10 cm diameter was used, taking $T_e(o)$, $n_e(o)$, Z_{eff}, and the deuteron/proton ratio from measurements. The distribution function of the injected fast deuterons was calculated from the Fokker Planck equation based on Coulomb collisions, the total number density was taken from both the beam composition and the fraction absorbed by the plasma. It was found that also the measured total neutron flux agrees with these classical calculations within a factor of 2.

In order to study the dependence of the decay time on plasma density and temperature, the D-beam was switched-off at various times through the discharge and the decay of the neutron fluxes recorded. A comparison of the measured and calculated (dashed line) curves shows remarkable agreement with collisional slowing down (fig. 3). For the same discharge also the slowing down of fast cx-particles has been measured and compared with calculated slowing down times (table 1). Within a factor of 2 agreement was found.

Therefore, in contrast to earlier hypotheses the conclusion from all these more detailed experiments is that the energy transfer in W VII-A with almost perpendicular injection (84^o with respect to the B-field) is in fact collisional. As a consequence of the collisional slowing down the assumption of preferential ion heating cannot be made anymore.

2.2.4 Ion heat conduction

Thus the measured high ion temperatures are compatible with the lower electron temperatures only if the ion heat conduction is smaller than the simple neo-classical prediction. Such a reduction may be expected indeed by proper consideration of the observed high radial electric fields.

Note that hydrogen is injected into a deuterium target plasma almost perpendicular to B, and $T_{i,cx}$ is measured perpendicular to B as well, but using the deuterium component. So if the distribution function were not Maxwellian one would not get the bulk temperature from these cx-measurements.

An additional measurement of T_i was performed via Doppler broadened oxygen lines, both parallel and perpendicular to B. The line used is a O VIII (8-7) line at 2977 Å produced by cx-recombination /11/.Within 10 % these Doppler-temperatures agree with $T_{i,cx}$ indicating a Maxwellian distribution.

With the usual neoclassical formulas of heat conduction in the plateau regime, the ion energy balance cannot be fulfilled for collisional slowing-down. These formulas for thermal transport are derived for thermal plasmas requiring only small electric fields for ambipolarity. However, in W VII-A the ambipolar potential may be dominated by the very energetic ions coming from the almost perpendicular neutral injection. Such strong radial electric fields have been deduced from poloidal rotation measurements and been found responsible already for the reduction of the fast particle orbit losses and the corresponding increase in heating efficiency.

In the plateau regime, the deviation of the drift surfaces of thermal ions from the magnetic surfaces is strongly reduced by the electric field, if the poloidal rotation velocity v_{ExB} is large compared to the poloidal component of the parallel velocity, $\iota \, {}^{r}/_{R} \, v_{th}$. Note the large aspect ratio in W VII-A of ${}^{R}/_{a} \simeq 20$. With increasing ExB drift, for more and more toroidally trapped particles the poloidal turning points vanish depending on particle energy. For the measured E-fields, there are practically no banana type orbits for thermal ions anymore. Consequently, the plateau transport coefficients are believed to be strongly reduced by these electric fields /15/.

2.3 Effect of rotational transform ι

Similar to the experiments with low ß Ba-plasmas in W II-A /12/ the confinement in W VII-A is strongly dependent on the rotational transform, ι. Fig. 4 displays the energy content W versus rotational transform for stationary ECRH sustained plasmas. In /3/, equivalent measurements have been reported for NI. Grossly, the energy content, hence the energy replacement time τ_E increases with ι. Therefore, in spite of the reduction of the effective plasma radius due to the ellipticity of the magnetic surface, a reduction of electron heat transport with increasing ι is found, as expected by theory. At rational values of the transform $\iota(a) = m/n$, with $m \leq 3$, $n < 10$, minima of confinement occur. At values of the transform, where the density of low order rational numbers is small, optimum confinement is found.

2.3.1. Plasma current for $U_L = 0$

The plasma current I_P observed for $U_L = 0$ modifies the rotational transform corresponding to the current density profile j(r). At the plasma edge the iota profiles are:

$$\iota(a) = \iota_o + \iota_p \quad \text{with } \iota_p \sim \int_o^a j(r) r / B \, dr$$

Therefore, currents produced by the plasma pressure (positional shift, "bootstrap" current originating from pressure gradients) or by the heating mechanism influence the confinement. For NI into W VII-A the plasma current I_P is observed to be almost proportional to the plasma energy content W. The direction of the current agrees with the prediction for the "bootstrap" current and is such as to increase the rotational transform.

The transition from co- to counter-injection by reversing all magnetic fields also changes the direction of the current. The unaffected dependence of $|I_p|$ on W may exclude NI heating as the source for this current. The magnitude of the observed current, $|I_p|$ up to 2 kA, is larger than the bootstrap current calculated from the measured pressure profiles by a factor of up to 5, but bootstrap theory is not yet well established for non-axisymmetric configurations.

During ECRH with a pulse duration of $\Delta t \lesssim 40$ ms, a steady increase of a current with $dI_p/dt \approx 20$ kA/s is observed. The dominant process responsible for this current seems to be the confinement of non-thermal electrons produced by the heating mechanism.

2.3.2 Control of the edge value of rotational transform

Variations of the external transform for different values of the plasma current show that it is mainly the edge value of the transform, $\iota(a) = \iota_o + \iota_p$, which determines the gross plasma behaviour. Details of the confinement depend on the entire iota profile which is influenced by the plasma pressure and residual currents, both of them introducing some shear /3/. By control either of the residual plasma current (ι_p) or of the current in the helical windings (ι_o), rational values of iota can be avoided ($\iota_o + \iota_p \neq m/n$) and stationary conditions at optimum confinement can be maintained. For NI experiments with constant ι_o, a loop voltage of $|U_L| < 0.3$ V has been used so far for controlling pre-programmed plasma currents within a range of $|I_p| < 2$ kA. At 3 T a current of Ip = 1 kA modifies the edge values of the transform by $\Delta\iota = 0.015$. During ECRH the increasing current I_p has been compensated by a corresponding change of the helical current I_H, controlled by feedback.

In fig. 5 the effects of current density distribution (shear!) on plasma confinement are demonstrated by comparing two discharges both with $\iota_o \approx 0.5$ and with small but different plasma currents, $I_p = 0$ and $I_p = 2$ kA respectively. In both cases the signals from the soft X-ray diode array indicate a deterioration of the confinement once the edge-value of iota passes through $\iota = 0.5$. The plasma with $I_p = 0$ even vanishes for $\iota = 0.5$ and recovers when iota is above 0.5. In contrast, the discharge with $I_p = 2$ kA (shear!) can be maintained even with t(a) = 0.5 because of $\iota(o) > 0.5$ resulting from peaked distributions of the plasma current. This way the perturbations remain localized at the plasma edge. The corresponding shrinking of the density and temperature profiles is observed.

2.3.3 Control of the ι profile

$\iota(a) \neq m/n$ is necessary for operation with optimum confinement. The vacuum transform profile, however, is modified by residual currents and effects due to the finite ß plasma. Equilibrium calculations using the Princeton code /14/ confirm the

effect of the plasma pressure. The ι profiles are not directly measureable, therefore plasma pressure effects can hardly be discriminated. First experiments slightly modulating the external transform, $\iota_0 + \tilde{\iota}$, indicate the localization of the resonant surface by analysis of soft-X or ECE-measurements with high spatial and time resolution. Fine adjustment of the transform ι_0 may then allow to modify impurity flow and plasma pressure profiles.

2.4 Magnetic islands convection

In stellarators at rational values of the transform magnetic islands are caused by small perturbing fields. Such perturbation fields are introduced, e.g. by the current leads or the helical bridges. Islands of significant width can be calculated for low order rational numbers ι = m/n: 1/3, 2/5, 3/7, 1/2, 2/3. The largest islands are formed at ι = 1/2.

Convection can be generated by inhomogeneous sources of particles, energy and momentum. On the basis of a fluid model it can be shown that the perturbation caused by these sources is localized to a very narrow vicinity of rational magnetic surfaces. In the case of anomalous electron heat conductivity such regions can be significantly enlarged. The effect becomes strong if the rational surface is close to the boundary, where the anomalous heat conductivity $\chi_{e\perp} \sim 1/T^{2/3} \cdot n$ /3/ has its maximum and the parallel conductivity $\chi_{e\parallel} \sim T^{5/2}/n$ has its minimum.

The presence of magnetic islands enhances that effect. It is shown that close to the separatrix of the island large Pfirsch-Schlüter currents, $j_\parallel$, arise, which lead to large electric fields and convective motion across the island.

Therefore a combined effect of magnetic island and convective motion may be responsible for the enhanced losses at rational ι = m/n, rather than a result of instabilities.

3. CONCLUSIONS

Two different heating methods, NI and ECRH, have been used to study stability and transport in the shearless l = 2 magnetic configuration of W VII-A. Good confinement can be maintained for particular values of the rotational transform in the vicinity of, but not at ι = m/n; e.g. 1/2, 1/3, 2/3. The available heating power seems to determine the maximum achievable ß. So far no limitations by MHD instabilities are found. At resonant magnetic surfaces island formation and convection perturb the plasma behaviour. By control of the edge value of the rotational transform ι-effects of a residual plasma current I_p can be compensated. Such currents are generated by plasma pressure (bootstrap current) or by the heating mechanism. Small shear produced by a non-homogeneous current density distribution apparently influences the localization and width of islands. Because of the small plasma radius and steep gradients of W VII-A

islands localized at the edge strongly influence even the global parameters. For higher plasma pressures than accessible at present in W VII-A modifications of the vacuum ι-profiles have to be considered. Therefore configurations with moderate shear and larger plasma diameter, as foreseen for W VII-AS, may experience smaller effects also at resonant magnetic surfaces.

Heating, magnetic configuration and confinement properties are closely linked together in a stellarator. This has been demonstrated with the help of small plasma currents I_p, which modify the magnetic configuration. In addition radial electric fields are present as a consequence of the nearly perpendicular injection. The corresponding reduction of the orbit losses increases the heating efficiency. Also corrections of the model for the ion heat conduction seem to be necessary. The high ion temperatures have been confirmed by means of various diagnostics, and $T_{i\perp}$ and $T_{i\parallel}$ found to be equal. Anomalous slowing down and preferential heating of the ions by the injected beam can now be excluded.

Consequently a significant reduction of the ion heat conduction has to be assumed to describe the ion heat balance. If the large radial electric fields, $E \approx 0.1$ kV/cm, are properly introduced in the neoclassical transport model, banana type orbits disappear and the transport coefficients in the plateau regime are strongly reduced. Certainly these findings need further investigations, both by theory and experiment.

REFERENCES

/1/ W VII-A TEAM and NEUTRAL INJECTION GROUP, in Plasma Physics and Controlled Nuclear Fusion Research (Proc. 8th Int. Conf. Brussels 1980) Vol. 1, IAEA, Vienna (1981) 185

/2/ W VII-A TEAM, NEUTRAL INJECTION GROUP, in Plasma Physics and Controlled Nuclear Fusion Research (Proc. 9th Int. Conf. Baltimore 1982) Vol. 2, IAEA, Vienna (1983) 241.

/3/ W VII-A TEAM, NI-GROUP, IPF STUTTGART, Plasma Phys., Vol. 26 No. IA p. 183 (1984). CN-44/DI-5.

/4/ ERCKMANN et. al., W VII-A GROUP, Plasma Phys. and Contr. Nucl. Fusion (1984).

/5/ UO, K. IIYOSHI, A., OBIKI, T. et al., in Proc. 4th Int. Symposium on Heating in Toroidal Plasmas, Rome 1984, Vol. II, 947.

/6/ TROYON, F. et. al., Plasma Physics, Vol. 26 No IA, 209 (1984).

/7/ LORTZ, D., NÜHRENBERG, J., Nucl. Fusion, 17 (1977) 125.

/8/ W VII-A TEAM, NEUTRAL INJECTION GROUP, Proc. 4th Int. Symposium on Heating in Toroidal Plasmas, Rome 1984, Vol. 1, 95.

/9/ MAASSBERG, H., HELLBERG, M.A., Proc. Intern. Conf. Plasma Phys. Lausanne 1984, Vol. I, 55.

/10/ W VII-A TEAM, NI GROUP, 11th Europ. Conf. Contr. Fusion and Plasma Physics, Aachen 1983, Vol. 7D, 453.

/11/ FONCK, R.J. et al., PPPL-2067 report 1983.

/12/ GRIEGER, G., OHLENDORF, W., PACHER, H.D., WOBIG, H., WOLF, G.H., in Plasma Physics and Controlled Nuclear Fusion Research (Proc. 4th Int. Conf. Madison 1971) Vol. 3, IAEA, Vienna (1971) 37.

/13/ SYKES, A. et al., 11th Europ. Conf. Contr. Fusion and Plasma Physics, Aachen 1983, Vol. 7D, 363.

/14/ ANANIA, G., JOHNSON, J.L., Phys. Fluids 26 (10) 1983, 3070.

/15/ STRINGER, T.E., Intern. School on Plasma Physics, Varenna 1971.

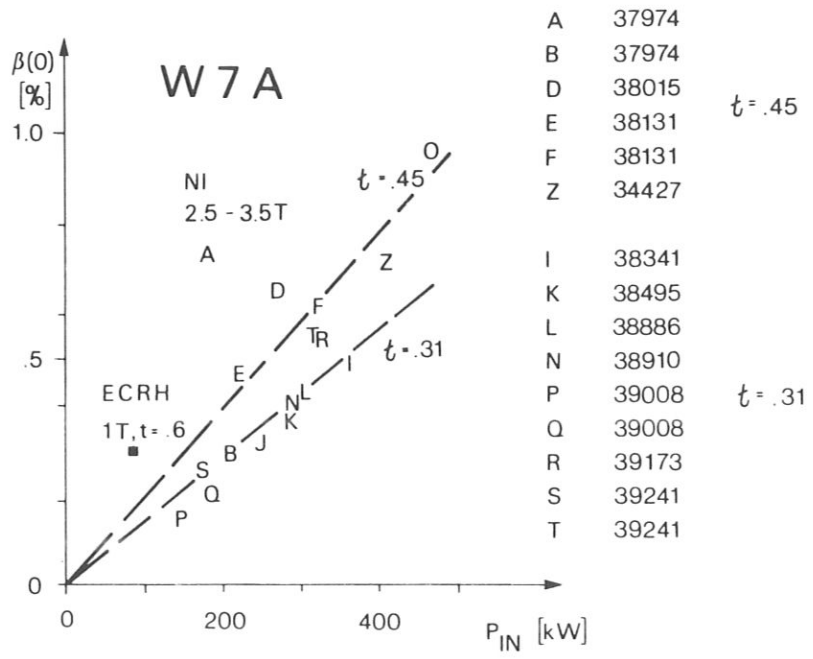

FIG. 1. Maximum ß(o) values in W VII-A depending on the effective heating power P_{IN}. Data for NI heating (2.5-3.5 T) and ECRH (1 T) are included.

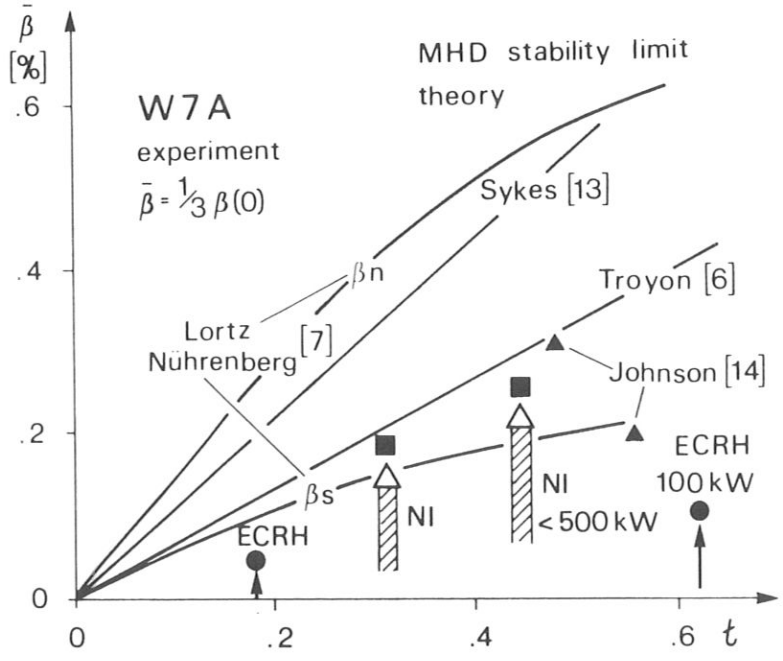

FIG. 2. Comparison of ß limits as predicted by theory for stability in W VII-A with experimental data.

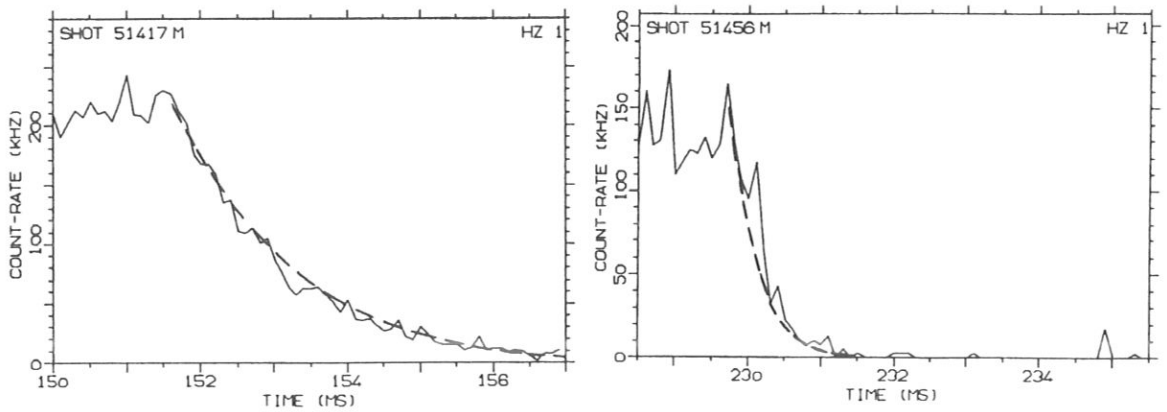

3a) 3b)

FIG. 3. Decay of the neutron flux after switching off the D^0-injector compared with the calculated decay (dashed lines).
3a) $n_{eo} = 3.5 \times 10^{13}$ cm^{-3}, $T_{eo} = 620$ eV.
3b) $n_{eo} = 8.3 \times 10^{13}$ cm^{-3}, $T_{eo} = 320$ eV

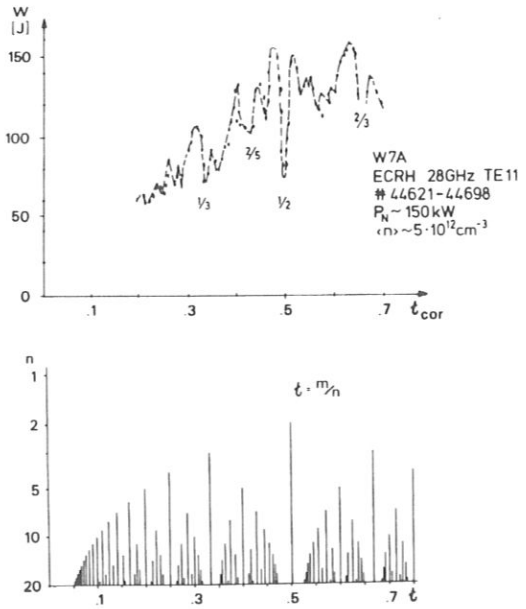

FIG. 4. Energy content depending on the rotational transform $\iota = \iota_0 + \iota_p$ for ECRH.
For correlation rational number $\iota = m/n$ are given and indicated for low n.

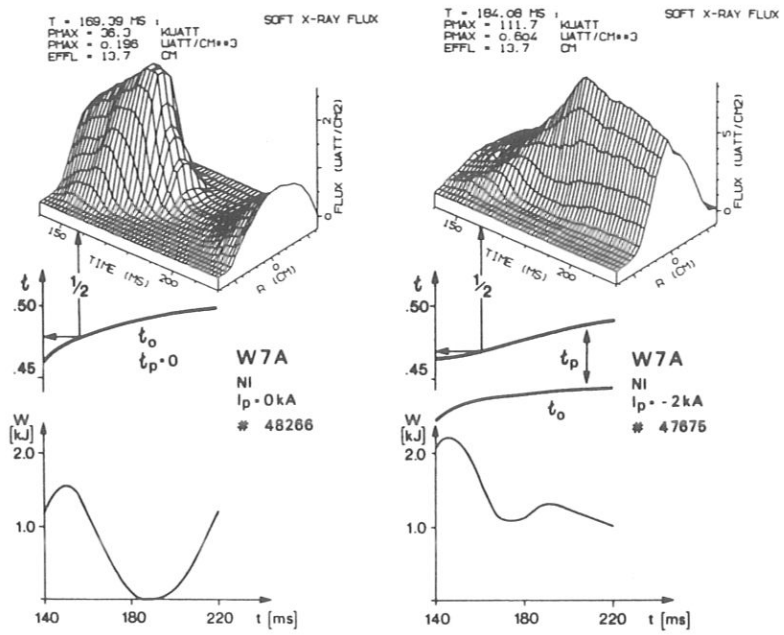

FIG. 5. Influence of shear. The time development of the energy content W, the rotational transform ι and soft-X profile measurements in the vicinity of $\iota = 1/2$ has been correlated for $I_p = 0$ and -2 kA (NI counter, $B_o = -3.2$ T).

Table I: Decay time (msec)

E(keV)	measured	calculated	measured	calculated
28.6 ± 3.9	0.4 ± 0.1	1.05 ± 0.25		0.5 ± 0.1
20.5 ± 2.3	2.45 ± 0.45	3.1 ± 0.5	1.3 ± 0.1	1.2 ± 0.3
12.7 ± 1.2	1.3 ± 0.3	1.6 ± 0.5	0.95 ± 0.25	1.25 ± 0.25
8.8 ± 0.7	2.6 ± 0.2	2.75 ± 0.3	1.75 ± 0.25	1.25 ± 0.25
6.3 ±0.5	4.35 ± 0.75	4.8 ± 0.9	2.15 ± 0.4	2.35 ± 0.5
Plasma Parameters	$n_{eo} = 5 \times 10^{13}$ cm^{-3} $T_{eo} = 540$ eV $T_{io} = 1200$ eV		$n_{eo} = 9 \times 10^{13}$ cm^{-3} $T_{eo} = 360$ eV $T_{io} = 475$ eV	

Energies of injected particles: $E_o = 27$ keV; $1/2\ E_o = 13.5$ keV,
$1/3\ E_o = 9$ keV

SOME ASPECTS OF MODULAR STELLARATOR REACTORS

ABSTRACT

The AS-configuration and a helical axis Stellarator with modular coils have been extrapolated to reactor dimension under the condition of having 1.8 m distance between plasma and modular coils. In case of 5 field periods this leads to reactor dimensions of R_o = 25 m and an averaged plasma radius of 1.6 m, B_o = 5.3 T (ASR). In a burn experiment with 1.2 m space between plasma and coils the dimensions are: R_o = 15 m, $\bar{a}$ = 0.9 m, B_o = 7 T (ASB).

Force and stress analysis in the ASR was done assuming a ring type support structure. Maximum reference stresses of 80 MPa were found.

With a simple neoclassical transport model ignition conditions are calculated. A minimum heating power of 30 MW is necessary for the start-up phase. An AS-type power reactor requires a $\bar{\beta}$-value of 5 %, with a thermal output of 3.6 GW. In ASB the necessary $\bar{\beta}$-value is 2-2.5 % and the output power 0.4 GW. The same start-up power of 30 MW is needed.

INTRODUCTION

Modular coils have been proposed for many Stellarator configurations: a standard 1 = 2 Stellarator /1/, the Advanced Stellarator W VII-AS /2/, the Symmotron /3/ and UWTOR-M /4/. This paper discusses some problems of modular coils for W VII-AS type configurations and HELIAC-type /5/ configurations. In principle for any Stellarator configurations poloidally closed coils can be found /6/, the trajectories Φ = const., Φ being the magnetic potential, are replaced by current filaments. This method, however, is not applicable if the coils are situated outside the last closed magnetic surface. In this case other methods have to be used in order to find the modular coils /7/. Concerning technical application in reactor size Stellarators there are several boundary conditions restricting the parameter space of modular coils.

- There has to be enough space for blanket and shield between first wall and coils.

- The twist of the coils has to be as small as possible in order to facilitate replacement.

- The maximum field on the coils has to stay below a certain limit given by the superconducting material. The field on the magnetic axis should be as large as possible.

- There are limits on forces and stresses in the twisted coils.

In the present paper the W VII-AS configuration and a modular HELIAC configuration are scaled up to reactor dimensions. Forces and stresses are calculated and a start-up scenario assuming neoclassical confinement is discussed.

1) THE ADVANCED STELLARATOR REACTOR (ASR)

In order to extrapolate the W VII-AS configuration to reactor dimensions a minimum distance of 1.8 m between plasma and coils was required /8/. This led to a major radius of 25.5 m and 1.65 m averaged plasma radius. Table I summarizes the parameters of ASR

TABLE I

Major radius	R_o	=	25.5	m
Plasma radius	$\bar{a}$	=	1.6	m
Magnetic field on axis	B_o	=	5.3	T
Maximum field on coils	B_{max}	=	8.7	T
Rotational transform	ι	=	0.58	
Aspect ratio			16	
Coil aspect ratio			4.9	
Coil current density	j_{max}	=	9.8	MA/m^2

Fig. 1 shows several poloidal cross sections of the configuration and fig. 2 a top view of the whole coil set.

The maximum magnetic field of 8.7 T allows to stay within the NbTi technology. Here ten coils per period are chosen in order to minimize the modular magnetic field ripple. Because of the tight arrangement of the coils maintainance and replacement of a single coil might be difficult or even impossible. A reduction to 4 coils per periods removes this problem. On the other hand the ratio B_{max}/B_o increases from 1.64 to 1.9 and a large modular ripple occurs. The ripple $1/2\ \delta B/B$ on the magnetic axis is 1.9 % in the 10 coil case and 8.5 % in the 4 coil case. The increased ripple certainly will increase plasma losses. Also the rotational transform, the magnetic well depth and the plasma radius are changed by this reduction.

Forces and stresses of the ASR coil set have been analyzed and described in /9/ and /10/. Besides radial forces also toroidal and poloidal forces react upon the coils. The basic concept of the support structure is an outer ring surrounding each coil and also side supports. Elastic paddings between stainless steel supports and the coil together with the ring

support minimize the bending stresses. This way the peak value of the reference stress (van Mises stress) can be reduced to 80 MPa. Work is in progress in order to study the mutual support of the coils /11/.

2. THE BURN EXPERIMENT (ASB)

The dimensions of the ASR are mainly determined by the necessary distance of 1.8 m between the coils and the plasma. In a burn experiment the minimum distance can be reduced to the space necessary for a shield. Under the assumption that a minimum distance of 1.2 m is sufficient for a shield the dimensions of a burn experiment are much smaller than in ASR.

TABLE II summarizes the parameters of ASB

Major radius	R_o	= 15.2	m
Mean plasma radius	$\bar{a}$	= 0.9	m
Rotational transform	ι	= 0.51	
Magn. field on axis	B_o	= 7	T
Max. magn. field on coils			
9 coils/period	B_{max}	= 11	T
6 coils/period	B_{max}	= 12.6	T
Coil current density	J_{max}	= 18	MA/m^2

The choice of B_o = 7 T on axis has been made in order to improve plasma confinement. Due to the higher magnetic field and the higher current density forces are also higher than in ASR. ($\bar{F}_{max}$ = 42 MN/m^3 in ASR and $\bar{F}_{max}$ = 90 MN/m^3 in ASB.

Correspondingly the stresses are also higher. $\bar{F}$ is the average force density over the cross section of the coil.

3. THE START-UP SCENARIO

A simple transport code calculating $T_i(r)$, $T_e(r)$ and density n(r) in cylindrical approximation is used in order to study the start-up procedure and the condition of the ignited plasma. The start-up is calculated as a sequence of equilibrium states, which is justified, if the time scale of start-up is much longer than the plasma confinement time. Neoclassical transport coefficients as modelled by Houlberg /12/ are used, an effective helical ripple of 2 % on axis and 7 % on the plasma edge takes into account localized particles and the $1/\nu$ -scaling of transport-coefficients in the long mean free path regime. Ion heat conduction is strongly reduced by a radial electrical field.

Heating mechanisms are α-particle heating and an external heating mechanism with a given deposition profile. Losses of trapped α-particles are not yet taken into account. Also the refuelling mechanism is not included selfconsistently, instead the particle deposition profile is given and the particle refuelling flux Φ_o is considered as a free parameter.

The following result was obtained: With a net heating power of P = 30 MW it is possible to heat ASR and ASB to ignition.

A low density plasma has to be heated to temperatures of 7-8 keV, then, by increasing the density α-particle production supports the heating until the ignited state is reached and the external heating power can be reduced to zero.

In table III the plasma parameters of the ignited state are given

TABLE III

	ASB	ASR (power)
$\bar{n}$ [m^{-3}]	2×10^{20}	1.4×10^{20}
n(o) [m^{-3}]	6×10^{20}	2.4×10^{20}
$\bar{T}_e$ [keV]	6.7	12
$\bar{T}_i$ [kev]	6.7	10.3
τ_E [s]	2.4	1.7
β_{max}	7.5 %	12 %
$\bar{\beta}$	2.5 %	5.3 %
$n\tau_E$ [s/m^3]	5.4×10^{20}	2.4×10^{20}
Fusion power [MW]	419	3600
α-heating power [MW]	104	720

The parameters of ASB are the minimum parameters for ignition. Raising the density leads to more α-particle heating power and higher β. In ASR the parameters are calculated for a total fusion power of 3.6 GW, in this case ignition is already possible at $\bar{\beta} \approx 2$ % and a α-particle heating power of 120 MW.

The parameters calculated above are consistent with neo-classical transport under moderate assumptions. A $\bar{\beta}$-value of 2-2.5 % is within the equilibrium limit of the AS-configuration, the problem of MHD-stability has not yet been investigated is detail, evaluation of the Mercier criterion yields a stability limit of $\bar{\beta} = 1$ % /13/.

4. HELICAL AXIS CONFIGURATIONS

Helical axis configurations are of interest because of the high MHD-stability limit of $\bar{\beta} = 30$ % in the linear case /14/. The problem of modular coils for this type of helical axis Stellarator has been discussed by A. Reiman and A. Boozer /15/; they proposed bean shaped planar coils for modelling a helical configuration with a magnetic well. The difficulty in using planar coils is the proximity of the coils to the plasma surface which leaves no space for blanket and shield. By twisting the coils appropriately this problem can be removed.

Starting from an analytic coil winding a study of HELIAC-type configurations has been made with 5 field periods. In fig. 4 and fig. 5 two periods of a coil set and the magnetic surfaces of a 5-period configuration are shown. The rotational transform is $\iota = 1.8$ and the magnetic well is marginal. The case shown in these figures is calculated for an experiment with 4 m major radius and a magnetic field of 3 T. The aspect ratio of the plasma is 10.

A similar case has been scaled up to reactor dimensions under the same conditions of 1.8 m distance for blanket and shield. The dimensions are: major radius 25 m, averaged plasma radius 1.6 m, $B_o = 5$ T, $B_{max} = 9.5$ T (fig. 6). Forces and stresses are comparable to those in the AS-reactor.

A certain optimization with respect to plasma confinement can be done by an appropriate arrangement of the twisted coils along the central helix. Equal distance of the coils leads to a large magnetic mirror along the magnetic axis whereas by an appropriate choice of the coil position this ripple can be reduced to 1-2 % (fig. 7). Consequently the number of trapped particle is reduced leading to a reduction of neoclassical particle losses. Although in the optimized configuration trapped particles are finally lost due to local minima of $|B|$ between the modular coils, the average drift velocity of the guiding centers is markedly reduced, in comparison to those of the non-optimized configuration. In fig. 8 the diffusion coefficient, calculated by Monte-Carlo methods, demonstrates the difference between these two cases. Due to this kind of optimization neoclassical losses can be made comparable to those of the AS-configuration.

CONCLUSIONS

The analysis of the modular AS-configuration and a modular HELIAC-type configuration under reactor dimensions shows that the space for blanket and shield is the critical parameter in determining the overall dimensions of the reactor. It leads to a large major radius of R_o = 25 m and a plasma aspect ratio of A = 15. If one stays within the limits of NbTi-technology the forces and stresses in the twisted coils are not excessively large if a suitable support scheme is chosen. Under neoclassical conditions plasma confinement is dominated by trapped particles. If the effective helical ripple is below 10 %, 30 MW net heating power are necessary to heat the plasma to ignition. This is a minimum value in case of a slow start-up scenario. The thermal stability of the ignited state needs further investigation. Also the question of ß-limits is still open. In the case of the burn experiment (ASB) the magnetic field B_o is assumed to be 7 T which is only possible within Nb_3Sn-technology. The required $\bar{\beta}$-value of 2-2.5 % for ignition is rather moderate. A power reactor requires an average ß of 5 %, it is not clear whether this can be achieved in an AS-configuration with a planar magnetic axis.

ACKNOWLEDGEMENTS

We should like to thank Dr. J. Lyon for a numerical code calculating the neoclassical transport coefficients.
Also the valuable assistance of Mrs. I. Ott in programming the transport code TEMPL is appreciated.

REFERENCES

/1/ MILLER, R.L., Los Alamos Report LA-8978MS.

/2/ BROSSMANN, U. et al., Paper Q-5, 9th Intern. Conf. on Plasma Physics and Contr. Nuclear Fus. Res. IAEA-CN-41, Baltimore 1982.

/3/ LYON, J.F. et al., Paper Q-3, 9th Intern. Conf. on Plasma Physics and Contr. Nuclear Fus. Res. IAEA-CN-41, Baltimore 1982.

/4/ BADGER, B. et al., UWTOR-M, Report UWFDM-550, University of Wisc., Madison, Wisc. 1982.

/5/ BOOZER, A.H. et al., Paper Q-4, 9th Intern. Conf. on Plasma Physics and Contr. Nuclear Fus. Res. IAEA-CN-41, Baltimore 1982.

/6/ REKHER, S., WOBIG, H., Proc. 7th Symp. on Fus. Technol. EURATOM-report EUR 4938e, (354-357) 1972.

/7/ DOMMASCHK, W., Z. Naturforsch. 37a 867 (1982).

/8/ BROSSMANN, U., GORENFLO, H. HARMEYER, E., KISSLINGER, J., RAEDER, J., RAU, F., WOBIG, H., Proc. 11th EPS-Conf. on Contr. Fus. and Plasma Physics, Aachen 1983, paper D08.

/9/ HARMEYER, E., BROSSMANN, U., GORENFLO, H., KISSLINGER, J., MUKHERJEE, S.B., RAEDER, J., RAU, F., WOBIG, H., IPP-Report IPP 2/269 1983.

/10/ MUKHERJEE, S.B., IPP-Report, IPP 2/271 1984.

/11/ HARMEYER, E., KISSLINGER, J., RAU, F., WOBIG, H., Proc. of 13th SOFT, Varese, Sept. 1984 to be published.

/12/ HOULBERG, W.A., SHAING, K.C., LYON, J.F., Proc. 4th U.S. Stellarator Workshop, p. 77, Oak Ridge, April 14-15, 1983.

/13/ NÜHRENBERG, J., IPP-Annual Report 1983 Garching, p. 122.

/14/ MERKEL, P., NÜHRENBERG, J., GRUBER, R., TROYON, F., Nucl. Fusion, Vol. 23, No. 8 (1983) p. 1061.

/15/ REIMAN, A., BOOZER, A., Phys. Fluids 26(11) Nov. 1983 p. 3167.

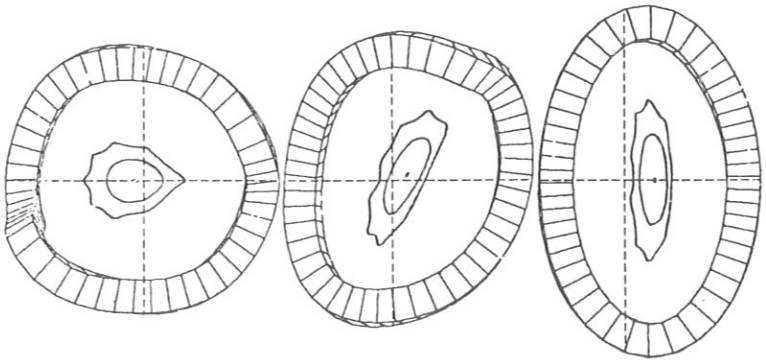

FIG. 1. Different cross sections of magnetic surfaces and coils in ASR.

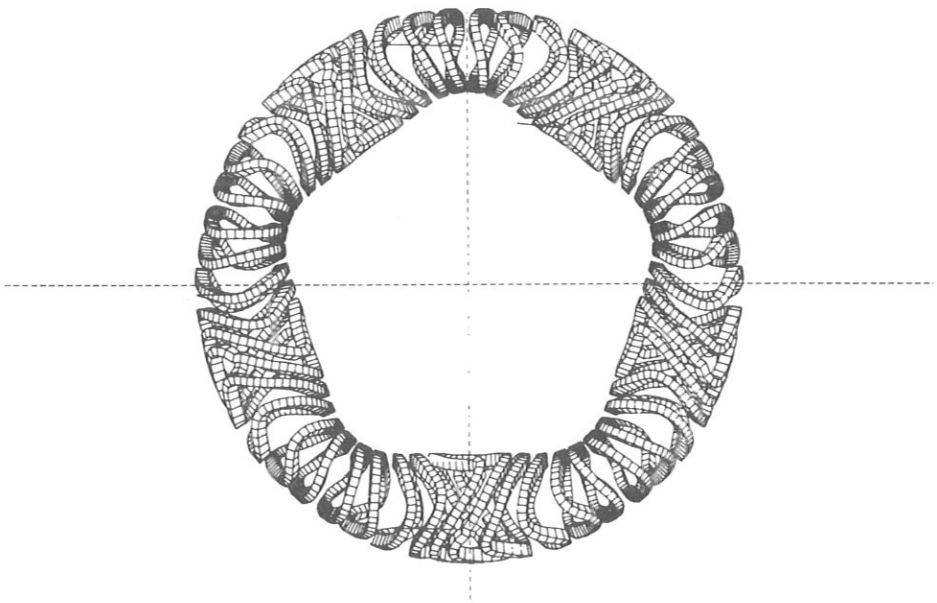

FIG. 2. Top view of the ASR coil set. 10 coils/period.

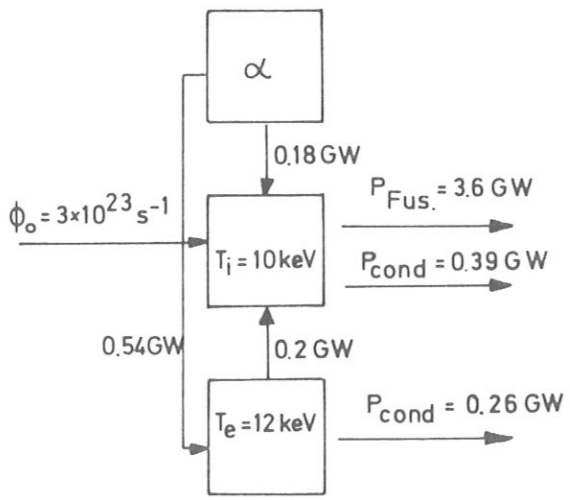

FIG. 3. Power flow diagram of the ASR reactor plasma.

$\bar{n}\tau = 2.4\times10^{14}\,(cm^{-3}s)$; $\bar{\beta} = 5.3\,\%$

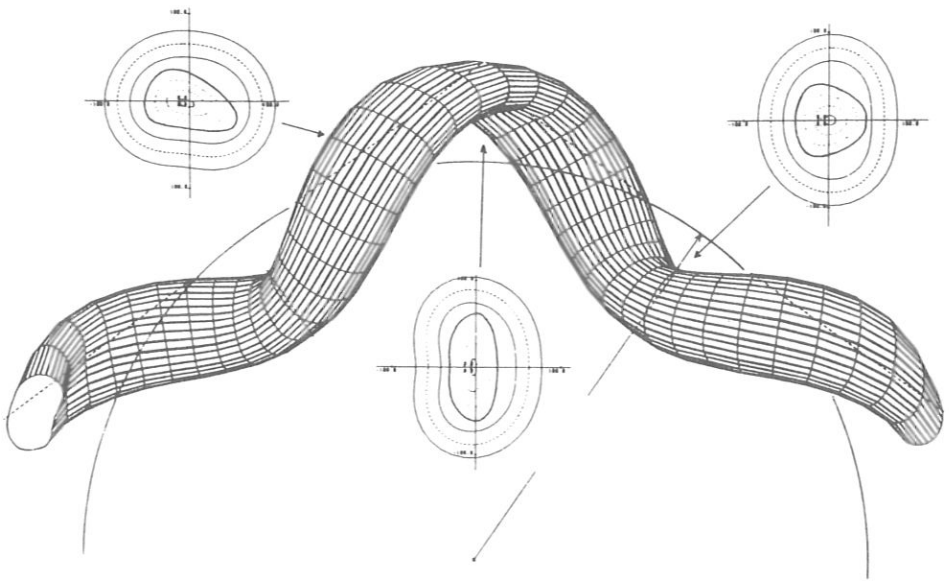

FIG. 4. Magnetic surface of a helical axis configuration. 5 field periods, ι = 1.9, marginal magnetic well, $R_o/\bar{a} \approx 10$.

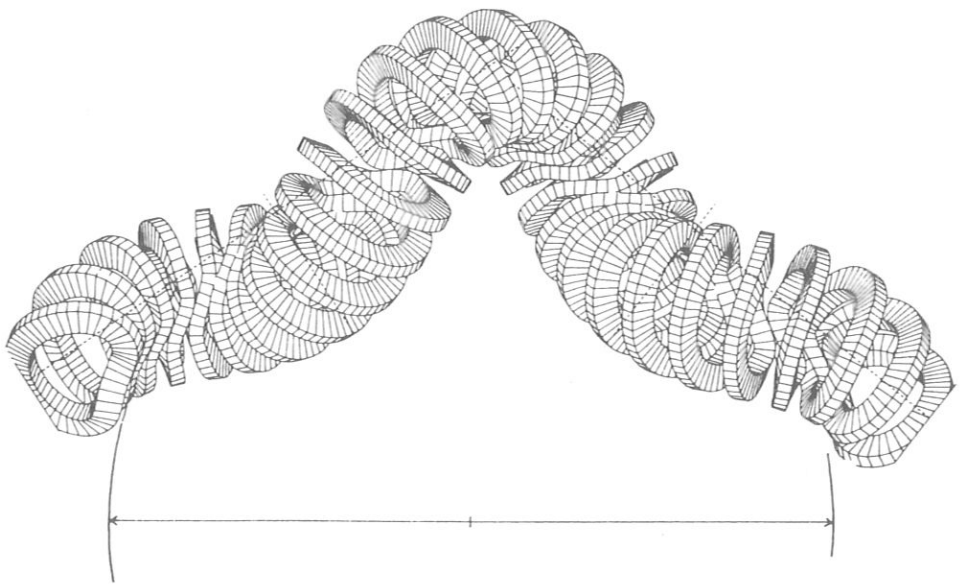

FIG. 5. Twisted coils of the helical axis configuration. 2 periods.

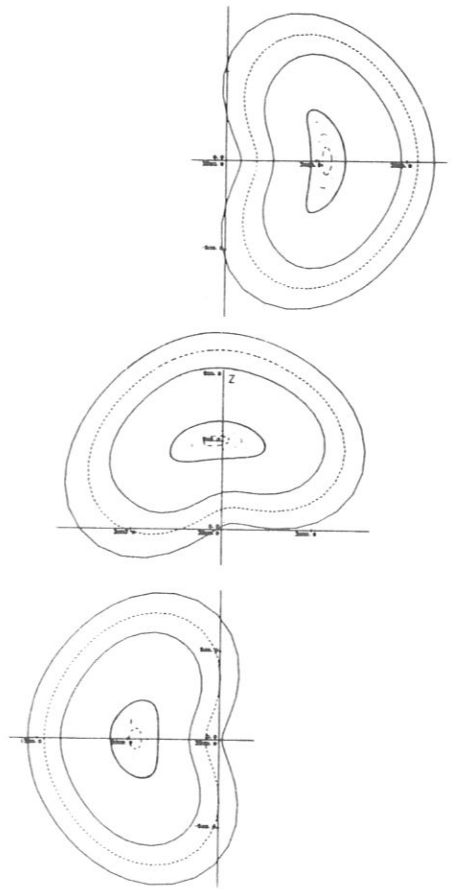

FIG. 6. Helical axis configuration with reactor dimensions. R_o = 25 m.

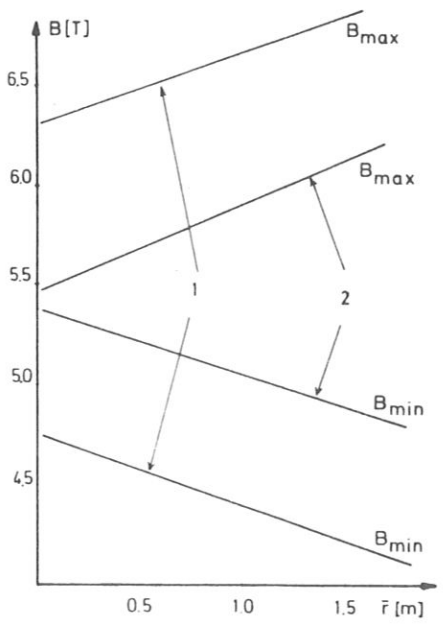

FIG. 7. B_{max} and B_{min} on magnetic surfaces will average radius $\bar{r}$. Case 1: coils with equal distance, case 2: coil position optimized. Reduction of mirror ratio.

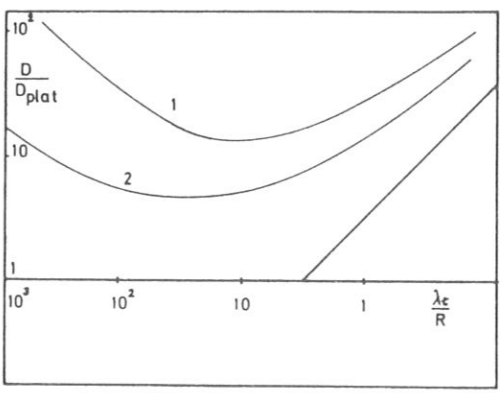

FIG. 8. Diffusion coefficient of helical axis configurations.
1: non - optimized case.
2: optimized case.

Plasma Physics and Controlled Fusion Vol.28, No.1A pp.43-53, 1986 0741-3335/86$3.00+ .00
Printed in Great Britain Institute of Physics and Pergamon Press Ltd.

CONFINEMENT OF STELLARATOR PLASMAS WITH NEUTRAL BEAM AND RF HEATING IN W VII-A

G. Grieger and W VII-A Team*,
NI-Team**, ECRH Group***, Pellet Injection Group (K. Büchl)

Max-Planck-Institut für Plasmaphysik
EURATOM-Association, D-8046 Garching, FRG

* G. Cattanei, D. Dorst, A. Elsner, V. Erckmann, G. Grieger, P. Grigull, H. Hacker, H.J. Hartfuß, H. Jäckel, R. Jaenicke, J. Junker, M. Kick, H. Kroiss, G. Kuehner, H. Maaßberg, C. Mahn, S. Marlier, G. Müller, W. Ohlendorf, F. Rau, H. Renner, H. Ringler, F. Sardei, M. Tutter, A. Weller, H. Wobig, E. Würsching, M. Zippe

** K. Freudenberger, W. Ott, F.-P. Penningsfeld, E. Speth

*** W. Kasparek, G. Müller, P.G. Schüller, K. Schwörer, M. Thumm, R. Wilhelm (Inst.f.Plasmaforschung, Univ. Stuttgart)

ABSTRACT

WENDELSTEIN VII-A has been operated for ten years. It is a low-shear, high-aspect-ratio device. The confinement properties have been thoroughly studied for both ohmically heated and net-current free plasmas. For the latter case, NBI- and ECF-maintained plasmas were of particular importance. It was found that under optimized conditions the core of high-pressure, net-current free plasmas is mainly governed by collisional effects. The experiment will now be shut down for upgrading it into the Advanced Stellarator WENDELSTEIN VII-AS.

KEY WORDS

Stellarator, WENDELSTEIN VII-A, Confinement, Radial electric fields, Net-current free operation, NBI, ECF-heating, Resonances.

INTRODUCTION

WENDELSTEIN VII-A started operation ten years ago. Towards the end of 1985 the machine will be shut down for upgrading it into the Advanced Stellarator WENDELSTEIN VII-AS. It is thus justified to start with a short summary of the main results obtained during the ten years of operation of W VII-A before concentrating on the main subject of this paper.

The definition of W VII-A, 15 years ago, was based on the results of the worldwide Stellarator programme which included race-track machines, like the C-Stellarator and URAGAN, HELIOTRONS, etc., together with the favourable results of the WENDELSTEIN I and II series operated with thermal cesium and barium plasmas. Whereas the plasma confinement in the other machines seemed to be more or less governed by Bohm diffusion, the results obtained by Berkl and others (1966) with cesium or barium plasmas in W I-B and W II-A clearly showed that collisional diffusion can be reached. These experiments also exhibited the effects of resonances in the twist number iota /2/ for $\iota = m/n$ as shown by Grieger and co-workers (1971) (see Fig. 1).

For these reasons, W VII-A was designed with the smallest possible deviation from axisymmetry: no race-track, TF-ripple $\leq 10^{-4}$ over the plasma cross-section, and even the helical ripple could be kept below $\varepsilon_h \leq 2$ %. In addition, the shear of the magnetic field, $\Delta\iota/\iota$, was arranged below 2 % in order to be able to exclude major resonances of the twist number from the confinement region. For stability, the configuration was provided with an average magnetic well. In order to achieve highest flexibility, the twist was introduced into the configuration by the field of an $l = 2$, $m = 5$ helix superimposed upon a purely toroidal

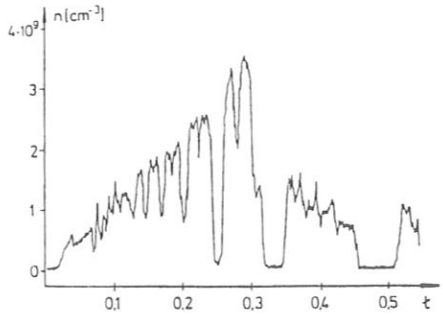

Fig. 1. Confinement vs. twist number ι for a barium plasma in the shearless Stellarator W II-A. For constant input flux of barium plasma the resulting density is a direct measure of the confinement time.

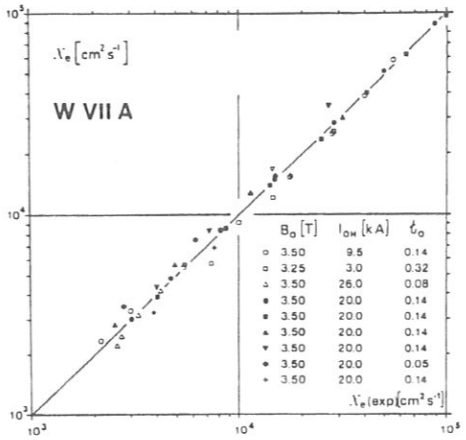

Fig. 2 Electron heat conduction for OH-plasmas in W VII-A for regions free of tearing modes and sawteeth.
$\chi_{e,OH} = 3.8 \cdot 10^{18} \cdot 1/n_e T_e^{2/3}$ is compared with experimental results.

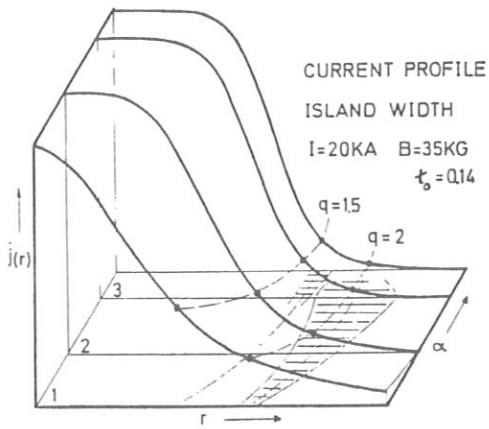

Fig. 3. Expected width of magnetic islands (hatched region) for various profiles of the OH-current distribution as they may result from the power deposition profile of NBI.

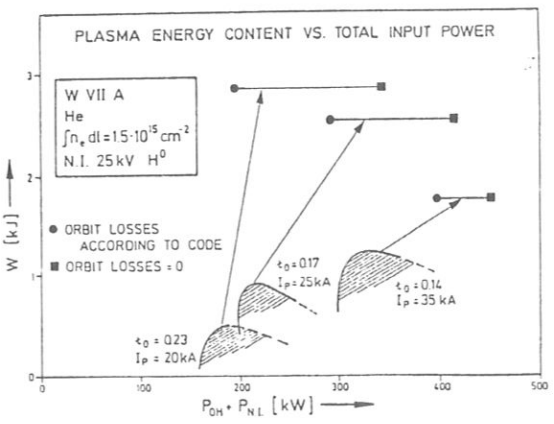

Fig. 4 Increase in plasma energy by NBI heating of OH target plasmas (hatched region). In all cases the curves indicate that the confinement time increases with the application of NBI.

main magnetic field. The major parameters of W VII-A are R = 2 m, $\bar{a} \approx 0.1$ m (depending on iota), $B \leq 4$ T, $t \leq 0.6$ at B = 3 T. For plasma heating, the machine was equipped with an air-core transformer for ohmic heating and later amended by 1.2 MW near-perpendicular neutral particle injection, 200 kW ECH with a frequency of 28 GHz first and 70 GHz later, and with about 500 kW ICH.

MAIN RESULTS

Ohmic Discharges

Already the first experiments with ohmic discharges (W VII-A Team, 1977) clearly showed that current disruptions could be fully stabilized by the Stellarator helical field whenever its contribution to the twist exceeded $t_o = 0.14$ or so. Under such conditions tearing mode evolution and island generation could be analysed even far into the regime which would be subject to disruptions under pure Tokamak operation (W VII-A Team, 1979). χ_e, the electron heat conduction coefficient was measured locally in such regions of the profile as were free of low order tearing modes and sawtooth oscillations, and yielded (see Fig. 2)

$$\chi_{e,OH} = 3.8 \cdot 10^{18} \frac{1}{n_e T_e^{2/3}} \text{ cm}^2 \text{ s}^{-1} \qquad (1)$$

with $[n] = \text{cm}^{-3}$ and $[T] = \text{eV}$. This relation was found for all the accessible parameter ranges. There was no explicit dependence on the plasma current except where tearing modes occurred. There the transport was certainly larger. For these measurements B was 3.5 T. From later experiments at lower magnetic fields there are indications that the coefficient of proportionality shows some decrease with decreasing magnetic field.

Ohmic Discharges With Additional Heating

Care has to be taken when applying high power neutral injection to an ohmic discharge. The differences in the power deposition profile can easily lead to a change in the electron temperature profile, thus to a change in the OH-current distribution and to an onset of one of the critical tearing modes (e.g. m = 2) in turn (Fig. 3). With the help of the externally produced iota the resonant surfaces can be shifted in radius and as long as the most critical ones (low m and n) can be kept out of the regions of steep gradients of current density the above effects can be avoided. Under such conditions high power neutral beam injection heating is found to be efficient, to lead to steep temperature gradients in the plasma edge region, and not to exhibit confinement deteriorations (Fig. 4), (W VII-A Team and others, 1981).

In Figure 5, 120 kW of 70 GHz ECH power were applied to an OH discharge and the parameters of the OH and the EC heated discharge compared. One observes a significant increase in electron temperature combined with an only slight increase in electron density. Since the total heating power, 160 instead of 130 kW, stays nearly constant, a strong increase in electron energy confinement results. The observed effect is in rather good agreement with the electron heat conduction of equation (1), which for the plasma parameters reached in this experiment still yields the major contribution to χ_e.

Transition from Ohmic to Net-Current Free Discharges

With sufficient neutral injection power, the discharge can be maintained by neutral particle injection alone and the initial ohmic current needed for the production of a target plasma be ramped down to zero. At the same time the current in the helical windings was increased so as to keep the total twist constant. Such net current-free plasmas are very quiescent in that all MHD fluctuations die out, and the global energy confinement time shows a corresponding improvement. Figure 6 shows also a remarkable reduction of the H_α-signal when the net-current free conditions are reached. Such signals can be observed at all observation ports around the torus, and when normalizing them by the increasing electron density, they indicate a substantial increase in particle confinement (W VII-A Team and others, 1983 a). The particle confinement time reaches values of 0.1 s or more. Figure 7 shows the effect of a pellet injected into such a current-free discharge. Although density and temperature show strong variations, there is no instantaneous change in the total plasma energy, since the

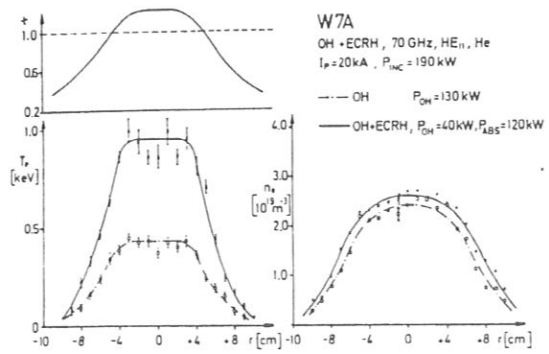

Fig. 5. Comparison of an OH-plasma without and with additional ECRH. The increase in plasma energy indicates a substantial increase of the confinement time for ECRH.

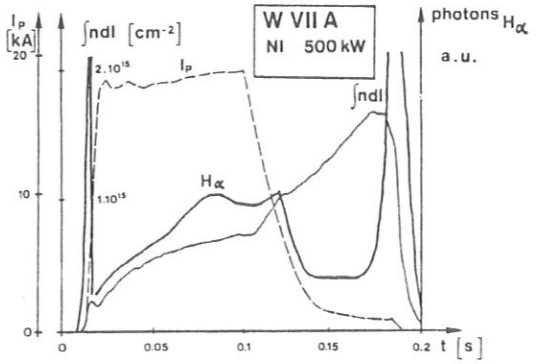

Fig. 6 Transition to net-current free, NBI-maintained operation. The decreasing H_α-signal, inspite of the strongly increasing density, indicates an increase of the particle confinement by about a factor of five at t = 0.17 s.

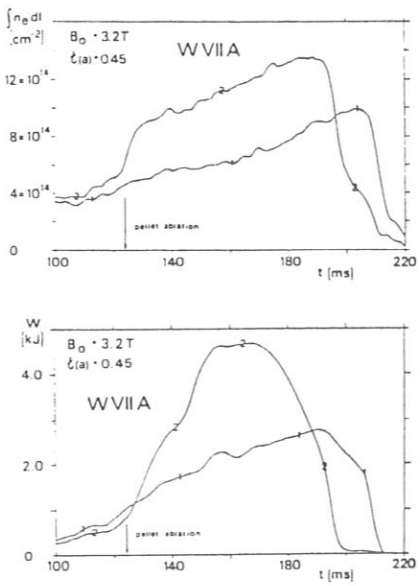

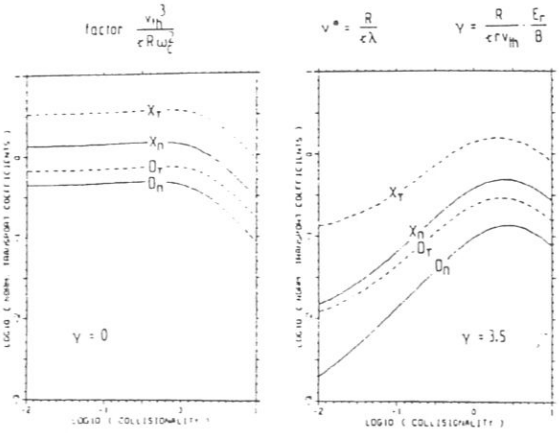

Fig. 8 Calculated transport coefficients vs. collisionality for two values of γ, which is proportional to the electric field, γ = 0 and γ = 3.5. The discharge mentioned in the text correspond to collisionality of 0.1. For this typical case γ = 3.5 corresponds to $E_r \approx 500$ V/cm.

Fig. 7 Pellet injection into an NBI-maintained discharge. Two discharges with and without pellet injection are compared. The top figure demonstrates that the pellet adds its amount of particles to the plasma density without appreciable loss during the course of the discharge. The continuous increase of n is caused by absorption from NBI. The bottom figure shows that there is no instantaneous change of the plasma energy when the pellet is launched. The steeper increase of W is caused by better NBI absorption with higher target density. The earlier decrease of W is caused by higher radiation with higher n.

ionization energy can be neglected. The density jump agrees with the number of the injected particles. The larger rate of increase of the plasma energy after pellet injection reflects the increased absorption of injection power due to the higher plasma density. The density trace indicates that nearly all injected particles remain within the discharge during its full duration which is consistent with a particle confinement time of 0.1-0.2 s or so. Similar particle confinement times were obtained for laser-ablated aluminum the dynamics of which is largely consistent with neo-classical confinement theory except for some regions in space and time where the transport is larger (W VII-A Team and others, 1985 a). There are indications that these deviations may result from the transient formation of magnetic islands or ergodic regions.

In this connection it is immediately obvious that the long confinement times achieved for all particle species in net-current free discharges provide problems with the impurity concentrations piling up during the period of the particle containment time (W VII-A Team and others, 1983 b). Particularly with the high particle densities reached by NBI-maintained discharges radiation mainly by oxygen lines - its ionization states being determined also by charge exchange recombination - becomes the dominant power loss at the end of the discharge. With a plasma radius of only 0.1 m and the high plasma densities reached in W VII-A it is not surprising that the impurities show the observed influence.

RADIAL ELECTRIC FIELD AND CONFINEMENT

Cross-field transport in net-current free Stellarator plasmas is strongly influenced by the formation of radial electric fields. It is well known that such electric fields modify the particle orbits. In particular, the excursion of passing particles from the magnetic surfaces becomes strongly reduced once the ExB-velocity becomes large compared to the poloidal component of the particle's parallel velocity, $v_{\parallel} \tau r/R$. Trapped particles might become untrapped by the same mechanism and then experience the same effect. Transport, being proportional to the square of the step size, will be affected in turn.

Neo-classical theory, within its range of validity, considers the effect of the electric field and takes it into account by requiring ambipolarity of the diffusion fluxes

$$\Gamma_e - \sum_i z_i \cdot \Gamma_i = 0 \qquad (2)$$

From the above arguments and $v_{\parallel,e} >> v_{\parallel,i}$ it is clear that the radial electric field mainly changes the radial transport of the ions whereas that of the electrons remains nearly unaffected. In the theoretical analyses, when determining the electric field via eq.(2) it is customary to assume that the distribution functions f_e and f_i are both Maxwellian and that the dimensions of the plasma are large compared to all essential scale lengths. In strongly heated real laboratory plasmas these assumptions are easily violated.

Caused by the geometric conditions, high power neutral particle injection (28 keV, $\leq$ 500 kW absorbed power) into W VII-A is nearly perpendicular (6° off normal) so that a considerable fraction of the injected neutrals will be born as ions on or scattered into orbits intersecting the wall if there were only the "thermal ambipolar" electric field. If the electron confinement is good, there were no change in electron flux to compensate the higher ion losses and to maintain ambipolarity. Thus for the reason of the corresponding high energy tail in the ion distribution function and of the plasma dimensions allowing the formation of a loss cone, a radial electric field will spring up so as to reduce the ion losses again to those of the electrons by acting on the ion orbits. The same effect might occur with any other heating scheme like ICH or even with ECH where it is observed that the waves interacting with the edge plasma lead to high ion energy tails.

Such electric fields have been found in W VII-A. They were deduced from the measured Doppler shift of impurity lines. Outside about half the plasma radius the measurements yield typical polodial rotational velocities between 10 and 30 km/s corresponding to radial electric fields of 0.3 to 1.0 kV/cm. Under these conditions the E=0-poloidal macroscopic motion of the radiating ions was negligibly small so that no correction needed to be applied. Also the toroidal plasma rotation, measured by the same technique, was typically only of the same order of magnitude as the poloidal one and thus negligible in this connection.

Figure 8 displays the transport coefficients for two values of the radial electric field, $E_r = 0$ and $E_r \approx 500$ V/cm, as they are obtained by analytical computations. The coefficients

are defined by the following two equations for particle and power transport respectively

$$\Gamma = - n[D_n \cdot (n'/n + z\,\phi'/T) + D_T \cdot T'/T] \quad (4)$$

$$Q = - nT[\chi_n (n'/n + z\,\phi'/T) + \chi_T \cdot T'/T] \quad (5)$$

The parameters of a typical discharge: ($n_e = 7.5 \cdot 10^{13}$ cm^{-3}, $T_i = 0.85$ keV, $T_e \approx 0.5$ keV, $B = 3$ T, $t \approx 0.5$) correspond to a collisionality of 0.1 in Fig. 8.
The discovery of these electric fields has three main and essential consequences: (i) The heating efficiency of the nearly perpendicular neutral beam injection increased by factors of up to three (or even more for counter-injection) by trapping a considerable fraction of the orbits lost otherwise. Thus the absorbed NBI power could reach values of up to 500 kW. (ii) According to Fig. 8, the ion particle confinement time should increase considerably. Since the resulting times are longer than the duration of the discharge, they are not accessible to direct measurement. The results displayed in Fig. 7 strongly indicate that the particle confinement time is very long indeed. (iii) As apparent from Fig. 8, also the ion heat conductivity, $\chi_{i,T}$, experiences a drastic reduction with E_r due to the reduced step width in the collisional transport. This effect is supported by the experimental results because without this reduction there was no chance to satisfy the power balance of the electrons and ions without violating laws resulting from basic collisional effects. It also predicts that in NBI heated plasmas the ions stay at higher temperature than the electrons which agrees with the observations.

Collisional slowing down of the high-energy ions resulting from neutral injection was verified from the measured charge exchange spectra and from the time-dependent neutron emission when using DD plasmas, (W VII-A Team and others, 1984).

Thus the occurrence and the influence of the radial electric field are basically understood. They result from classical effects and geometrical limitations only. The connected influence on particle orbits and transport is large and supported by experimental results.

ELECTRON CYCLOTRON FREQUENCY PLASMAS

Electron cyclotron frequency (ECF) plasmas could be generated in W VII-A without any special means for pre-ionisation and without using OH currents. 200 kW RF power were available for this purpose, with a frequency of 28 GHz in the earlier experiments and 70 GHz later. These plasmas are highly interesting for two reasons: (i) to serve as a target plasma for further heating by more intense heating sources like NBI or ICF, and (ii) to preferentially study the transport properties of the electron component of the plasma.

As far as case (i) is concerned, only plasmas generated by using the 70 GHz frequency have a chance to reach interesting parameters since the low cut-off density connected with 28 GHz only allows plasmas to be established with densities not exceeding 10^{13} cm^{-3}. Fig. 9 shows an example of an ECF generated plasma ($n_{eo} = 2 \cdot 10^{13}$ cm^{-3}, $T_{eo} = 1.4$ keV) further heated and maintained by NBI. It reaches densities of $n_{eo} = 1.1 \cdot 10^{14}$ cm^{-3} and temperatures of $T_{e,o} = 350$ eV so that this method of plasma generation is experimentally proven and available. Densities of up to $5 \cdot 10^{13}$ cm^{-3} are accessible by ECF (70 GHz) application alone. The cut-off density is $6 \cdot 10^{13}$ cm^{-3}.

First information on electron transport was obtained by using the 28 GHz gyrotron. The plasma parameters achieved are plotted in Fig. 10 (label 28 GHz). Taking the density profile from the measurement the various contributions to the heat conduction are calculated and shown in Fig. 11a. The axisymmetric part, $\chi_{e,HH}$, is taken from Hinton-Hazeltine (1976), the ripple contribution, $\chi_{e,ripple}$, from Shaing and others (1984). The anomalous part is given by eq. (1) of this paper but the coefficient reduced to $1.5 \cdot 10^{18}$ (for $B = 1$ T) to obtain best agreement with the experiment. The sum of the three contributions very well agrees with the values of χ_e derived from the local temperature gradients and the assumption of central power deposition. Contributions by radiation are small under these conditions (10-30 kW).

Also in Fig. 10 the data for a 70 GHz discharge at $B = 2.5$ T are shown. The results clearly exhibit a considerable increase in density and temperature for about the same ECF power applied as before, indicating a large increase of confinement as qualitatively expected from neo-classical theory. Fig.11(b), however, shows that in the region of the steepest gradients the neo-classical effects have already become smaller than $\chi_{e,OH}$ so that a clear-cut verifi-

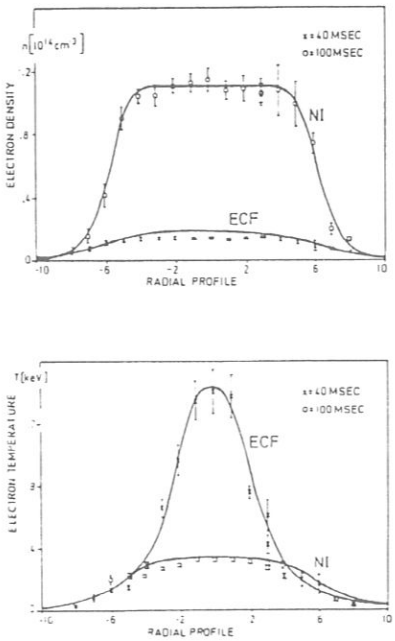

Fig. 9 A target plasma produced from the gas phase by 100 kW absorbed ECF-power is "taken over" by NBI with three injectors (220 kW absorbed power).

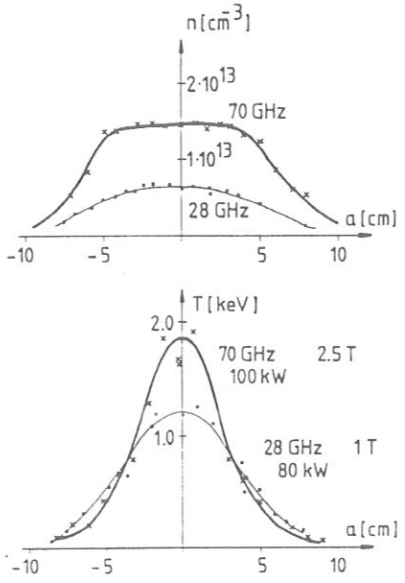

Fig. 10 ECF produced net-current free discharges for two cases: 28 GHz at 1 T and 70 GHz at 2.5 T. One immediately observes the difference in gradients. Please note that the particle source is at the edge but the power source at the plasma center.

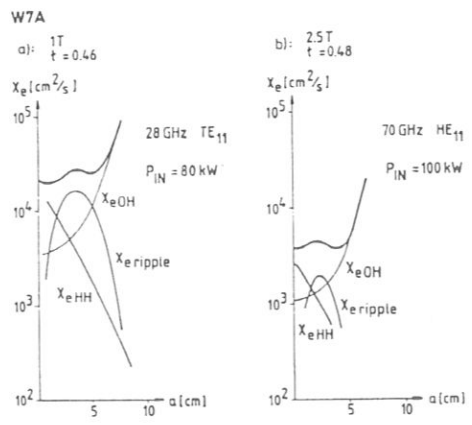

Fig. 11: Electron heat transport coefficients for the two discharges shown in Fig. 10. The bold trace is the sum of the three contributions:
$\chi_{e,HH}$, $\chi_{e,ripple}$ and $\chi_{e,OH}$ (see text).

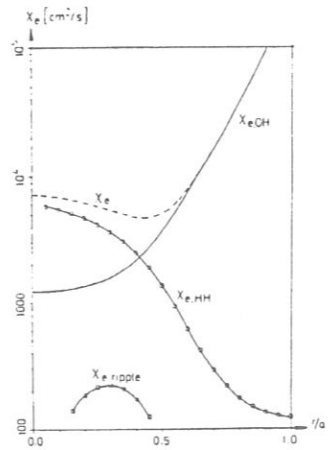

Fig. 12 Calculated transport coefficients for a discharge with $t(o) = 0.1$, $t(a) = 0.35$, $T_e(o) = 0.87$ keV, $n_e(o) = 2.2 \cdot 10^{13}$ cm^{-3}, B = 2.5 T and $\chi_{e,OH} = 2.5 \times 10^{18}/nT^{2/3}$.

cation of their variation with B is difficult.

The essential result of these experiments is that in cases where n and T are high enough for the anomalous contribution of eq. (1) to become small against the neo-classical transport coefficients the latter ones determine the discharge. Since the neo-classical transport coefficients for the electron channel strongly increase with temperature whereas the opposite behaviour is found (at least for all the plasma parameters accessible) for $\chi_{e,OH}$ of eq. (1) one should be able to conclude that the influence of $\chi_{e,OH}$ becomes more and more restricted to the plasma edge the higher the plasma parameters grow. Since this is an important point it is useful to add information about a discharge produced by 70-GHz RF power but with a small plasma current superimposed to reduce the twist value mainly at the plasma center and thus to increase the neo-classical transport coefficients as compared to the OH ones. Fig. 12 shows that the bulk plasma region of this discharge is governed by neo-classical effects indeed. Ripple effects are not expected to contribute. With these coefficients the temperature profile has been calculated and compared with the measurements in Fig. 13. The agreement is very satisfactory. Please note that there is no normalization factor for the peak temperature, thus the comparison is on absolute terms.

The determination of the electron heat transport will remain an essential element of future experimental work. In this connection, the method of modulating part of the gyrotron power in an on-off fashion of a few hundred cycles per second has proven to be a powerful method. Figure 14 shows the results of such an experiment. Assuming that the main RF power is deposited around the plasma center, one clearly observes the time delay of the arriving heat wave and its effect on the local (magnetic surface) plasma energy.

CONFIGURATIONAL EFFECTS

When describing the main results obtained with W VII-A it was implicitly assumed that the magnetic configuration was adjusted for optimum confinement conditions and the minima seen already in Fig. 1 avoided by proper choice of iota and its variation over the plasma cross-section. It should be understood, however, that major resonances in iota ($\iota = m/n$, with m and n not too large integers), wherever they occur in the plasma, have strong effects on confinement for all the plasmas investigated in W VII-A. These effects are basically understood but the details prevailing in a particular discharge are often difficult to analyse.

At rational values of iota the basic concept of simple nested magnetic surfaces is violated. Under such conditions, the configuration is sensitive either to formation of magnetic islands or ergodic regions by small error fields so that parallel heat transport can "short-circuit" certain confinement regions, or to the creation of convective cells also leading to enhanced transport. Thus, the confinement properties of a particular plasma in a particular configuration are governed by the actual values of iota, its resonances, and the amount of shear. The determining factors for the individual configurations are threefold: (i) the vacuum configuration including all error fields, (ii) any iota and shear produced by j(r) either deliberately introduced by a small loop voltage or resulting from the particular conditions of plasma heating, and (iii) any iota and shear resulting from the finite plasma pressure as given by Kisslinger and Wobig (1985) which reduces |B| by the diamagnetic effect and causes pressure driven currents (bootstrap current?). All these effects are interrelated by the transport conditions depending on them, (W VII-A Team and others, 1985 b).

With the aim to separate these effects, very low beta plasmas were investigated in W VII-A where pressure effects should still be negligible. Fig. 15 shows that for vanishing plasma current a deep minimum occurs at $\iota = 0.5$ accompanied by maxima at both sides. The shear produced by a plasma current of 2 kA already shows some influence on the confinement properties. At I = 4 kA the shear is large enough but not yet too large (see later) to drastically improve the situation for $\iota(a) = 0.5$ and to reach the maxima, but now for all values of iota around $\iota = 0.5$. Under these conditions iota is about 0.7 in the plasma center. The contribution of the plasma current to plasma heating is still negligibly small ($\lesssim 2$ kW).

In Fig. 16 the results of similar experiments are described but for higher plasma pressures. In this case pressure driven currents contribute to the variation of iota over the cross-section. The optimum confinement is achieved for a plasma current of $I \approx 2$ kA for which the loop voltage is just zero. Higher or lower plasma currents require positive or negative loop voltages to be applied. The same measure is necessary if the pressure driven current varies as a consequence of the confinement (and thus pressure) variation with iota. For a plasma

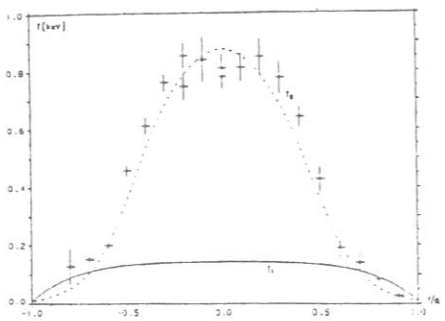

'ig. 13 Comparison of the calculated T_e-profile with the experimental data points. The calculated ion temperature is also given.

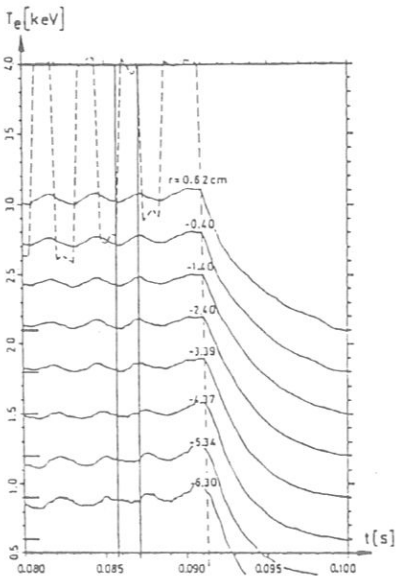

Fig. 14 Time variation of ECE measured electron temperature for different plasma radii. As indicated by the dashed line at the top of the figure, a fraction of the 70 GHz gyrotron power is pulsed in an on-off fashion. The two vertical lines, for the times of switching on or off the gyrotron power, allow the detection of the corresponding heat wave travelling from the inside to the edge of the plasma. Please note from the right-hand end of the traces that the individual traces have been displaced in vertical direction to make relative comparison easier.

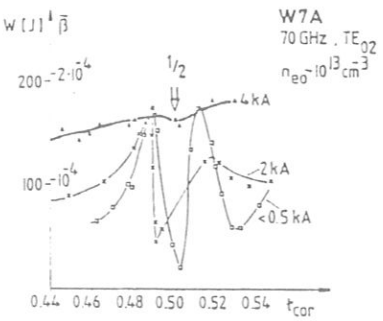

Fig. 15 Achieved plasma energy vs. $\iota(a)$ for constant gyrotron power aiming at low beta. Shear is varied by small plasma currents. The values indicated are adjusted by proper selection of small loop voltages.

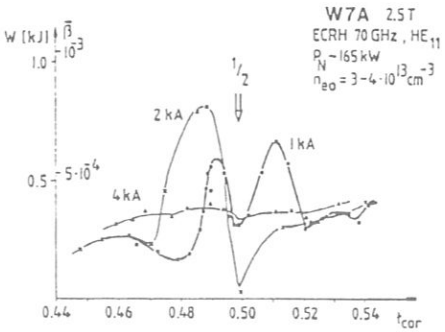

Fig. 16 The same as Fig. 15, but for higher beta values. In this case, also pressure driven currents contribute to the details of the magnetic configuration.

current of 4 kA the confinement parameters become rather independent of iota (except for the general trend to increase with iota). This is similar to the conditions of Fig. 15 but now the maxima of the 2 kA-case are not reached anymore. With the expected distribution of the pressure driven current this result may be explained by the fact that for I = 4 kA and high enough pressure the local shear has become too large to be able to keep the regions of steepest pressure gradients free of low order resonances.

The obvious conclusion from these experiments is that some shear has a positive effect on confinement indeed. Its magnitude has to be limited, however, to avoid the occurrence of major resonances at those regions where the steepest pressure gradients are expected. The vacuum magnetic configuration selected has to consider the contributions by pressure driven currents. As indicated by Fig. 16 it can be chosen such that for the self-adjusting pressure driven current optimum confinement conditions are reached. With the available heating power the maximum beta values achieved in W VII-A ($\beta_o \leq 1\%$, $\bar{\beta} \approx 0.3\%$) were a factor of four higher than those of Fig. 16 without any indication of a limitation in β being reached already, as pointed out by the W VII-A Team and others (1984).

SUMMARY AND CONCLUSIONS

WENDELSTEIN VII-A is a low-shear, high-aspect-ratio Stellarator. It has now been operated for 10 years. Its main results were:

Ohmically heated discharges were found to be sensitive to tearing modes. Already with a small external contribution to the twist of the magnetic lines, $\iota_o \gtrsim 0.14$, the disruptions could be stabilized and the tearing modes studied in a quasi-stationary fashion. Regions free of tearing modes and sawtooth oscillations exhibited anomalous electron heat transport $\chi_{e,OH} \sim n_e^{-1} T_e^{-2/3}$, independent of plasma current. It is very satisfactory to note that at reactor plasma densities and temperatures this formula leads to values by orders of magnitude smaller than the neo-classical contributions to χ_e.

Ohmically heated Stellarator plasmas, further heated either by NBI or ECF, do not show degradation in confinement if care is taken in avoiding major resonances in the confinement region. Typically, the discharge follows the above law as long as it yields the major contribution to χ_e according to the plasma parameters reached.

Net-current free discharges could be maintained by NBI or ECF application. These discharges show no MHD-fluctuations anymore and show the corresponding improvements of confinement. Particle confinement is very long and also the dynamics of laser-ablated impurities (aluminum) seems to be largely consistent with neo-classical confinement theory except for some regions in space and time where the transient formation of magnetic islands or ergodic regions tend to increase the transport.

The self-formation of radial electric fields was found to strongly increase the confinement properties by acting on the ion particle orbits. These fields originate from high energy ions born on orbits intersecting the wall and the condition of ambipolarity. They increase the heating efficiency of NBI and reduce the ion heat conduction. A necessary prerequisite for their occurrence is good electron confinement. ECF-heated plasmas allow the conclusion that for the body of the plasma ($r/a < 2/3$) electron transport is close to neo-classical values including ripple effects which, however, are small for W VII-A.
Confinement in W VII-A is very dependent on the extent to which major resonances in the configuration can be avoided. Some shear is helpful in broadening the maxima of confinement but too much shear does not allow avoiding major resonances in the confinement region around which the transport is increased. Plasma currents driven by the plasma pressure and by the particular heating scheme used are contributing to the details of the magnetic configuration and have thus to be considered carefully. The above results have been obtained for optimized confinement conditions, where the plasma energy has maxima with respect to the value of iota.

WENDELSTEIN VII-A will now be shut down for upgrading it into the Advanced Stellarator WENDELSTEIN VII-AS. By making proper use of the non-axisymmetry of Stellarators, this concept promises to reduce the secondary currents and thus the Shafranov shift, and also to lead to further improvements of the particle confinement, as reported by Brossmann and others (1983). W VII-AS also has a larger plasma radius than W VII-A, thus reducing wall effects accordingly. Together with the increased capacity of the available heating schemes, this should also allow further increase of the plasma parameters.

REFERENCES

Berkl, E., D. Eckhartt, G. von Gierke, and G. Grieger (1966). Resistive diffusion of cesium plasma in a Stellarator. Phys. Rev. Letters, 17, 906.

Brossmann, U., W. Dommaschk, F. Herrnegger, G. Grieger, J. Kißlinger, W. Lotz, J. Nührenberg, F. Rau, H. Renner, H. Ringler, J. Sapper, A. Schlüter, and H. Wobig (1982). Plasma Physics and Controlled Nuclear Fusion Research 1983, (Proc. 9th Int. Conf. Baltimore), Vol. III. IAEA Vienna. p. 141.

Grieger, G., W. Ohlendorf, H.D. Pacher, H. Wobig, and G.H. Wolf (1971). Particle-confinement minima in the Wendelstein II-a-Stellarator. Plasma Physics and Controlled Nuclear Fusion Research 1971, (Proc. of 4th Int. Conf. Madison/USA), Vol.III. IAEA Vienna. pp 37-48.

Hinton, F. L. and W.N.G. Hazeltine (1976).Theory of plasma transport in toroidal confinement systems. Rev. Mod. Phys., 48. p. 239.

Kißlinger, J., and H. Wobig (1985). Stellarator Equilibrium by low-beta-expansion. To be published in Europhysics Conference Abstracts 11th EPS Conference on Controlled Fusion and Plasma Physics, Budapest, 1985. Paper No. 144.

Shaing, K.C., R.H. Fowler, D.E. Hastings, W.A. Houlberg, E.F. Jaeger, J.F. Lyon, J.A. Rome, J.S. Tolliver, and J.D. Callen (1984). The radial electric field in a non-axisymmetric torus. Plasma Physics and Controlled Nuclear Fusion Research.Vol. 2. IAEA Vienna. p. 189.

W VII-A Team (1977). Ohmic heating in the W VII-A Stellarator. Plasma Physics and Controlled Nuclear Fusion Research 1977, (Proc. 6th Int. Conf. Berchtesgaden 1976), Vol.II. IAEA Vienna. p.81.

W VII-A Team (1979). Investigation of the m = 2 mode at q-values around 2 in the W VII-A. Plasma Physics and Controlled Nuclear Fusion Research 1979, (Proc. 7th Int. Conf. Innsbruck 1978), Vol. II. p. 277.

W VII-A Team and NI Group (1981). Neutral injection in the Wendelstein VII-A Stellarator with reduced ohmic current. Plasma Physics and Controlled Nuclear Fusion Research 1981, (8th Int. Conf. Brüssel 1980). Vol. I. IAEA Vienna, p. 185.

W VII-A Team and NI Group (1983 a). Energy and particle confinement in currentless W VII-A Discharges. In S. Methfessel (Ed.),Europhysics Conference Abstracts 11th EPS Conference on Controlled Fusion and Plasma Physics, Aachen, 1983 a, Vol. 7D, Part 1, European Physical Society, Geneva. pp. 191-194.

W VII-A Team and NI Group (1983 b). Neutral injection heating in the Wendelstein VII-A Stellarator. Plasma Physics and Controlled Nuclear Fusion Research 1983, (Proc. 9th Int. Conf. Baltimore 1982), Vol. II. IAEA Vienna. p. 241.

W VII-A Team and NI Group (1984). Plasma confinement and the effect of the rotational transform. Plasma Physics and Controlled Nuclear Fusion Research 1984, (Proc. 10th Int. Conf. London 1984), Vol.2. IAEA Vienna. p. 371.

W VII-A Team and NI Group (1985 a). Impurity transport in the Wendelstein VII-A Stellarator. Accepted for publication in Nuclear Fusion. IAEA Vienna.

W VII-A Team, NI Team, and ECRH Group (1985 b). Influence of the Magnetic Configuration on Plasma Behaviour in the Wendelstein VII-A Stellarator. To be published in Europhysics Conference Abstracts 11th EPS Conference on Controlled Fusion and Plasma Physics, Budapest, 1985. Paper No. 146.

WENDELSTEIN STELLARATORS

G. GRIEGER, H. RENNER, H. WOBIG
Max-Planck-Institut für Plasmaphysik,
Euratom Association,
Garching,
Federal Republic of Germany

ABSTRACT. Experiments on plasma confinement in stellarators started at the Max-Planck-Institute of Physics and Astrophysics immediately after the 1958 Geneva Conference and were continued at IPP Garching. The first devices of the Wendelstein line were W I–A and W I–B, both racetrack-type stellarators. In the circular $\ell = 2$ stellarator W II–A, steady-state barium plasmas were investigated and were found to be governed by collisional diffusion. In W II–B, mainly Ohmic heating was applied. The main stellarator experiment at IPP Garching is W VII–A; after a period of Ohmic heating, the first net-current-free plasma was achieved in 1980. Plasma parameters of up to $T_i = 1$ keV and $n(0) = 10^{14}$ cm^{-3} could be reached by this method. A further heating method is ECRH, which yields maximum electron temperatures of $T_e \geqslant 2$ keV. The paper describes the major results of the devices mentioned and gives a short survey of further planning.

1. STELLARATORS

In the second half of the 1950s, astrophysicists of the Max-Planck-Institute of Physics and Astrophysics started to explore the potential of thermonuclear fusion for contributing to the world energy supply. Soon there was agreement among them that toroidal magnetic confinement offered the best chance of leading to an attractive fusion reactor [1]. However, theoretical investigations showed many potential confinement configurations to be susceptible to severe instabilities, particularly those configurations for which a net plasma current was an essential constituent [2].

In 1958, work on thermonuclear fusion was declassified world wide and at the Geneva Conference the Princeton Group (represented by Spitzer) introduced the stellarator as a confinement concept [3]. At the Max-Planck-Institut, the conceptual elegance of this system was found to be very attractive; this led to the start of the Wendelstein line. The first device (see Fig.1), W I (later called W I–A), had rather small dimensions but incorporated all ideas of the Princeton Group. It was a racetrack, $\ell = 3$ device, since shear was considered to be important for stability. A list of all Wendelstein Stellarators is given in Table I.

Of great importance for the orientation of the Wendelstein work were two papers presented at the IAEA Conference in Salzburg in 1962: (i) The Princeton group reported on the first experimental results of the C-Stellarator [4], one of the biggest fusion devices at that time. As in earlier Princeton Stellarator experiments, anomalous diffusion ('Bohm diffusion') was found, scaling with T_e/B and leading to losses totally unacceptable for future reactors. (ii) Rynn and D'Angelo [5] reported that a thermal (0.2 eV) caesium plasma, produced by contact ionization on two end-plates connected by a homogeneous magnetic field (Q-machine), exhibited classical resistive diffusion as the only loss process. It was a challenging idea to

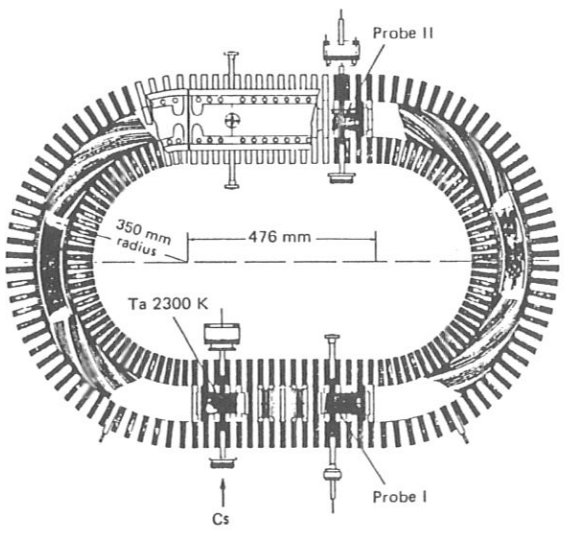

FIG.1. Scheme of the racetrack-type stellarator W I.

TABLE I. WENDELSTEIN STELLARATORS

Name	Type	Major radius (m)	Plasma radius (m)	B_0 (T)	Rotational transform
W I–A	Racetrack $\ell = 3$	0.35	0.02	1	$\iota(a) = 0.2$ $\iota' > 0$
W I–B	Racetrack $\ell = 2$	0.35	0.02	1	$0-0.2$ $\iota' \approx 0$
W II–A	Circular $\ell = 2, m = 5$	0.5	0.05	0.6	$0.0-0.6$ $\iota' \approx 0$
W II–B	Circular $\ell = 2, m = 5$	0.5	0.05	1.25	$\leqslant 0.5$ $\iota_0' \approx 0$
W VII–A	Circular $\ell = 2, m = 5$	2	0.1	3.5	$0.05-0.6$ $\iota_0' \approx 0$
W VII–AS (under construction)	Circular $m = 5$ modular	2	0.2	3	$0.2-0.6$ $\iota_0' \approx 0$

introduce a thermal caesium plasma into our small W I–A stellarator and to determine the confinement properties for such a 'truly Maxwellian plasma'. If Bohm diffusion would result again, then this confinement concept would have clearly disproved its ability to confine a plasma effectively. If, however, classical diffusion would result, then much greater care would have to be taken to minimize all deviations from a Maxwellian distribution function. At the anticipated plasma parameters the difference between these two kinds of loss rates was three orders of magnitude and should thus be easy to detect.

As shown in Fig.2, a vertical extension of the plasma was found in W I–A, yielding an integral loss rate of approximately the Bohm value [6]. The result thus seemed to be clearly negative. However, the particular plasma shape observed led to two further investigations aimed at clarifying the reasons for the observed high loss rate. If the curvature of the magnetic field was indeed responsible for the higher losses in toroidal machines, then serious degradation of confinement should occur when curvature was gradually introduced into the homogeneous magnetic field of a Q-machine; this was investigated [7].

However, as shown in Fig.3, there is only a small change in losses, and this change can be understood as being due to the violation of the $\oint dl/B$ criterion. This result gave some encouragement.

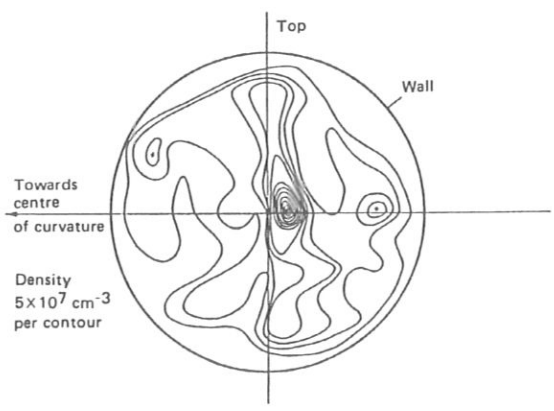

FIG.2. Distribution of density in W I–A (peak electron density 6×10^8 cm^{-3}).

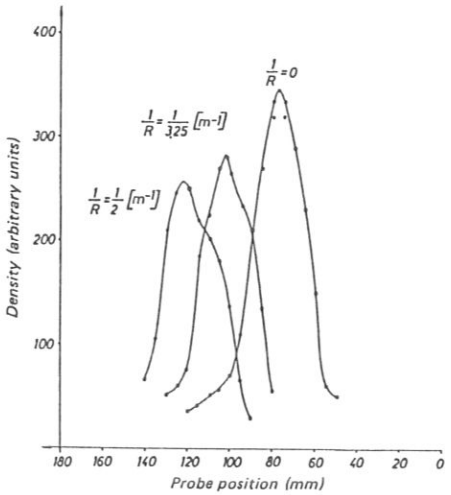

FIG.3. Effect of toroidal curvature on plasma confinement in a Q-machine. Probe measurements of density profiles as a function of 1/R.

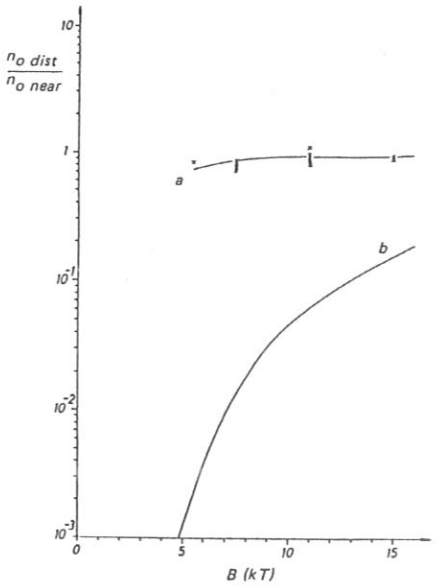

FIG.4. Density measurement in W I–B. Ratio of probe signals (distant probe to near probe) versus main magnetic field. Crosses indicate experimental values. Curve a: assumed resistive diffusion. Curve b: pump-out losses.

On the other hand, an analysis of the full Pfirsch-Schlüter theory [8] showed that not only did the secondary currents present a problem but also a balancing mass flow parallel to B was necessary for equilibrium. The only force to drive this mass flow is a pressure gradient parallel to B, so that a necessary condition for achieving equilibrium is that the ratio of the flow velocity to the ion thermal velocity ($V_\parallel/V_{th}$) remain small relative to unity. For an $\ell = 3$ stellarator (such as W I–A) for which the rotational transform $\iota \sim r^2$, this condition is easily violated in the inner part of the plasma column. In order to check this hypothesis, W I–B was built. This device was equipped with an $\ell = 2$ helical field, yielding a large enough iota all over the plasma cross-section; in all other respects it was identical to W I–A.

In W I–B, classical diffusion was found to be the prevailing cross-field transport (see Fig.4) [9, 10]. This transport was so small that the largest plasma losses occurred on the probes, although these were made extremely thin (50 μm).

A prerequisite for achieving these results was careful adjustment of all correcting magnetic fields, which had to be done with extreme care and which became reproducible only after the unused iron transformer cores (for Ohmic heating) had been removed from the device. These transformer cores had interacted with the configuration via their remanent magnetization and had thus made the field adjustment dependent even on the cores' history.

1.1. W II–A

In today's terms, the configuration of W I–B was highly susceptible to disturbing magnetic fields and corresponding island formation. It was strongly suspected that problems mainly arose from the circularizers for providing the transition from the curved helical field to the homogeneous field of the straight sections. The next device, W II–A, was therefore built as a circular torus. It was operated with a barium plasma produced by contact ionization on a small tantalum ball (3 mm diameter) hanging from a thin (50 μm) wire and heated by CO_2 laser irradiation. The barium plasma allowed probes to be dispensed with and optical methods to be used for measuring the ion density (resonance fluorescence). The experimental results obtained clearly supported the results of W I–B. As expected, the configuration of W II–A was much less sensitive to the adjustment of correction magnetic fields, but, as a new effect, maxima and minima in the confinement properties were clearly displayed when the twist of the lines of force, as measured by the rotational transform ι, was changed (see Fig.5) [11, 12]. The maxima occurred for irrational values of iota and their magnitude closely followed the values expected for classical Pfirsch-Schlüter diffusion, whereas the minima occurred

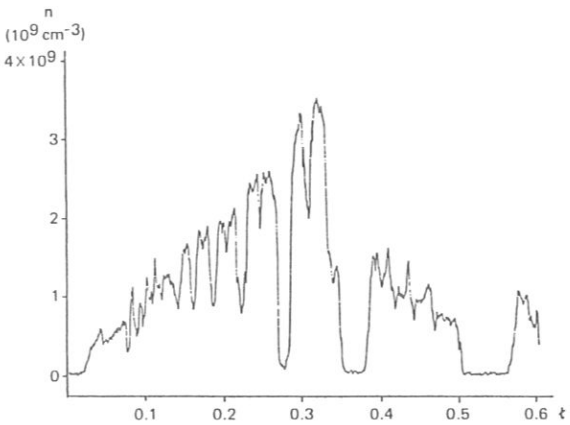

FIG.5. Plasma confinement in W II–A. Electron density on the magnetic axis versus external rotational transform ι_0.

for rational values of iota of low order, with the field lines being closed upon themselves after a few revolutions around the machine instead of forming magnetic surfaces. The latter configurations are highly susceptible to forming convective cells, particularly in combination with a limiter or with external field errors.

The stellarator confinement picture was supported by these results to a considerable degree of detail. Although beta was very low, the balancing mass flow already exceeded reactor conditions. Two essential conclusions were drawn from the above experiments for later stellarator configurations: both too small iota and major reconances within the stellarator confinement region had to be avoided.

Already when W II–A was still producing results, it was felt necessary to extend experiments to higher-temperature hydrogen plasmas. For this purpose, W II–B was built and the definition of W VII was considered. Apart from being equipped with a stray-field free-air core transformer to allow for Ohmic heating, W II–B was identical to W II–A, so that direct comparison of the two stellarators was possible. W VII was conceived as a major step forward in the stellarator line.

1.2. W II–B

W II–B started operation at the beginning of 1971. At that time, only Ohmic heating was available for heating plasma to temperatures above the radiation threshold. The main results [13] of Ohmic heating in W II–B were as follows. For the ohmically heated plasmas, tokamak-like behaviour of the electron heat flux was found, up to electron temperatures $T_e \leqslant 300$ eV, but compared to tokamaks with the same plasma current the externally produced transform, ι_0, led to an improvement of the observed energy content, $nkT \sim B_0 (\iota_p + \iota_0) I_p$, and of the energy replacement time, $\tau_E \sim (1 + \iota_0/\iota_p)\tau(\iota_0 = 0)$. This result was more or less in line with 'pseudo-classical heat conduction', $\chi_e \sim \rho^2_{e\Theta}\nu_{ei}$ [14], which was fashionable at that time. In the above formulae, ι_p is the transform of the magnetic lines as produced by the plasma current I_p. The ion heat conduction was found to be close to neoclassical predictions. Shear arising from the profile of the plasma current density moderated the effect of resonances in the rotational transform ι. Furthermore, the externally produced poloidal magnetic field improved the equilibrium and stability of ohmically heated plasmas. At sufficiently large external transform, $\iota_0 \geqslant 0.14$, no disruptive instabilities occurred any more and the displacement of the plasma column was reduced without the necessity of a compensating vertical field.

These experiments suffered from the small size of the W II–B device and the related radiative problems. It also became evident that any scaling of the electron confinement in tokamak-like operation had to be considered with care because MHD effects arising from the plasma current strongly influenced the containment. It was the global confinement behaviour (which integrates over regions with and without MHD activities) that could apparently be improved by decreasing the plasma current in order to reduce the MHD activities. It is thus only a phenomenological statement to say that the global confinement time apparently followed the drift parameter scaling.

In 1971, the first RF plasma was produced in W II–B by application of $P_N = 40$ kW of 2.4 GHz [15]. A slow-wave antenna produced a low-density, low-temperature plasma ($n < 5 \times 10^{12}$ cm^{-3}, $T_e \leqslant 10$ eV) by turbulent heating. In addition, in today's terms, this experiment also demonstrated the possibility of current drive by RF waves. Currents of up to 1 kA could be generated, and their magnitude and direction could be influenced by varying the vertical magnetic field, i.e. by affecting the confinement properties of wave-accelerated high-energy electrons.

1.3. WEGA

In co-operation with CEA Grenoble, the WEGA stellarator ($R = 0.72$ m, $a = 0.15$ m, $B_0 = 1.4$ T,

$\ell = 2$, m = 5) was built. The experiment was carried out in Grenoble and its main purpose was to heat a plasma by lower hybrid heating. A 500 MHz generator with 200 kW power and a grill-type antenna were available to heat a target plasma produced by Ohmic heating. About 100 kW was coupled to the plasma; this led to an ion temperature rise of about 50% (100→150 eV). Comparison of such a current-carrying plasma with pure tokamak operation did not exhibit any essential difference. Without an ohmically heated target plasma and lower hybrid heating only, a plasma of $\bar{n} \cong 10^{13}$ cm^{-3} could be produced. The temperature, however, remained low, around 10 eV, since the heating power was not sufficient to overcome the radiation barrier.

1.4. W VII–A

At the end of 1975, the larger W VII–A stellarator went into operation and demonstrated right away that the magnetic surfaces were very close to their design values. During the first period of W VII–A's life the experiments were concentrated on the investigation of ohmically heated plasmas. At the beginning of 1980, a breakthrough with 'currentless' operation was achieved; plasma parameters of about $n = 10^{14}$ cm^{-3}, $T_e < T_i \approx 1$ keV could be maintained by application of neutral injection only.

For ohmically heated plasmas the results obtained in W II–B could be confirmed and considerably expanded. Especially the importance of current-driven MHD modes and thus of the deterioration of stability and transport caused by the plasma current I_p were clearly demonstrated. Caused by the comparatively large aspect ratio of W VII–A and the twist introduced by the externally generated helical field, ι_0, the maximum current density at the plasma centre, $j(0) \sim B_0/R)(1 - \iota_0)$, leading to $\iota(0) = 1$, was already reached for low plasma currents, $I_p \approx 10$ kA. Associated with strong 'sawtooth' instabilities occurring under these conditions, any further increase of the plasma current causes a radial extension of the q = 1 region. With an external transform of $\iota_0 \geqslant 0.14$, discharges could be generated and maintained with plasma currents as large as 45 kA. In this case, even $\iota(a)$ became close to one; within the q = 1 region, i.e. within nearly the entire inner part of the plasma, internal sawteeth flattened the density and temperature profiles and only a thin isolation sheath remained at the plasma edge. This isolation sheath is susceptible to further disturbances by various tearing modes localized around resonant surfaces. Their mode amplitudes have been shown to be dependent on the external rotational transform ι, the plasma current and its radial distribution. The saturated amplitude of the most dangerous tearing mode (2/1) could be calculated from standard tearing mode theory, taking into account the measured current density profiles (from T_e profiles) and plasma densities; reasonable agreement with the experiment was found (Fig.6). Above an external rotational transform $\iota_0 = 0.14$, any disruptive instability could be prevented [16].

It is an advantage of the stellarator contribution to the total transform that the radial position of the q = 2 surface can be shifted in radius rather independently of other parameters just by varying ι_0. In particular, by increasing ι_0 the q = 2 surface can be shifted to regions where the current density profile is flat enough for the (2/1) mode to be stable. In addition, it is advantageous that the external helical fields being produced by currents in rigid conductors provide strong positional stability of the plasma and slow down the dynamic behaviour of the disruption.

When plasma disruptions were suppressed at sufficiently high external transform, maximum plasma densities of $\bar{n} \approx 10^{14}$ cm^{-3} were reached in W VII–A.

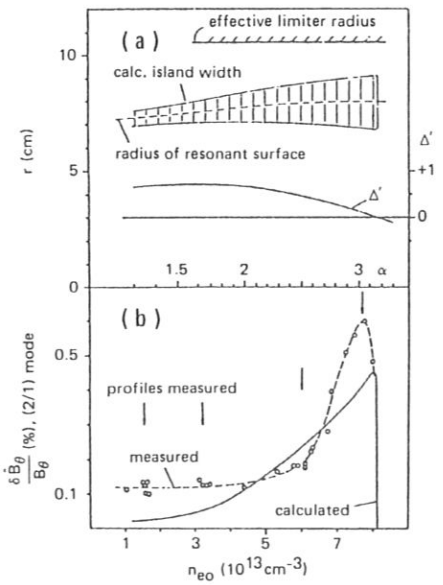

FIG.6. Tearing mode (2/1) in W II–A. (a) Calculated island width of the (2/1) mode and of Δ' in dependence of plasma density $n_e(0)$. (b) Comparison of the measured and calculated amplitude of the (2/1) tearing mode.

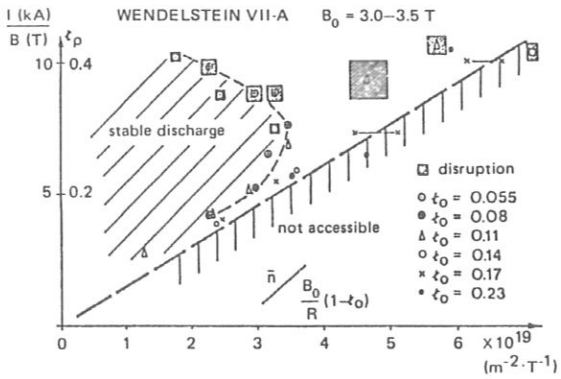

FIG. 7. Hugill plot of maximum density in ohmically heated discharges. External rotational transform leads to an increase of maximum density. The squares indicate the disruptive limit of the discharges.

Any further increase of the plasma density is limited by increasing the radiative losses, by the deterioration of confinement by edge cooling, by the corresponding quenching of the current profile, and finally by the depletion of Ohmic power (Fig. 7).

In ohmically heated discharges the energy balance is dominated by the electron energy losses which show enhanced anomalous transport. The ion heat conduction is found to be close to the neoclassical predictions. Considering the various physical mechanisms influencing the electron heat flux, one has to conclude that the global energy containment is very dependent on the particular discharge conditions (Fig. 8). For regions outside q = 1 and for discharges not showing strong tearing mode activity, local heat conduction coefficients have been derived from the local electron energy balance. These evaluations are based on local measurements of density, temperature, and radiation power density. Within the magnetic field range $B_0 = 2.5–3.5$ T, an empirical heat diffusivity, $\chi_e = 3 \times 10^{16} n^{-1} \cdot T_e^{-2/3}$ $(cm^2 \cdot s^{-1})$ (T_e in keV), has been evaluated which shows outside the q = 1 surface no explicit dependence on the current I_p or on the rotational transform ι [17]. So far, the physical mechanism of the dependence of χ_e is unexplained, but its particular dependence on n and T shifts its importance more and more to the plasma edge the higher the energy density of the plasma grows. At the plasma edge, χ_e may even have beneficial effects in widening the scrape-off layer. This result is

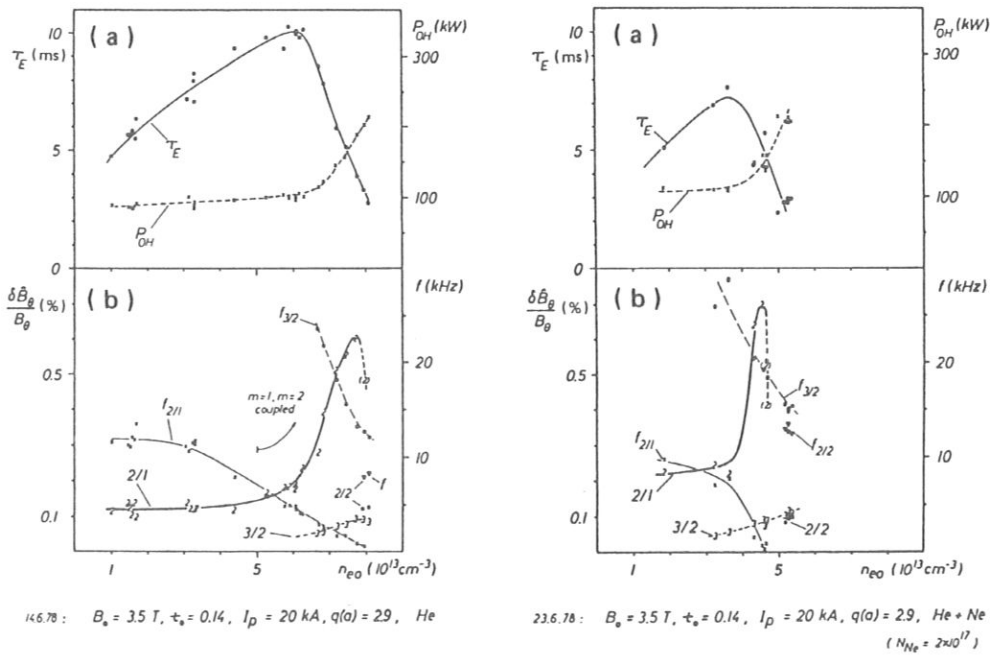

FIG. 8. (a) Confinement time τ_E and Ohmic heating power P_{OH} versus density.
(b) Relative amplitude and frequency of the tearing modes (2/1) and (3/1) versus density.
The right-hand pictures show the effect of additional impurities (Ne, 2×10^{17} particles).

compatible with recent tokamak scaling laws which involve the aspect ratio of the device. W VII–A has an aspect ratio of A = 20. If one compares the data for W VII–A with those for Pulsator and Alcator C [18] by using the formula $\chi_e = B_0/A \cdot n^{-1} T_e^{-2/3}$, relatively good agreement is obtained. This suggests that a large aspect ratio is beneficial in reducing the anomalous part of the electron heat transport in regions not perturbed by tearing modes.

1.5. Net-current-free plasma in W VII–A

In 1980, net-current-free plasmas were established in W VII–A with the help of neutral injection. This was achieved by starting from an OH-produced target plasma. With the beginning of the neutral injection pulse the plasma current was gradually reduced to zero and the plasma was maintained by neutral injection power alone. During the transition phase it was important to avoid destruction of confinement by the fast-rising tearing modes (2/1) or (3/2). This was achieved by careful compensation of the decreasing transform connected with the plasma current by increasing the current in the helical windings and by staggering the neutral injection power. Particular care has to be taken with regard to effects connected with the difference in power deposition profiles between OH and neutral injection. The resulting change in temperature and thus in current profiles may destabilize tearing modes which were otherwise stable. When the plasma current was reduced to values below $I_p \approx 5$ kA, almost no MHD activity was seen. As reported at the Brussels meeting in 1980 [19] and at Baltimore in 1982 [20], plasma parameters with appreciable energy densities ($n \approx 10^{14}$ cm^{-3}, $T_i = 800$ eV) and with $\beta(0) \approx 1\%$ were obtained for optimized values of the rotational transform ι_0. These results were achieved at magnetic field strengths as high as 3 T and in spite of the small plasma cross-section of W VII–A and the low available heating power of $P_N \leqslant 500$ kW. The vanishing MHD activity and the significant reduction of the fluctuation level, $\tilde{n}/n$, were a strong indication of an improvement in confinement. A detailed transport analysis, however, was very difficult to establish since it was masked by strong radiative losses at the high densities achieved, $n \geqslant 10^{14}$ cm^{-3}, and by uncertainties in the beam power deposition profile.

In principle, one would expect that the nearly perpendicular neutral injection at W VII–A would lead to significant orbit losses and consequently to a low heating efficiency, as had been predicted by Monte Carlo calculations. The experimental data, however, can only be explained by an increased heating efficiency, together with either preferential ion heating or reduced ion heat losses, rather than by straightforward neoclassical predictions for the plateau regime. As a possible mechanism causing preferential ion heating, beam-driven ion cyclotron instability was considered. Experiments with D^0 injection into D^+ target plasma, however, clearly confirmed classical collisional slowing down of the injected ions. In addition, the theory of ion cyclotron instability could only explain effects during the initial phase of switching on the neutral beam.

The above observations can be explained by the occurrence of injection-generated radial electric fields. The ions born on lost orbits generate radial electric fields within the plasma which pull the orbits of such particles closer to the magnetic surfaces until the electron and ion loss rates become equal again. The existence of such electric fields was proved by Doppler

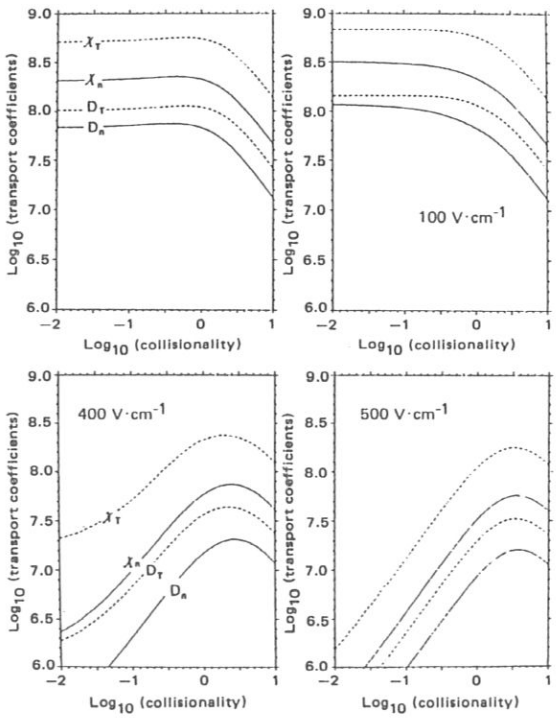

FIG.9. Neoclassical transport coefficients in dependence of a radial electric field ($E_r = 0$, 100, 400, 500 V·cm^{-1}). The horizontal axis is the collisionality; D_T, D_n are diffusion coefficients; χ_T, χ_n are coefficients of thermal conduction.

shift measurements of the poloidal rotation of impurity ions [21]. The toroidal rotation speed is found to be small compared to the thermal velocity of the plasma ions. Monte Carlo calculations taking these effects into account explain the observed heating efficiency. Since all particles mainly contributing to the perpendicular ion heat conductivity feel the same electric field, it is not surprising that also the ion heat conduction is reduced to values below those calculated for a Maxwell-Boltzmann distribution function with a temperature equal to the bulk plasma temperature (Fig.9). Under the conditions of the experiment, this reduction can amount to one or even two orders of magnitude.

As compared with Ohmic heating, increased particle confinement has been observed during neutral injection. Careful studies on particle diffusion were made by observing the local diffusion of aluminium used as tracer ion. Aluminium was introduced by means of the laser blow-off technique. In almost all details the

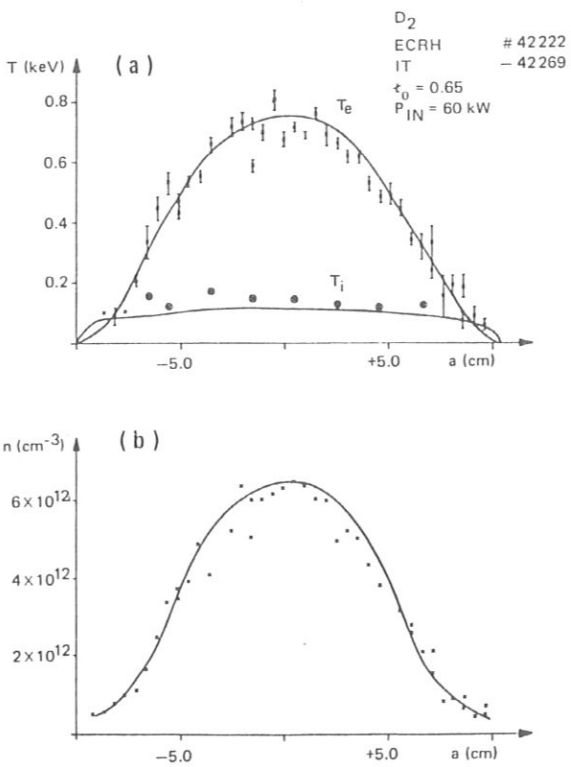

FIG.10. ECRH in W VII–A (B = 1 T, f = 28 GHz, P = 60 kW, t_0 = 0.65). (a) Ion and electron temperature profiles. (b) Density profile.

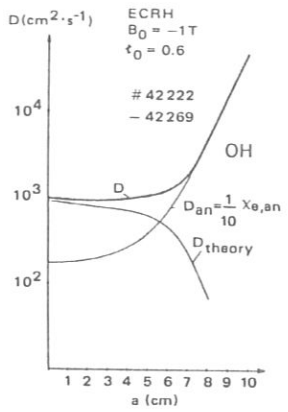

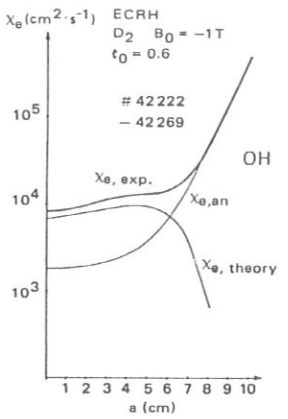

FIG.11. Profile analysis of ECRH plasmas in W VII–A. Diffusion coefficient D and thermal conductivity $\chi_{e,\,exp}$ from profile analysis. D_{theory}, $\chi_{e,\,theory}$: neoclassical transport coefficients including ripple effects. D_{an}, $\chi_{e,\,an}$: anomalous transport coefficients found in ohmically heated discharges.

results obtained were in agreement with the accompanying neoclassical calculations based on the experimentally observed density and temperature profiles [22]. Also the observed inward diffusion of impurities is in accordance with neoclassical predictions.

More detailed information on the electron channel is expected from ECRH experiments. Such experiments, using a 28 GHz gyrotron at P_N = 200 kW, have been performed in co-operation with the Institut für Plasmaforschung, Stuttgart [23]. With an advanced waveguide system, different modes of irradiation have been applied, including cases with full linear wave polarization. Unfortunately, the frequency of 28 GHz

restricted the magnetic field to 1 T and the density to $n_{e0} \leqslant 10^{13}$ cm$^{-3} \leqslant n_{cutoff}$. Nevertheless, plasmas could be produced by starting from the gas phase and could be heated to electron temperatures of up to $T_e \leqslant 1.5$ keV. The analysis of such plasmas possessing low collisionality for the electrons agrees with neo-classical calculations, where ripple effects become important. Only for the edge region, r/a $\geqslant 0.6$, does enhanced electron heat conduction have to be assumed to fit the flat temperature gradients in this region (Figs 10, 11); this situation is also observed in ohmically heated plasmas.

Further ECRH experiments were done by using a 70 GHz gyrotron. This allows operation at higher magnetic field (B = 2.5 T) and higher densities ($n \leqslant 5 \times 10^{13}$ cm^{-3}). Combined heating with neutral injection and ICRH in addition to ECRH will also become possible when starting from the ECRH plasma as target plasma, thus allowing an extended parameter range to be explored.

In the 'shearless' W VII–A, good confinement properties for 'currentless' operation could be demonstrated at optimum values of the rotational transform. High plasma pressures with $\beta(0) \approx 1\%$ could be maintained without significant MHD perturbations. The maximum beta so far seems to be restricted by the available heating power only. The maximum beta values already correspond to about one half of the equilibrium beta limit of W VII–A (Fig.12).

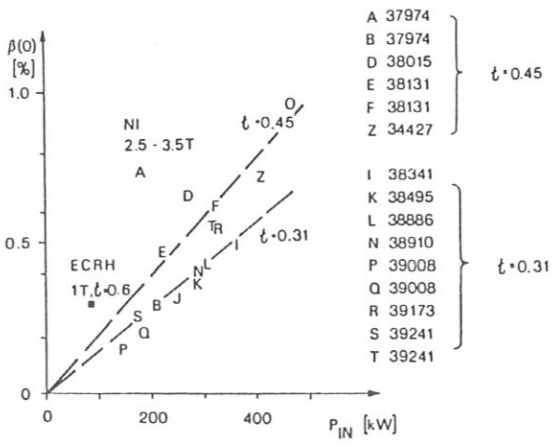

FIG.12. Maximum beta in W VII–A versus net heating power (NI is neutral injection heating). A, B, etc. indicate different discharges, with values of external transform as indicated. The confinement improves with ι_0.

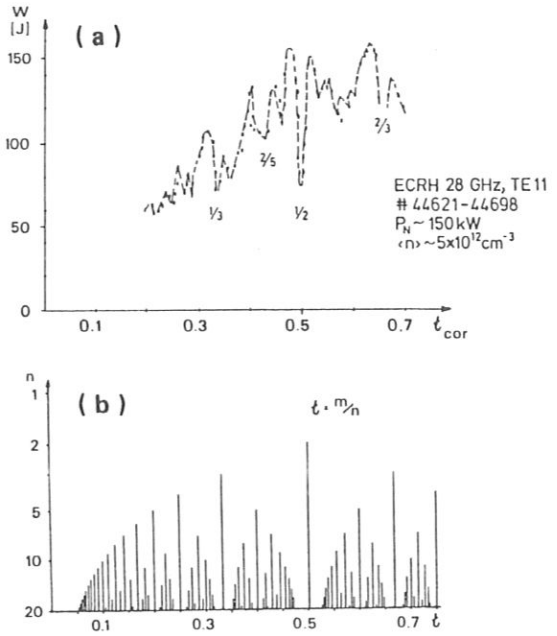

FIG.13. ECRH in W VII–A (B = 1 T, f = 28 GHz, total heating power = 150 kW).
(a) Energy content in dependence of external rotational transform. Confinement is deteriorated at ι_0 = 1/3, 2/5, 1/2, 2/3.
(b) n versus ι. The denominator of ι = m/n is a figure of merit for the disturbance of confinement on rational surfaces.

Similar to results of earlier experiments with very low plasma pressure in W II–A, a strong dependence of confinement on the magnetic twist has been detected for both neutral injection and ECRH. 'Resonances' with reduced confinement appear to be associated with low-order rational values of the rotational transform (ι_0 = 1/3, 1/2, 2/3) (Fig.13). Close to such resonances, where low-order rational values are less dense, optimum confinement is obtained and can be maintained by controlling the edge value of the transform. In setting the operating parameters it has to be considered, however, that the vacuum transform profiles become modified by plasma pressure effects and by residual plasma currents. Such currents could be generated by the plasma pressure anisotropy or by the heating mechanism. For higher beta values, therefore, rational values of the rotational transform cannot be excluded from the entire volume of the plasma. However, with sufficient but still moderate shear, their influence can be made negligible, external perturbations having less influence on the confinement.

From experiments in which the shear was varied by controlling the residual plasma currents it can be concluded that the effect of the resonances on confinement is due to island formation and subsequent plasma convection. Resonant magnetic surfaces are very susceptible to even small perturbing fields which can create extended islands. Convection becomes particularly important if such islands are localized at the low-temperature plasma edge where parallel transport, $\chi_{e,\parallel} \sim T^{5/2} n^{-1}$, has its minimum and anomalous transport, $\chi_{e,OH} \sim n^{-1} T_e^{-2/3}$, has its maximum.

2. ADVANCED STELLARATORS

2.1. Basic physics

An intrinsic new property of advanced stellarators is the reduction of Pfirsch-Schlüter currents $j_\parallel$ in the plasma. A decrease of the Pfirsch-Schlüter currents in W VII–AS as compared with standard $\ell = 2$ stellarators or with any axisymmetric device (tokamak) having the same global parameters (R, a, B, ι, or q, p(r), ...) would lead to a reduced Shafranov shift and thus to a higher equilibrium limit of the plasma pressure (Fig.14). The rationale of this procedure is discussed in Ref.[24]. This reduction of Pfirsch-Schlüter currents is achieved by appropriate shaping of the magnetic surfaces, with the aim of reducing the effective geodesic curvature of the field lines. The decrease of the Shafranov shift has been verified by computing finite beta equilibria with the aid of the Beta code.

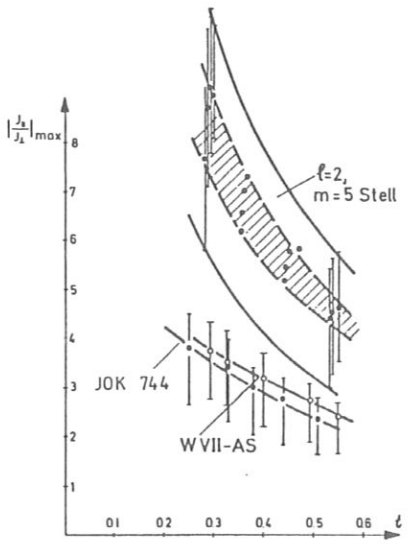

FIG.14. Pfirsch-Schlüter currents for $|j_\parallel/j_\perp|_{max}$ versus external rotational transform. W VII–AS is compared with a conventional $\ell = 2$ stellarator. In W VII–AS, $|j_\parallel/j_\perp|_{max}$ is approximately a factor of two lower than in the $\ell = 2$ stellarator; accordingly, the Shafranov shift is reduced.

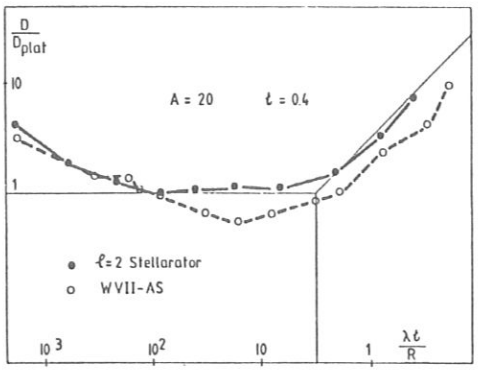

FIG.15. Diffusion coefficient versus collisionality, $(\lambda\iota/R)^{-1} = \nu^*$ (λ is mean free path). Comparison between W VII–AS and a conventional $\ell = 2$ stellarator. The results are obtained by a Monte Carlo code (Lotz code).

Another effect achieved by the same measures is the optimization of particle drift orbits. In standard stellarators and equivalent axisymmetric devices, the drift orbits of transiting particles and magnetic surfaces differ by ρ/ι (ρ being the gyroradius). In W VII–AS (see below) this distance is reduced by a factor of two, thus leading to smaller collisional diffusion losses in the Pfirsch-Schlüter and plateau regimes. Monte Carlo calculations have confirmed this result (Fig.15). In the long mean-free-path regime, the losses are comparable to those of standard stellarators.

2.2. The W VII–AS project

As mentioned above, advanced stellarators introduce advanced physics elements, such as reduced secondary currents and improved orbit confinement, the viability of which should be checked before going to a significantly larger experiment. At present, W VII–AS is being built at the Max-Planck-Institut and will be used for such a check. W VII–AS is an upgraded version of W VII–A and utilizes as many components of W VII–A as possible. Within these constraints the aims of the experiment are the following:

- to demonstrate the optimization principle (reduction of Shafranov shift and neoclassical losses)
- to increase the plasma parameters beyond those of W VII–A and to test the beta limits
- to produce net-current-free, high-energy plasmas and to test several powerful heating methods
- to demonstrate the viability of a modular coil system producing the required magnetic configuration.

The geometry of the existing structure of the W VII device considerably narrows down the choices among the interesting configurations, but it still allows a large enough step towards optimized configurations so that the underlying physics can be clarified with the available diagnostics. The reduction in the secondary currents will be approximately a factor of two. The maximum beta of this configuration will not yet reach the desired high reactor values but it will allow a check on the prediction method. The main new components are a modular coil system and a new vacuum tube. As compared with W VII–A, the plasma radius of W VII–AS is increased by a factor of two, thus giving rise to better decoupling of the main body of the plasma and the walls. The modular twisted coils replacing the old TF-coil and the helix system are technical novelties. This arrangement prevents electromagnetic forces on the vacuum tube. Additional circular TF-coils permit the rotational transform to be varied in a wide parameter range. The upgrading of W VII–A to W VII–AS will take place during 1985 and 1986. By the end of 1986 the new device (Fig.16) will go into operation.

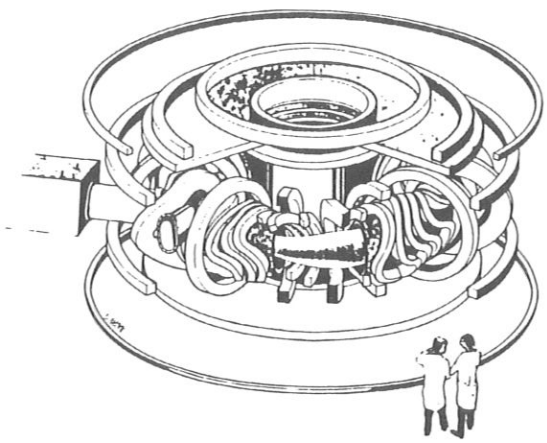

FIG.16. Artist's view of the W VII–AS device. Tangential neutral beam heating is indicated.

2.3. Heating methods

The Ohmic heating transformer available in W VII will no longer be used, except for special purposes. Net-current-free plasmas will be produced and preheated by electron cyclotron heating at 70 GHz (2.5 T) and with a power of 1 MW. Further heating by neutral beam injection (1.5 MW) or ICRH (3 MW) should lead to net-current-free high-density ($n \geqslant 10^{14}$ cm^{-3}) plasmas in the 1–2 keV regime. In contrast to W VII–A, tangential neutral beam injection in the co- and counter-direction will be applied. Because of the tangential injection the absorption length is sufficiently large to absorb all the neutral injection power. In contrast to W VII–A, direct production of locally trapped particles is avoided.

Transport calculations on the basis of neoclassical confinement predict that the available power should be sufficient to produce a plasma in the long mean-free-path regime and to test the beta limits of the configuration.

2.4. The modular coil system

The design of the modular coils started with the optimization of the magnetic-field given in terms of Dommaschk potentials [25]. The constituents of the field were found by an optimization code developed by Schlüter and co-workers [24]. In a further step, surface currents were computed that generate the prescribed field. These surface currents were then discretized into finite-size coils with some modifications to provide access to tangential neutral injection. There are nine coils per field period, only five of which are different from each other.

New problems arose from the coil manufacturing process: the accuracy of the geometrical form of the coils had to stay within 1–2 mm and the spring-back effect had to be avoided. To overcome the latter problem, the coils were made of 1 cm × 1 cm filaments of flexible copper windings and impregnated with epoxy resin. Tests with samples exposed to force and stress analysis indicate that the design value of B = 3 T can be reached by this method. A prototype coil is being tested at present.

2.5. Plans for the future

For the next step after W VII–AS, plans are being made to develop a W VII–X stellarator experiment which, together with the results of other experiments,

will demonstrate the reactor potential of optimized advanced stellarators. Thus, the basic aim of W VII–X is to demonstrate stable confinement at reactor-relevant beta values. For this purpose, studies are under way to find magnetic field configurations which are predicted to be MHD-stable up to $\beta = 5\%$ or higher. Above this beta value the additional gain is only small. Neo-classical confinement is investigated by Monte Carlo methods. Important questions in this context are the role of particle loss cones in combination with the occurrence of radial electric fields which have the potential to drastically improve confinement above the conventional values.

The W VII–X experiment will have at least twice the dimensions of W VII–AS. As in W VII–AS, modular coils will be used to produce the magnetic field. The experiment aims at quasi-stationary operation at plasma temperatures around 5 keV. For this purpose a superconducting magnetic field system is also under consideration.

REFERENCES

[1] BIERMANN, L., SCHLÜTER, A., Z. Naturforsch., A **12** (1957) 805.
[2] HAIN, K., LÜST, R., Z. Naturforsch., A **13** (1958) 936.
[3] SPITZER, L., Jr., Phys. Fluids **1** (1958) 253.
[4] GROVE, D.J., SINCLAIR, R.M., STODIEK, W., HARRIES, W.L., GOLDBERG, L.P., in Plasma Physics and Controlled Nuclear Fusion Research (Proc. Conf. Salzburg, 1961), Nucl. Fusion Suppl. Part 1 (1962) 203.
[5] RYNN, N., D'ANGELO, N., in Plasma Physics and Controlled Nuclear Fusion Research (Proc. Conf. Salzburg, 1961), Nucl. Fusion Suppl. Part 3 (1963) 1141.
[6] D'ANGELO, N., DIMOCK, D., FUJITA, J., GRIEGER, G., HASHMI, M., STODIEK, W., in Ionized Phenomena in Gases (Proc. 6th Int. Conf. Paris, 1963), Vol.3 (1963) 9.
[7] ECKHARTT, D., GRIEGER, G., GUILINO, E., HASHMI, M., Particle Loss Rates of a Cesium Plasma in a Curved Magnetic Field Geometry, Max-Planck-Institut für Physik und Astrophysik, Munich, Rep. MPI-PA-20/64 (1984).
[8] PFIRSCH, D., SCHLÜTER, A., Der Einfluss der elektrischen Leitfähigkeit auf das Gleichgewichtsverhalten von Plasmen niedrigen Drucks in Stellaratoren, Max-Planck-Institut für Physik und Astrophysik, Munich, Rep. MPI-PA-7/62 (1962).
[9] ECKHARTT, D., VON GIERKE, G., GRIEGER, G., in Plasma Physics and Controlled Nuclear Fusion Research (Proc. 2nd Int. Conf. Culham, 1965), Vol.2, IAEA, Vienna (1966) 719.
[10] BERKL, E., ECKHARTT, D., VON GIERKE, G., GRIEGER, G., Phys. Rev. Lett. **17** (1966) 906.
[11] BERKL, E., ECKHARTT, D., VON GIERKE, G., GRIEGER, G., HINNOV, E., VON HAGENOW, K.U., OHLENDORF, W., in Plasma Physics and Controlled Nuclear Fusion Research (Proc. 3rd Int. Conf. Novosibirsk, 1968), Vol.1, IAEA, Vienna (1969) 513.
[12] GRIEGER, G., OHLENDORF, W., PACHER, H.D., WOBIG, H., WOLF, G.H., in Plasma Physics and Controlled Nuclear Fusion Research 1971 (Proc. 4th Int. Conf. Madison, 1971), Vol.3, IAEA, Vienna (1971) 37.
[13] HACKER, H., PACHER, G., RENNER, H., REHKER, S., RINGLER, H., WÜRSCHING, E., in Plasma Physics and Controlled Nuclear Fusion Research 1974 (Proc. 5th Int. Conf. Tokyo, 1974), Vol.2, IAEA, Vienna (1975) 3.
[14] ARTSIMOVICH, L.A., Nucl. Fusion **12** (1972) 215.
[15] CORTI, S., LISITANO, G., et al., in Controlled Fusion and Plasma Physics (Proc. 6th Europ. Conf. Moscow, 1973), USSR Acad. Sci., Moscow (1973) 565.
[16] W VII–A TEAM, Nucl. Fusion **20** (1980) 1093.
[17] W VII–A TEAM, NI GROUP, in Heating in Toroidal Plasmas (Proc. 3rd Joint Varenna-Grenoble Int. Symp. Grenoble, 1982), Vol.2, Commission of the European Communities, Brussels (1982) 813.
[18] GRUBER, O., Nucl. Fusion **22** (1982) 1349.
[19] W VII–A TEAM and NI TEAM, in Plasma Physics and Controlled Nuclear Fusion Research 1980 (Proc. 8th Int. Conf. Brussels, 1980), Vol.1, IAEA, Vienna (1981) 185.
[20] CATTANEI, G., DORST, D., ELSNER, A., GRIEGER, G., HACKER, H., et al., in Plasma Physics and Controlled Nuclear Fusion Research 1982 (Proc. 9th Int. Conf. Baltimore, 1982), Vol.2, IAEA, Vienna (1983) 241.
[21] CATTANEI, G., DORST, D., ELSNER, A., ERCKMANN, V., GRIEGER, G., et al., in Plasma Physics and Controlled Nuclear Fusion Research 1984 (Proc. 10th Int. Conf. London, 1984), Vol.2, IAEA, Vienna (1985) 371.
[22] CATTANEI, G., DORST, D., ELSNER, A., ERCKMANN, V., GRIEGER, G., et al., ibid., p.635.
[23] ERCKMANN, V., JANZEN, G., KASPAREK, W., MÜLLER, G., RÄUCHLE, E., SCHÜLLER, P.G., SCHWÖRER, K., THUMM, M., WILHELM, R., W VII–A TEAM, ibid., p.419.
[24] CHODURA, R., DOMMASCHK, W., HERRNEGGER, F., LOTZ, W., NÜHRENBERG, J., SCHLÜTER, A., IEEE Trans. Plasma Sci. **PS-9** 4 (1981) 221.
[25] DOMMASCHK, W., Z. Naturforsch., A **36** (1981) 251.

IMPURITY TRANSPORT IN THE WENDELSTEIN VII-A STELLARATOR

W VII-A TEAM*, NI GROUP**
Max-Planck-Institut für Plasmaphysik,
Association Euratom-IPP,
Garching bei München,
Federal Republic of Germany

ABSTRACT. Impurity radiation losses in net-current-free neutral-beam-heated plasmas in the Wendelstein W VII-A stellarator are the combined effect of particularly strong impurity sources and improved particle confinement as compared with ohmically heated tokamak-like plasma discharges. Experiments are described and conclusions are drawn about the impurity species, their origin and their transport behaviour. The impurity transport is modelled by a 1-D impurity transport and radiation code. The evolution of the total radiation in time and space deduced from soft-X-ray and bolometer measurements can be fairly well simulated by the code. Experimentally, oxygen was found to make the main contribution to the radiation losses. In the calculations, an influx of cold oxygen desorbed from the walls of the order of $10^{13}-10^{14}$ $cm^{-2} \cdot s^{-1}$ and a rate of fast injected oxygen corresponding to a 1% impurity content of the neutral beams in combination with neoclassical impurity transport leads to quantitative agreement between the simulation and the observed radiation. The transport of Al trace impurities injected by the laser blow-off technique was experimentally studied by soft-X-ray measurements using a differential method allowing extraction of the time evolution of Al XII, XIII radial profiles. These are compared with code predictions, together with additional spectroscopic measurements. The main features of the impurity transport are consistent with neoclassical predictions, which explain particularly the central impurity accumulation. Some details, however, seem to require additional 'anomalous' transport. Such an enhancement is correlated with distortions of the magnetic configuration around resonant magnetic surfaces.

1. INTRODUCTION

Plasmas with $\beta(0) \leqslant 1\%$ were confined by external magnetic fields in Wendelstein VII-A ($R = 200$ cm, $a = 10$ cm, $\ell = 2$, $m = 5$ helical windings). After build-up of an ohmically heated target plasma, neutral-beam heating is applied (27 kV, H^0 or D^0, three to four beam lines each with a power of 200–350 kW, almost perpendicular injection (6°)). The transition to currentless operation is achieved by controlled reduction of the plasma current during the NI start-up phase. During the current ramp, the helical field is increased in order to keep the total rotational transform at the plasma edge constant [1]. This procedure allows one to prevent current disruptions at rational ι-values at the plasma edge and to achieve quiet stellarator discharges without MHD fluctuations [2]. $\iota(a) \cong 0.46$ was used for most of the experiments. Under these conditions regimes with good confinement properties ($\tau_p \approx 100$ ms) have been found. Typically, this phase can be maintained for about 100–150 ms. After this time, radiation losses from accumulated impurities with radial profiles sharply peaked in the plasma centre have increased so much that they lead to a significant decay of the electron temperature.

For discussion of the steep increase of the central radiation power it is important to note that the plasma density steadily increases during neutral-beam injection at a rate increasing with the neutral-beam particle flux. An increasing radiation power proportional to n_e or n_e^2 (apart from T_e effects) would therefore be expected anyhow in the case of plasma fuelling with a pure working gas or fuelling with the impurity concentration kept constant (constant Z_{eff}), respectively. Since the rate of increase in the central radiation clearly exceeds the variation by density effects, an increasing impurity concentration is obvious. This result is also verified by calculations of Z_{eff} from the enhancement of the measured soft X-continuum radiation with respect to a pure hydrogen plasma [3].

Impurity problems in the W VII stellarator are expected because of the comparatively small plasma

* G. Cattanei, D. Dorst, A. Elsner, V. Erckmann, G. Grieger, P. Grigull, H. Hacker, H.J. Hartfuss, H. Jäckel, R. Jaenicke, J. Junker, M. Kick, H. Kroiss, G. Kühner, H. Massberg, C. Mahn, S. Marlier, G. Müller, W. Ohlendorf, F. Rau, H. Renner, H. Ringler, F. Sardei, M. Tutter, A. Weller, H. Wobig, E. Würsching, M. Zippe.
** K. Freudenberger, W. Ott, F.-P. Penningsfeld, E. Speth.

radius, the short distance between the plasma edge and the vacuum vessel and the unfavourable ratio between the plasma surface and the plasma volume. In particular, the almost perpendicular neutral-beam injection leads to a large amount of high-energy particles lost to the walls. Typical fractions of the neutral-beam power including orbit losses of fast ions deposited on the wall vary between 0.7 and 0.5 of the injected power, mainly depending on the density of the target plasma.

Many possible origins of impurity release and impurity sources, therefore, have to be considered:

- plasma-wall interaction may introduce light impurities (O, C) by desorption and chemical sputtering or metal impurities such as Fe, Cr (stainless-steel vacuum vessel), Mo (limiter) and Ti (getter) by sputtering effects. Additional contributions may result from impact of runaway electrons on the walls;
- Mo influx from sputtering at the neutral-beam dump plates, induced by unabsorbed injected particles;
- impurity release induced by fast ions injected on bad orbits, drifting out of the plasma before slowing-down;
- light impurities (O, C) injected with the neutral hydrogen beams (and metal impurities, e.g. filament material (Ta));
- metal vaporization at places of high thermal load (injector ports with an aperture of only 8 cm);
- enhanced plasma-wall interaction due to distortions of the magnetic field topology, particularly during the transition of an OH plasma to a NBI-heated plasma;
- enhanced plasma-wall contact due to position shifts during this phase or incomplete compensation for position shifts originating from changes of the plasma pressure;
- fluctuating currents at the plasma boundary generated by the large voltage ripple of the OH-power supply.

Effects which may contribute to the increase of the central radiation power loss during NBI are:

- deposition of neutral-beam-injected impurities predominantly in the plasma centre;
- good particle confinement in the central plasma region;
- neoclassical inward flows of the impurities induced by the friction between impurities and background plasma ions. Radial electric fields or toroidal rotation due to momentum transfer from neutral-beam injection can also influence the radial flows;
- temperature dependence of the radiation power leading to an increase of radiation during electron temperature decay, particularly in the case of light impurities with a large fraction of fully stripped ions (thermal instability);
- modifications of the charge state distribution of intrinsic impurities by charge exchange reactions with the neutral particles from neutral-beam injection (injected hydrogen plus halo) [4];
- absence of instabilities during the currentless phase of the discharge (disappearance of sawtooth oscillations and tearing modes).

Experiments were performed in order to investigate the different items enumerated above and to achieve some degree of impurity control. In particular, for the transport studies test impurities were injected by laser ablation. This method has become a standard technique that is applied in many tokamak experiments [5–13] and also in the Heliotron-E device [14]. In some of these experiments, the impurity transport is presumed to be neoclassical, and in others 'anomalous'.

The one-dimensional simulation code for impurity transport and radiation, SITAR [15, 16], was used to describe the total radiation observed by soft-X-ray and bolometer measurements as well as line radiation from oxygen and aluminium, the latter being injected as a tracer impurity.

In 'currentless' operation (residual current $\leqslant 2$ kA) resonance-like deterioration of the confinement is observed if the rotational transform at the plasma edge passes through rational values [17, 18]. Small perturbation fields cause the formation of magnetic islands of comparatively large size, owing to the small shear of the configuration at resonant surfaces $\frac{1}{2}, \frac{1}{3}, \frac{2}{3}$, and convective transport processes are expected under these circumstances [19]. Reduced plasma ion and impurity ion confinement times are deduced from deuterium pellet injection and laser-driven Al injection experiments, respectively [20, 21]. Transport simulations were restricted to discharges at non-resonant conditions which were apparently not influenced by these effects.

Four different types of plasma discharges (see Table I) were studied in particular: discharges with comparatively low density and narrow density profiles (without gas puff) are compared with high-density discharges characterized by significantly broader density profiles (with steady gas flow), which are expected to have a beneficial influence on the retardation of the central impurity density build-up. A second comparison was made between experiments corresponding to 'co' and 'counter' neutral-beam injection, where for currentless discharges these conditions are defined by

TABLE I. DISCHARGE PARAMETERS FOR 'CURRENT-FREE' NEUTRAL-BEAM-HEATED PLASMAS. $B = 3.2$ T, $\iota \approx 0.47$, D_2, $H^0 \rightarrow D^+$ (3 inj.), $I_p \leqslant 2$ kA, $a \approx 10$ cm

Discharge density	A 'high'	B 'low'	C 'high'	D 'low'
NBI	'co'	'co'	'counter'	'counter'
D_2 gas feed [s^{-1}]	$\sim 3.8 \times 10^{21}$	0	$\sim 3 \times 10^{21}$	0
$\bar{n}_e$ [cm^{-3}][a]	8×10^{13}	5×10^{13}	5.7×10^{13}	4×10^{13}
$n_e(0)$ [cm^{-3}][a]	1.25×10^{14}	9.6×10^{13}	1×10^{14}	8.2×10^{13}
$T_e(0)$ [eV][a]	470	610	570	600
$T_i(0)$ [eV][a]	500	850	–	–
$P_{rad}(0)$ [$W \cdot cm^{-3}$][a]	1.2	1.6	1.1	1.4
Z_{eff}[a]	2	4–5	2.5	4
Code:				
O beam impurity	1%	1%	1%	1%
O influx [$cm^{-2} \cdot s^{-1}$]	3×10^{13}	8×10^{13}	3×10^{13}	3.5×10^{13}
Fe influx [$cm^{-2} \cdot s^{-1}$][a]	0	0	0	3×10^{12}
Γ_{Al} [atoms][b] (code, $\Delta t = 0.1$ ms)	$\sim 2.8 \times 10^{16}$	$\sim 3.8 \times 10^{16}$	$\sim 3.7 \times 10^{16}$	$\sim 2.7 \times 10^{16}$
$n_{Al}(0)$ [cm^{-3}][a]	2×10^{11}	6.5×10^{11}	3.4×10^{11}	6×10^{11}
Transport modelling	neocl. + add. diffusivity	neocl.	neocl.	neocl.

[a] Max. during pulse.
[b] Injected by laser blow-off.

the rotational transform ι (by analogy with the safety factor $q = 1/\iota$, which defines the currents in a tokamak).

Additionally, the global impurity confinement properties were investigated for many different discharge conditions with test impurity injection using the laser blow-off technique, impurity gas puffing with neon and injection of deuterium pellets doped with neon.

The need to produce high target densities for neutral-beam heating and to avoid resonances of the rotational transform leads, however, to a restriction of the space available for parameter scans.

Before the results of the measurements are discussed, the experimental methods and the impurity transport model will be introduced. Then the model predictions are tested for the case of laser-driven Al tracer impurity injection. Finally, the same model is used to simulate quantitatively the intrinsic impurity radiation.

2 IMPURITY DIAGNOSTICS

Total radiation measurements were performed with a ten-channel bolometer system [22] and a soft-X-ray camera built up from 30 surface barrier diodes [23], which are sensitive to radiation $E \geqslant 400$ eV.

The radiances of various resonance lines along a chord through the plasma centre were recorded with a flat-crystal Bragg spectrometer operating between 7 and 20 Å and a grazing-incidence spectrometer. In particular, the VUV spectrometer also provides measurements of lines excited during charge exchange recombination in the interaction volume of a neutral beam with the plasma, thus also allowing the temporal evolution of the fully ionized species to be obtained.

Another VUV spectrometer supplied with a rotating mirror can also provide radial scans of resonance radiation from lower ionization states. But generally

the radiation originating near the plasma edge shows significant asymmetries which do not allow the measurements to be compared with one-dimensional transport calculations [24].

The radial profiles from all the line-integrated measurements have to be corrected owing to the elliptic plasma shape and the 45° observation with respect to the axes of the ellipse ($\ell = 2$ configuration). A transformation procedure is applied [25] to the measured radiances and the radial co-ordinates, thus allowing further treatment by the usual Abel inversion techniques.

From X-ray pulse height analysis with a thin filter (40 $\mu g \cdot cm^{-2}$ Al on 15 $\mu g \cdot cm^{-2}$ C), it is also possible to draw conclusions about the energy distribution of the soft X-radiation in the range 0.4–1 keV. In particular, the relative amount of iron line radiation compared with the intensity of the oxygen resonance lines can be estimated, although the individual lines cannot be resolved. Generally, iron line radiation does not significantly contribute to the total soft-X-ray intensity [1]. This is also confirmed by measurements of impurity fluxes to the wall by probes exposed to the plasma during particular experiments [26].

A Q-switched ruby laser (~ 0.5 J, ~ 7 15 $J \cdot cm^{-2}$) was used for generation of a short pulse of metallic test impurities. First results concerning impurity confinement times were obtained from Si- and Fe-laser ablation [1]. In addition, the contribution of iron line radiation to the total radiation losses (10 20%) could be derived from the Fe laser blow-off experiment.

Transport simulations were performed for Al laser ablation experiments.

For the study of the impurity penetration into the plasma the physical composition of the ablated material is important. In Refs [11, 27] the fast penetration times are explained by the generation of clusters or small pellets during ablation. Detailed experimental investigations [28, 29], however, only show a negligible fraction of particles not evaporated as individual atoms, at least for the experimental set-up and material used in our experiments.

Aluminium injected in measurable quantities from 0.5 μm targets (about 3×10^{16} Al atoms into a plasma of about $1-2 \times 10^{19}$ electrons) turned out to be the most preferable tracer element because of the almost negligible influence on plasma parameters and the low background radiation (no intrinsic Al impurities, Al XII lines well separated from other lines). Further advantages are the dominant role of the He-like state, which allows the transport in the main plasma volume to be studied by the observation of just a few resonance

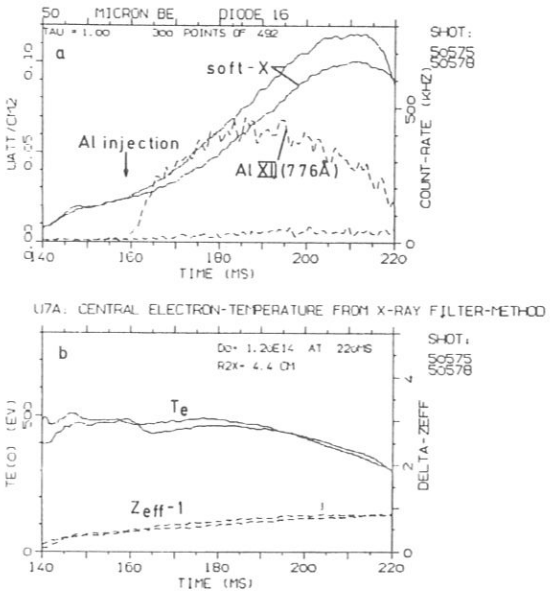

FIG.1. a) Signals of central soft-X-ray diode and signals of Al XII from crystal spectrometer for discharges with and without Al injection; b) T_e and Z_{eff} from soft-X-continuum radiation.

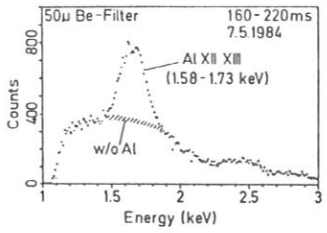

FIG.2. Soft-X-ray pulse height spectrum obtained through 50 µm Be-filter after laser ablation of Al.

lines which have transition energies clearly above the energy of the intrinsic impurity radiation (around 550–700 eV). Consequently, radial and time-resolved data on the combined radiation power from Al XII and Al XIII resonance lines can be derived from soft-X-ray measurements using a 50 μm Be-filter, which attenuates the radiation by a factor of about 100, compared with the case without filter, whereas the Al radiation at about 7 Å is only reduced by a factor of about 5.

Typically, a 10–30% increase in the filtered X-radiation was observed when Al was injected into the plasma in tolerable doses by laser blow-off (Fig. 1).

Taking the difference between similar shots with and without Al injection after Abel inversion, the local power of the sum of Al XII and Al XIII can be evaluated.

From measurements of X-ray pulse height spectra obtained with a Be filter of equal thickness it could be verified that the enhancement of soft X-radiation by Al injection indeed results from the resonance lines in the 7–8 Å region (Fig.2).

To correct for small changes in n_e, T_e, Z_{eff} of the shots taken for subtraction, HCN laser interferometer signals (line density) and T_e and Z_{eff} measurements from X-continuum radiation are used. Oxygen continuum radiation was assumed to be responsible for producing the radiation without Al injection. The determination of T_e for this correction is derived by the filter method from signals of two large surface barrier diodes supplied with 0.35 and 0.7 mm thick Be-filters [3].

If for a shot which was selected for comparison with transport calculations the X-ray temperature differed from the central value as given by the Thomson scattering fitting curve, the Thomson profile was normalized to the X-ray temperature.

Also ECE and line density measurements were used to improve the time interpolation between the Thomson scattering measurements.

3. IMPURITY TRANSPORT CODE

The one-dimensional transport code used for the simulations will be described in more detail elsewhere [15]. The following basic set of coupled continuity equations is solved for the impurity ion density n_z:

$$\frac{\partial n_z}{\partial t} + \frac{1}{r}\frac{\partial}{\partial r}(r\Gamma_z) = n_e(S_{z-1}\cdot n_{z-1} - S_z\cdot n_z + R_{z+1}\cdot n_{z+1} - R_z\cdot n_z) + Q_z^{dep} \quad (\text{for } z > 1)$$

$$\frac{\partial n_1}{\partial t} + \frac{1}{r}\frac{\partial}{\partial r}(r\Gamma_1) = n_e(-S_1\cdot n_1 + R_2\cdot n_2) + Q^{ext} + Q_1^{dep} \quad (\text{for } z = 1)$$

The subscripts refer to the charge state of the impurity ions. Γ is the radial transport flux, and S, R are the rate coefficients for electron impact ionization and recombination (radiative, dielectronic and charge exchange recombination).

The source of impurity influx can be modelled by two terms: Q^{ext} describes the influx from the walls contributing only to the first ionization state (includes recycling). Q^{dep} models the deposition of neutral-beam-injected impurities and their radial profile after thermalization. This term is calculated separately by the ODIN Monte-Carlo beam injection code [30], which also gives the ionization state after slowing down.

The transport fluxes are modelled within neoclassical theory. Adjustable 'anomalous' contributions are used, in particular cases, to show to which extent the neoclassical transport fluxes have to be enhanced in order to approximate the measured radiation. The classical, Pfirsch-Schlüter and plateau fluxes corresponding to collisions of the impurity ions with the background plasma were taken from [31]. They are derived for axisymmetric configurations, but the non-axisymmetric contributions to the impurity fluxes [32] are estimated to be at least two orders of magnitude smaller and can therefore be neglected. This is mainly a consequence of the geometry of the W VII-A stellarator, which is characterized by a very small helical field ripple ($\epsilon_h \leq 2\%$) and a large aspect ratio (A = 20), resulting in a quite extended plateau region. Moreover, for the discharges discussed in this study, the thermal plasma components are well within the Pfirsch-Schlüter or plateau regime. The above conclusion is also valid if radial electric fields of 600–900 $V\cdot cm^{-1}$ are present in the discharge which can be derived from measured poloidal rotations of up to 20–30 $km\cdot s^{-1}$.

Such strong electric fields are generated by losses of fast ions from the nearly perpendicular neutral-beam injection. As a consequence, the transport of the thermal background ions is reduced significantly in the plateau regime [17, 18]. The transport of impurities may be affected as well by radial electric fields, once they get large and the particles under consideration are in the right regime of collisionality. The importance of this effect is under study but not fully clear up to now. Therefore, in the absence of a reliable estimation of these contributions, we only deal with the collisional effects in this paper.

The Pfirsch-Schlüter fluxes, including the interaction of impurity ions in different charge states, were evaluated by means of the formalism given in Ref.[33] with the modification proposed in Ref.[34] to account for the mixed collisionality of background and impurity ions. For typical W VII-A experimental conditions, it

was found that the Pfirsch-Schlüter fluxes due to impurity-background collisions are in close agreement with the expression given in Ref.[31].

The classical fluxes due to impurity-impurity collisions are taken from Ref.[35]. The corresponding Pfirsch-Schlüter fluxes were represented without loss of accuracy by using a simplified expression which differs from the classical impurity-impurity fluxes by the same factor of $2q^2$ (q = safety factor) as for the impurity-background fluxes given in Ref.[31].

The use of this representation leads to a considerable reduction of computing time. Particularly in the case when oxygen concentrations exceed about 1%, impurity-impurity collisions lead to a considerable enhancement of the transport fluxes.

Then the whole expression used for modelling the neoclassical transport fluxes is given by

$$\Gamma_z = 1.25\,\frac{q}{r}\sqrt{m_z}\,\frac{T^{3/2}c^2 n_z}{B_T^2 z z_b e^2 n_b}\left(\frac{\partial n_b}{\partial r} - \frac{n_b z_b}{n_z z}\,\frac{\partial n_z}{\partial r} + \frac{1.5 n_b}{T}\,\frac{\partial T}{\partial r}\right)$$

$$+ \frac{\rho_b^2}{\tau_{bz}}\,\frac{z_b}{z}\,(0.5+q^2)\left(\frac{\partial n_b}{\partial r} - \frac{n_b z_b}{n_z z}\,\frac{\partial n_z}{\partial r} - \frac{1}{2}\,\frac{n_b}{T}\,\frac{\partial T}{\partial r}\right)$$

$$+ \sum_{z'\neq z}\frac{\rho_{z'}^2}{\tau_{z'z}}\,\frac{1}{\sqrt{2}}\,\frac{z'}{z}\,(0.5+q^2)\left(\frac{\partial n_{z'}}{\partial r} - \frac{n_{z'}z'}{n_z z}\,\frac{\partial n_z}{\partial r} - \frac{1}{4}\left(\frac{z'}{z}-1\right)\frac{n_{z'}}{T}\,\frac{\partial T}{\partial r}\right)$$

The subscript b denotes background ions (deuterium), ρ the Larmor radius and τ the collision time.

Ion temperatures were assumed to be equal to the electron temperature. In all neutral-beam-heated plasma discharges, however, the ion temperatures are well above the electron temperature. Using T_e instead of T_i in the expression for Γ_z will, therefore, lead to an underestimation of the plateau fluxes, which, however, do not significantly contribute to the total fluxes of the most relevant charge states. The effect on the classical and PS fluxes is comparably lower, owing to the weak temperature dependence.

The neoclassical transport fluxes can be separated into a diffusive and a convective term

$$\Gamma_z = -D_z\,\frac{\partial n_z}{\partial r} - v_z\,n_z$$

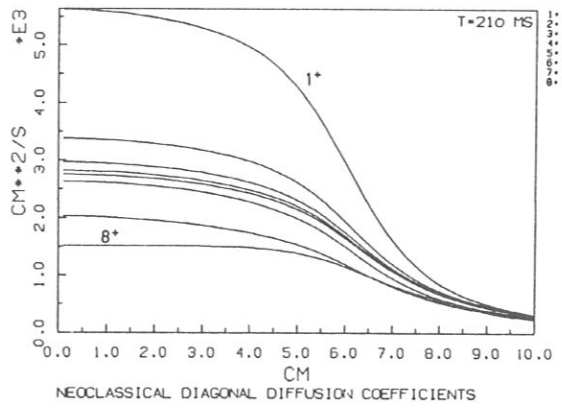

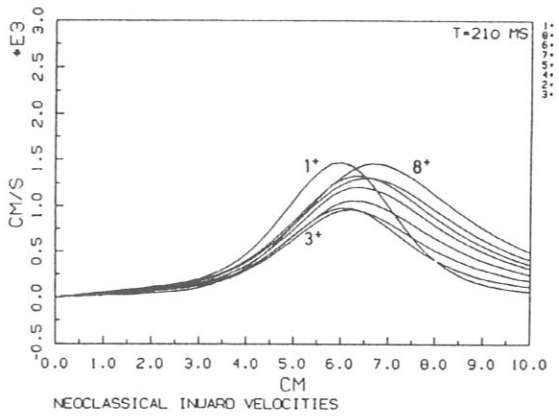

FIG.3. Calculated radial distribution of neoclassical diffusion coefficient and inward drift velocity of oxygen ions (sum of classical, Pfirsch-Schlüter and plateau terms) for a particular time (210 ms) during high-density discharge.

The anomalous transport, if it applies, is also modelled this way, with D and v equal for all charge states. For the anomalous transport, v = 0 was used in all the calculations presented in this study.

Figure 3 gives an example of the calculated neoclassical diffusion coefficients and drift velocities for various oxygen charge states. For typical density and temperature profiles in W VII-A the velocity is generally inward, which means that background ion gradient effects dominate temperature screening.

Since the plasma parameters vary appreciably during neutral-beam-heated W VII-A discharges, the time variations of the temperature and density profiles are taken into account. The excitation rate coefficients are taken in the form given in Ref.[36] for the calculation of the line radiation power.

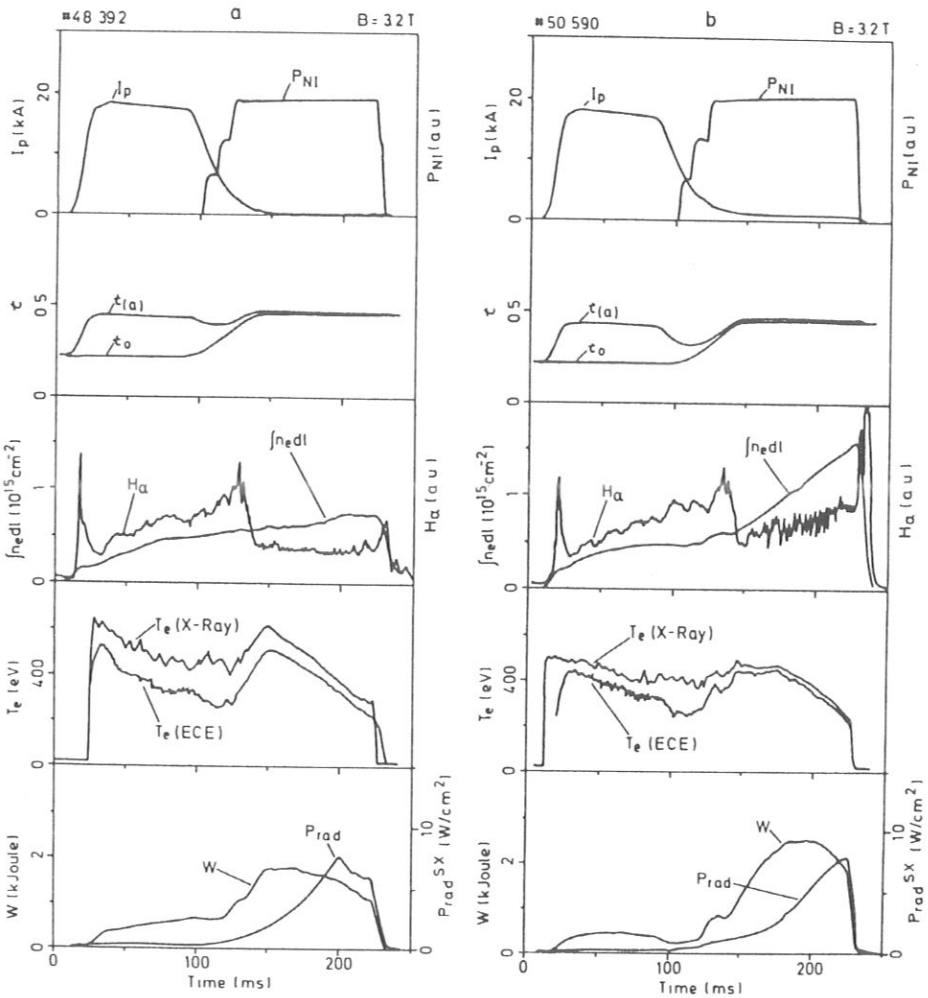

FIG.4. Evolution of global discharge parameters for low- (a) and high-density (b) neutral-beam-heated discharges (types D, A of Table I). Signals from top to bottom: OH current and time of NBI, external and total rotational transforms, line-integrated electron density and H_α production signal at limiter, central electron temperature from soft-X-ray filter method and from ECE, total stored plasma energy, line-integrated central soft-X-radiation power.

4. RESULTS FOR Al LASER BLOW-OFF EXPERIMENTS

In the case of a well-defined source of trace impurities, switched on only for a time which is very short compared with any transport time-scale, absolute values of the transport parameters D and v used can be verified by using the transient response of the radiation signals. Quasi-stationary radiation profiles may, in principle, be described by different transport terms with a fixed relation between the absolute values of D and v.

Compared with the impurity source strengths of the intrinsic plasma impurities, the flux of test impurities into the plasma from laser ablation can be given with much greater accuracy, in particular for the case of Al or similar material which is not recycled. Consequently, the transport fluxes follow uniquely from the transport equations, whereas in the case of rather unknown source terms different combinations of transport fluxes and source terms can provide similar results.

Within the boundary layer and at the instant of injection, however, the laser ablation yields strong

disturbances and asymmetries in the concentration of the ablated material, which may result in an additional convective transport. These asymmetries become negligible after a time which is short compared with the cross-field transport times. This is particularly true for the higher ionization states in the main part of the plasma volume where most of the comparisons between experiment and 1D transport calculations are done. Large poloidal variations of the plasma density and electrostatic potential which may occur at the plasma edge could contribute considerably to the radial fluxes in this region [37]. In the central plasma region, however, where the background plasma ions are deep in the plateau regime, the frictional forces due to collisions between background and impurity ions and the associated electrostatic potential variation on a flux surface are too small to drive additional impurity radial fluxes.

The global behaviour of the two discharges A, D (Table I) with a maximum achievable difference in plasma parameters (without change of injection power and without use of deuterium pellet injection) is compared in Fig.4. The upper two plots of Fig.4a, b illustrate the method of producing 'current-free', neutral-beam-heated plasma discharges, starting with an OH target plasma. The total rotational transform at the plasma edge, $\iota(a)$, could be kept constant apart from a small dip during the transition phase. In the case of the discharge D presented in Fig.4a the gas feed was switched off at the start of neutral-beam heating. With continuous cold-gas feed during the discharge (discharge A, Fig.4b), a higher electron density is reached. In both cases, the density increase during the currentless phase until the end of the discharge, along with a reduction of the H_α signal at the limiter, indicates improved particle confinement. The central electron temperatures measured by the X-ray filter method and by electron cyclotron emission, the total stored energy and the central soft-X-ray signals are given in the lower part of Fig.4.

Examples of radial profile measurements by Thomson scattering at different times, which are necessary as input parameters for the transport code, are plotted in Fig.5 for discharges D, A. In the case of gas feeding broader density profiles are maintained (Fig.5b), which are even slightly hollow before beam fuelling becomes dominant. Since the main plasma parameters are non-stationary (Fig.4), profile measurements were made at six characteristic times during the currentless phase. It should be mentioned that the so-called 'low-density' discharges reach central density values slightly below $1 \times 10^{14}\,\mathrm{cm}^{-3}$.

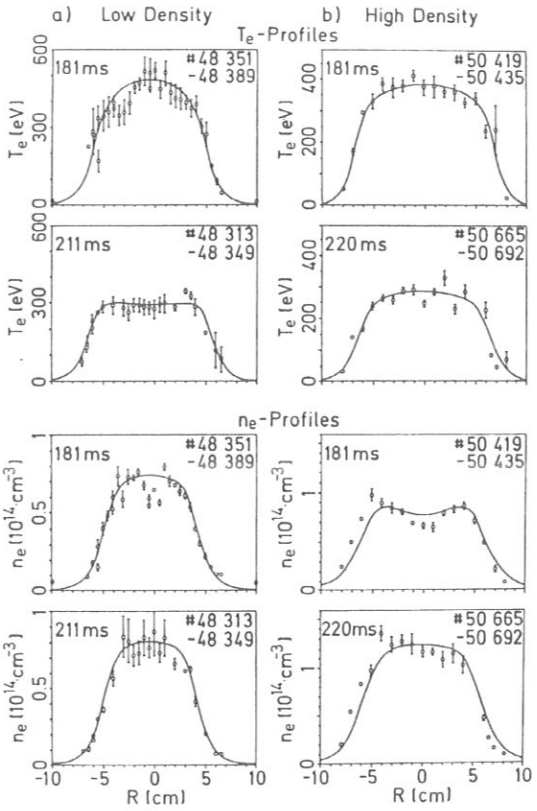

FIG.5. Electron temperature and density radial profiles from Thomson scattering at two different times.
a) Low-density discharge D (no gas feed during NBI), same as in Fig.4a;
b) high-density discharge A, same as in Fig.4b.

Another distinction between the discharges introduced in Figs 4 and 5 is the reversal of the magnetic fields (toroidal field, helical field, OH transformer) corresponding to a change from 'co' to 'counter' neutral-beam injection. For 'counter' injection increased poloidal rotation velocities (in opposite direction) are measured, indicating a compensation of the otherwise reduced confinement behaviour of the high-energy particles [38]. The global features of discharges with comparable gas feed programme are very similar.

Figure 6a shows the evolution of the spatial distribution of the radiation power density of the Al XII and Al XIII resonance lines, as derived from soft-X-ray measurements, after laser blow-off (about 3×10^{16} Al atoms) into the high-density discharge (type A, Table I).

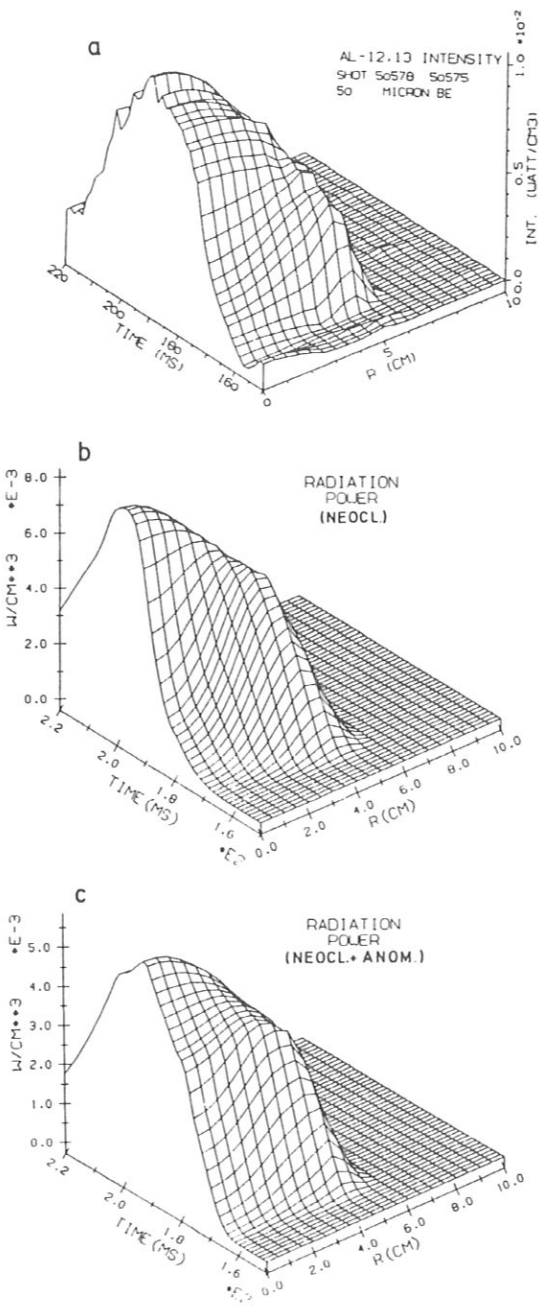

FIG.6. a) Evolution of Al XII, XIII radiation power from soft-X-ray measurements after Al injection into a high-density discharge (type A);
b) code simulation of a) with neoclassical transport fluxes;
c) code simulation of a) with neoclassical transport fluxes and additional locally distributed anomalous diffusion coefficient.

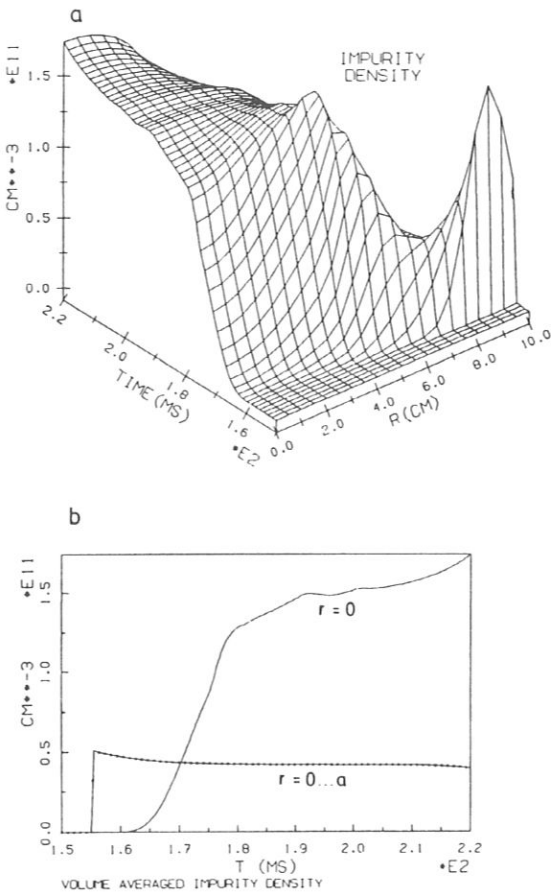

FIG.7. a) Evolution of Al ion density;
b) central and volume-averaged Al ion density, as predicted by code, corresponding to calculation of Fig.6c.

During the penetration of the test impurities into the plasma, a peak of Al density is formed at about 5 cm, as indicated by the hollow radiation profiles. After 10–15 ms a transition to peaked Al density profiles occurs.

In Fig.6b a code calculation is presented with pure neoclassical transport fluxes. These terms cannot completely account for the faster increase of Al radiation in the plasma centre observed in the experiment since small, outward directed convective fluxes and relatively small diffusion coefficients of the order of 500 $cm^2 \cdot s^{-1}$ are expected in the presence of hollow density profiles.

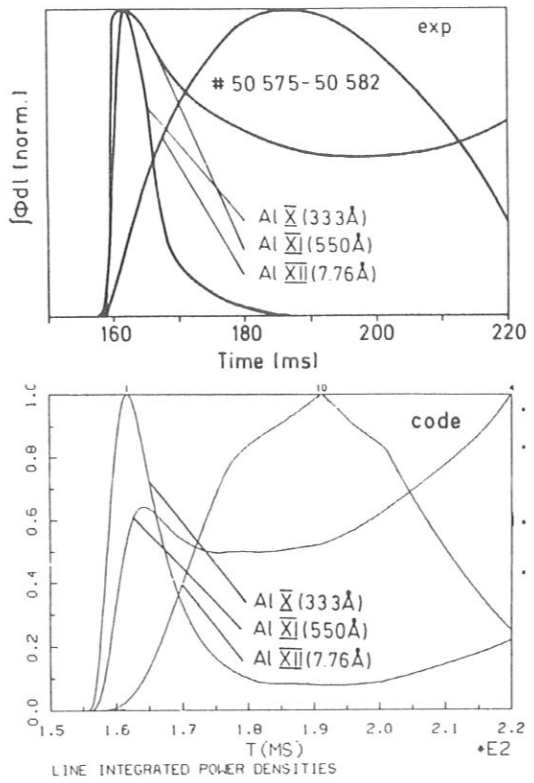

FIG.8. a) Experimentally observed line-integrated intensities of three Al resonance lines for case shown in Fig.6; b) code simulation with modified neoclassical transport fluxes as used in Figs 6c and 7.

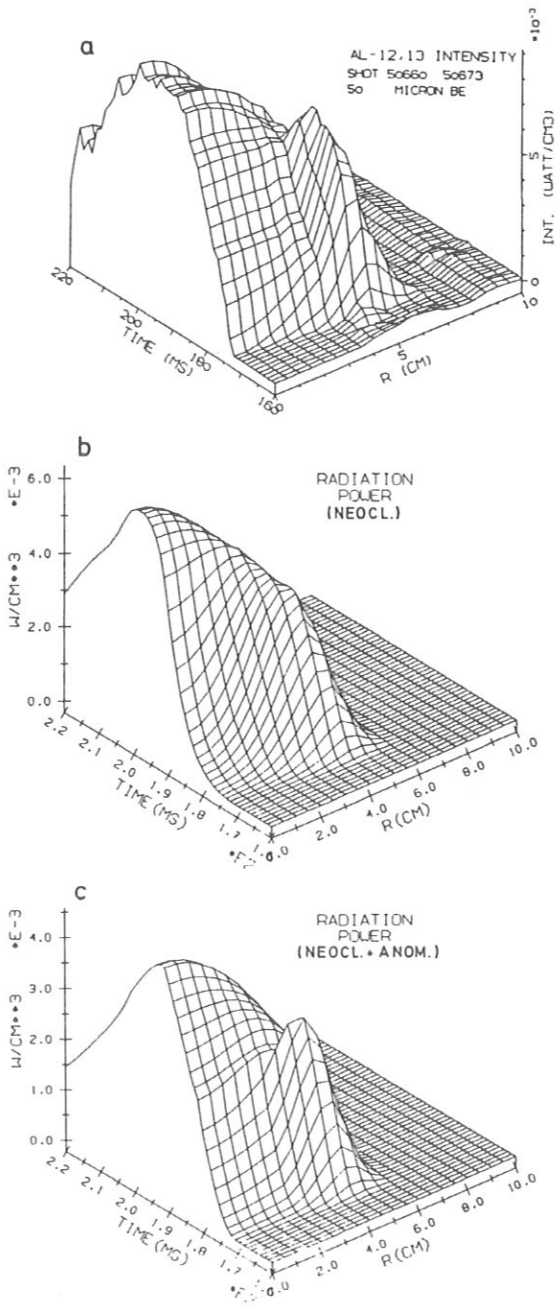

FIG.9. a) Al XII, XIII radiation power from soft-X-ray measurements after delayed Al injection in discharge similar to Figs 6 to 8 (type A). Sudden anomalous transport effects are seen; b) code simulation with neoclassical transport fluxes; c) code simulation of Al radiation with anomalous fluxes during short time.

Therefore, to simulate the faster increase of the central radiation and the accelerated transition to peaked profiles, an additional anomalous diffusion coefficient of the order of 1000–3000 $cm^2 \cdot s^{-1}$ was added predominantly in the central plasma region. The intensity simulation resulting from this modification is given in Fig.6c. The rather local deviation from neoclassical transport may possibly be caused by magnetic-island formation near the plasma centre. This hypothesis is supported by the observation of fairly flat temperature and density profiles around the plasma centre for typical discharges.

The decay of the Al radiation intensity after 190 ms is almost entirely caused by the electron temperature reduction at the end of the discharge. This is illustrated in Figs 7a, b, where the Al density corresponding to the calculation of the radiation intensity (Fig.6c) is plotted.

The measurement is thus consistent with only negligible losses of Al ions for the whole duration of the discharge. In the plasma centre, even a steady increase of the Al density can be observed, apparently as a result of the neoclassical inward velocity in combination with the continuous steepening of the plasma density profile in the plasma centre.

The characteristic time behaviour of the line integrated intensities from three different ionization states (Al X (333 Å), Al XI (550 Å), Al XII (7.76 Å)) is also in good agreement with the calculation, as follows from comparison of Fig.8a (exp. data) with Fig.8b (code calculation).

The relaxation of the initially hollow Al profiles with steep gradients towards centrally peaked profiles provides a way to obtain the transport fluxes quantitatively, at least in the main plasma volume, where Al^{11+} is the dominant charge state. In particular, this makes it possible to detect, if it exists, an enhancement of the transport fluxes beyond the neoclassical transport during the discharge and across the plasma radius.

In order to study details of the Al penetration into the plasma centre under different plasma conditions, the Al injection time was varied during a series of plasma discharges. Figure 9a shows an Al ablation measurement (Al radiation deduced from soft-X-ray signals) into a similar high-density discharge, but with the time of ablation delayed by about 10 ms. The sudden redistribution of the Al ion density occurring within a short time interval (1–2 ms) at about 190 ms cannot be explained by neoclassical transport calculations (Fig.9b).

Qualitatively, the observed behaviour could be reproduced by switching on an anomalous transport flux for 1–2 ms, restricted to a spatial width of about 3 cm. This leads to a shift of Al impurities outward, flattening the Al density peak at about 5 cm. The flat radiation profiles in the central region inside about 3 cm again seem to be produced by anomalous effects. A possible explanation of these observations, also seen in other discharge types, is the generation and shift of zones with enhanced transport (localized magnetic islands at rational ι-values induced by β-effects [19]) from the centre to the gradient region.

As regards the Al transport in the low-density discharges, which always show fairly peaked plasma density profiles, good agreement is obtained between the experimentally observed Al radiation and code predictions based only on neoclassical transport.

Figure 10 illustrates the result for the low-density discharge type D (see Table I) already introduced in Figs 4a and 5a. The increase in the Al radiation from

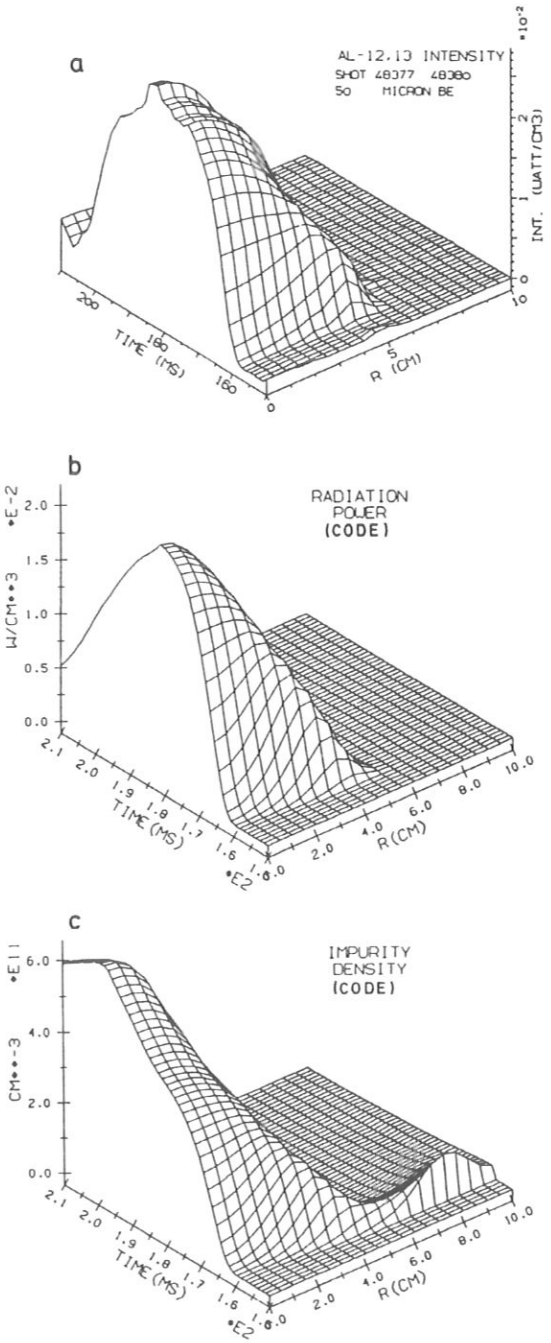

FIG.10. *a) Evolution of Al XII, XIII radiation power from soft-X-ray measurements after Al injection into low-density discharge with 'counter' NBI (type D);*
b) code simulation with neoclassical transport fluxes;
c) code simulation of the Al ion density corresponding to b).

the He- and H-like ionization states observed experimentally (Fig. 10a) seems to be faster in the plasma centre than in the high-density case. Figure 10b is the result of a simulation with purely neoclassical transport fluxes. The evolution of the corresponding Al density, summed over all ionization states, is plotted in Fig. 10c. The accumulation in the plasma centre can be seen again. The volume-averaged Al density does not indicate a noticeable loss until the end of the discharge.

For this discharge type and also for the other ones shown in Table I, the agreement between the absolute radiation levels in experiment and code simulation is rather good.

With respect to the comparison of 'co' and 'counter' experiments, no significant difference was found in their global behaviour or in the transport of Al test impurities. This suggests that potential modifications of the impurity fluxes due to beam-driven toroidal rotation are negligible owing to the nearly perpendicular injection and to measured toroidal rotation velocities of $\leqslant 2 \times 10^5$ cm·s^{-1} in the plasma centre, which are significantly lower than the thermal velocities of the intrinsic impurity ions [12, 39, 40].

5. SIMULATION OF THE TOTAL RADIATION

To describe the radiation from the intrinsic impurities within the same impurity transport model, soft-X-ray emission and bolometer measurements are simulated by summation over the relevant resonance lines of the dominant impurity element (oxygen). In particular, the same discharge types used for the Al tracer injection experiments were investigated.

As already mentioned in Section 3, a source term is used in the calculations for modelling beam-deposited oxygen impurities. A 1% oxygen contamination of the neutral beams was assumed in the calculations for all injectors. This amount is believed to be an upper limit for the contamination in the case of Ti-gettered ion sources, according to earlier in situ measurements with laser fluorescence for one of the injectors [41].

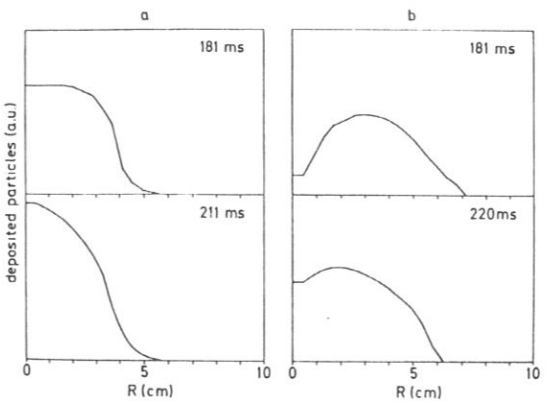

FIG. 11. Deposition profiles of beam-injected oxygen calculated by ODIN code (normalized amplitudes) for temperature and density profiles given in Fig. 5.
a) Low-density discharge ('counter' injection), type D;
b) high-density discharge ('co' injection), type A.

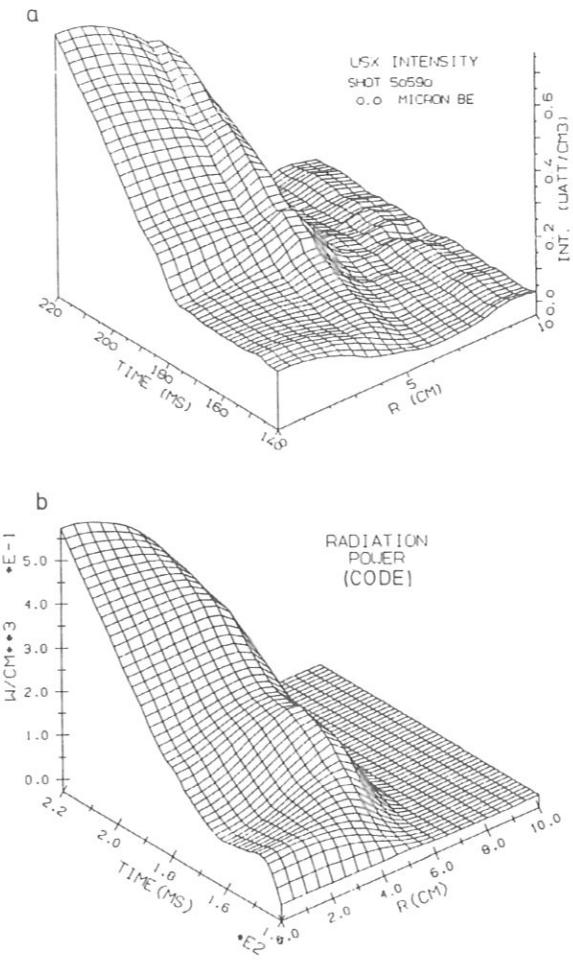

FIG. 12. a) Soft X-radiation ($E \geqslant 400$ eV) for high-density discharge (type A, same experimental conditions as in Figs 4b, 5b and 6);
b) code simulation of soft-X-radiation with oxygen.

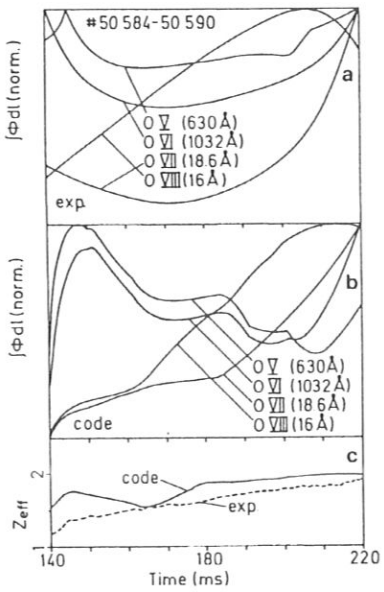

FIG.13. Comparison of measured line-integrated intensities from four resonance lines (a) and of Z_{eff} (c) with simulation (b,c).

Investigations of the ion beam impurity content of one injector [42] with mass spectrometry gave similar results.

Normalized radial profiles for beam-deposited oxygen (after thermalization) from Monte-Carlo calculations are shown in Fig.11 for the discharges D, A and the same times for which the T_e and n_e profiles are given in Fig.5 (Fig.11a: low-density, 'counter' (type D); Fig.11b: high-density, 'co' (type A)).

In Fig.12 the local soft-X-radiation (Fig.12a) observed for the high-density discharge (type A, see Figs 4b, 5b and 6) is compared with a code simulation based on oxygen impurities and neoclassical transport which was modified by the addition of the same anomalous term already used in Fig.6c (Fig.12b). The need for including additional anomalous transport is not very stringent since the impurity profiles of the oxygen ions always approach the background ion profile owing to the continuous source terms. Almost all oxygen calculations with neoclassical transport lead to good agreement with the measurements.

Since it was not possible to simulate the observed radiation level with beam-deposited oxygen alone, an additional flux of oxygen ($\Gamma = 2.8 \times 10^{18}\,s^{-1}$) from the walls, corresponding to a flux density of about $3 \times 10^{13}\,cm^{-2} \cdot s^{-1}$, had to be assumed for the calculations shown in Fig.12b. In the high-density case, the two impurity sources contribute in almost equal parts.

In Fig.13 the measured brightnesses of individual resonance lines (O V–O VIII, Fig.13a) are compared with the code calculations (Fig.13b). For radiation from outside the hot plasma core (O V, O VI), good agreement may not be expected owing to asymmetric distributions of the impurity sources. Z_{eff}, as obtained from the soft-X-ray continuum (Fig.13c), reaches a value of about 1.8, corresponding to an oxygen concentration of about 2.2% of the electron density. This is in reasonable agreement with the central value of the code calculation.

The low-density discharges (without gas puff during NI) are characterized by significantly higher central radiation losses with Z_{eff} up to 4.5 and n_O/n_e increasing up to 7%. The oxygen influx from the walls has to be increased to $8 \times 10^{13}\,cm^{-2} \cdot s^{-1}$ (about $7.5 \times 10^{18}\,s^{-1}$) in the calculation to fit the experimental data. In this case a beam impurity content of 1% contributes only 15% of the central impurity content.

The low-density discharges probably have a higher contribution of heavy impurity radiation, originating from wall material (iron). This is particularly evident for the low-density discharge with 'counter' injection, type D.

Figures 14a and 14b show the total radiation intensity measured by bolometers and the soft-X-ray intensity, respectively. The result of the simulation using oxygen impurities (1% in neutral beams, $5 \times 10^{13}\,cm^{-2} \cdot s^{-1}$ cold oxygen influx from walls) is plotted in Fig.14c. The drop of the measured intensity after about 200 ms cannot be simulated with oxygen. because the recombination of the fully ionized state compensates the reduction due to the decreasing excitation rates of the dominant resonance lines.

Separate calculations were therefore performed with iron impurity radiation. At the moment the SITAR code does not allow different impurity species to be treated simultaneously, which corresponds to neglecting their mutual interaction. The resulting total radiation power in the soft-X-ray energy range (Fig.14d), obtained by summing up the radiation of two separate calculations, fits very well to the experimental data. The adjustment to the observed absolute radiation power was achieved by reducing the oxygen influx from the walls to $3–4 \times 10^{13}\,cm^{-2} \cdot s^{-1}$ and introducing an increasing flux of iron from the walls of up to about $7 \times 10^{12}\,cm^{-2} \cdot s^{-1}$ ($\cong 6.6 \times 10^{17}\,s^{-1}$).

Under these conditions the contribution of Fe-line radiation is about 40% of the total radiation in the plasma centre at maximum radiation power. In particular, the simulated profiles become slightly more peaked to the axis, improving the agreement with the

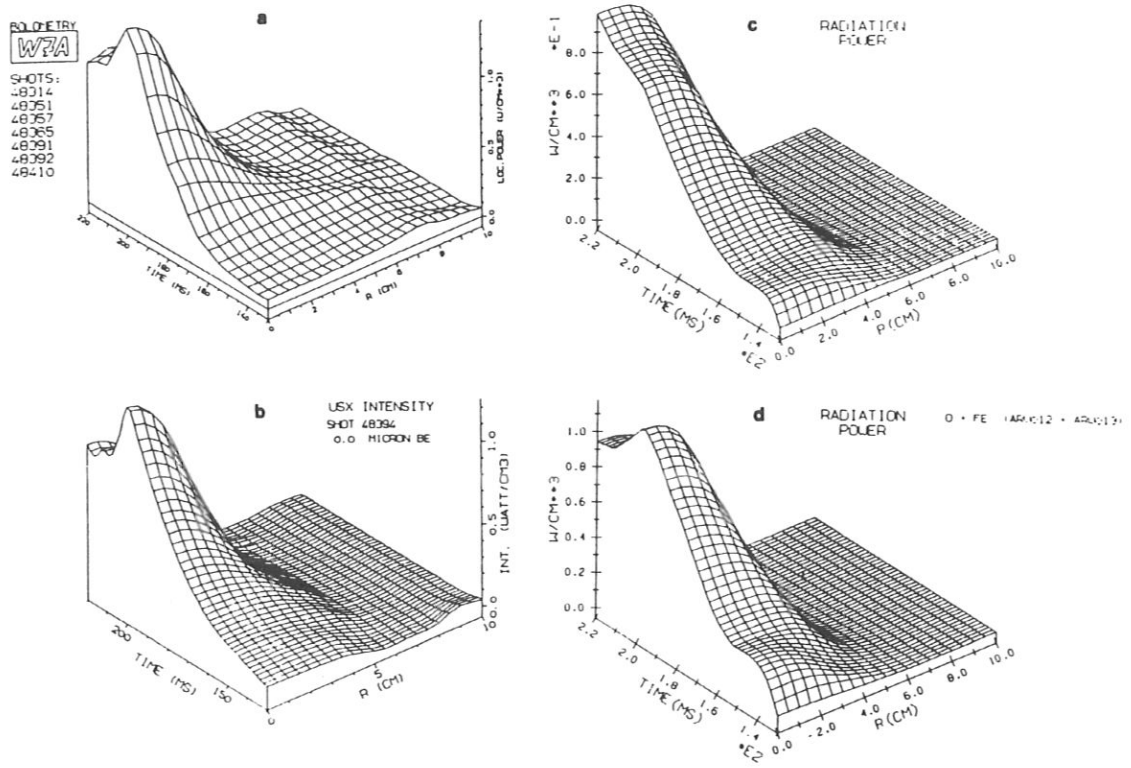

FIG.14. a) Evolution of total radiation power (bolometer) in low-density discharge ('counter' NBI), type D;
b) evolution of soft-X-radiation ($E \geqslant 400$ eV);
c) code simulation with oxygen impurities and neoclassical transport fluxes;
d) code simulation with combination of oxygen and iron impurities (neoclassical transport fluxes).

soft-X-ray measurements. Experimental evidence of the role of the iron radiation in this low-density discharge is also found by crystal spectrometer measurements. The radiances of the Fe XVII and Fe XVIII resonance lines, which dominate the central iron radiation, show the significant decrease at the end of the discharge, when the electron temperature drops.

The temporal evolution of the measured intensity of the most important lines of oxygen and iron is compared in Fig.15 with the code calculations. As in the oxygen case, calculated neoclassical transport fluxes were used for the iron transport simulations. The remaining discrepancy between the experiment and the code calculations may be partly attributed to the background signals contributing to the measured line intensities.

Although the influx of oxygen and iron from the walls assumed in the simulations in order to reproduce the observed radiation level was not measured quantitatively, these fluxes can be qualitatively explained by impurity release mechanisms from the wall or limiting structures. In the case of oxygen radiation, ion-induced desorption of loosely bound oxygen or oxygen-containing molecules, which can be produced by reactions between incident ions and surface oxides, are considered to be the dominant process [43–47]. The oxygen desorption cross-sections measured for different metal-adsorbate systems are in the range of about $1 \times 10^{-16}\,\mathrm{cm}^2$, probably even higher for adsorbed water molecules [44, 48, 49]. Additional desorption with comparable cross-sections is expected from charge exchange neutrals.

An additional aspect of ion-induced desorption of light impurities is the relatively high energy transfer to the desorbed particles, thus leading to better penetration of the scrape-off layer [49]. In addition, the

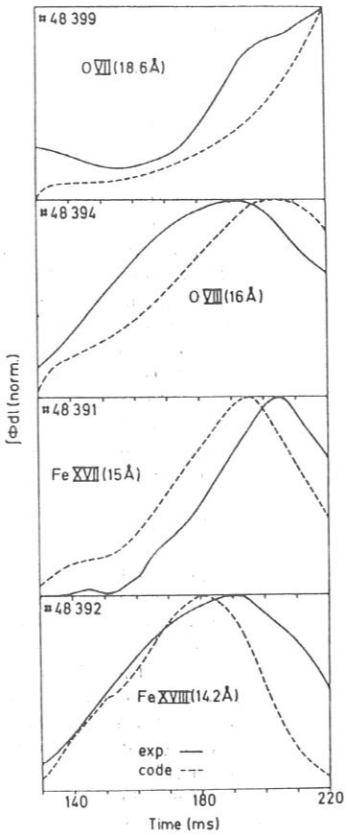

FIG.15. Temporal evolution of radiances of resonance lines from oxygen and iron for discharge type D discussed in Figs 10 and 14. Comparison with code calculations. a) O VIII, 16 Å; b) O VII, 18.6 Å; c) Fe XVII, 15 Å; d) Fe XVIII, 14.2 Å.

ionization lengths for neutral light impurities are larger than those for heavy elements. Crude estimates of the desorbed oxygen flux can be obtained with the following assumptions:

- a surface concentration of at least one monolayer of oxygen atoms or molecules (about $10^{15}\,cm^{-2}$)
- a particle confinement time of about 100 ms for the H and D ions
- a total number of confined H and D ions of about 1×10^{19}, which is a typical value for medium-density values

Then the particle outflux from the plasma at the wall is of the order of about $1 \times 10^{15}\,cm^{-2} \cdot s^{-1}$, leading to an oxygen influx of about $5 \times 10^{13}\,cm^{-2} \cdot s^{-1}$. This value is close to what was assumed in the code calculations.

With respect to the iron influx, values of about $2 \times 10^{17}\,s^{-1}$, originating from sputtering by lost fast ions from NBI, are derived experimentally from resonance fluorescence measurements [17, 18]. They agree with the values calculated by the ODIN code. An additional contribution of comparable size was estimated for iron sputtering by charge exchange neutrals from the plasma core. Thus, this iron influx seems to be compatible with the value used to simulate the radiation of the low-density discharge.

6. DISCUSSION, CONCLUSIONS AND SUMMARY

In general, the main features of the impurity transport in W VII-A are consistent with neoclassical predictions. An important consequence of this behaviour is the central impurity accumulation associated with the density and temperature gradients observed in W VII-A.

For the special conditions of some particular discharges, the introduction of an enhanced diffusivity during a part of the discharge duration and at a particular range in radius was required in the code calculations in order to achieve good agreement with the experimental data. Such enhancements in transport, localized in time and radius, are well known to be caused by distortions of the magnetic configuration occurring around rational ι-values (islands, ergodic regions). Occurrence and position of such resonant magnetic surfaces are determined by the vacuum magnetic configuration, by β-effects, changes of the residual plasma current profiles and fluctuations of the helical magnetic field caused by the usual imperfections of the power supplies. They thus have the tendency to vary during the course of the discharge. For most of the experiments the conditions were such that major resonances were excluded from the confinement regions so that such effects could not occur.

Simulations with Al tracer and intrinsic impurities provide a consistent description of the transport.

The study of the impurity transport behaviour with laser-driven injection of Al tracer impurities has several advantages compared with the study of the intrinsic impurities:

- the source strength is fairly well known, it is well defined in time and recycling effects can be excluded;
- transport fluxes can be derived quantitatively from observation of the dynamics during the penetration

of the impurity ions into the plasma. In this phase the impurity radiation profiles are very sensitive to localized and fast changes of the transport, which can hardly be detected in the case of quasi-stationary profiles;
- the He-like state generally dominates the whole hot central plasma region and fully stripped ions can be neglected. The representative transport behaviour can therefore be obtained with only one or two ion charge states. For these states no effects of poloidal and toroidal asymmetries are expected either.

Complications can arise, however, from:
- the strong dependence of the Al radiation intensity on the electron temperature;
- the high sensitivity of the calculations using transport fluxes which depend on gradients of measured density and temperature profiles;
  High accuracy of the input profile data is therefore needed.

Measurements of the total radiation from the intrinsic impurities, which are mainly oxygen besides a significant contribution of iron in low-density discharges, can generally be simulated reasonably well with neoclassical transport.

The observation of radiation profiles highly peaked to the axis does not exclusively require direct deposition of impurities in the plasma centre. Already the relatively high local values for the diffusion coefficients and the inward drift velocities for the impurity ions expected from neoclassical theory can explain their fast penetration into the plasma and the good confinement.

The analysis of the total radiation in discharges with and without additional D_2 gas feed indicates a reduction of the impurity radiation level in the plasma centre in the first case, due to broad plasma density profiles. This is to be expected from neoclassical transport theory because of the small inward velocity in the plasma centre.

Al injection experiments also show a higher central Al density for discharges without gas feed. A certain degree of impurity control can, therefore, be achieved with strong gas puffing, which also has a beneficial effect because of the reduction of the impurity production due to edge cooling. But the broad plasma density profiles are generally maintained only in the first phase of neutral-beam injection. Afterwards, beam fuelling always leads to peaked density profiles (only about 10 cm plasma radius in W VII-A), which favour the central impurity accumulation.

In the case of dominant oxygen radiation, recombination effects of fully ionized oxygen induced by beam neutrals and reduction of the electron temperature provide some contribution to the central radiation power. In the calculations, the charge exchange reactions typically lead to an enhancement of 20–30%, as compared with calculations not including this effect.

A significant contribution of neutral-beam-induced transport effects could not be observed, probably owing to the almost perpendicular neutral-beam injection.

ACKNOWLEDGEMENTS

The authors would like to acknowledge the excellent support of the technical staff, the data acquisition group and the computer centre, in particular that of J. Bömerl, A. Eschlwech, D. Gonda, A. Gronmayer, K. Iraschko, P. Voigt, and G. Abele. The authors are also indebted to Margot Richter-Gloetzl and W. von Zeppelin for their contributions to the software of the SITAR transport code and for performing the ODIN beam deposition code calculations. The contribution of K. Behringer relating to the atomic data used is gratefully acknowledged. The authors also wish to express their appreciation to A.J. Wootton and E.C. Crume for valuable discussions on impurity transport effects.

REFERENCES

[1] W VII-A TEAM, NI GROUP, in Plasma Physics and Controlled Nuclear Fusion Research 1982 (Proc. 9th Int. Conf. Baltimore, 1982), Vol.2, IAEA, Vienna (1983) 241.
[2] W VII-A TEAM, NI GROUP, in Plasma Physics and Controlled Nuclear Fusion Research 1980 (Proc. 8th Int. Conf. Brussels, 1980), Vol.1, IAEA, Vienna (1981) 185.
[3] SMEULDERS, P., Soft X-ray Fluxes as a Diagnostic for Hot Plasmas, Max-Planck-Institut für Plasmaphysik Garching Rep. IPP-2/233 (1979).
[4] W VII-A TEAM, NI GROUP, Evolution of Radiation Losses and Importance of Charge Exchange between Plasma Impurities and Injection Beam Neutrals in the W VII-A Stellarator (paper read at 5th General Conf. EPS, Istanbul, 1981).
[5] COHEN, S.A., CECCHI, J.L., MARMAR, E.S., Phys. Rev. Lett. **35** (1975) 1507.
[6] MARMAR, E.S., RICE, J.E., ALLEN, S.L., Phys. Rev. Lett. **45** (1980) 2025.
[7] SUCKEWER, S., CAVALLO, A., COHEN, S., DAUGHNEY, C., DENNE, B., et al., Ion Transport Studies on the PLT Tokamak during Neutral Beam Injection, PPL Princeton Univ. Rep. PPPL-2063 (1983).

[8] ALLEN, S.L., MOOS, H.W., MARMAR, E.S., RICE, J.E., Nucl. Fusion **23** (1983) 303.
[9] MARMAR, E.S., RICE, J.E., TERRY, J.L., SEGUIN, F.H., Impurity Injection Experiments on the ALCATOR C Tokamak, Plasma Fusion Center, MIT, Rep. PFC/JA-82-12 (1982).
[10] ALCATOR C GROUP, Energy and Impurity Transport in the ALCATOR C Tokamak, Plasma Fusion Center, MIT Rep. PFC/CP-82-7 (1982).
[11] BURRELL, K.H., WONG, S.K., MULLER, C.H., HACKER, M.P., KETTERER, H.E., et al., Nucl. Fusion **21** (1981) 1009.
[12] ISLER, R.C., MURRAY, L.E., CRUME, E.C., BUSH, C.E., DUNLAP, J.L., et al., Nucl. Fusion **23** (1983) 1017.
[13] TFR GROUP, Nucl. Fusion **23** (1983) 559.
[14] RICE, J.E., TERRY, J.L., MARMAR, E.S., MOTOJIMA, O., KANEKO, H., et al., Transport of Injected Impurities in HELIOTRON-E, Plasma Fusion Center MIT, PPL Kyoto Univ. Rep. PFC/JA-83-42 (1983).
[15] SARDEI, F., WELLER, A., The One-Dimensional Transport and Radiation Code SITAR for Modelling Impurity Radiation in the Wendelstein VII-A Stellarator (in preparation).
[16] W VII-A TEAM, NI GROUP, in Plasma Physics and Controlled Nuclear Fusion Research 1984 (Proc. 10th Int. Conf. London, 1984), Vol.2, IAEA, Vienna (1985) 635.
[17] W VII-A TEAM, NI GROUP, ibid., 371.
[18] W VII-A TEAM, NI GROUP, 5th Int. Workshop on Stellarators (Proc. IAEA Techn. Commit. Meeting on Plasma Confinement and Heating in Stellarators, Schloss Ringberg (FRG), 1984), Vol.1, CEC, Brussels (1984) 259.
[19] WOBIG, H., ibid., 363.
[20] W VII-A TEAM, NI GROUP, in Controlled Fusion and Plasma Physics (Proc. 11th Europ. Conf. Aachen, 1983), Vol.7D, Part I (1983) 195.
[21] W VII-A TEAM, NI GROUP, ibid., 191.
[22] JÄCKEL, H., KÜHNER, G., Bolometer Diagnostic at W VII-A, Max-Planck-Institut für Plasmaphysik Garching, to appear as IPP Report (1986).
[23] W VII-A TEAM, Mode and Sawtooth Behaviour during Neutral Beam Injection in the W VII-A Stellarator, Max-Planck-Institut für Plasmaphysik Garching Rep. IPP 2/250 (1980).
[24] W VII-A TEAM, in Controlled Fusion and Plasma Physics (Proc. 9th Europ. Conf. Oxford, 1979), paper BP26, 80.
[25] WOBIG, H., private communication (Max-Planck-Institut für Plasmaphysik, 1979).
[26] SCHOU, J., SCHERZER, B.M.U., RENNER, H., J. Nucl. Mater. **111&112** (1982) 162.
[27] BURRELL, K.H., WONG, S.K., AMANO, T., Nucl. Fusion **20** (1980) 1021.
[28] MARMAR, E.S., CECCHI, J.L., COHEN, S.A., Rev. Sci. Instrum. **46** (1975) 1149.
[29] MANOS, D., RUZIC, D., MOORE, R., COHEN, S., J. Vac. Sci. Technol. **20** (1982) 1230.
[30] LISTER, G.G., OTT, W., SPETH, E., in Heating in Toroidal Plasmas (Proc. 3rd Joint Grenoble-Varenna Int. Symp. Grenoble, 1982), Vol.1, CEC, Brussels (1982) 103.
[31] TFR GROUP, Nucl. Fusion **22** (1982) 1182.
[32] HASTINGS, D.E., HOULBERG, W.A., SHAING, K.C., Nucl. Fusion **25** (1985) 445.
[33] HIRSHMAN, S.P., Phys. Fluids **20** (1977) 589.
[34] HAWRYLUK, R.J., SUCKEWER, S., HIRSHMAN, S.P., Nucl. Fusion **19** (1979) 607.
[35] HIRSHMAN, S.P., Summary of Collisional Particle Fluxes in Tokamak Plasma, Oak Ridge National Laboratory Rep. ORNL/TM-6481.
[36] KATO, T., Ionization and Excitation of Ions by Electron Impact – Review of Empirical Formulae, Nagoya Univ. Inst. of Plasma Physics Rep. IPPJ-AM-2 (1977).
[37] CHANG, C.S., HAZELTINE, R.D., Nucl. Fusion **20** (1980) 1397.
[38] NI TEAM, W VII-A TEAM, in Heating in Toroidal Plasmas (Proc. 4th Int. Symp. Rome, 1984), Vol.1 (1984) 95.
[39] STACEY, W.M., SIGMAR, D.J., Rotation and Impurity Transport in a Tokamak Plasma with Directed Neutral Beam Injection, Georgia Inst. of Techn., Atlanta, Rep. GFTR 47 (1984).
[40] STACEY, W.M., BENNETT, R.B., SIGMAR, D.J., Neutral Beam Driven Impurity Flow Reversal in Tokamaks, Georgia Inst. of Techn., Atlanta, Rep. GFTR 42 (1983).
[41] BOGEN, P., SCHWEER, B., RINGLER, H., OTT, W., J. Nucl. Mater. **111&112** (1982) 67.
[42] OTT, W., FREUDENBERGER, K., PENNINGSFELD, F.P., PROBST, F., SÜSS, R., Rev. Sci. Instrum. **54** (1983) 50.
[43] McCRACKEN, G.M., STOTT, P.E., Nucl. Fusion **19** (1979) 889.
[44] KOMA, A. (Ed.), Desorption and Related Phenomena Relevant to Fusion Devices, Nagoya Univ. Inst. of Plasma Physics Rep. IPPJ-AM-22 (1982).
[45] SAGARA, A., KAMADA, K., J. Nucl. Mater. **111&112** (1982) 812.
[46] TAGLAUER, E., private communication (Max-Planck-Institut für Plasmaphysik, Garching, 1985).
[47] DEWALD, B., A Review of Plasma Impurity Sources during Tokamak Operation, Georgia Inst. of Techn., Atlanta, Rep. GFTR 30 (1982).
[48] TAGLAUER, E., HEILAND, W., BEITAT, U., Surface Sci. **89** (1979) 710.
[49] TAGLAUER, E., BEITAT, U., J. Nucl. Mater. **111&112** (1982) 800.

(Manuscript received 17 May 1985
Final manuscript received 9 August 1985)

ELECTRON CYCLOTRON RESONANCE HEATING EXPERIMENTS IN THE WENDELSTEIN VII-A STELLARATOR

V. ERCKMANN, G. JANZEN, W. KASPAREK, G. MÜLLER,
P. G. SCHÜLLER, K. SCHWÖRER, M. THUMM, and R. WILHELM
Institut für Plasmaforschung, Universität Stuttgart, D-7000 Stuttgart 80
Federal Republic of Germany

W VII-A TEAM* *Max-Planck-Institut für Plasmaphysik*
EURATOM Association, D-8046 Garching, Federal Republic of Germany

Received July 12, 1984
Accepted for Publication November 16, 1984

Plasma buildup and heating of ohmically heated currentless plasmas by electron cyclotron resonance heating (28 GHz, 200 kW, 40 ms) were investigated in the WENDELSTEIN VII-A stellarator. Two different kinds of wave launching were examined in detail. First, the gyrotron mode mixture, containing 50% of the total power in ordinary (O)-mode and 50% in extraordinary (X)-mode polarization, was irradiated from the low-field side. Then a linearly polarized wave in O-mode polarization was launched from the low-field side, the nonabsorbed fraction being reflected back to the plasma from the high-field side in X-mode polarization.

An increase of the central electron temperature from 0.6 keV (first case) to 1.2 keV (second case) was observed, which is explained as being due to the narrow power deposition profile in the latter case rather than due to the slight increase of the heating efficiency from 40 to 50%. Strong evidence of parametric decay of the X-mode fraction is found. Transport calculations using neoclassical plateau coefficients for the electron heat conduction including ripple losses fit well with the measured profiles, if enhanced losses at the plasma edge are introduced.

*The W VII-A Team consists of D. Dorst, A. Elsner, G. Grieger, P. Grigull, H. Hacker, H. J. Hartfuß, H. Jäckel, R. Jaenicke, J. Junker, M. Kick, H. Kroiss, G. Kühner, C. Mahn, S. Marlier, G. Müller, W. Ohlendorf, F. Rau, H. Renner, H. Ringler, F. Sardei, M. Tutter, A. Weller, H. Wobig, E. Würsching, and M. Zippe.

I. INTRODUCTION

In addition to such well-established methods of heating fusion plasmas as ohmic heating (OH) and neutral injection, heating by radio-frequency (rf) waves over a wide range of frequencies [at the lower hybrid (LH) frequency, the ion cyclotron frequency, and the electron cyclotron frequency] have attracted increasing interest during the past few years. Electron cyclotron resonance heating (ECRH) seems favorable for different reasons. Application of ECRH for fusion plasma heating became possible since high-power gyrotrons at reasonable frequencies in the 100-kW range were successfully developed by several manufacturers and laboratories. This development is rapidly progressing toward higher frequencies in the 100-GHz range at power levels of 200 kW/tube in continuous-wave operation, thus extending the accessible parameter range (magnetic field and plasma density) to fit the present day machine data, for tokamaks as well as for stellarators.

One of the most interesting aspects of ECRH for toroidal devices with a confining vacuum magnetic field configuration, where no plasma current is necessary for stability, such as stellarators and torsatrons, is that plasma buildup and heating from the neutral gas without ohmic preheating and hence "net-current-free" operation become possible.[1-4]

In the WENDELSTEIN (W) VII-A stellarator ($R = 2.0$ m, $a = 0.1$ m, $l = 2$, $m = 5$), experiments were performed with a VARIAN gyrotron VGA 8050 A, emitting 200-kW rf output power at 28 GHz for 40 ms. This frequency restricts the stellarator operation to $B_0 = B_{res} = 1$ T (nominal field $B_0 = 3.5$ T) and densities $n_{e0} \lesssim n_e$, cutoff $= 1 \times 10^{19}$ m^{-3}. The experiments are a preparatory step for the ECRH system of the

future W VII-AS at 70 GHz (corresponding to the designed magnetic field of 2.5 T) and higher power (1 MW) (Refs. 5 and 6).

Different kinds of wave launching were examined to find optimal coupling conditions that meet the special stellarator requirements, i.e.,

1. plasma buildup
2. heating of a "cold" plasma to overcome the "radiation barrier"
3. heating of a "hot" plasma.

Section II deals with the technical aspects of different launching systems. A summary of the results concerning wave absorption and heating efficiency for the investigated launching systems is given in Sec. III. Finally, a description of the confinement and transport properties of ECRH plasmas is given in Sec. IV.

II. TRANSMISSION LINES AND LAUNCHING SYSTEMS

In a first step, the output mode mixture of the gyrotron, containing 80% of the total power in the axisymmetric TE_{02} mode (7% TE_{01}, 9% TE_{03}, 4% others) was radiated to the plasma from the low-field side in the equatorial plane. The power was transmitted through an oversized, circular ($2\frac{1}{2}$-in. i.d.) corrugated, smooth 90-deg bend that was optimized with respect to mode conservation[7-9] and a straight circular waveguide section 25 m in length with the same i.d. In the straight section a mode selective directional coupler[10] and a multiple thermographic paper mode pattern analyzer for measurement of the mode content are inserted. The antenna is an open-ended circular waveguide with the same i.d., the axis of which is oriented perpendicular to the main magnetic field. The arrangement is shown schematically in Fig. 1 and is referred to later as the "TE_{02} case."

The far-field radiation pattern of the TE_{02} mode is double-coned with a divergence angle of 27 deg (3-dB points); 50% of the total rf power is in ordinary (O)-mode polarization ($\vec{E} \parallel B_0$) and can propagate to the resonance region in the plasma center. The other 50% is orientated in extraordinary (X)-mode polarization ($\vec{E} \perp B_0$) and is reflected back from the X-mode cutoff layer $\omega_{pe}^2 = \omega(\omega - \omega_{ce})$ near the outer plasma edge (indicated in Fig. 1). Penetration of this

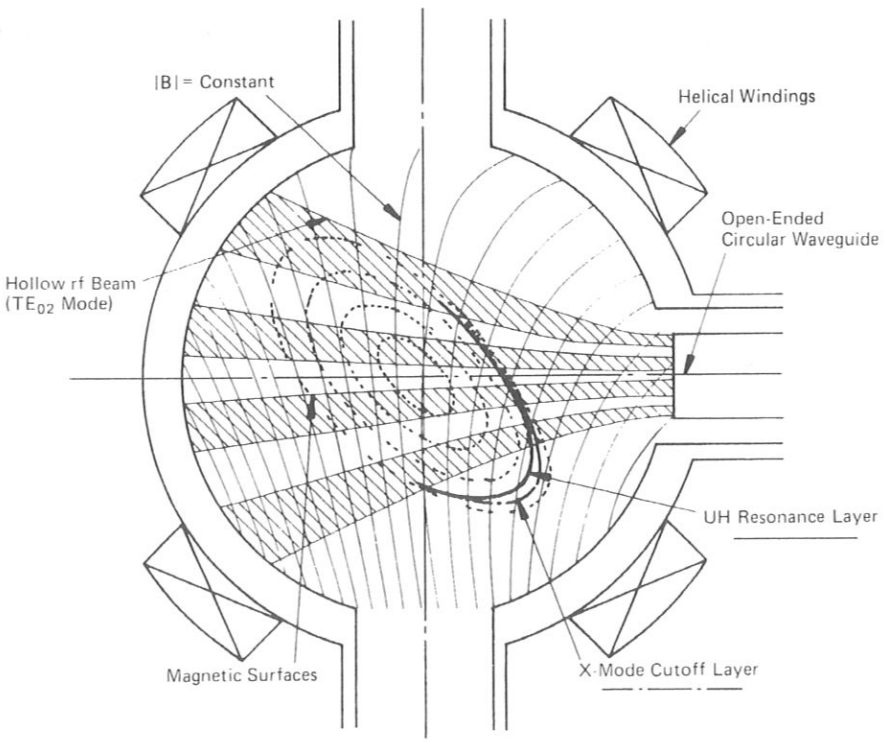

Fig. 1. Stellarator configuration and launching geometry of the axisymmetric TE_{02} mode.

portion toward the plasma center is only possible after multiple reflection from the torus walls. From ray-tracing calculations it follows that this kind of wave launching results in a broad power deposition profile.

In a second step, an almost linearly polarized wave was launched. The gyrotron output mode mixture was converted step by step from the TE_{02}/TE_{01} mixture to an almost pure TE_{01} mode, and finally to the almost linearly polarized TE_{11} mode. The first mode converter (TE_{02}/TE_{01} to TE_{01}) has a sinusoidal $m = 0$ wall perturbation with the beat wavelength of the two modes considered. The incoming phase-coupled mixture of TE_{02} and TE_{01} can be converted to a pure TE_{01} by properly choosing the amplitude of the perturbation and the number of perturbation wavelengths if the mode mixture enters the converter with the appropriate phase difference.[7,9] The phase matching was realized by shifting the converter along the waveguide axis and optimizing the TE_{01}-mode output behind the converter. A schematic drawing of this mode converter is given in Fig. 2a. The TE_{01} mode is weakly damped (10^{-3} dB/m) and therefore used for long-distance transmission. Conversion to the TE_{11} mode is made in close proximity to the antenna to reduce losses along the transmission line.

The TE_{01} to TE_{11} mode converter again has a sinusoidal wall perturbation, but with an $m = 1$ symmetry and the beat wavelength of the two modes.[7,9] The mode converter is shown schematically in Fig. 2b. To reduce the total length of the mode converter, the i.d. is reduced to 40 mm, which requires up and down tapering. The necessary tapers are numerically optimized with respect to mode conservation and have a nonlinear contour.[11,12] The polarization of the generated TE_{11} mode with respect to the magnetic field (O or X mode) can be chosen by 90-deg rotation of the mode converter. The TE_{11} mode has a very narrow far-field radiation pattern with a divergence angle of 6 deg (E plane, 3-dB points). This should result in a strongly localized narrow power deposition profile in the plasma.

As shown in Fig. 3, a focusing polarization twist reflector[13] is mounted at the inner torus wall opposite the antenna mouth. The nonabsorbed fraction of the incident radiation (O mode) is twisted in polarization by 90 deg (X mode) and focused back to the plasma from the high-field side. This coupling system (referred to later as the "TE_{11} case") switches automatically from X-mode heating in the plasma buildup phase (low temperatures in the electron-volt range, low absorption of the incident O mode) to O-mode heating in the high-temperature phase (T_e in the kiloelectron-volt range), where the plasma becomes optically thick for the O mode. The mirror is equipped with three rf measuring ports that allow measurement of the rf power distribution incident on the mirror and thus of the fraction absorbed by the plasma.

III. HEATING EFFICIENCY AND WAVE ABSORPTION

The heating efficiency, defined as $\eta = P_{abs}/P_{inc}$ (P_{abs} is the absorbed and P_{inc} the injected rf power), was determined by pulse modulation techniques. During a fast (compared to the energy confinement time) and short reduction of the incident rf power in the

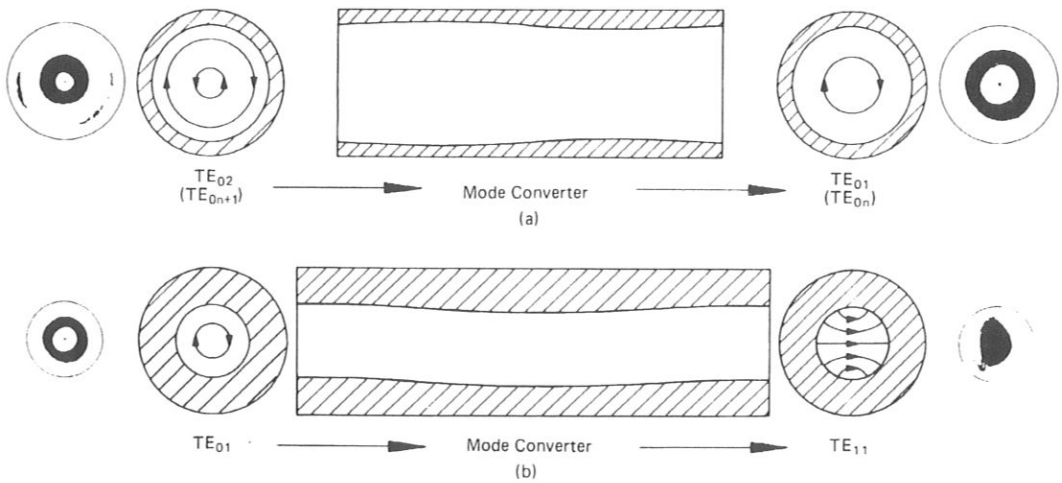

Fig. 2. Schematic drawing of (a) the $TE_{02} \rightarrow TE_{01}$-mode converter and (b) the $TE_{01} \rightarrow TE_{11}$-mode converter. Thermal paper prints from the mode pattern analyzer (hot measurement) are shown on the left and right side.

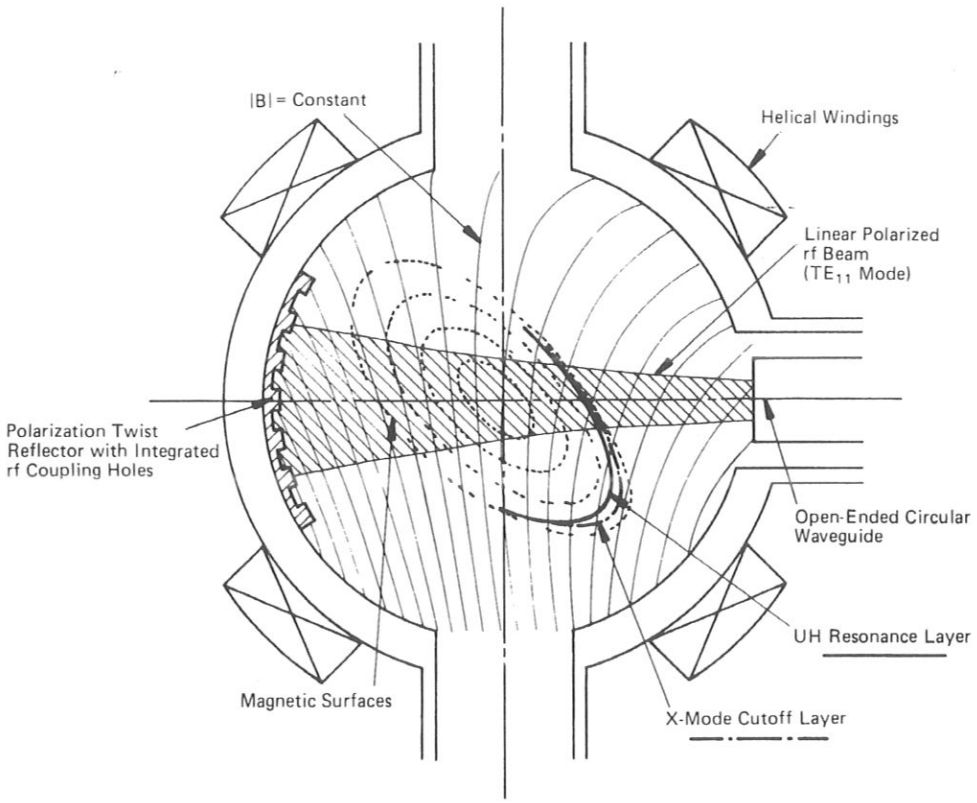

Fig. 3. Stellarator configuration and launching geometry of the almost linearly polarized TE_{11} mode.

steady-state phase of the discharge from an initial value $P_{rf,1}$ to an arbitrary value $P_{rf,2}$ (which may be even zero), the associated time response of the total plasma energy content W_p was measured by diamagnetic loop. An example is given in Fig. 4.

The time resolution of the diamagnetic loop is by an order of magnitude higher than the measured energy decay or rise times. Assuming that the energy confinement time τ_E remains constant during power modulation, the heating efficiency can be evaluated with high accuracy according to

$$\eta = \frac{\dfrac{dW_p}{dt}}{P_{rf,2} - P_{rf,1}} ,$$

by using different modulation depths. The heating efficiency was found to be 40% in the TE_{02} case and 50% in the TE_{11} case. The latter is less than expected for the advanced coupling system.

The single-pass absorption of the incident O mode was measured to be 50% of the incident power; this leads to a surprising result: The O-mode absorption alone is sufficient to explain the measured overall heating efficiency. The X-mode fraction, which is reflected back to the plasma from the high-field side mirror, does not significantly contribute to the total energy content.

Theory predicts[14] that an X-wave perpendicularly incident on the magnetic field from the high-field side propagates toward the upper hybrid (UH) resonance layer, where it undergoes linear mode conversion to backward traveling electron Bernstein modes (EBMs). The absorption layer of the EBM strongly depends on the wave vector $\boldsymbol{k}_{EBM}$.

One possible explanation of the poor contribution of the X mode to the global heating efficiency is that small density fluctuations at the plasma boundary may cause a spatial disturbance of the UH layer located at the very edge of the plasma (see Fig. 1). The EBMs will then have high $k_\parallel$ components and the absorption will take place in the outer plasma region, where no significant contributions to the experimentally determined heating efficiency can be expected.

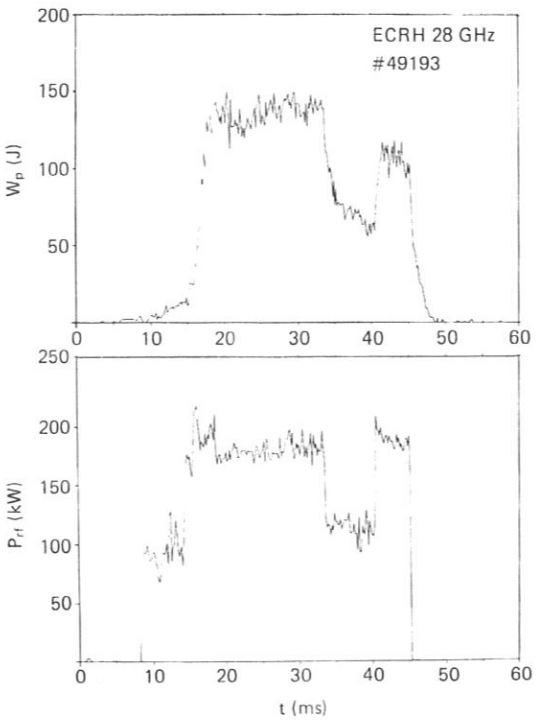

Fig. 4. Injected rf power P_{rf} and total plasma energy content W_p from diamagnetic loop as a function of time.

A second explanation to be considered is parametric decay of the incident pump wave near the UH resonance layer into daughter waves, one of which is the LH wave. This process was identified in the VERSATOR II tokamak[15] and in the FT-1 tokamak[16] during ECRH.

The observation of high-energy ion tails by charge-exchange (CX) measurements indicates the occurrence of parametric decay processes in the W VII-A experiments. As shown in Fig. 5, the mean energy of these tails is 500 eV and the population is ~1% of the total particle number. These ion tails may be created by absorption of the LH wave and do not exist in the TE_{02} case. From energy conservation it follows that the LH wave carries a maximum power of 1 kW. This is sufficient to create and maintain the observed ion tail, if total absorption of the wave and classical slowing down of the ions is assumed.

The high-frequency decay wave spectrum is detected by a microwave antenna; the frequency resolution is done with a ten-channel heterodyne system with a tunable local oscillator. As seen in Fig. 6a, nonsymmetric sidebands appear near the pump wave frequency (28 GHz). The intensity of the downshifted sideband is about one order of magnitude larger than the upshifted one.

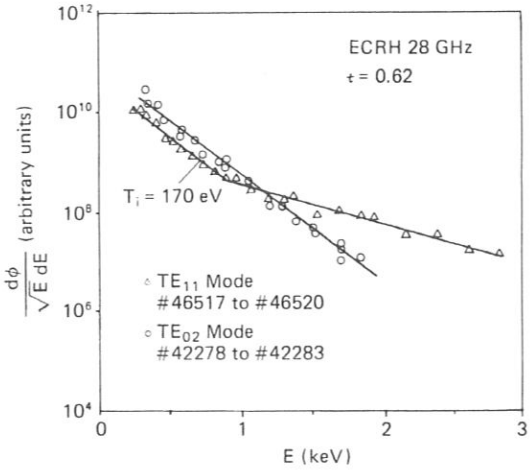

Fig. 5. Ion energy distribution from CX measurements for the TE_{11} and the TE_{02} cases.

The frequency separation of the lower sideband fits well with the low-frequency spectrum from Langmuir probes. As seen in Fig. 6b, the low-frequency decay spectrum shows a sharp drop at 220 MHz, which is the LH frequency near the plasma boundary. The intensity of the lower sideband and the intensity of the CX flux of the high-energy ion component were found to be correlated. This observation would fit the picture of wave decay near the UH resonance layer.

IV. ENERGY CONFINEMENT

The W VII-A stellarator has a vacuum magnetic field configuration with very low shear $\Delta\iota/\iota \approx 1\%$ ($\iota = 1/q$ is the rotational transform; q is the safety factor). Crossover and current leads in the helical windings lead to magnetic field perturbations and island formation near low-order rational numbers of ι ($\iota = \frac{1}{2}, \frac{1}{3}, \frac{2}{3} \ldots$). The confinement of net-current-free plasmas is strongly affected by the edge value of ι (Ref. 17). As seen in Fig. 7, the total plasma energy content W_p is plotted versus the external rotational transform ι and shows minima at rational ι numbers and maxima of the confinement in between. The same behavior is qualitatively found for the TE_{02} irradiation.[2] The total stored plasma energy is clearly found to be dependent on ι for irrational values of ι (Ref. 18).

A detailed analysis of the electron heat conduction for the TE_{02} and the TE_{11} cases was carried out under

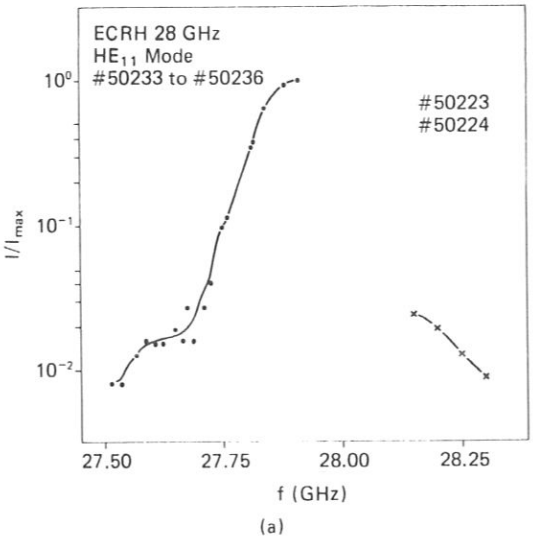

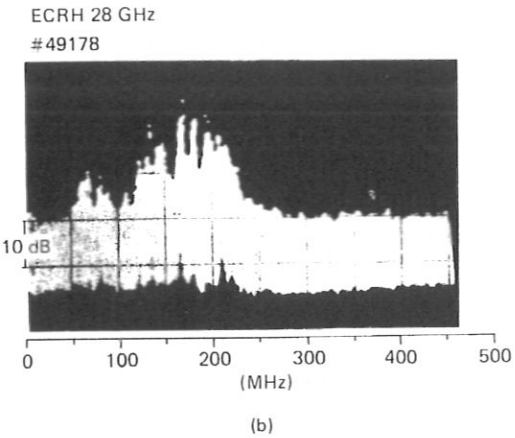

Fig. 6. Parametric decay wave spectra: (a) high-frequency sidebands detected by a microwave antenna and (b) low-frequency spectrum detected by Langmuir probes.

optimum confinement conditions at $\iota = 0.46$, indicated by a circle in Fig. 7. During the rf pulse an almost linearly increasing plasma current up to 700 A ($U_{loop} = 0$) is generated, which affects the $\iota(r)$ profile. In order to achieve steady-state discharges, the external rotational transform ι_0 (current in the helical windings) was feedback controlled to keep the total rotational transform

$$\iota = \iota_0 + \iota_p(a) \quad , \quad \iota_p(a) \sim \int_0^a \frac{j(r) r\, dr}{B}$$

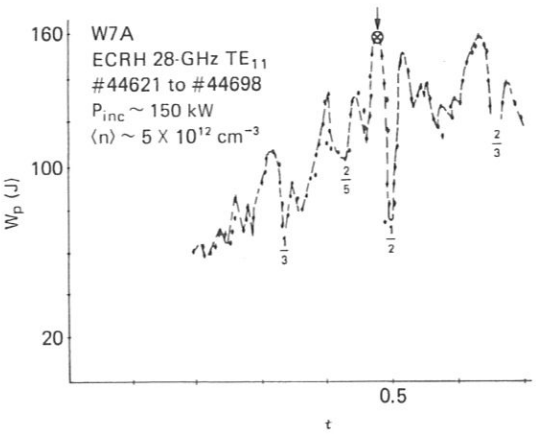

Fig. 7. Plasma energy content W_p versus rotational transform ι during ECRH at constant incident power (TE_{11} case).

constant at the plasma edge; ι_p gives the contribution of a plasma current distribution $j(r)$ to the total rotational transform ι.

The experiments are performed with the resonance field at the plasma axis. Because of the low densities ($n_{e0} \approx 5 \times 10^{18}$ m^{-3}), the ions are almost energetically decoupled from the hot electrons and remain at low temperatures ($T_i \approx 150$ eV). The energy balance is thus dominated by the electron behavior. For the low collisionality of the plasma, ripple effects should become important. The measured profiles of n_e and T_e (Thomson scattering) for both kinds of wave launching are given in Fig. 8.

The profiles were calculated with the Garching steady-state transport code TEMPL and the modified (stellarator configuration) time-dependent BALDUR code. Good agreement between measured and calculated profiles is achieved if the electron heat diffusivity χ_e is taken to be

$$\chi_e = \chi_{e,neo} + \chi_{e,rip} + \chi_{e,OH}$$

where $\chi_{e,neo}$ is the axisymmetric neoclassical coefficient

$$\chi_{e,neo} \propto T_e^{3/2}/R\iota B^2 \ ,$$

and

$$\chi_{e,rip} \propto \chi_{e,neo} \cdot \epsilon_H^{3/2} \lambda \iota / R$$

gives the losses induced by a magnetic field ripple $\epsilon_H = \frac{1}{2}\delta B/B$, where ϵ_H is a function of radius and λ is the mean-free-path of the electrons.[19]

The third term $\chi_{e,OH}$ was obtained empirically from OH discharges in W VII-A (Ref. 20)

$$\chi_{e,OH} \propto 1/n_e T_e^{2/3}$$

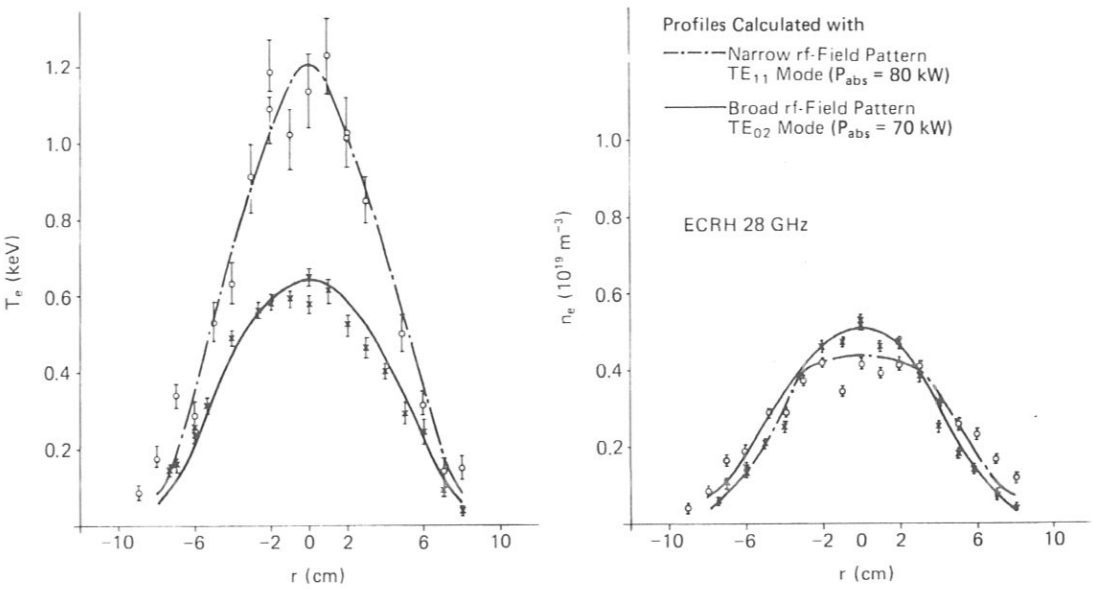

Fig. 8. Comparison of measured and calculated profiles of n_e and T_e for both kinds of wave coupling.

and introduces enhanced losses at the plasma edge, where density and temperature are low. The measured radiation losses of ~10 kW are taken into account. The power transfer from the electrons to the ions is assumed to be classical (Coulomb collisions). The power deposition profile is described by the parabolic expression

$$P = P_{abs}[1 - (r/a)^2]^{\beta} \ .$$

The appreciable increase of the central electron temperature from 0.6 keV (TE_{02} case) to 1.2 keV (TE_{11} case) is modeled just by changing the power deposition profile from a broad ($\beta = 2$, TE_{02} case) to a narrow ($\beta = 14$, TE_{11} case) profile corresponding to the measured far-field radiation pattern of both modes. The measured absorbed power is only slightly different in the two cases (70 kW in the TE_{02} case and 80 kW in the TE_{11} case). These calculations show that the improvement of the central electron temperature by a factor of 2 is due to the localized power deposition in the good confining plasma center rather than to the slight increase of the absorbed power.

V. CONCLUSIONS

In the W VII-A stellarator, ECRH discharges at 28 GHz ($P_{rf} = 200$ kW, $B_0 = 1$ T, $n_{e0} \leq 10^{19}$ m^{-3}) with different kinds of wave launching were investigated. Simple irradiation of the gyrotron output mode mixture (mainly TE_{02}, containing 50% in O-mode and 50% in X-mode polarization) from the low-field side is compared with an advanced coupling system where an almost linearly polarized TE_{11} mode is launched in O-mode polarization from the low-field side. The nonabsorbed fraction hits a polarization twist reflector mounted at the inner torus wall and is focused back to the plasma from the high-field side in X-mode polarization. Plasma buildup from the neutral gas and heating to appreciable plasma parameters is achieved with both coupling systems.

The heating efficiency is measured as 40% in the TE_{02} case and is only slightly increased (50%) in the TE_{11} case. In both cases single-pass O-mode absorption is sufficient to explain the measured overall heating efficiency; in other words, the contribution of X-mode heating (TE_{11} case) to the total plasma energy content is weak and less than predicted by theory. This result may be attributed to a turbulent UH resonance layer, leading to power deposition at the plasma edge, where the confinement is bad, and/or parametric decay processes near the UH layer. The latter is supported by measurements of the decay waves. The low-frequency wave may be absorbed by the ions, thus leading to the observed high-energy ion tails.

The energy confinement in W VII-A is strongly influenced by the rotational transform ϵ and shows minima at low rational values of ϵ and pronounced maxima in between. For good confinement conditions ($\epsilon = 0.46$), an increase of the central electron temperature from 0.6 keV (TE_{02} case) to 1.2 keV (TE_{11} case)

is found at comparable densities of $n_{e0} \approx 4 \times 10^{18}$ m^{-3}. From transport calculations it follows that this improvement is due to the narrow and well centered deposition in the high confinement plasma center for the TE_{11} case rather than to the slight increase in heating efficiency.

REFERENCES

1. K. UO et al., "Heliotron Studies," *Proc. 9th Int. Conf. Plasma Physics and Controlled Nuclear Fusion Research*, Baltimore, Maryland, September 1-8, 1982, Vol. II, p. 209, International Atomic Energy Agency (1982).

2. H. RENNER et al., "Recent Results on Plasma Behaviour in W VII-A Stellarator," *Plasma Phys. Controlled Fusion*, **26**, *1*, 183 (1984).

3. D. W. ATKINSON et al., "ECRH and Neutral Injection Experiments in the Cleo Stellarator," *Proc. 8th Int. Conf. Plasma Physics and Controlled Nuclear Fusion Research*, Brussels, Belgium, July 1-10, 1980, Vol. I, p. 153, International Atomic Energy Agency (1980).

4. R. WILHELM et al., "First ECRH Experiments on the W VII-A Stellarator," *Plasma Phys. Controlled Fusion*, **26**, *1A*, 259 (1984).

5. U. BROSSMANN et al., "Concept of an Advanced Stellarator," *Proc. 9th Int. Conf. Plasma Physics and Controlled Nuclear Fusion Research*, Baltimore, Maryland, September 1-8, 1982, Vol. III, p. 141, International Atomic Energy Agency (1982).

6. R. WILHELM et al., "Electron Cyclotron Resonance Heating System for the Stellarator W VII-AS," IPF-84-5, Institut für Plasmaforschung Stuttgart (1984).

7. C. P. MOELLER, "Launcher and Transmission Systems for Electron Cyclotron Heating," *Proc. 3rd Int. Symp. Heating in Toroidal Plasmas*, Grenoble, France, March 22-27, 1982, Vol. III, p. 1085; see also *Int. J. Electron.*, **53**, 587 (1982).

8. J. L. DOANE, "Mode Converters for Generating the HE_{11} (Gaussian Like) Mode from TE_{01} in a Circular Waveguide," *Proc. 10th Symp. Fusion Engineering*, Philadelphia, Pennsylvania, December 5-9, 1983; see also *Int. J. Electron.*, **53**, 573 (1982).

9. M. THUMM et al., "Conversion of Gyrotron TE_{0n} Mode Mixtures into a Linearly Polarized HE_{11} Mode," *Proc. 8th Int. Conf. Infrared and Millimeter Waves*, Miami Beach, Florida, December 12-17, 1983, paper TH 4.

10. G. JANZEN et al., "Mode Selective High Power Measurements on a 28 GHz Gyrotron," *Proc. 8th Int. Conf. Infrared and Millimeter Waves*, Miami Beach, Florida, December 12-17, 1983.

11. C. C. H. TANG, "Optimization of Waveguide Tapers Capable of Multimode Propagation," *IRE Trans. Microwave Theory Tech.*, **MTT-9**, 442 (1961).

12. V. ERCKMANN et al., "Electron Cyclotron Resonance Heating System for the Garching Stellarators W VII-A and W VII-AS," *Proc. 5th Topl. Conf. Radio-Frequency Plasma Heating*, Madison, Wisconsin, February 21-23, 1983, paper C-E.2.

13. P. G. SCHÜLLER et al., "Application of a Polarization Twist Reflector in ECRH Experiments," *Proc. 4th Int. Workshop on ECE and ECRH*, Frascati, Italy, paper C-8 (1984).

14. T. H. STIX, "Radiation and Absorption Via Mode Conversion in an Inhomogeneous Collision Free Plasma," *Phys. Rev. Lett.*, **15**, 878 (1965).

15. F. S. McDERMOTT, G. BEKETI, K. E. HACKETT, J. S. LEVINE, and M. PORKOLAB, "Observation of the Parametric Decay Instability During Electron Cyclotron Resonance Heating on the Versator II Tokamak," *Phys. Fluids*, **25**, *9*, 1488 (1982).

16. P. G. BULYGINSKY et al., "ECR-Heating of Plasma in FT-1 Tokamak and Its Influence on the Ion Component," *Proc. 11th European Conf. Controlled Fusion and Plasma Physics*, Aachen, FRG, September 5-9, 1983, Part I, p. 457, European Physical Society (1983).

17. W VII-A Team et al., "Plasma Confinement and the Effect of Rotational Transform in the WENDELSTEIN VII-A Stellarator," *Proc. 10th Int. Conf. Plasma Physics and Controlled Nuclear Fusion Research*, London, September 1984, IAEA-CN-44-D-I-1 (to be published).

18. V. ERCKMANN et al., "ECRH on the WENDELSTEIN W VII-A Stellarator with Different Kinds of Wave Launching," *Proc. 4th Int. Symp. Heating in Toroidal Plasmas*, Rome, Italy, Vol. II, p. 846 (1984).

19. W. A. HOULBERG, K. C. SHAING, and J. F. LYON, "Transport Modelling-Toward Self Consistent Determination of Radial Electric Field," *Proc. 4th U.S. Stellarator Workshop*, Oak Ridge, Tennessee (1983).

20. W VII-A Team, "Electron Heat Transfer and Particle Confinement in the WENDELSTEIN VII-A Stellarator," *Bull. Am. Phys. Soc.*, **26**, 891 (1981).

Plasma Physics and Controlled Fusion Vol.28, No.9A pp.1277-1290, 1986
Printed in Great Britain

0741-3335/86$3.00+ .00
Institute of Physics and Pergamon Journals Ltd.

ELECTRON CYCLOTRON RESONANCE HEATING IN THE WENDELSTEIN VII-A STELLARATOR

V. Erckmann and W VII-A Team*,
NI-Team**, ECRH Group***,

Max-Planck-Institut für Plasmaphysik
EURATOM-Association, D-8046 Garching, FRG

* G. Cattanei, D. Dorst, A. Elsner, U. Gasparino, G. Grieger
P. Grigull, H. Hacker, H.J. Hartfuß, H. Jäckel, R. Jaenicke,
J. Junker, M. Kick, H. Kroiss, G. Kuehner, H. Maaßberg, C. Mahn,
G. Müller, W. Ohlendorf, F. Rau, H. Renner, H. Ringler, F. Sardei
M. Tutter, A. Weller, H. Wobig, E. Würsching, M. Zippe

** K. Freudenberger, W. Ott, F.P. Penningsfeld, E. Speth

*** W. Kasparek, G. A. Müller, E. Räuchle, P.G. Schüller,
M. Thumm, R. Wilhelm (Inst.f.Plasmaforschung, Univ. Stuttgart)

ABSTRACT

Plasma build-up and heating of net-current-free plasmas in W VII-A was investigated by ECRH. Experiments were performed at two ECR-frequencies (28 and 70 GHz) and different heating scenarios were investigated such as 1st harmonic ordinary mode heating and 2nd harmonic extraordinary mode heating . The basic effects predicted by theory, i.e. localized wave absorption and optical thickness of the plasma were verified. The electron heat conduction was found to be governed by neoclassical losses in the plasma core for high enough temperatures, whereas enhanced losses have to be assumed in the outer plasma regions. Generation of a target plasma with sufficient parameters to allow further heating by NBI was successfully demonstrated. Configuration studies showed a beneficial influence of small shear on the confinement, where internal currents have to be taken into account.
W VII-A was shut down in Nov. 85 and will be upgraded into the advanced stellarator W VII-AS, where an ECRH-power of 1 MW will be available.

KEY WORDS

Stellarator, WENDELSTEIN VII-A, net-current-free operation, electron cyclotron resonance heating, electron heat conduction, heating efficiency, confinement.

1. INTRODUCTION

The ten years lifetime of WENDELSTEIN VII-A operation until the shut down of the machine by fall of 1985 may be characterized by three major phases: In a first period ohmic heating was the only available heat source and thus investigations were concentrated on tokamak-like discharges.

By application of neutral beam injection in 1980 the transition from an ohmically preheated plasma to net current free operation was achieved for the first time /1/ setting a milestone for the second phase, where pure stellarator physics investigations became possible. However, only a restricted machine parameter window with respect to the toroidal field B_0 and the rotational transform ι was accessible in this operation mode.

Application of ECRH marks the 3rd experimental phase, where the specific ECRH-capability of plasma build-up from the neutral gas phase opened the field of net-current-free operation without restrictions in the accessible parameter range, except for those given by ECRH itself. Rotational transform, plasma density and electron temperature could be chosen more or less independently. The ECRH-activities on W VII-A started 1983 /2, 3, 4/ using a 28 GHz, 200 kW, 0.04 s gyrotron, which restricted the machine operation to $B_{res} = 1$ T and $n_{eo} \lesssim 10^{19}$ m^{-3}. The system was replaced in 1984 by a 70 GHz gyrotron with the same rf-power for pulse lengths of 0.1 s. This frequency was

chosen to match the design magnetic field of the upgraded Stellarator W VII-AS being under construction now and extended the accessible parameters to $B_0 = 2.5$ T and $n_{e0} \lesssim 6.2 \times 10^{19}$ m^{-3}. The ECRH system operated at W VII-A will be part of a 1 MW system (four additional gyrotrons are on order) for W VII-AS.

The ECRH experiments performed in W VII-A may be considered two fold:

On one hand ECRH physics, i.e. wave absorption and correlated phenomena for different heating scenarios such as 1st harmonic ($\omega = \omega_{ce}$) ordinary wave heating and 2nd harmonic ($\omega = 2\omega_{ce}$) extraordinary wave heating, were studied.

On the other hand the narrow power deposition around the resonance layer and the energy transfer mainly to the electrons made ECRH a tool for investigation of stellarator specific behaviour. Electron heat transport was examined by conventional steady state analysis of the plasma profile and compared to a heat wave propagation analysis /5/, the wave being excited by a modulation of the input rf-power.

One of the major claims attributed to ECRH was the generation of an OH-current free target plasma with sufficient parameters to allow taking over of the heating by NBI and thus overcoming the density limitations given by ECRH. Whereas NBI-heating of an ECR heated target plasma was not possible in the 28 GHz experiments due to the low target plasma density, further heating of the plasma by NBI could be demonstrated in the 70 GHz experiments.

Last not least, configuration studies were performed, where the standard stellarator, which has negligible shear in the vacuum magnetic field configuration was compared to a torsatron-like configuration, where shear was introduced by running nonbalanced currents in the helix of the machine. The influence of shear on the confinement was also examined by superposition of small plasma currents ($I_p \leq 4$ kA) induced by an ohmic transformer.

2. PLASMA PARAMETERS AND WAVE ABSORPTION

2.1 Experimental arrangement

WENDELSTEIN VII-A was a conventional $l = 2$, $m = 5$ stellarator with low shear ($\Delta t/t \approx 1$ %), the major radius was 2 m, the average minor radius was 0.1 m. The EC-waves were launched to the plasma from the low field side in the equatorial plane of the torus with the wave vector orientated perpendicular to the direction of the magnetic field B_0. An almost linearly polarized wave (HE_{11}-mode) was generated in the transmission line from the gyrotron mode (TE_{02}) making use of several mode convertors in the transmission line /6/. Two different heating scenarios were investigated:
By choosing the EC-wave polarization parallel to the magnetic field ($E_\sim \parallel B_0$) the 1st harmonic ordinary (O-) wave ($B_{res} = 2.5$ T) propagates in the plasma as long as the cut-off density $n_{e,crit} = 6.2 \times 10^{19}$ m^{-3} is not exceeded. By turning the EC-wave polarization by 90° ($E_\sim \perp B_0$) and lowering the magnetic field ($B_{res} = 1.25$ T), the 2nd harmonic extraordinary (X-) wave is excited. The cut-off density for this mode is reduced to half the value of the ordinary mode ($n_{e,crit} = 3.1 \times 10^{19}$ m^{-3}). The incident power available in the polarized mode was 170 kW, which was determined calorimetrically at the torus end of the 25 m transmission line.

2.2 1st harmonic ordinary mode heating ($B_0 = 2.5$ T)

Given the boundary conditions of perpendicular injection and low magnetic field side access to the plasma and $\omega = \omega_{ce}$, only the ordinary mode can propagate towards the resonance layer $\omega = \omega_{ce}$. The X-mode meets a cut-off layer at the very outer edge of the plasma which was verified experimentally, resulting in strong reflections of the incident wave back into the antenna waveguide. With the O-mode incident, plasma breakdown occurs after several milliseconds and the plasma develops depending on the density, which is controlled by gas puffing. The central electron temperatures range from $T_{e0} = 2.3$ keV at $n_{e0} = 1.7 \times 10^{19}$ m^{-3} to $T_{e0} = 0.6$ keV at $n_{e0} = 5.4 \times 10^{19}$ m^{-3}. Radial profiles of n_e and T_e obtained from Thomson scattering are shown in Fig. 1 for three different densities.

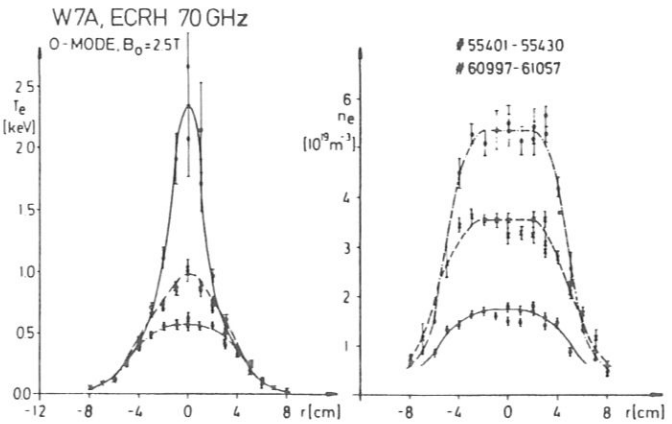

Fig. 1: Radial profiles of the electron temperature T_e and of the plasma density n_e obtained from Thomson scattering for high, intermediate and low densities.

The EC-wave propagation and absorption was examined by ray tracing calculations based on the actual geometry and the measured T_e and n_e-profiles. For the low density (n_{eo} = 0.3 $n_{e,crit}$), high temperature case, bending of the incident rays is negligible resulting in a narrow power deposition profile, whose maximum width is determined by the natural free space divergence of the incident beam. As seen from Fig. 2, at high densities (n_{eo} = 0.85 $n_{e,crit}$) strong bending of the rays occurs leading to a broadening of the power deposition profile, which in turn affects the profile width of the electron temperature.

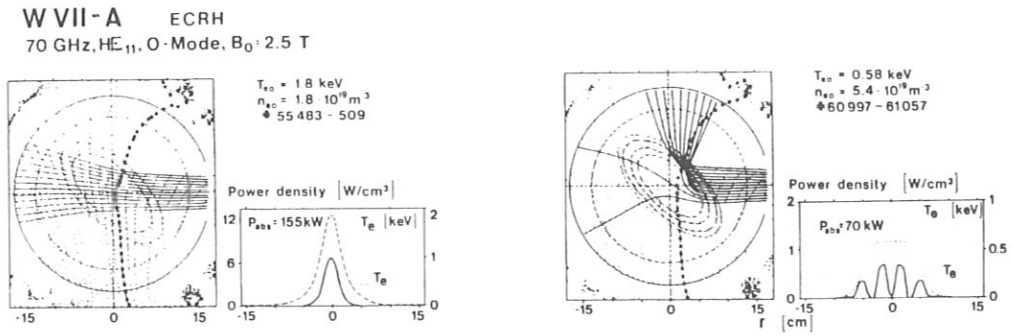

Fig. 2: Ray tracing calculations for a low and high density discharge with n_{eo} = 0.3 $n_{e,crit}$ (left) and n_{eo} = 0.85 $n_{e,crit}$ (right), respectively. The corresponding computed power deposition profiles (solid line) as well as the measured electron temperature profiles (dashed line) are also shown.

The calculated single pass heating efficiency η defined as

$$\eta = \frac{P_{abs}}{P_{inc}} ,$$

where P_{abs} is the total absorbed power obtained from ray tracing calculations and P_{inc} is the total measured incident power, was compared to the experimentally determined overall heating efficiency

$$\eta_{exp} = \frac{d\,W_p/dt}{P_{inc}} .$$

Here dW_p/dt is the time response of the total stored plasma energy W_p to a fast reduction of the incident power. As seen from Fig. 3, the calculated single pass heating efficiency exceeds the measured efficiency at low densities, wheras at densities close to the cut-off-density the opposite behaviour is found.

In the high density branch, where the single pass absorption is low, the discrepancy may be explained by additional absorption of waves being multiple reflected from the torus walls. This assumption is supported by the heat-wave experiments (see Sec. 3) where additional off-axis power deposition has to be assumed to explain the measurements. Please, note that due to the strong ray bending a large fraction of the incident power hits the walls.

In the low density branch the discrepancy is not satisfactorily explained so far. There is, however, some evidence, that suprathermal electrons being generated in the wave particle interaction region may play a role in the observed reduction of the heating efficiency. Theoretical work points into that direction /7, 8/.

A comparison of the electron temperature profiles obtained from ECE and from Thomson scattering in low density discharges shows characteristic deviations being attributed to the presence of suprathermal electrons. The hump in the low field side wing of the Te-profile shown at the top in Fig. 4 represents the down shifted ECE frequency of the suprathermal electrons due to the relativistic increase of mass. A fit of ECE-evaluations with the measured data is obtained assuming 9 keV electrons with a population of $n_{e,sup}/n_{eo} = 3 \times 10^{-3}$.

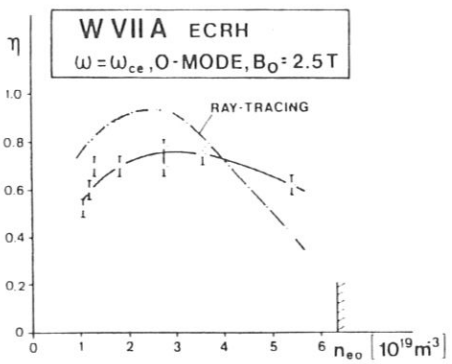

Fig. 3: Comparison of the single pass heating efficiency η obtained from ray-tracing calculations and the measured overall heating efficiency as a function of the central density n_{eo}. The cut-off density is indicated.

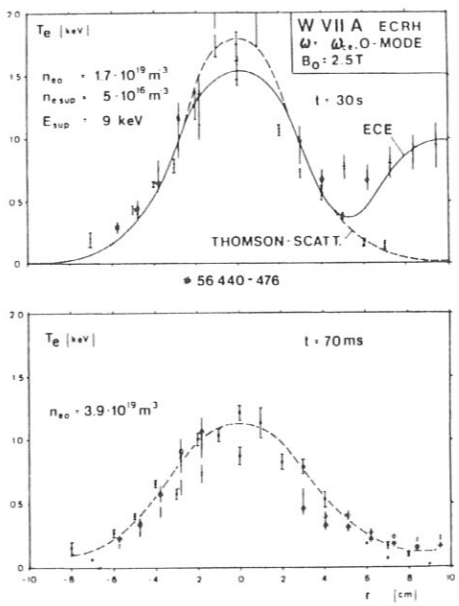

Fig. 4: Comparison of electron temperature profiles obtained from ECE-diagnostics and Thomson-scattering for low (top) and high density (bottom). A best fit of ECE calculations to the measured data is obtained assuming suprathermal electrons with E = 9 keV and $n_{e,sup}/n_{eo} \simeq 3 \times 10^{-3}$ (top, solid line).
At $n_{eo} = 3.9 \times 10^{19}$ m^{-3} the T_e-profiles measured by both diagnostics agree within the experimental errors.

The population of suprathermal electrons decreases with increasing plasma density and almost vanishes at $n_{eo} \simeq 0.6 \cdot n_{e,crit}$, as seen at the bottom of Fig. 4. Two mechanisms may be responsible for the observed behaviour: First, the coupling of suprathermals to the bulk electrons becomes stronger with increasing density and second, the power density of the pumping wave decreases with increasing density due to the broadening of the power deposition profile.

The total plasma losses detected by a 30 channel bolometer camera were measured ranging from 25 kW up to 45 kW, depending on the plasma density. If particles hitting the detector were suppressed by proper filtering, the remaining impurity line radiation ($E > 100$ eV) ranges from 5 to 20 kW. Abel inverted impurity line radiation profiles were found to be hollow, the main contribution coming from plasma regions outside the hot core.

2.3 2nd harmonic extraordinary wave heating (B_o = 1.25 T)

Plasma build up from the neutral gas phase is also obtained without problems for the X-mode incident at $\omega = 2\,\omega_{ce}$. This kind of heating is comparable to the 28 GHz, 1st harmonic, O-mode experiments (B_{res} = 1 T, $n_{e,crit} = 1 \times 10^{19}$ m^{-3}) with respect to the magnetic field. The cut-off-density, however, is extended by a factor of 3.1 . Some major plasma parameters for 2nd harmonic heating are listed in Table 1 and compared to the data obtained in the 28 GHz experiments.

	B_o /T/	n_{eo} /10^{19} m^{-3}/	T_{eo} /keV/	T_{io} /keV/	W_p /kJ/	η_{exp}
28 GHz O-mode 1st harm.	1.0	0.5	1.2	0.15	0.15	0.55
		0.9	0.4	0.1	0.1	0.45
70 GHz X-mode 2nd harm.	1.25	1.1	1.0	0.15	0.25	0.8
		2.4	0.7	0.1	0.50	0.9

Table 1: Comparison of major plama parameters for 28 GHz first harmonic and 70 GHz second harmonic heating.

The total incident power was about the same for all data shown (170 - 180 kW).
For 2nd harmonic heating the measured heating efficiency was found close to the theoretically predicted single pass absorption, which exceeds the 90 % level and is more or less independent on temperature as long as $T_{eo} > 0.2$ keV. A comparison of the measured total heating efficiency with the calculated single pass heating efficiency as defined in Sec. 2.2 is given in Fig. 5 as a function of the central density n_{eo}.

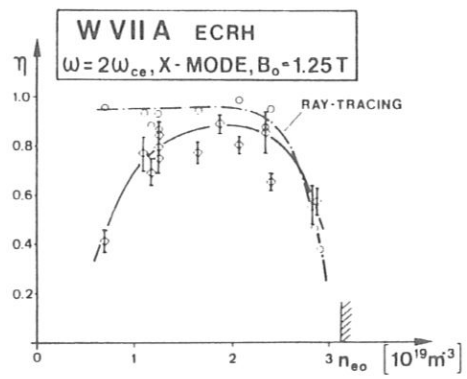

Fig. 5: Comparison of the single pass heating efficiency η obtained from ray-tracing calculations and the measured overall heating efficiency for 2nd harmonic heating as a function of the central density n_{eo}. The cut-off density is indicated.

For $n_{eo} \lesssim 0.3\ n_{e,crit}$ a similar behaviour as for the 1st harmonic O-mode heating was observed, i.e. the measured overall heating efficiency is significantly lower than the data obtained from ray-tracing calculations (see Sec. 2.2).

The benefical property of high single pass absorption in W VII-A even at low temperatures qualifies second harmonic heating for off-axis-experiments. Figure 6 shows electron-temperature and density profiles for discharges, where the resonance layer was positioned at the magnetic axis and shifted to a position $r/a \simeq 0.6$, respectively, by tuning the magnetic field.

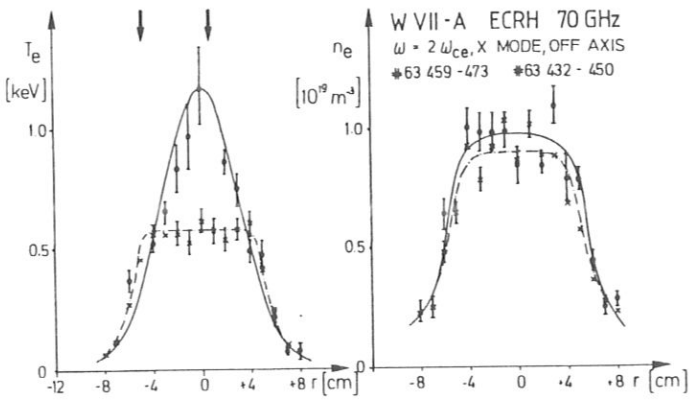

Fig. 6: Electron temperature and density profiles for on-axis (solid line) and off-axis (dashed line) heating. The arrows indicate the position of the resonance layer $\omega = 2\omega_{ce}$.

A characteristic broadening of the temperature profiles was observed correlated to the off-axis shift of the resonance layer, as has also been found in the 28 GHz experiment at low densities.

3. ELECTRON HEAT TRANSPORT STUDIES

In purely ECR-heated plasmas, the wave energy is transferred to the electrons, while the ions gain energy from collisional coupling to the electrons, which is weak at the given densities. Thus, the ion temperatures were measured in the range $0.1 < T_i < 0.3$ keV and remain small compared to the electron temperatures. Electron heat conduction was found to be the major loss, other loss channels such as impurity line radiation and ion charge exchange losses play a minor role in the energy balance.

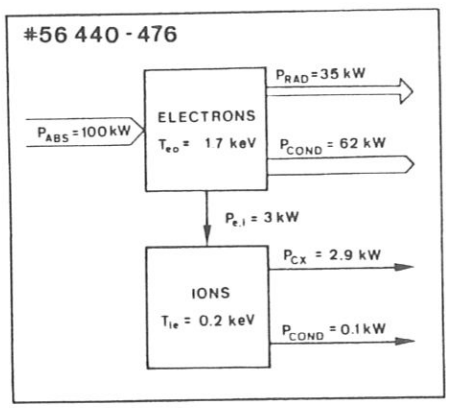

Fig. 7: Power flow diagram obtained from steady state transport code modeling of the radial n_e- and T_e profiles for an ECR-heated discharge.

A typical power flow diagram obtained from a steady state temperature profile analysis by modelling measured profiles with the Garching transport code TEMPL is shown in Fig. 7.

The data base available for parameter studies of the electron heat diffusivity χ_e ranges from B = 1.0 - 2.5 T, n_e = 0.5 - 5.4 x 10^{19} m^{-3}, ι_0 = 0.16 - 0.7, T_e = 0.3 - 2.3 keV. Good agreement between measured and calculated profiles for the broad variety of examined discharges was obtained by making the following Ansatz for the heat diffusivity χ_e /9/:

$$\chi_e = \chi_{e,HH} + \chi_{e,rip} + \chi_{e,OH} ,$$

here $\chi_{e,HH}$ is the neoclassical axisymmetric Hazeltine-Hinton term /10/,

$$\chi_{e,HH} \propto \frac{T_e^{3/2}}{t\, B^2}$$

$\chi_{e,rip}$ gives the neoclassical losses induced by a helical magnetic field ripple /11/ and

$$\chi_{e,OH} \propto \frac{1}{n_e\, T_e^{0.6}}$$

is a term, which was earlier derived empirically from ohmic discharges in W VII-A by transport analysis outside the q = 1 surface.

The influence of the different terms is illustrated in Fig. 8 for two discharges, where the centre rotational transform ι_0 was varied from 0.1 (a) to 0.8 (b) by superposition of small plasma currents of + and - 4 kA, respectively. An ι-change is expected to act on both neoclassical terms only. Impurity line radiation (measured) and ion cx-losses are included in the calculations. With the radial dependence of χ_e shown in Fig. 8 excellent agreement with the measured profiles of n_e and T_e was obtained.

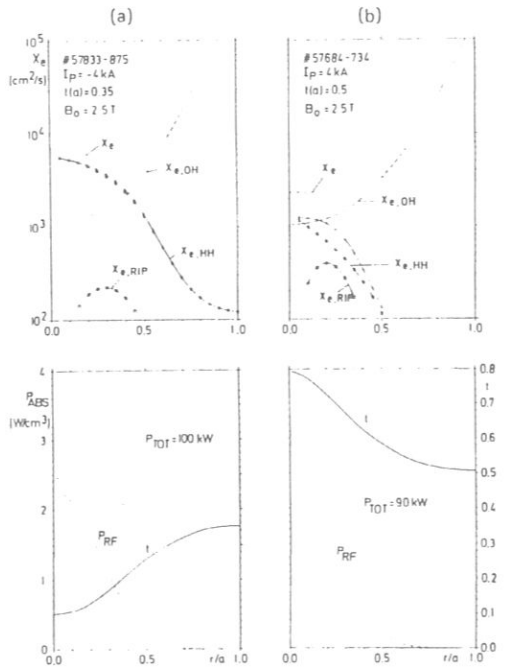

Fig. 8:

Calculated electron heat diffusivity for discharges (B_o = 2.5 T, $n_{eo} \simeq 2.2 \times 10^{19}$ m^{-3}) with different ι-profiles. (a) T_{eo} = 0.9 keV, (b) T_{eo} = 1.2 keV. The three terms $\chi_{e,HH}$, $\chi_{e,rip}$ and $\chi_{e,OH}$ as well as the sum of all terms is plotted versus the plasma radius at the top, the power deposition profile and the ι-profile is seen at the bottom.

It is clearly seen, that in the low τ_0-case neoclassical losses dominate in the plasma centre, whereas by reduction of neoclassical losses (increase of τ) the anomalous contribution just reaches the neoclassical one at the given density and temperature.

While analyzing discharges at 1.0, 1.25 and 2.5 T, the central confinement was found to scale $\propto B^2$ /12/ for fixed T_e and τ according to neoclassical predictions, as long as the temperature is sufficiently high.

A variation of the central electron temperature was obtained by varying the input power while keeping all other parameters fixed. For temperatures high enough to make neoclassical heat diffusion the leading loss in the plasma centre, T_{eo} is expected to scale $\propto P_{abs}^{2/5}$. If the anomalous term $\chi_{e,OH}$ dominates, $T_{eo} \propto P_{abs}^3$ is expected. Figure 9 shows the change of T_{eo} with increasing absorbed ECRH-power.

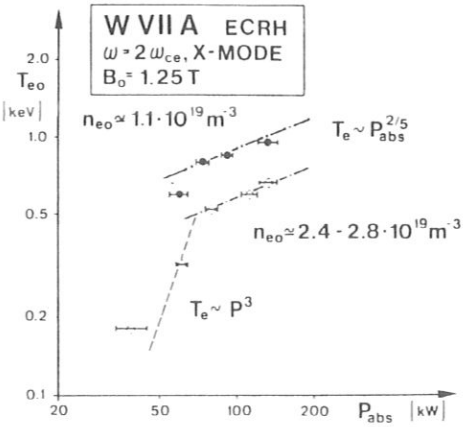

Fig. 9: Central electron temperature T_{eo} versus absorbed rf-power P_{abs} for two different plasma densities.

Within the restricted power range available, it is seen, that T_{eo} tends to scale $\propto P_{abs}^{2/5}$, if a certain temperature is exceeded. Below that value a much faster increase of T_{eo} is found with increasing power. As a guide for the eyes, the dashed line indicates the expected pure anomalous behaviour. In the low temperature branch the measurements show some behaviour in between the two extreme cases, i.e. the neoclassical and the anomalous contribution become comparable. One may conclude, therefore, that with increasing electron temperature the importance of the anomalous losses may be reduced while being shifted towards the very edge of the plasma, where the temperature is low ($T_e \lesssim 300$ eV) and atomic processes have to be taken into account. Under such conditions the neoclassical losses dominate the major part of the plasma, as has been found in all high temperature discharges in W VII-A.

In principle, the absolute local values of the electron heat diffusivity can be obtained experimentally by a nonstationary method, i.e. by excitation of a heat wave by modulation of the deposited ECRH power and measurement of its propagation radially outward in phase and amplitude. A simple analysis of the measurements can be performed, if the power deposition zone and the heat diffusion zone are clearly separated. For discharges fulfilling this condition, the electron heat diffusivity was determined by fitting the solution of the 1st order heat diffusion equation to the measured phase shift and amplitude data /5/. Note, that the small plasma radius of W VII-A allows evaluation of χ_e only in a range 3 cm $< r <$ 8 cm. The experiments were performed in a low density discharge in order to keep the power deposition profile narrow, the incident ECRH-power was square wave modulated at various frequencies (100 - 600 Hz), the modulation depth was in the 10 - 30 % range. An example is given in Fig. 10, where the time delay and the normalized heat wave amplitude detected by ECE-diagnostics in plotted versus the plasma radius.

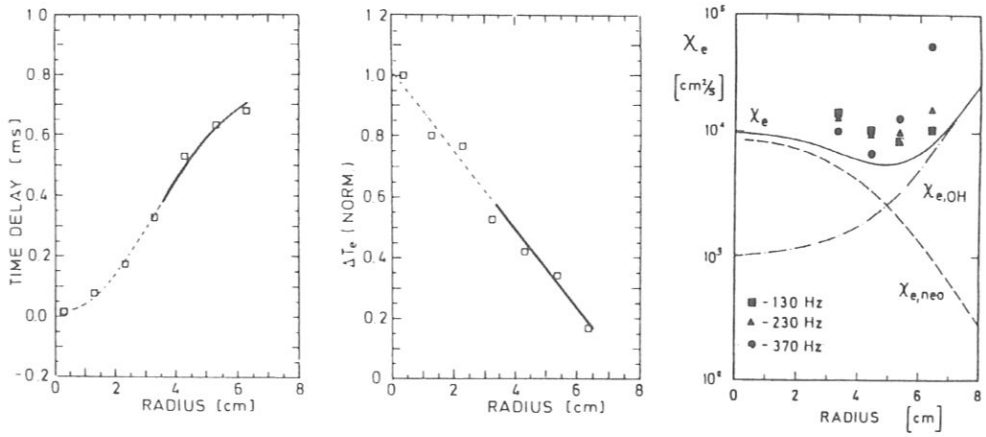

Fig. 10: Time delay and normalized amplitude of the temperature change ΔT_e as a function of radius for a heat wave propagating radially outward from the plasma centre. Absolute values of χ_e as a function of radius derived from the experimental data for different modulation frequencies and a comparison with a steady state transport code analysis is also given.

Within the experimental errors, the χ_e-values obtained from this technique fit to the data obtained from steady state analysis.

In high density discharges, the time delay of the phase planes increases up to $r \simeq 6$ cm, but then tends to decrease, which indicates additional power deposition at the edge of the plasma, as has been mentioned in Sec. 2.

4. COMBINATION of ECRH AND NBI

The neutral beams at W VII-A were injected almost perpendicularly to the main field (offset $\simeq 6^o$) from accessibility reasons. The total beam-plasma interaction length is about 0.2 m and as a consequence, the heating efficiency remains low at low densities. For this reason NBI heating of an ECR-heated target plasma could not be achieved in the 28 GHz experiments, where $n_{eo} < 10^{19}$ m^{-3}.

At the higher target plasma densities in the 70 GHz ECR-heated discharges, taking over of the heating by NBI was successfully shown by proper adjustment of the overlapping period of both heating pulses and appropriate gas puffing. Three out of four available neutral injectors ($P_{tot} \simeq 750$ kW, $P_{abs} \simeq 250$ kW) were found to be sufficient. The typical time behaviour of the total stored plasma energy W_p, line integrated density $\int n_e dl$, electron temperature $T_{e,sx}$ (soft X-ray) and the heating power is shown in Fig. 11 (a).

After some time required for profile reformation, the NBI heated plasma develops in the same way as was previously found with ohmically preheated target plasmas. In particular,the density increases almost linearly with all external gas sources switched off. The density increase is explained by the total particle influx from the neutral beams. Two particle sources have to be considered, i.e. direct particle deposition in the plasma centre by the neutral beams and neutral particle influx from the plasma edge by recycling processes.

As seen in Fig. 11 (b), a flattening of the density increase is observed during application of a second ECRH-pulse in the later NBI-phase, while simultaneously the plasma energy increases due to an increase of the electron temperature. After ECRH pulse switch-off, the line integrated density

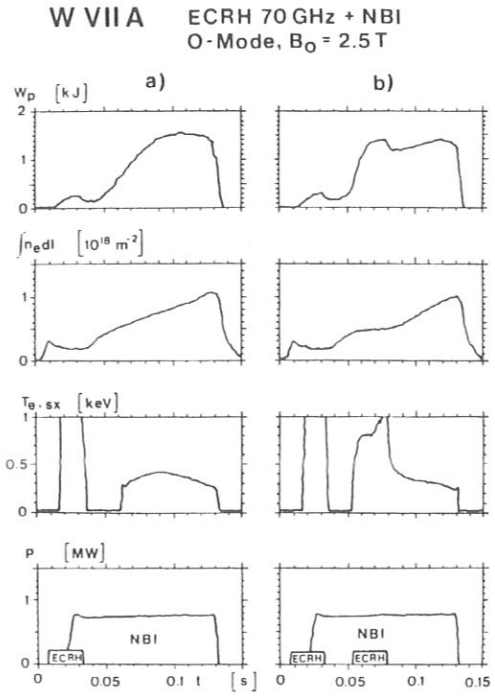

Fig. 11:
Total stored plasma energy W_p (diamagnetic loop), line integrated density $n_e dl$, electron temperature $T_{e,sx}$ (soft-X-diagn.) and heating power as a function of time for two discharges, where a target plasma generated by ECRH was further heated by NBI. On the right side a second ECRH pulse is applied in the late NBI-phase.

starts increasing again with more or less the same slope as before. The behaviour may be explained by the following processes: At the given high plasma densities ($n_{eo}/n_{e,crit} \simeq 0.9$ - 1.2) a major fraction of the incident EC-waves intersects with the resonance layer at the very edge of the plasma or even outside the last closed flux surface thus reducing the neutral gas density at the edge of the plasma by ionization processes. The ionized particles may hit the limiter while following ergodic field lines. The picture of changed particle recycling fluxes is supported by the observation of shrinked density profiles in the ECRH time interval. While shifting the second ECRH-pulse in time, i.e. towards higher target plasma densities, the gain in the stored plasma energy decreases and almost vanishes at central densities $n_{eo} \simeq 1.3 \cdot n_{e,crit}$, whereas the flattening of the density rate of change was still observed. This effect could be counteracted by additional gas puffing. Another possible explanation for the observed behaviour is a degradation of the particle confinement by ECRH. It may be concluded, that ECR-edge heating is a useful tool for density control in NBI-heated discharges, which may be also important for impurity control.

The transition from ECR-core-heating to edge heating is shown in Fig. 12 for two discharges, where the second ECRH-pulse is shifted in time. The NBI-target plasma densities are $n_{eo} \simeq 0.85\ n_{e,crit}$ and $n_{eo} \simeq 1.2\ n_{e,crit}$, respectively. In the latter case no temperature increase at all was observed in the plasma centre.

From these experiments, the heating efficiency of ECRH could be obtained in a plasma with overcritical density, which is not accessible in purely ECR-heated discharges. As seen from Fig. 13, the heating efficiency drops sharply while approaching the cut-off density. The non zero efficiency at $n_{eo} > n_{e,crit}$ illustrates the effect of a successive outward shift of the power deposition profile by strong ray bending. The absolute values in this range depend on the density profile shape, which is typically very broad (flat top, steep gradients) in NBI-heated plasmas. For a bell-shaped density profile one would expect to find a non zero heating efficiency at even higher central densities.

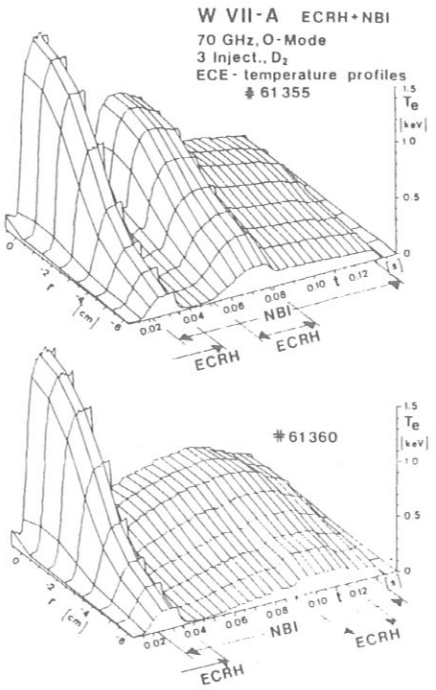

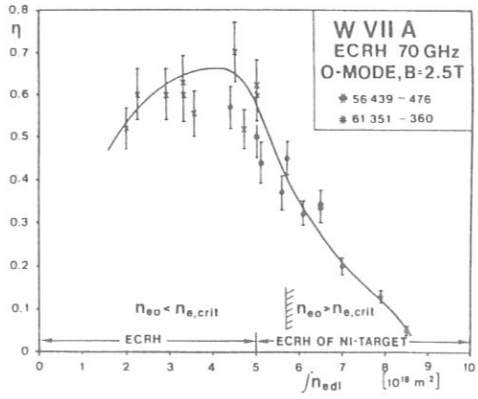

Fig. 13: Measured heating efficiency versus line integrated density.

Fig. 12: Time development of spatial half-profiles of T_e obtained from ECE-diagnostics. A 2nd ECRH-pulse is applied in an early (top) and a late phase (bottom) of an NBI-heated discharge with n_{eo} = 0.85 $n_{e,crit}$ and n_{eo} = 1.2 $n_{e,crit}$, respectively.

5. CONFIGURATION STUDIES

The concept of a shearless vacuum magnetic field configuration is based on the idea of keeping resonant low numbered rational values of ι = m/n out of the confining region of the plasma. Experiments which were performed at low pressure (= low density) to provide conditions close to the vacuum magnetic field configuration, indeed showed a serious deterioration of the confinement at major resonances ι = 1/2, 1/3, 2/3..., whereas optimum conditions were found in the direct neighbourhood of these values /13/. This result is explained by the occurence of magnetic islands at resonant surfaces, which would appear already at small perturbations of the magnetic field ($\delta B/B \simeq 10^{-3}$) by unavoidable symmetry errors caused by the helix construction /14/.

In ECR-heated discharges nonstationary plasma currents up to 1 kA were observed, which were incrasing more or less linearly in time without saturation throughout the pulse length available. The rate of current increase depends on the plasma pressure, the rotational transform and the radial position of the resonance layer. An outward shift of the resonance position even leads to a current inversion. At least three different mechanisms were identified to contribute to the measured net current:

- currents representing the net effect of ECRH-generated fast electrons, which are differently confined depending on their drift direction with respect to the magnetic field /15/.
- pressure driven currents, which may be the neoclassical bootstrap currents
- direct rf-driven currents.

These nonstationary currents contribute to the total rotational transform thus resulting in nonstationary discharges. A fixed edge value of ι is required to obtain stationary conditions and is maintained by either feedback control of the helix currents to keep the total ι constant or by superposition of small regulated currents (OH-transformer) thus keeping the total plasma current constant in time.

The influence of shear was investigated by adding small regulated plasma currents $I_p \leq 4$ kA, the heating effect of which being negligible. Experiments at low plasma pressure showed, that the deterioration of the confinement at resonant ι-values could be completely suppressed without reduction of the maximum achievable stored plasma energy at 4 kA plasma current /12/. Maintaining the same current in finite pressure discharges, the deterioration at resonant ι was negligible, too, but the plasma energy obtained was reduced by about a factor of two compared to discharges with 2 kA plasma current. This behaviour is illustrated in Fig. 14, where the line integrated density $\int n_e dl$ is plotted versus the stored plasma energy W_p for three different plasma currents.

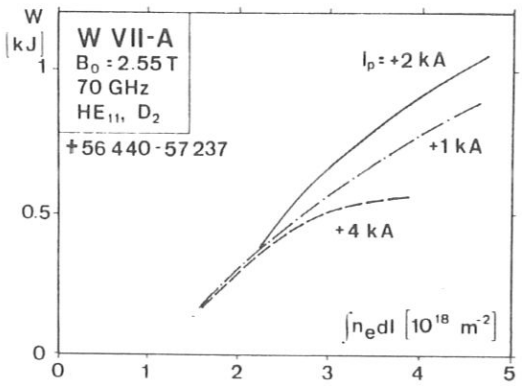

Fig. 13: Total stored plasma energy W_p versus line integrated density $\int n_e dl$ for 3 different plasma currents.

In the low pressure (low density) branch approximately the same plasma energy was obtained for all currents at an optimized edge value of ι, whereas in the finite pressure (high density) branch the three curves diverge significantly, indicating the growing influence of pressure driven currents on the initial ι-profile /16/. From these experiments one may conclude, that an optimum shear exists excluding major resonances from the plasma, which may be a result of two competing processes, i.e. the beneficial effect of shrinking island width is counteracted by the appearance of an increasing number of rational surfaces with increasing shear. From these considerations the basic question about the influence of shear in the vacuum configuration should be put in a more relevant way: Which shear is required in the vacuum configuration to end up with the optimum shear in the finite β-state of the discharge?

By running unbalanced currents in the helix, vacuum shear in the range $\Delta\iota/\iota = \pm 10$ % was introduced in the W VII-A configuration. For finite pressure discharges, both, centre and edge localized major resonances were found to be of importance for the global confinement. In general, discharges with positive vacuum shear showed better behaviour compared to those with negative shear. This may be explained by the effect of pressure driven currents which are expected to flow in the pressure gradient region and thus generate hollow current-density distributions. Such currents tend to leave the vacuum shear unaffected in the centre while increasing it at the edge of the plasma.

The experiments point into the direction, that a low shear configuration at finite pressure shows beneficial behaviour. There are in general two ways to meet this goal:

- The vacuum shear has to be chosen in a way, that the final state of the plasma has a low but finite shear performance. Finite β equilibrium effects on ι as well as pressure driven currents have to be taken into account carefully.

- The more elegant way is to choose a vacuum configuration, whose ι-profile is maintained even at high plasma pressure. Such configurations were recently presented /17/ showing a negligible change of the ι-profile up to $\langle\beta\rangle = 5$ % at zero current.

6. CONCLUSIONS

Plasma build up from the neutral gas phase and heating to remarkable parameters was achieved in W VII-A by means of ECRH, thus allowing net current free stellarator start up and operation. Two different ECR-frequencies (28 GHz and 70 GHz) were applied. Whereas for the 28 GHz experiments the main interest was focussed on the influence of different launched modes, in the 70 GHz experiments under improved confinement conditions two different heating scenarios, such as first harmonic ordinary wave and second harmonic extraordinary wave heating were investigated in detail.

The heating efficiency for both kinds of heating was measured to be consistent with theoretical single pass absorption predictions in an intermediate density range whereas deviations were found at low densities, and close to the cut-off density. The latter discrepancy is explained by additional power deposition due to multiple reflections from the torus walls.

Electron heat transport investigations in a wide parameter range with respect to magnetic field, plasma density, plasma temperature and rotational transform showed, that under optimized conditions and for high enough electron temperatures the plasma core is governed by neoclassical heat conduction, whereas in the edge region enhanced losses have to be assumed.

Generation of a target plasma by ECRH with sufficient parameters to allow further heating by NBI was demonstrated. During ECRH of an NBI-heated plasma with central densities close to or above the cut-off density, a flattening of the density increase was observed being attributed to a change of the particle recycling by edge heating.

As a result of configuration studies, a beneficial effect of some shear was found, as long as major resonances of the rotational transform are avoided within the confined plasma region.

REFERENCES

/1/ W VII-A Team and NI Group. Neutral injection in the WENDELSTEIN VII-A Stellarator with reduced ohmic current. Plasma Phys. and Contr. Nucl. Fusion Research 1981, Vol. I, IAEA Vienna, p. 185.

/2/ R. Wilhelm et al., W VII-A Team. First ECRH experiments on the W VII-A Stellarator, Plasma Physics and Contr. Fusion, Vol. 26, No. 1A, 1984, p. 259.

/3/ V. Erckmann, W VII-A Team, ECRH Group. ECRH on the WENDELSTEIN VII-A Stellarator with different kinds of wave launching. Proc. 4th Intern. Conf. on Heating in Toroidal Plasmas, Rome 1984, Vol. II, p. 846.

/4/ V. Erckmann, W VII-A Team, ECRH Group. Electron cyclotron resonance heating experiments in the WENDELSTEIN VII-A Stellarator. Fusion Technology Vol. 7, 1985, p. 275.

/5/ H.J. Hartfuß, W VII-A Team, ECRH Group. Evaluation of local heat conductivity coefficient by power-modulated electron cyclotron heating in the WENDELSTEIN VII-A Stellarator. Accepted for publication in Nucl. Fusion.

/6/ M. Thumm et al., Generation of the Gaussian-like HE_{11}-mode from gyrotron TE_{on} mode mixture at 70 GHz. Intern. Journal of Infrared and Millimeter Waves, Vol. 6, No. 6, 1985, p. 459.

/7/ I. Fidone, R.L. Meyer, G. Granata. Quasilinear saturation effects on electron cyclotron wave damping of the ordinary mode in tokamak plasmas. Phys. Fluids 26 (11), 1983, p. 3292.

/8/ M. Bornatici, U. Ruffino. Electron cyclotron absorption and emission in non-maxwellian plasmas. Spring College on Plasma Physics, Trieste, 1985.

/9/ H. Wobig, W VII-A team. A transport model of ECR-heated plasmas in W VII-A. 13th Europ. Conf. on Contr. Fusion and Plasma Heating, Schliersee, 1986.

/10/ F.L. Hinton, W.N.G. Hazeltine. Theory of plasma transport in toroidal confinement systems. Rev. Mod. Phys., 48, 1976, p. 239.

/11/ K.C. Shaing et al.. The radial electric field in a non axisymmetric torus. Plasma Physics and Contr. Nucl. Fusion Research 1984, Vol. 2, IAEA Vienna, p. 189.

/12/ G. Grieger, W VII-A Team, NI-Team, ECRH Group. Confinement of Stellarator plasmas with neutral beam and RF heating in W VII-A. Plasma Physics and Contr. Fusion, Vol. 28, No. 1A, 1986, p. 43.

/13/ W VII-A Team, NI Team, ECRH Group. Plasma confinement and the effect of the rotational transform. Plasma Physics and Controlled Nucl. Fusion Research, 1984, Vol. 2, IAEA Vienna, p. 371.

/14/ H.J. Jäckel, J. Kißlinger, F. Rau, H. Wobig. Torus with Helix W VII-A. 8th Symp. on Fusion Technology, Jutphaas, Netherlands, 1974, p. 235.

/15/ K.D. McLenithan, J.L. Shohet, G. Grieger. Runaway current generation by Cyclotron Resonance in the Wendelstein VII-A Stellarator. 11th Europ. Conf. on Contr. Fusion and Plasma Physics, Aachen, 1983, Vol. 1, p. 219.

/16/ W VII-A team, ECRH group, NI team. Influence of shear $\Delta\iota/\iota$ on the confinement in the W VII-A Stellarator. 13th Europ. Conf. on Contr. Fusion and Plasma Heating Schliersee, 1986.

/17/ J. Nührenberg, R. Zille. Stable Stellarators with medium β and aspect ratio. Physics Letters 114 A, 1986, p. 129.

ADVANCED STELLARATOR REACTOR AND BURNER STUDIES

G. GRIEGER, E. HARMEYER, J. KISSLINGER,
F. RAU, H. WOBIG
Max-Planck-Institut für Plasmaphysik,
Euratom-IPP Association,
Garching,
Federal Republic of Germany

Abstract

A survey is given on studies of critical issues regarding Advanced Stellarator Reactors (ASR) and Burner Experiments (ASB), where the magnetic topology is similar to that of the Garching Advanced Stellarator experiment Wendelstein VII-AS.

Stationary thermal fusion power values are calculated between $P_{th} \approx 4\,GW$ in ASR, and about 10 % of this value in ASB, respectively, using moderate aspect ratios around 15 in both cases. Values of the major radii are 25 to 20 m in ASR, and 15 m in ASB.

Under these conditions, for the plasma pressure normalized by the magnetic field energy, an average $\beta \approx 5\,\%$ is present in ASR, which is comparable to the computed result of β_{eq}, the equilibrium value of this configuration. Regarding a similar value for stability, β_{stab}, a promising new configuration exists. Due to the larger fields, in ASB an average $\beta \approx 2.5\,\%$ is found under burn conditions.

In ASR the average neutron power load at the first wall, around $2\,MW/m^2$, is at a moderate level; local enhancement factors of about 2 are caused mainly by the Shafranov shift of the finite-β configuration. A comparatively thin blanket helps to reduce the system size; pumped limiters and a radiative layer are considered for edge control.

Analyzing the stresses and strains produced by the electromagnetic forces, the modular coils seem to be feasible, although considerable shear stresses are seen in the computations.

1. INTRODUCTION

Stellarator fusion reactors with continuous helical windings or those using systems of non-planar modular coils constitute viable options for their development towards an alternative to Tokamak reactors. Start-up from existing magnetic surfaces and the possibility of a stationary burn in

the absence of dangerous disruptions are distinct advantages of stellarators. The prospect for continuous operation of the reactor allows different approaches for the coil engineering, and avoids problems associated with cyclic loads as to be envisaged in pulsed systems, especially in the first wall and in the coils with their support structure. Furthermore, less circulating power is required in stationary systems. A moderate aspect ratio alleviates problems regarding the first wall power loading, although in general small systems offer advantages due to a scaling of costs with magnet size or with stored magnetic energy. Modular systems of non-planar coils avoid problems which result from the geometry of interlinked coils present in certain stellarators with continuous helices as well as in most tokamaks.

Advanced Stellarator Reactor or Burner systems are investigated in the Federal Republic of Germany at the Institut für Plasmaphysik at Garching in a collaboration with the Kernforschungszentrum Karlsruhe, working together with a group at the University of Madison, Wi (USA). During the recent years, these stellarator reactor considerations focussed on the clarification of critical issues in studies based on stationary systems with moderate aspect ratios, of the non-planar modular coils and of the fields produced by them.

The present paper starts in Chapter 2 with a short description of the main properties of Advanced Stellarators. The following Chapter 3 briefly summarizes the development of several earlier Advanced Stellarator Reactor and Burner systems. Two reference configurations, ASRA6B and ASRA6C of Advanced Stellarator Reactors described by analytical coils are introduced in Chapter 4, along with the field topology of a finite-beta calculation for ASRA6C. Heating and burn scenarios are commented shortly in Chapter 5, and results are given for an ASR, in comparison to an ASB. Chapter 6 introduces shortly the main elements of the reactor lay-out for ASRA6C, summarizes the estimates on the neutron load on the first wall and its spatial dependence, and lists the main features of blanket and shield. Short remarks on the electromagnetic forces, their support and the resulting stress and strain calculations are given in Chapter 7. The paper ends in Chapter 8 with a summary and some conclusions.

Several other papers presented at this meetings will be mentioned in their relation to this survey.

2. PROPERTIES OF ADVANCED STELLARATORS

Advanced Stellarators are distinguished from standard ones by a certain reduction of the secondary plasma currents for all magnetic surfaces of the system, and a magnetic well between the magnetic axis and the last closed surface of the vacuum fields, combined with reasonable values of the aspect ratio and of the rotational transform. Thus, the associa-

ted neoclassical particle and energy losses, as well as the deformation of the magnetic surfaces by a finite plasma pressure (Shafranov–shift) are reduced, and drift surfaces of charged circulating particles deviate less from the magnetic surfaces, in comparison to the respective results for standard stellarators. The principles of optimization to arrive at an Advanced Stellarator topology are given in [1]. They consist of a reduction of the poloidal variation of $\int dl/B$, as taken for different poloidal starting points of the magnetic surface, and integrating along one field period. A difficult side condition is to keep the property of a magnetic well for the configuration at a reasonably low aspect ratio. This optimization is performed by a proper combination of poloidal fields, which also influence the rotational transform ι and the shear.

Modular coils are essential to produce such Advanced Stellarator fields. The Garching experiment Wendelstein VII–AS (with a major radius 2 m, a plasma radius 0.2 m, and a magnetic induction of 3 T) is the first Advanced Stellarator to be built, and is expected to begin operation early in 1987. It has 5 toroidal field periods (FP) and is equipped with 9 non–planar modular coils per FP. Details of its design and of the expected parameter range are given in [2]. The value of the rotational transform can be varied considerably in this experiment. A fusion reactor is expected to be built for operation at optimized conditions.

3. ADVANCED STELLARATOR REACTOR AND BURNER SYSTEMS

A schematic view of an Advanced Stellarator Reactor or of a Burner experiment is given in Fig. 1, showing for three of the 5 field periods the contours of the non–planar modular coils, along with nested toroidal volumes representing the shield and the blanket, as well as the last closed magnetic surface of this particular coil system. There are 6 coils per FP; three different coil shapes are present in the whole system, if one considers the twofold mirror symmetry.

In Fig. 2 , several earlier approaches of the coil configurations for ASR are shown in the same scale with ASB systems. The data set ASR2510 is a configuration derived directly from the coil geometry of the Wendelstein VII–AS experiment by an increase of the average major radius to a value $R_0 = 25.5\,m$ with a number of 10 coils per FP. The system ASR254E is obtained by reducing the coil number to 4 coils/FP, in order to alleviate the maintenance of the reactor. In this configuration, the modulation of the magnetic induction along and near the magnetic axis (magnetic field ripple) is considerably larger than in the other systems. As will be detailed in [3], this enlarges the neoclassical losses in the long mean free path regime of reactor plasma operation. Therefore, the configuration ASR25T7 is derived which produces the same average value of the induction along the magnetic axis, $B_0 = 5.3\,T$, by smaller coils

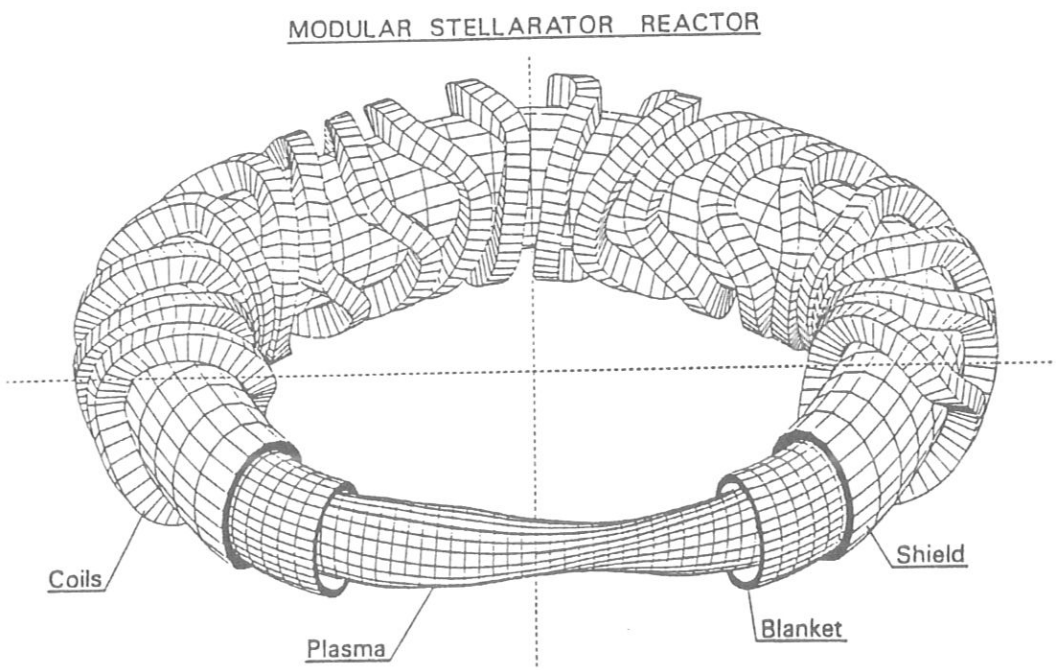

Fig. 1. Advanced Stellarator Reactor or Burner, schematic view of plasma, blanket, shield, and coils.

at a larger current density. Simultaneously, the rotational transform ι is increased to a value of about 0.6 in order to achieve a larger value of the equilibrium-beta. In a standard or 'classical' stellarator, this quantity roughly scales as $\beta_{eq} \approx \iota^2 / A$, where the aspect ratio $A = R_o/r_p$, and $r_p \approx 1.6\,m$ is the plasma radius. Note that for an Advanced Stellarator a larger value of the equilibrium-β applies, due to the reduction of the secondary currents, and the smaller vertical fields which then introduce a smaller Shafranov-shift of the configuration.

The rotational transform $\iota = 1/q$ is related to the safety factor q of a Tokamak, with the distinguishing difference that in stellarators the poloidal field is produced by external currents, whereas in Tokamaks currents flowing in the plasma are required for equilibrium.

In the two systems with 10 coils per FP, the current densities and coil cross sections are matched to keep the maximum value of the induction at the coil surface at values $B_m < 9\,T$, such as to stay within the limits of $NbTi$ as superconducting material operating at the temperature of liquid helium.

Coil configurations for a Burner experiment are derived from the data set ASR25T7 by a reduction of the major radius to about $15\,m$. The effective coil current density is raised by a factor of 2 to a value of $j_{eff} = 18\,MA/m^2$. The effective current density is an average over

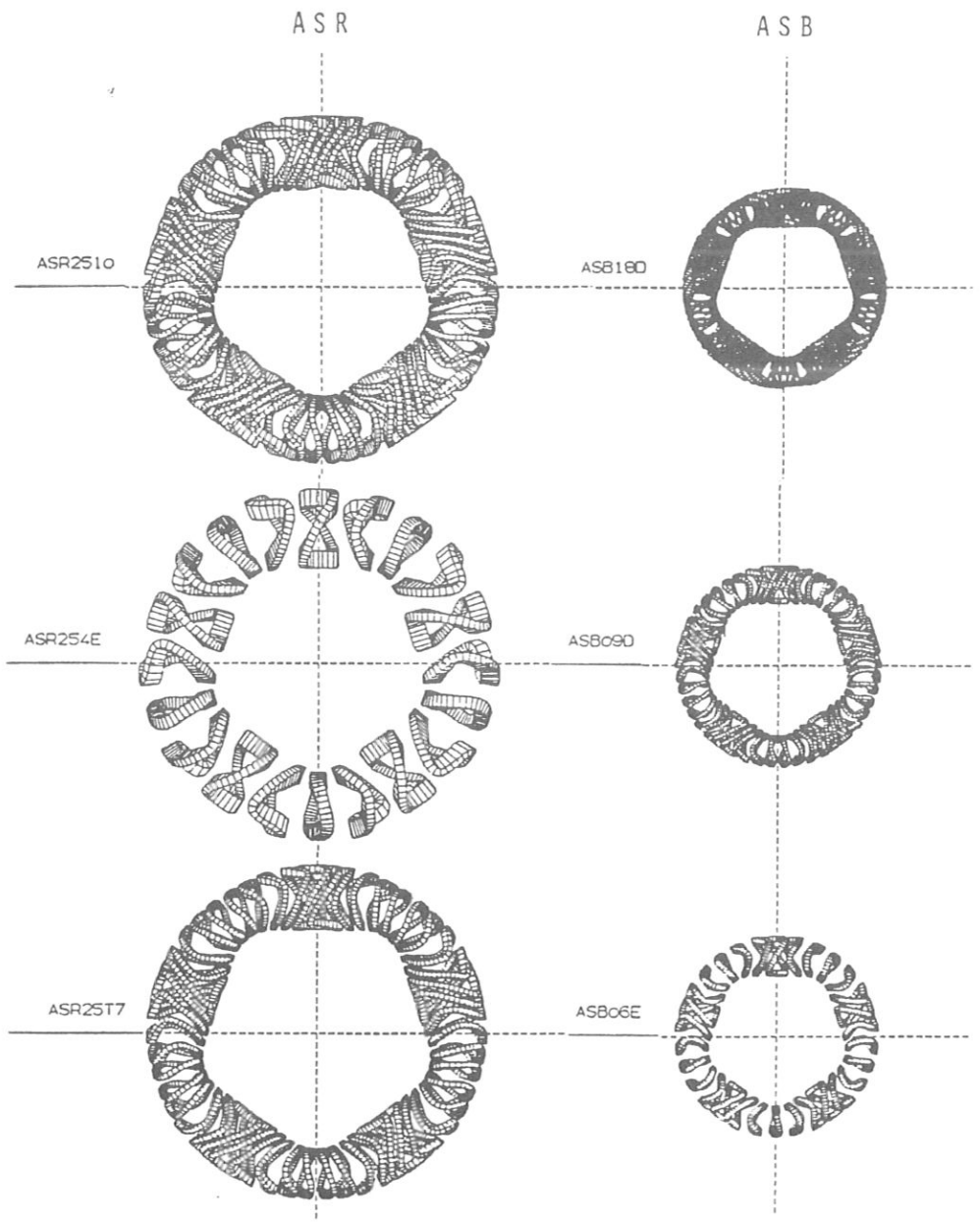

Fig. 2. Coil configurations of Advanced Stellarator Reactor or Burner systems with different numbers of coils per field period, shown in same scale.

the whole conducting cross section, i.e. including superconductor, stabilizer, internal structure as well as insulation and helium channels. The induction at the axis is increased in ASB to $B_o = 7\,T$ in order to obtain ignition at the comparatively small plasma radius, $r_p = 0.9\,m$.

The number of coils per field period is changed from 18 to 6 in the ASB configurations in order to study the influence on field quality within the plasma radius, along with the effect on the peak induction at the coils. Decreasing the coil number per field period increases the latter value since the coils are larger. The magnetic well depth is reduced and for 6 coils/FP a small negative shear is present. On the other hand, the assembly and maintenance are easier at low coil numbers. A number of 6 coils per field period is regarded as reasonable compromise.

More details of the magnetic field properties and their dependence on the comparatively large number of parameters describing the coils are given in [4] for these ASR and ASB systems, in comparison to those of the presently investigated data sets, ASRA6B and ASRA6C, two cases of Advanced Stellarator Reactors with coils derived from an Analytic winding law, 6 coils per field period. The label C indicates a more compact version of the preceding data set ASRA6B.

4. REFERENCE SYSTEMS ASRA6B AND ASRA6C

The further development of these Advanced Stellarator Reactor systems is performed in a collaboration with KfK-Karlsruhe (Germany) and their co-operation with the University of Wisconsin, Madison (USA). The aims of this activity are to arrive at an optimized scheme for assembly and maintenance, as obtained in the data set ASRA6B, and to reduce the dimensions of the reactor. In ASRA6C, a compact system size is made possible by introducing a modern design for blanket and shield, see [5,6], by reducing the decisive distance Δ between the first wall of the system and the inner contour of the coil winding cross section from the previous value of 2.1 m to 1.2 m. In consequence, the major radius can be changed from $R_o = 25\,m$ to a value of $20\,m$, keeping other parameters constant, e.g the effective coil current density and the induction at the magnetic axis.

In Table I we compare characteristic data of the Garching Advanced Stellarator experiment Wendelstein VII-AS and of the earlier system ASR25T7 to those of the two new reference systems ASRA6B and ASRA6C. The values of the average β and the fusion power will be commented in subsequent chapters.

In ASR25T7 the smaller peak field is within the limits of $NbTi$. Due to their larger current density and peak fields, Nb_3Sn is foreseen as superconductor for ASRA6B and ASRA6C. Note the large reduction of the stored magnetic energy when decreasing the size, whereas the peak values of the induction at the coils remain nearly unchanged.

TABLE I. Characteristic data of WVII-AS and ASR25T7, compared to those of the reference data sets ASRA6B and ASRA6C

System			WVII-AS	ASR25T7	ASRA6B	ASRA6C
Aver. major radius	R_o	$[m]$	2.0	25.5	25.0	20.0
Aver. coil radius	r_c	$[m]$	0.48	5.24	5.22	4.57
Conductor			Cu	NbTi	Nb_3Sn	Nb_3Sn
Coils / FP			8+1	10	6	6
Coil current	I_c	$[MA]$	0.6/1.5	13.7	22.5	18
Effect. current density	j_{eff}	$[MA/m^2]$	27	9.8	15	15
Max. induction at coil	B_m	$[T]$	5.2	8.7	11.0	10.4
Stored mag. energy	W_m	$[GJ]$	0.04	170	193	117
Induction on axis	B_o	$[T]$	3.0	5.3	5.3	5.3
Rotat. transform	ι_o		0.39	0.58	0.39	0.47
Aver. plasma radius	r_p	$[m]$	0.2	1.75	1.6	1.6
Distance to coils	Δ	$[m]$		> 1.8	2.1	1.2
Average β	β	$[\%]$		5	5	5 - 6
Fusion power	P_{th}	$[GW]$		3.6	4	3.9 - 5.6
Radiation loss	P_{rad}	$[GW]$				0 - 0.3

For one of the 5 field periods of the smaller system, in Fig. 3 the contours of single cryostats for the 6 coils are shown in the upper part, along with the shape of the last closed magnetic surface; the lower picture is a cut through the mid-plane. It demonstrates the finite distance at the critical inside position. In ASRA6B these gaps are larger due to the increased dimensions. There are three different coil shapes if one regards the mirror symmetry.

The coil centers are at slightly different radial positions. All coils have identical elliptic bores , as visible in Fig. 4, left part. A distance $\Delta = 1.2\,m$ is seen between the inner side of the coil and the dashed line outside of the last magnetic surface. This contour can be used as shape of the first wall. Then a rather thin blanket is required. In a different approach the first wall is matched to the shape of the last closed magnetic surface, easing the blanket design at the expense of a slightly increased neutron power load of the first wall, see [5,6].

Fig. 4 applies for ASRA6C. The system of magnetic surfaces in the right part is calculated for an average value of $\beta \approx 5\,\%$. The shift of the magnetic surfaces due to the finite plasma pressure is clearly visible. More details of the finite-β computations are given in [4], showing the deepening of the magnetic well by the effect of the finite plasma pressure as well as a reduction in the radial profile of the rotational transform for the net current free case.

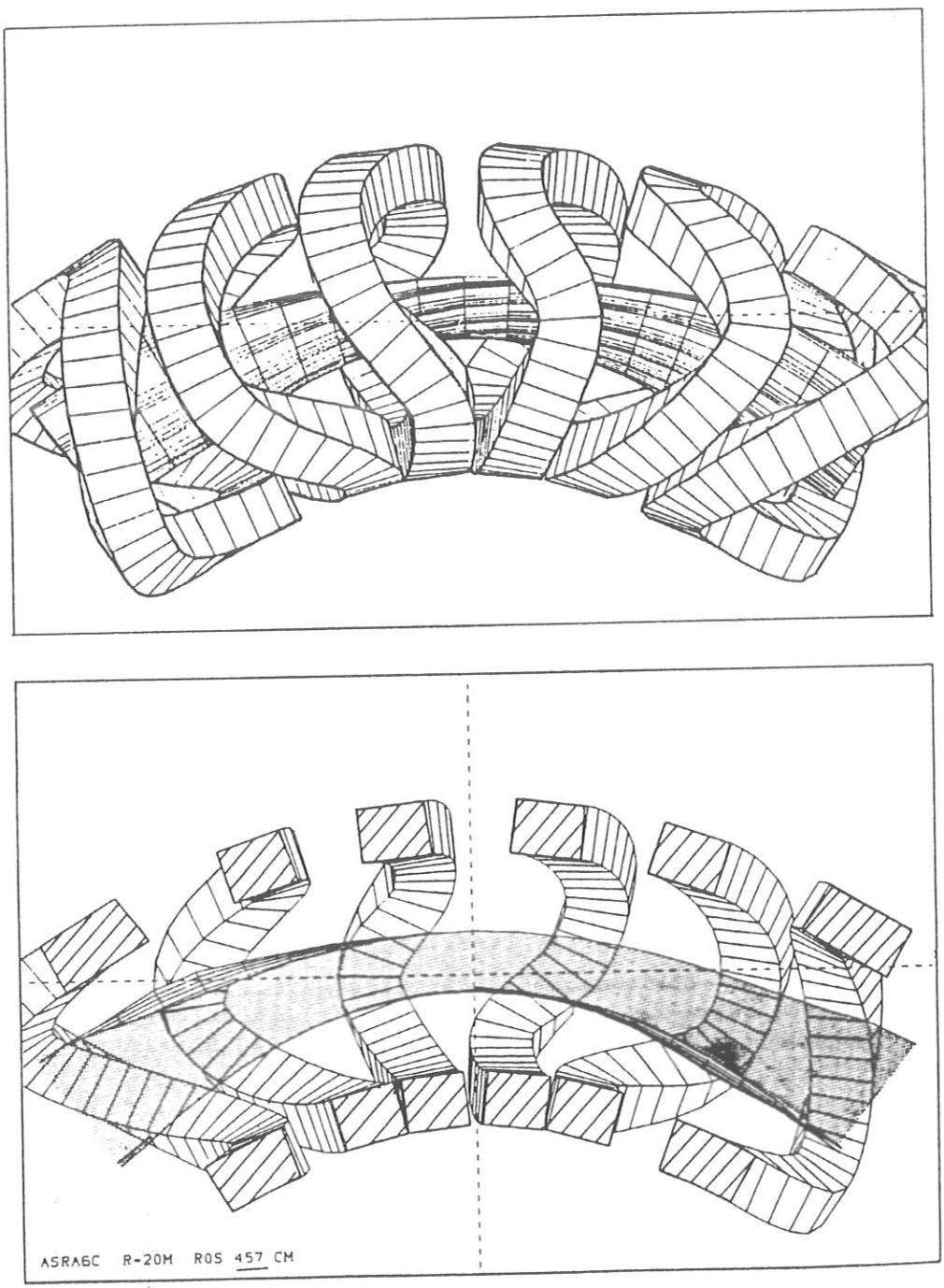

Fig. 3. Contours of single cryostats for ASRA6C
along with shape of last magnetic surface
upper part: top view, lower part: cut at mid–plane

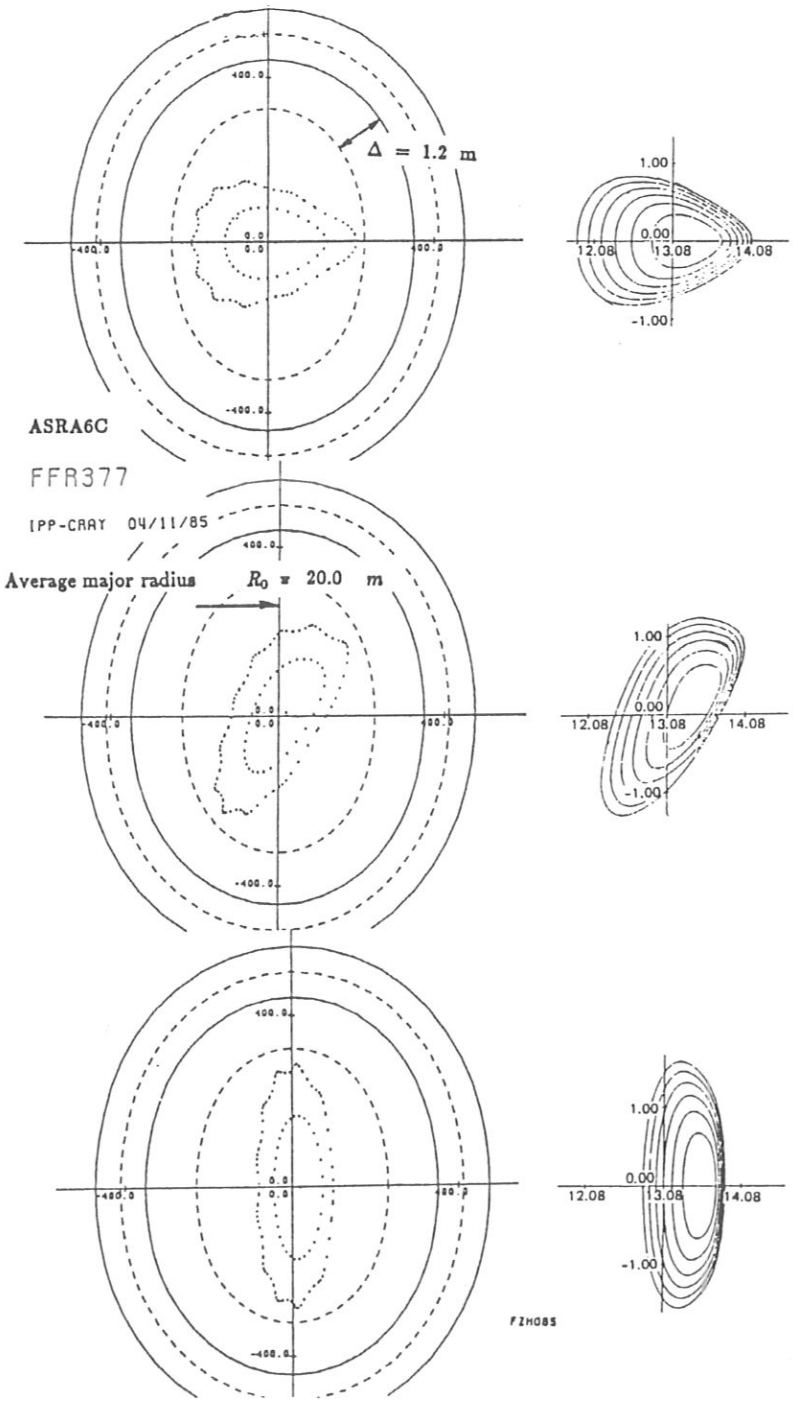

Fig. 4. Coil shape and system of magnetic surfaces for ASRA6C along with shape of elliptic contour at distance $\Delta = 1.2\,m$ inside of coils (left part); magnetic surfaces at average value of $\beta = 4.7\,\%$ shown slightly enlarged in right part.

hown in the following chapter, an average $\beta \approx 5\,\%$ is typical tion regime of the reactor. The shift of the magnetic surfaces found above computation can be taken as determining a 'soft' limit for the equilibrium-β. Regarding the critical value for stability, β_{stab}, theory predicts lower numbers for this type of configurations.

In this respect, an interesting new configuration, 'Helias' was recently published in [7], having the prospect of attaining stable values of $\beta_{stab} \approx 5\,\%$. This type of configuration combines elements of a 'Heliac', with its typical indented (= bean-shaped) contours of magnetic surfaces and a helical magnetic axis, with the described elements of an Advanced Stellarator of the Wendelstein VII-AS type. Furthermore, in [8] Bean-shaped Advanced Stellarators and their modular coil systems are described. The plasma aspect ratios of these two new configurations are at reasonably low values of about $A = 10 \ldots 12$, and a magnetic well exists in the vacuum fields.

The detailed reactor properties of these new systems remain to be studied. From the experience gained in the ongoing investigations it can be concluded that such new configurations do not require qualitatively new and differing engineering approaches, so that the present sytem studies remain significant.

5. HEATING AND BURN SCENARIOS FOR ASR AND ASB

Computations of the burn conditions for a typical ASR and an ASB are given in [9]. The stationary thermal fusion power of ASR amounts to typically $P_{th} = 3.6\,GW$ at an average $\beta = 5\%$. For ASB a fusion power of about 420 MW is obtained. Due to the increased field, the average β amounts to about 2.5 % for this example. These studies were continued, including also the start-up scenarios via an additional heating term.

A one-dimensional transport code is used iteratively. The coupled equations of particle and heat transport are solved, using neoclassical transport coefficients. The transport coefficients are large in the long mean free path regime and increase with the temperature and with the effective modulation (mirror ratio, 'ripple') of the magnetic field. These ripple data are taken from the magnetic field studies, see [4]. A radial electric field is optional and reduces the losses. Radial profiles of plasma temperature and density as well as the local fusion power are calculated. The density is governed by the refuelling rate. Radiative losses can be included, in addition to bremsstrahlung. The variable radial profiles of these input parameters strongly influence the result. The boundary conditions and open questions are discussed in [3], along with the dependence of the results on the major radius of the system, and the effects of additional radiation losses,either with a centered profile or peaked at the edge.

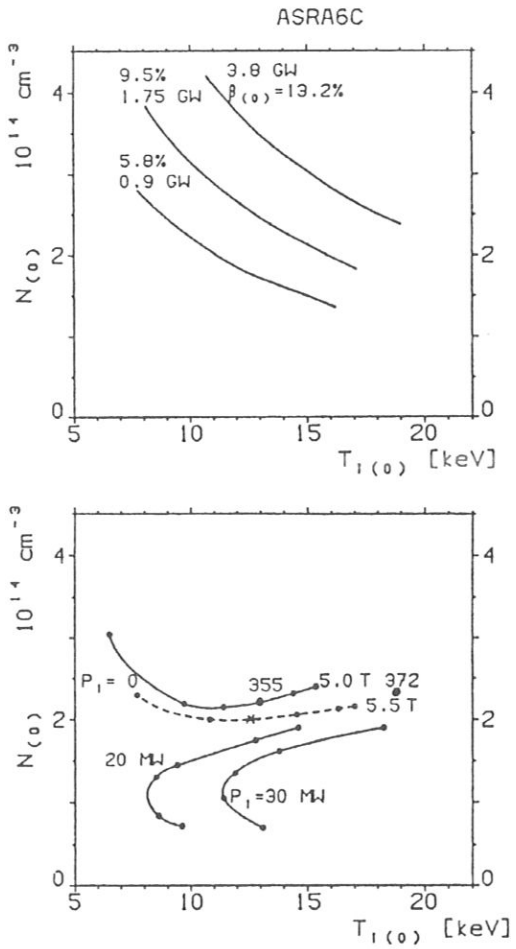

Fig. 5. Versus the axis values of density and temperature:
Fusion power output and peak values of $\beta(0)$
for the reference case ASRA6C (upper part)
Lower part: external heating power P_i of start–up.
Ignition curves at two different values of the induction.

In Fig. 5, upper half, the relation between the fusion power output and the peak values of $\beta(0)$ are given for the reference case ASRA6C under optimized conditions, versus the axis values of density and temperature. The lower half of the figure shows the dependence of these quantities on the external heating power P_i of start–up. The upper two curves characterize the ignition at two different values of the magnetic induction. For ASR (as well as for ASB), an effective heating power of 30 to 50 MW is sufficient for start–up. These dynamic processes are treated in a series of computations as sequences of static equilibria. By increased refuelling,

power, preferentially at a moderate temperature

..., and reducing the ripple losses by a factor of 2 in ... account for the improved confinement porperties of an Advanced Stellarator, in the ASRA6C reactor an additional radiative power loss of 300 MW can be tolerated at a thermal fusion power of 3.9 GW. In this computation $T \approx 19\,keV$ at a value of $\beta_{eq} = 5\,\%$.

The question of thermal stability of the operation points remains to be studied in further detail.

6. REACTOR APPROACH OF ASRA6C

First studies regarding the approach towards an Advanced Stellarator reactor are done in cooperation with KfK Karlsruhe (Germany) and members of the University of Wisconsin, Madison (USA). The data set ASRA6C is used for reference. The question regarding the value of β_{stab} of this type of configurations is addressed in Chapter 4 above. There the two options regarding the shape of the first wall are also mentioned.

The lay-out of the ASRA6C as a fusion reactor is described briefly; details are given in [5] and [6], also regarding estimates of the breeding ratio. In the two cross sections shown in Fig. 6, the contour of the first wall is assumed at some distance outside of the last closed magnetic surface. Thus, a blanket with variable thickness is foreseen, accomodating space for structure. A system of many pumped limiters is chosen for edge control of the plasma. Their heat load is assumed to be reduced by edge radiation. The choice of pumped limiters is a result of magnetic field studies near and outside of the separatrix of such systems, see [10]. This study shows a rather complicated radial structure of field lines started at some distance outside of the last closed magnetic surface.

The cross-hatched area outside of the blanket region provides volume for reflector and shield. The outer elliptical contours enclose the superconducting coils and their cryostats, their position being indicated for the different toroidal angles. Open space between the radial arrangement of reactor elements is available for assembly and maintenance. The upper part of the figure is at the beginning of the field period, the lower half applies for some adjacent toroidal position.

Not shown in the figure are openings for the start-up heating. Note that Stellarators in principle allow a stationary burn, provided that refuelling and ash removal can be accomodated appropriately, and the impurities in the system do not pose serious problems. Then, after start-up, the openings for the initial heating can be closed and shielded against the neutrons. This neutron wall load increases with the power of the burning plasma and shows a characteristic spatial dependence.

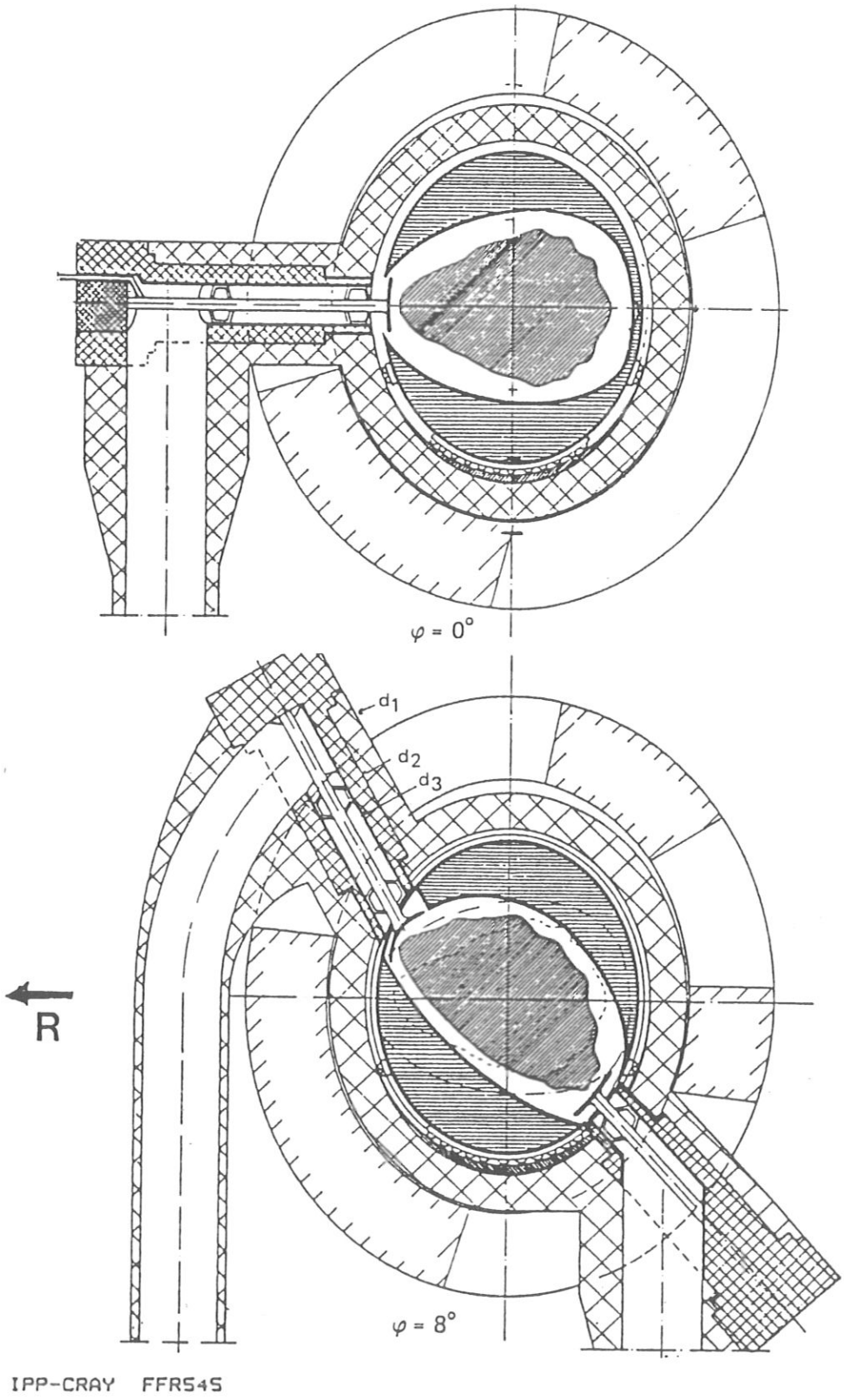

Fig. 6. ASRA6C as Fusion Reactor
shown at beginning of field period and at some toroidal position.
For details see text.

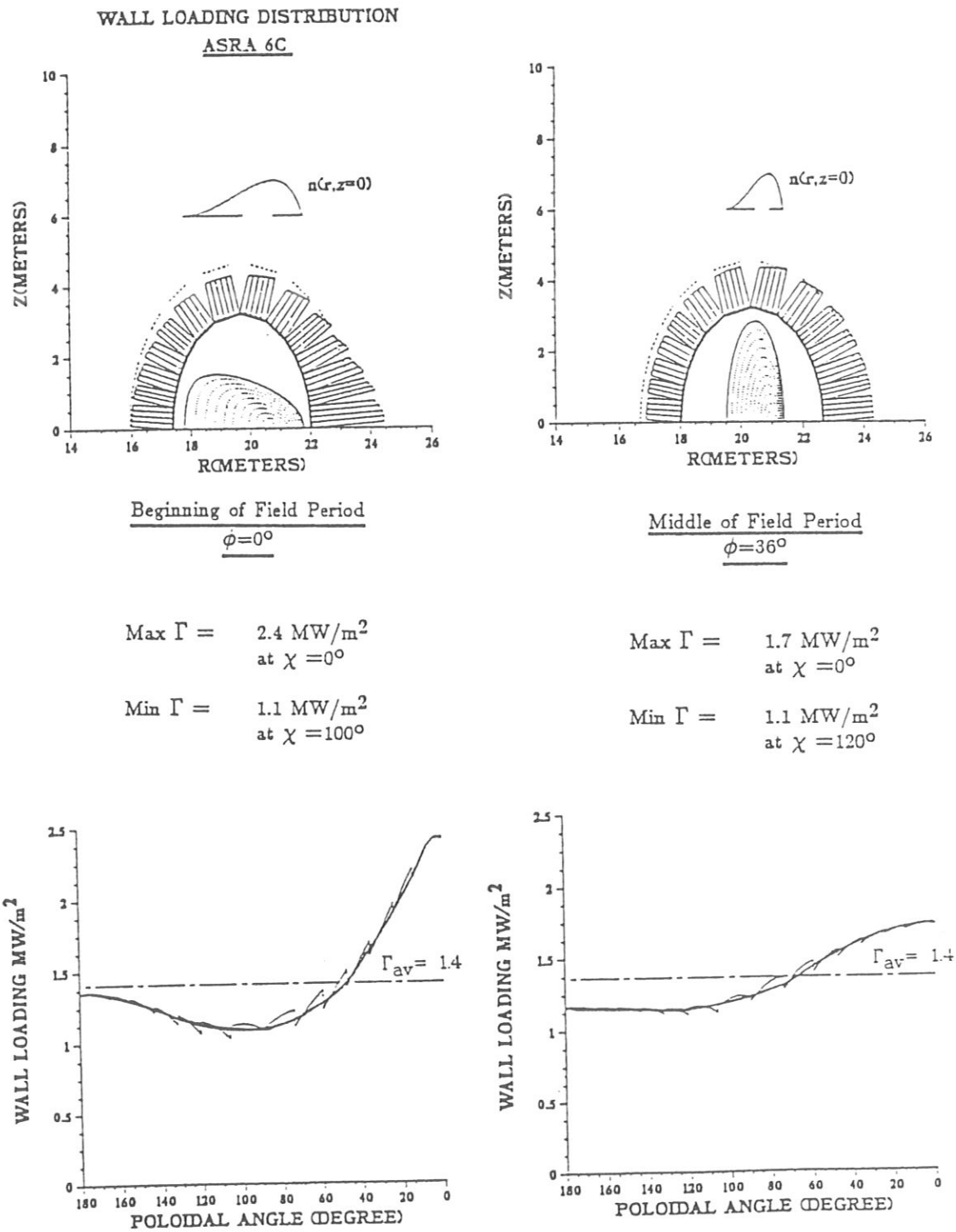

Fig. 7. Neutron wall load distribution for ASRA6C
Beginning and middle of the field period,
elliptic contour of first wall as shown.

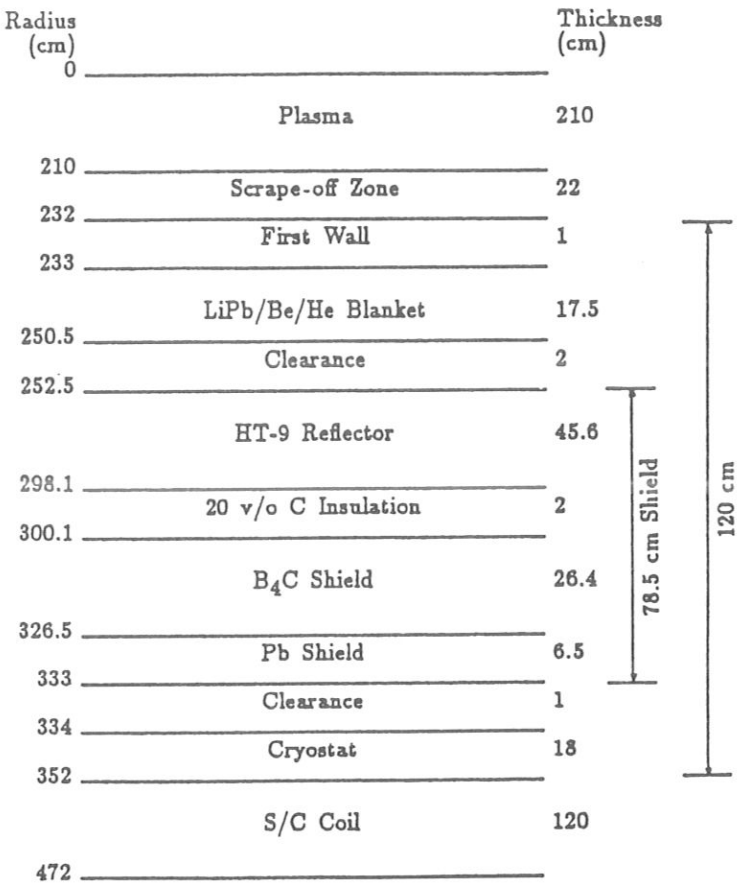

Fig. 8. Radial dimensions for ASRA6C, used for neutronics calculations as in [6].

The local power enhancement is estimated by two axisymmetric computations performed for ASRA6C at the beginning and the middle of the field period. As detailed in [6], the first wall is assumed at a distance $\Delta = 1.2\,m$ inside the coil bores, and the plasma center is assumed at a radial position of $R_p = 20.8\,m$. This value is in good agreement with the position of the magnetic axis at a finite $\beta \approx 5\%$. The geometry is shown in the upper part of Fig. 7. Taking a fusion power of $P_{th} = 3.6\,GW$, the average neutron load at the first wall amounts to $\Gamma_{av} = 1.4\,MW/m^2$; local enhancement factors are around a factor of two, as can be seen in the lower part of the figure.

For the first wall used in Fig. 6, the average neutron wall load is $\Gamma_{av} \approx 2\,MW/m^2$ with similar local enhancement factors. In both estimates, this enhancement is mainly due to the Shafranov-shift of the finite-β plasma; other geometrical effects are smaller due to the aspect ratio of the first wall of about 7 to 9 for the two cases.

Neutronics calculations are given in [6] for the geometry of ASRA6C modelled for the one-dimensional code as shown in Fig. 8. An averaged

breeding ratio of 1.05 is computed, using a fraction of 3 % of the 2200 m^2 surface of the first wall for openings, and taking a 10 % drop of the breeding efficiency during three full power years of operation into account. In this computation, the blanket is comparatively thin with a radial dimension of $\approx 20\,cm$, and consists of static $Li_{17}Pb_{83}$, with Be as moderator and neutron multiplier. The blanket uses He gas as coolant and to remove the Tritium. A HT-9 reflector and a B_4C shield are further decisive elements for this compact system of blanket and shield.

7. ENGINEERING CONSIDERATIONS FOR ASRA6C

For the smaller of the two reference data sets, ASRA6C, engineering considerations regarding the electromechanical forces and their support, as well as the correlated stresses and strains are given in more detail in [11], in comparison to results obtained for ASRA6B in a recent publication [12]. The present chapter summarizes the essentials of this comparison.

As mentioned above, in the compact version ASRA6C, the system size is reduced from a major radius $R_o = 25\,m$ in ASRA6B to a smaller value of $20\,m$, keeping the current density in the coils (average radius $r_c = 4.57\,m$ as compared to the previous $5.22\,m$) at a constant value of $j_{eff} = 15\,MA/m^2$. In order to attain an identical induction at the magnetic axis of $B_o = 5.3\,T$, the smaller coils in ASRA6C carry a current of $I_c = 18\,MA$, whereas those of ASRA6B require $22.5\,MA$.

In non-planar coils arranged toroidally, in addition to the main centripetal force of the torus geometry, considerable lateral forces act locally on the coils. Although these forces are balanced over one field period, they need to be considered in the support scheme. For both coil systems, local maximum force densities, $f_m = 165$ and $155\,MN/m^3$, are found; the slightly larger value applies for ASRA6B. Differences in the force components are shortly discussed in [11]. The maximum force density of the complete coil system ASRA6C is about a factor 1.5 larger than the local force density of the coil with the largest toroidal excursion, if treated as a single coil at design current. A stress analysis indicates that also for this situation some structural material around the coil is required, as to be seen schematically in Fig. 9, upper part.

The analysis of the stresses and strains of the complex coil arrangement of ASRA6C is done for a system of 10 coils (i.e the 6 coils of one field period and 2 side coils of the two adjacent ones), in a mutual coil support as shown in Fig. 9, lower part. Between the coils and their lateral and radial support rings, elastic paddings are foreseen. The isotropic or orthotropic material data is given in [12]. The material data are the same as used for the computations for ASRA6B. For this data set and using orthotropic coil data, the maximum of the equivalent (von Mises)

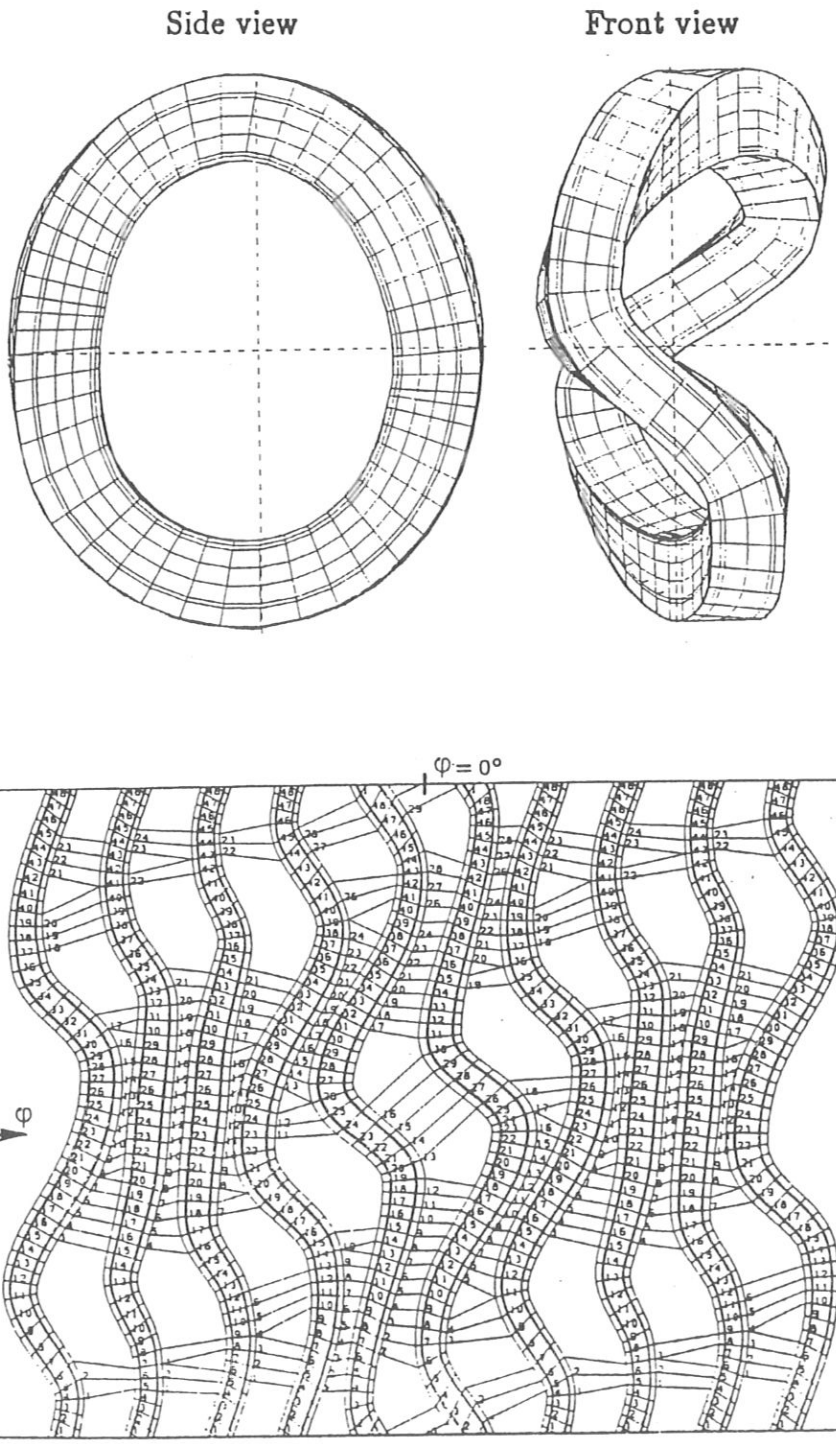

Fig. 9. Non-planar coil for ASRA6C with housing, and system of mutual support.

stress amounts to 180 MPa at a tangential strain of 0.23 %. A maximum of the shear stress of 60 MPa is seen. Similar calculations for ASRA6C yield similar values. This can be seen also by a comparison of the 'virial stress', the stored magnetic energy normalized by the total coil volume, W_m / nV_c. Here $n = 30$ is the coil number and $V_c = 2\pi r_c wt \cdot f$, where $f > 1$ is a measure of the non-planar coil shape. The quantities w and t are the lateral width and the radial height of the coils, respectively. Inserting the numbers of ASRA6B and ASRA6C, the virial stresses amount to 120 and 100 MPa.

From this comparison we conclude that the coils seem to be feasible, although the shear stresses require some attention in further iterations of the support system. These are directed towards replacing the lateral and radial support rings by a complete coil housing.

8. SUMMMARY AND CONCLUSIONS

A survey is given on studies of critical issues of Advanced Stellarator Reactor and Burner systems, ASR and ASB, respectively, with a field topology similar to that of the Garching Advanced Stellarator Experiment Wendelstein VII-AS. During the course of these studies, considerable progress is made regarding the desired reduction in size by utilizing a modern approach for a comparatively thin blanket and shield.

The general lay-out of some of the elements for a reactor is discussed. Evidently, much work remains to be done before arriving at a point design. Regarding engineering considerations for the non-planar coils and their forces, stress computations show considerable shear values, but in general the coils seem to be feasible.

The fusion power is computed for neoclassical losses (including effects of a radial electric field) and yields about 4 to 5 GW for an ASR; the power output of an ASB is typically 10 % of this value. For start-up, an effective power of about 30 to 50 MW is sufficient for both systems. A radiative power loss of 300 MW near the plasma edge can be tolerated.

Then, the average plasma β amounts to about 5 % for ASR. This value agrees with that obtained numerically for the equilibrium-β of ASRA6C. Regarding a similar value for β_{stab}, an interesting new configuration was recently published.

The detailed reactor properties of these new systems remain to be studied, however. From the experience gained in the ongoing investigations it can be concluded that such new configurations do not require qualitatively new and differing engineering approaches, so that the present system studies remain significant.

REFERENCES

[1] R. Chodura, W. Dommaschk, W. Lotz, J. Nührenberg, A. Schlüter,
Three-dimensional MHD Equilibrium Studies,
Proc. Plasma Phys. and Contr. Nucl. Fusion Research,Brussels 1980,
Vol. I, 807, (1981).

[2] U. Brossmann, W. Dommaschk, F. Herrnegger, G. Grieger,
J. Kisslinger, W. Lotz, J. Nührenberg, F. Rau, H. Renner,
H. Ringler, J. Sapper, A. Schlüter, H. Wobig,
Concept of an Advanced Stellarator,
Proc. Plasma Phys. and Contr. Nucl. Fusion Research,Baltimore,
1982, Vol. III, 141, (1983).

[3] E. Harmeyer, J. Kisslinger, F. Rau, H. Wobig,
Heating and Burn Scenarios for ASR and ASB,
this conference.

[4] E. Harmeyer, F. Herrnegger, J. Kisslinger, F. Rau, H. Wobig,
Magnetic Field Studies for Advanced Stellarator Reactors,
this conference.

[5] J. Hübener and W. Maurer,
General Design of a Modular Stellarator Reactor,
this conference.

[6] B. Badger, L. A. El-Guelbaly, G. A. Emmert, G. L. Kulcinski,
E. M. Larsen, J. F. Santarius M. E. Sawan, J. E. Scharer,
I. N. Sviatoslavsky, W. F. Vogelsang, P. L. Walstrom,
L. J. Wittenberg,
Annual Report on Contributions to ASRA6C,
a Commercial Stellarator Fusion Reactor,
FPA-85-4 , Madison Wi (1985).

[7] J. Nührenberg and R. Zille,
Stable Stellarators with Medium β and Aspect Ratio,
Physics Letters 114A, 129, (1986).

[8] F. Herrnegger and F. Rau,
Bean-shaped Advanced Stellarators with Modular Coil Systems,
13^{th} Eur. Conf. on Contr. Fusion and Plasma Heating,
Schliersee, Germany, 1986.

[9] E. Harmeyer, J. Kisslinger, F. Rau, H. Wobig,
Some Aspects of Modular Stellarator Reactors,
Proc. Plasma Phys. and Contr. Nucl. Fusion Research,
London 1984 Vol. III, 363, (1985).

[10] E. Harmeyer, J. Kisslinger, F. Rau, H. Wobig,
Magnetic Field Studies Near Separatrix,
13^{th} Eur. Conf. on Contr. Fusion and Plasma Heating,
Schliersee, Germany, 1986.

[11] E. Harmeyer, J. Kisslinger, F. Rau, H. Wobig, Engineering Considerations of Modular Coils for ASRA6C, an Advanced Stellarator Reactor, this conference.

[12] E. Harmeyer, J. Kisslinger, F. Rau, H. Wobig, On Modular Coils of a Stellarator Reactor, Proc. 11^{th} Sympos. on Fusion Engineering, Austin, Tx (USA) 1985, in press.

ENGINEERING CONSIDERATION OF MODULAR COILS FOR ASRA6C, AN ADVANCED STELLARATOR REACTOR

E. HARMEYER, J. KISSLINGER, F. RAU, H. WOBIG
Max-Planck-Institut für Plasmaphysik,
Euratom-IPP Association,
Garching,
Federal Republic of Germany

Abstract

In an Advanced Stellarator, the magnetic topology is produced by a set of non-planar modular coils. For the reactor configurations as studied at present, two reference coil sets are developed. The compact system ASRA6C is characterized by a major radius $R_o = 20\,m$, an average minor coil radius of $4.6\,m$, and by a distance $\Delta = 1.2\,m$ between the plasma edge and the coils. The coils produce an induction of $B_o = 5.3\,T$; the total stored magnetic energy amounts to $W = 117\,GJ$.

The force distribution within the coils is calculated and yields a local maximum force density of $155\,MN/m^3$. A characteristic feature of non-planar coil systems are lateral forces with local values of the order of the maximum of the radial component. Within a field period the lateral forces are balanced. The mechanical stress and strain distributions are investigated inside the coils by finite-element calculations, using the SAP V (2) program system. A mutual support between adjacent coils is applied. With orthotropic material data, a maximum of the equivalent (von Mises) stress of $\sigma_{vM} = 170\,MPa$ is obtained, associated with a considerable shear stress. The tangential strain amounts to about 0.2 % for this case.

1. INTRODUCTION

The configuration ASRA6C is an "Advanced Stellarator" coil system similar to that of the Garching experimental device Wendelstein VII-AS. This configuration comprises 5 field periods (FP) and uses 8 elliptically shaped modular coils and one large special coil per FP. Compared to earlier stellarator fusion reactor coil systems with differing numbers of coils per FP, as desribed shortly in [1], the compact system ASRA6C is reduced in size as compared to the preceding data set ASRA6B. Both coil systems have 6 coils in each of the 5 field periods. The choice of this coil number is made as a compromise between 'field quality' and ease of

assembly and maintenance of such systems. The main feature of the coils is their identical approximately elliptic coil bore. The uniform shape of the coil bores permits an uncomplicated design of blanket and shield and simplifies maintenance.

The present paper starts in Chapter 2 with a short description of the main properties of the coil system ASRA6C in comparison to those of ASRA6B. The following Chapter 3 briefly summarizes details of the electromagnetic force distributions present in non-planar coil systems, and compares the results for the two reference systems. In Chapter 4, the stress analysis is performed for the coils of ASRA6C. A system of mutual coil support is employed. A summary and the conclusions are given in Chapter 5.

2. PROPERTIES OF THE COIL SYSTEMS ASRA6B AND ASRA6C

The abbreviations of these two data sets stand for Advanced Stellarator Reactors with coils described by an Analytic winding law and 6 coils per field period, version B and C. The label C indicates a more compact version than the preceding data set ASRA6B. This is made possible by introducing a modern design for blanket and shield, see [2], by reducing the decisive distance Δ between the first wall of the system and the inner contour of the coil winding, from the previous value of about 2 m to 1.2 m. In consequence, the major radii can be changed from R_o = 25 m in ASRA6B to a value of 20 m in ASRA6C. Fig. 1 shows one field period of the coil configuration ASRA6C. There are 6 coils per FP and three different coil shapes are present in the complete coil system, if one considers the twofold mirror symmetry. All coil apertures are of the same elliptic cross section with an axis ratio of about 1.17, centered at major radii according to $R(\varphi) = R_o\,(1 - k\,cos(5\varphi))$, where k = 1.6 % for both cases, and φ is the toroidal angle.

The spatial contours of the non-planar modular coils of ASRA6B and ASRA6C follow an analytical relationship or "winding law", describing the coil centerline for arbitrary position and orientation of the modular coils, as detailed in [3]. The edge contours of the coils are obtained by adding half of the lateral width and shifting by half of the radial height.

The characteristic data of the two coil systems for the Advanced Stellarator Reactors ASRA6B and ASRA6C are entered in Table I. Equal values of the effective current density, $j_{eff} = 15\,MA/m^2$ are used in both cases. Here, the effective current density is the total coil current I_c divided by the whole cross section of the coil winding pack, i.e. averaging over the complex structure of superconductor with stabilizer, internal structure, insulation and helium channels. Because the magnetic induction at the axis of the plasma is kept at equal values of $B_o = 5.3\,T$ for both data sets, the total coil current I_c = 22.5 and 18 MA for ASRA6B

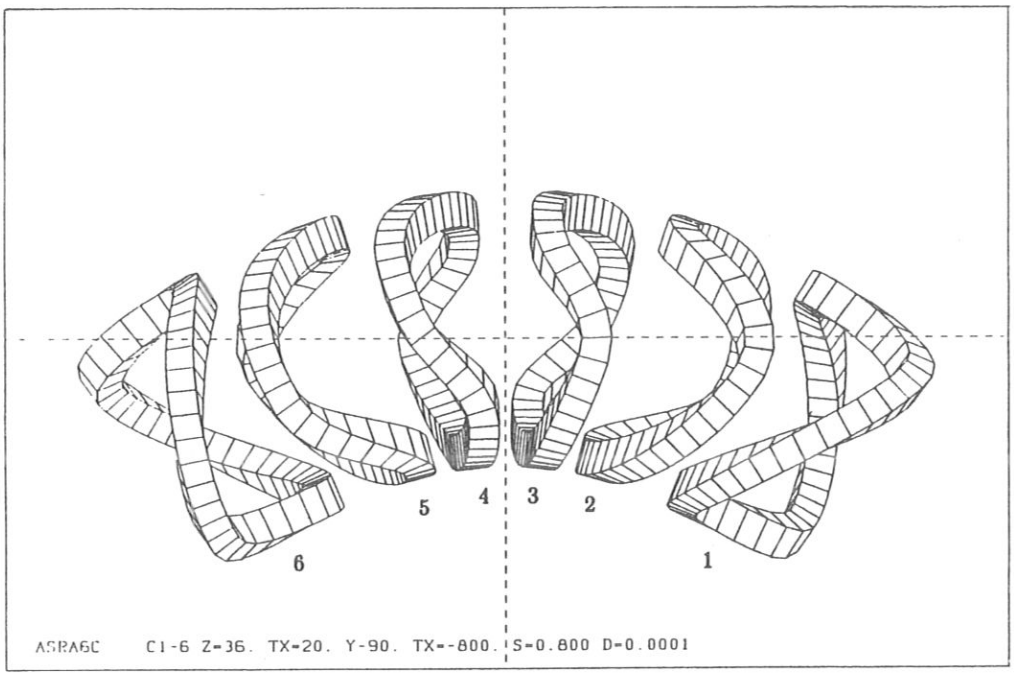

Fig. 1. Coil configuration ASRA6C, one field period.

and ASRA6C, respectively, scaling proportional to the major radius. The coil volumes V_c as given in the Table are estimated including a correction factor f which describes the average toroidal excursion of the coils.

Within the coils in their toroidal arrangement a complicated distribution of the induction is present, showing components in all spatial directions and having considerable gradients. The maximum value of the induction is at the coil bore. Due to the non-planar coil shape and the differing coil distances, this coil maximum field is different for the three different coils of a field period, and not necessarily at the inner mid-plane. The global maximum is entered in the table and amounts to $B_m = 11.0$ and $10.4\,T$ for the two systems.

Note the remarkable decrease in the magnetic energy when reducing the size of ASRA6B to that of the compact system ASRA6C. On the other hand, the minimum radius of curvature has a smaller value in ASRA6C which might influence the material choice and winding techniques of coil fabrication. In Table I, the global minimum of the radius of curvature is entered, measured at the coil corners.

3. ELECTROMAGNETIC FORCES

In order to describe the distributions of magnetic field, forces, and stresses a local orthogonal coordinate system R, S, T is used, with R in-

TABLE I. Characteristic data of ASRA6B and ASRA6C

Average major radius	R_o	$[m]$	25.0	20.0
Average coil radius	r_c	$[m]$	5.22	4.57
Radial coil height	w	$[m]$	1.25	1.20
Lateral coil width	t	$[m]$	1.20	1.00
Average coil volume	V_c	$[m^3]$	54.7	40.0
Min. radius of curvature	ρ_c	$[m]$	1.05	0.77
Coil number total / per FP	n/np		30/6	30/6
Total coil current	I_c	$[MA]$	22.5	18.0
Effective current density	j_{eff}	$[MA/m^2]$	15.0	15.0
Total stored magnetic energy	W	$[GJ]$	193.	117.
Induction on axis	B_o	$[T]$	5.3	5.3
Max. induction at coil	B_m	$[T]$	11.	10.4
Rotat. transf. on axis	ι_o		0.39	0.47
Average plasma radius	r_p	$[m]$	1.6	1.6
Average force density	$< F' >$	$[MN/m^3]$	50.	50.
Local max. force density	F'_m	$[MN/m^3]$	165.	155.
Virial stress	σ_V	$[MPa]$	118.	99.

dicating the radial, S the lateral, and T the tangential directions, respectively, see [4]. Inside the coils, in general, all field components B_R, B_S, B_T are present, whereas the current density has one component in the tangential direction only. Hence, according to

$$\vec{F}' = \vec{j} \times \vec{B}, \tag{1}$$

there are two components of the force density, namely F'_R and F'_S, acting on the twisted coils. These local forces are different for the three differently shaped coils. Thus, considering the twofold mirror symmetry of each field period, the lateral forces are balanced over one field period.

Because of the toroidal arrangement of the system, each coil of the assembly envisages a net force in the direction towards the torus center. This force amounts to about 150 MN per coil for the ASRA6C configuration, in comparison to a value of about 200 MN in ASRA6B, see [5].

In order to obtain the distribution of the force density inside the coils the cross-section is subdivided into three radial and two lateral "microelements". Earlier studies, given in [4], demonstrate that this rather coarse grid yields a sufficient degree of accuracy.

Fig. 2 shows for ASRA6C the radial (F'_R) and the lateral (F'_S) components of the force density of coil 1 versus the coil circumference. The values are computed in the center of the "microelements", as shown in the insert of the figure. The average magnitude of the force density is

$$< F' > = \frac{1}{N} \sum_{i=1}^{N} |\frac{1}{V_i} \int_{V_i} \vec{j} \times \vec{B} \, ds \, dA|, \qquad (2)$$

where ds denotes a line element in the direction of the current, dA an area element perpendicular to ds, V_i the volume of a GCE (general current element), and N the number of the GCE's, respectively. For ASRA6B and ASRA6C, the same value of about 50 MN/m^3 is calculated as average of all coils. The nearly identical result of the two configurations is due to the following facts: The average radial component of the force density in ASRA6B is larger than in ASRA6C. But the lateral component of the force density in ASRA6B is smaller than in ASRA6C, because of the larger lateral radius of curvature in ASRA6B. This results in about the same magnitude of the force density. The local maximum of the magnitude of the force density in ASRA6B is slightly larger than in ASRA6C: 165 MN/m^3 as compared with 155 MN/m^3. This local maximum force density results in both systems at coil 2, GCE No 11, see Fig. 3. The five curves of the figure are equally spaced at the coil bore, showing some spread caused by the different local values of the induction, the current density j being a constant across the coils. Comparing these local maximum force densities with the averaged ones, a factor of approximately three is seen, caused by the steep field gradients within the coils.

4. MECHANICAL STRESS ANALYSIS

In order to investigate the mechanical stress and strain distributions, finite-element calculations are done using the SAP V (2) program system. This is done inside the coils, in some cases also within the support structure. The complex coil construction is simplified by using appropriate average values for the material data, as given in [5]. The calculations of stress and strain are done for coils in the assembly, as well as for a single coil in its own magnetic field.

A single coil separated from the coil assembly is free of net force, and no external forces are required to support it. The main data of the single coil 1 of ASRA6C at the operating current are listed in Table II.

Already in such a load case, a complex distribution of the force density is present, due to the non-planar coil shape. The stress calculations indicate that a coil support similar to that of Fig. 4 is required, having a lateral and inside radial thickness of 10 cm, and 40 cm at the radial

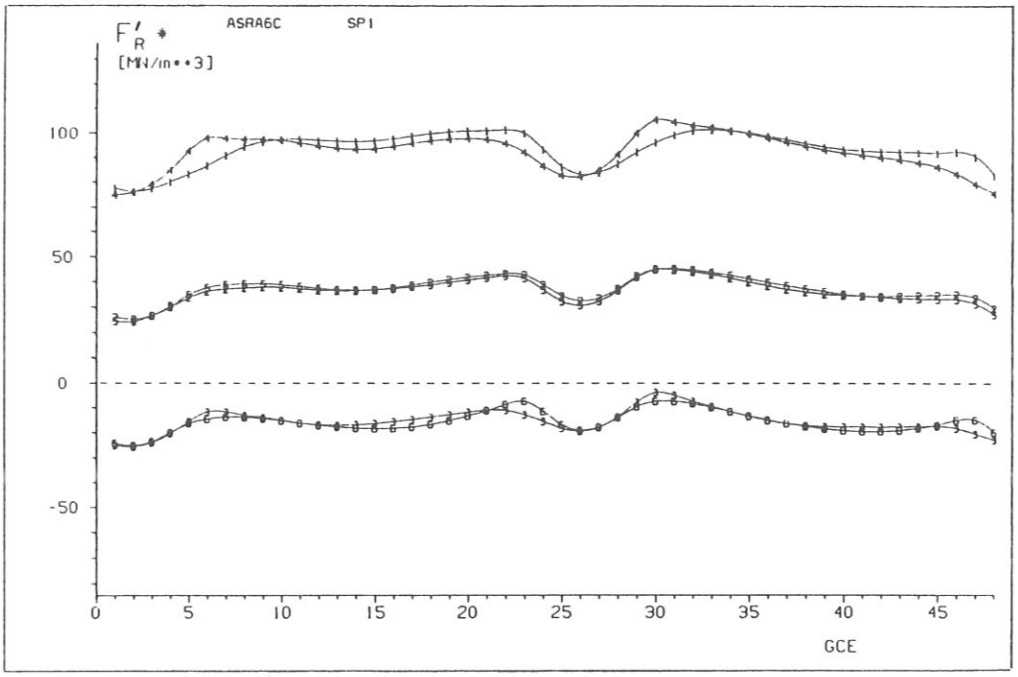

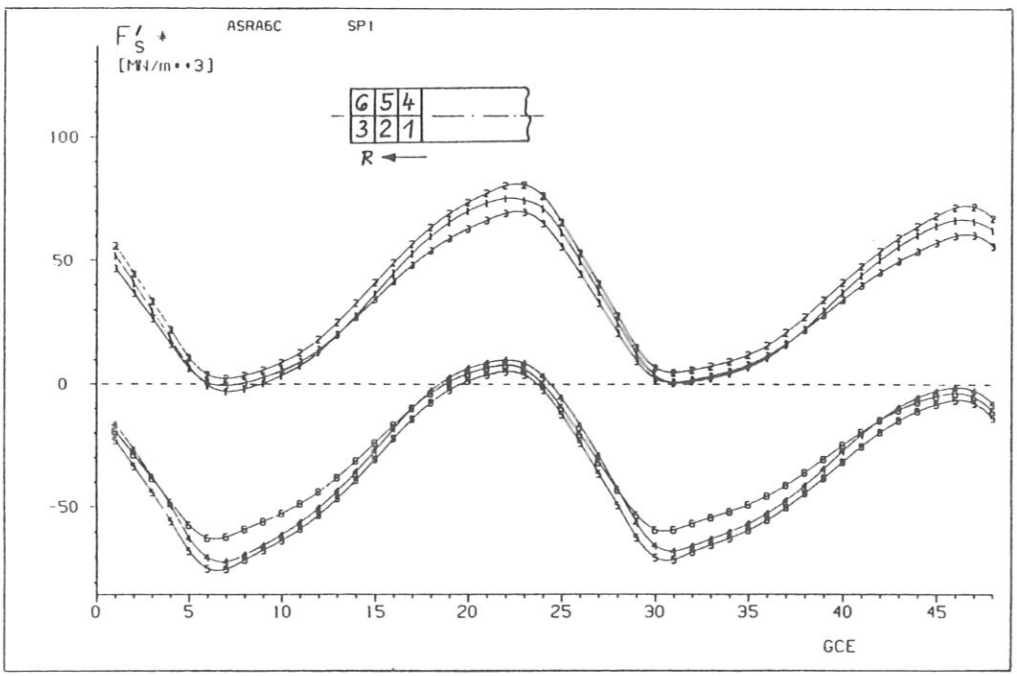

Fig. 2. Magnetic force densities in radial and lateral direction, ASRA6C , coil 1.

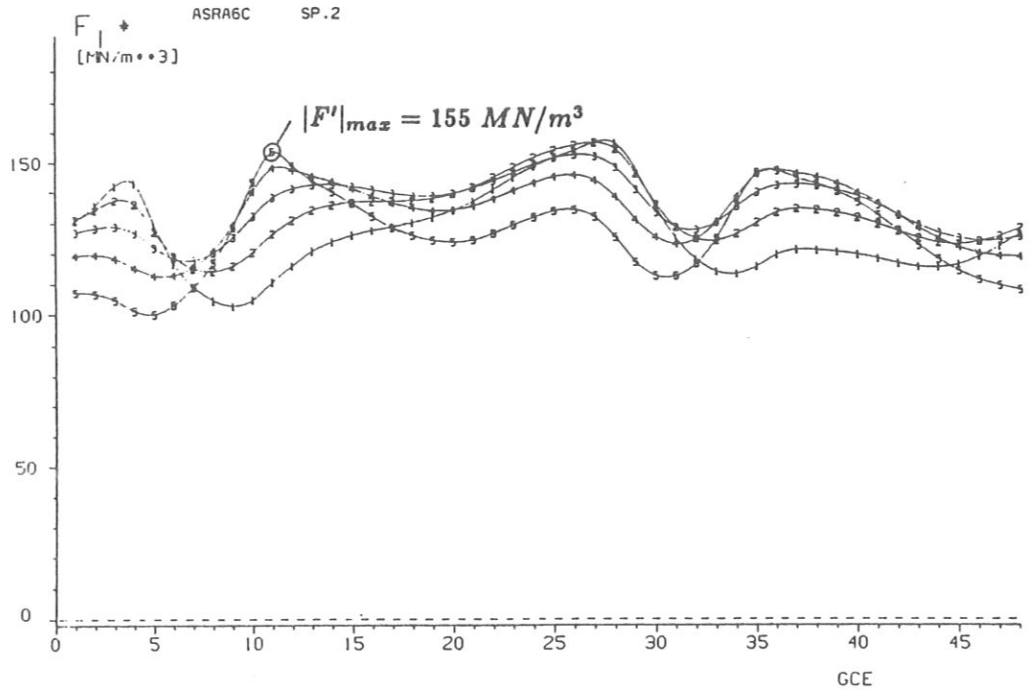

Fig. 3. Magnitude of the force densities
calculated at the inner side of coil 2
for 5 contours along the circumference of the coil bore.

TABLE II. Characteristic data of single coil 1 of ASRA6C

Total coil current	I_c	$[MA]$	18.0
Overall current density	j_c	$[MA/m^2]$	15.0
Total inductance (one turn)	L	$[\mu H]$	15.1
Magnetic energy	W	$[GJ]$	2.45
Max. induction at coil	B_m	$[T]$	7.7
Local max. force density	F'_m	$[MN/m^3]$	115.
Coil volume (winding pack)	V_c	$[m^3]$	41.0

outside. Elastic paddings are between the coil and the structure. The ratio of structure volume to coil volume amounts to 1.1. Then the bending stresses inside the coil are reduced to uncritical values. Regarding this coil support, the local maximum value of σ_{vM} reaches $470\,MPa$ at the center of the microelements, well below the stress limit of steel.

As support system for the assembly of coils in the system ASRA6C we use again the previously introduced concept of mutual support between

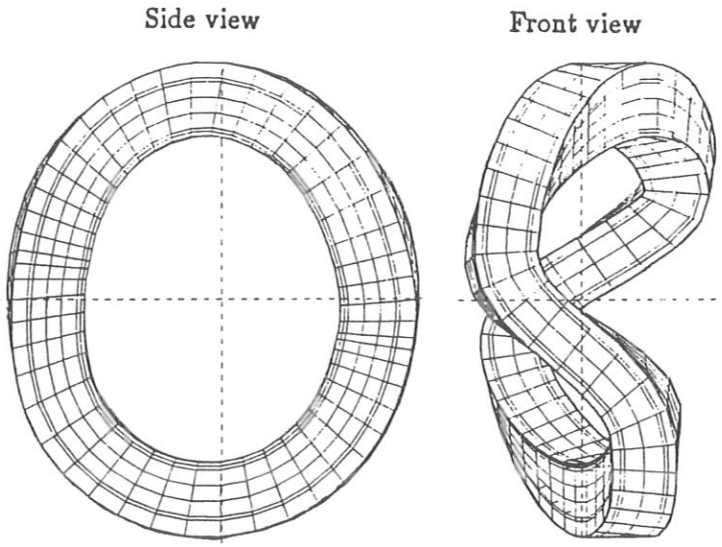

Fig. 4. ASRA6C: coil 1 with coil housing.

adjacent coils, see [5] and [6]. An outer ring and two lateral rings are provided for each coil. The upper part of Fig. 5 shows a vertical view on 10 coils, i. e. those of one field period and 2 coils on either side. The radial and lateral support rings can be seen in the picture, elastic paddings are between the coils and structure.

Boundary elements are provided at the first and the last coil of the arrangement and on the outer rings in the region towards the torus center. In the space between the lateral rings of the coils, lateral support elements are located in order to achieve mutual support of the coils, as shown in the lower part of Fig. 5 in the $\varphi - \vartheta -$ plane. The positions of the lateral support elements are varied in many iterations to minimize the stress and strain values of the coil system.

The finite element computations are based on both isotropic and orthotropic material data of the coils as given in [5]. With the orthotropic material data, which are close to the measured values for the non-planar coils of the Garching Advanced Stellarator experiment Wendelstein VII-AS, one obtains for the data set ASRA6C a maximum value of about 170 MPa for the von Mises stress, and a maximum tangential strain of about 0.2 % , as shown in Fig. 6 and Fig. 7. In these figures, the abscissae are the number of the GCE. and the different curves apply for the 10 coils treated simultaneously. The stress values include an enhancement factor of 2.5 in order to take local maxima of the force density and an overall filling factor of 0.8 into account. The equivalent stress contains considerable local maxima of shear stress of about 50 MPa, see Fig. 8, which might exceed the permissible stress. These local maxima of the shear stress occur mainly at the edges of the lateral support elements

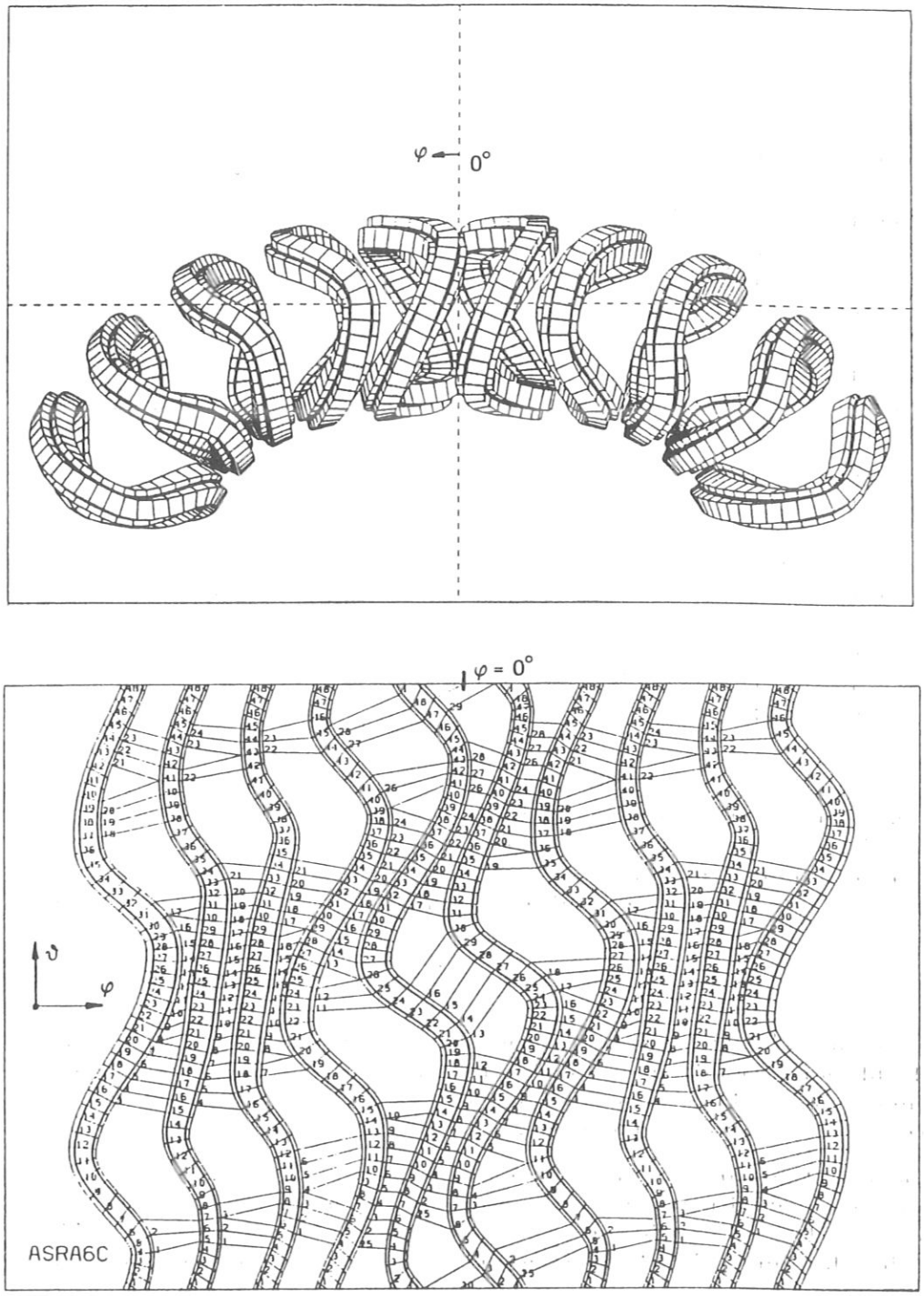

Fig. 5. ASRA6C: 10 coils with radial and lateral support, rings and padding, (upper part);
Mutual support of the coils shown in the lower part in the $\varphi - \vartheta -$ plane.

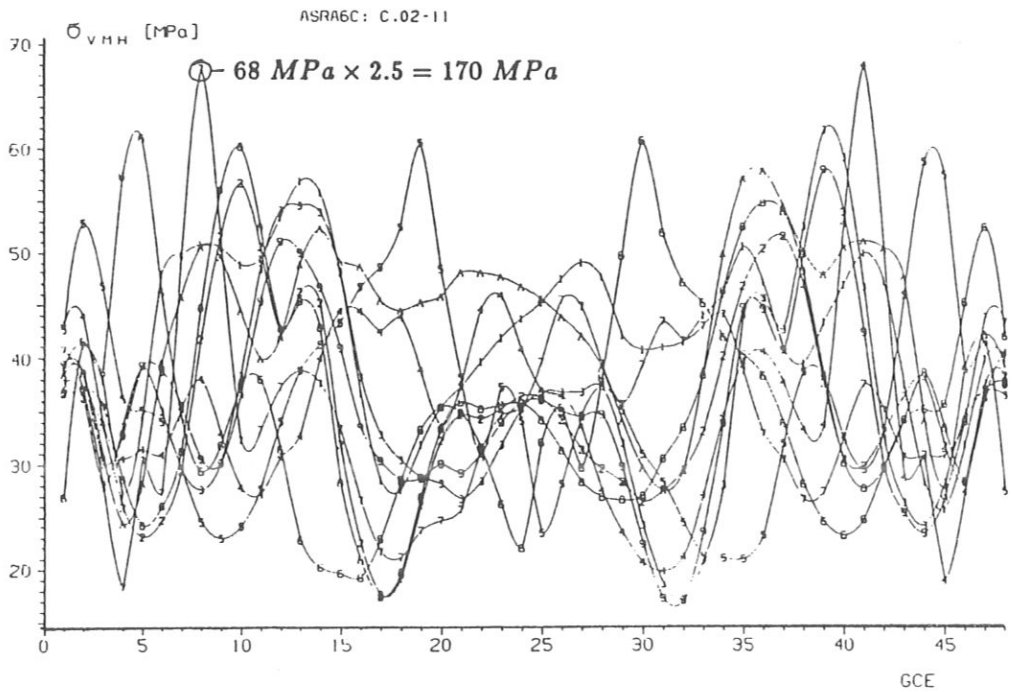

Fig. 6. ASRA6C: equivalent stress σ_{vM}, orthotropic coil data.

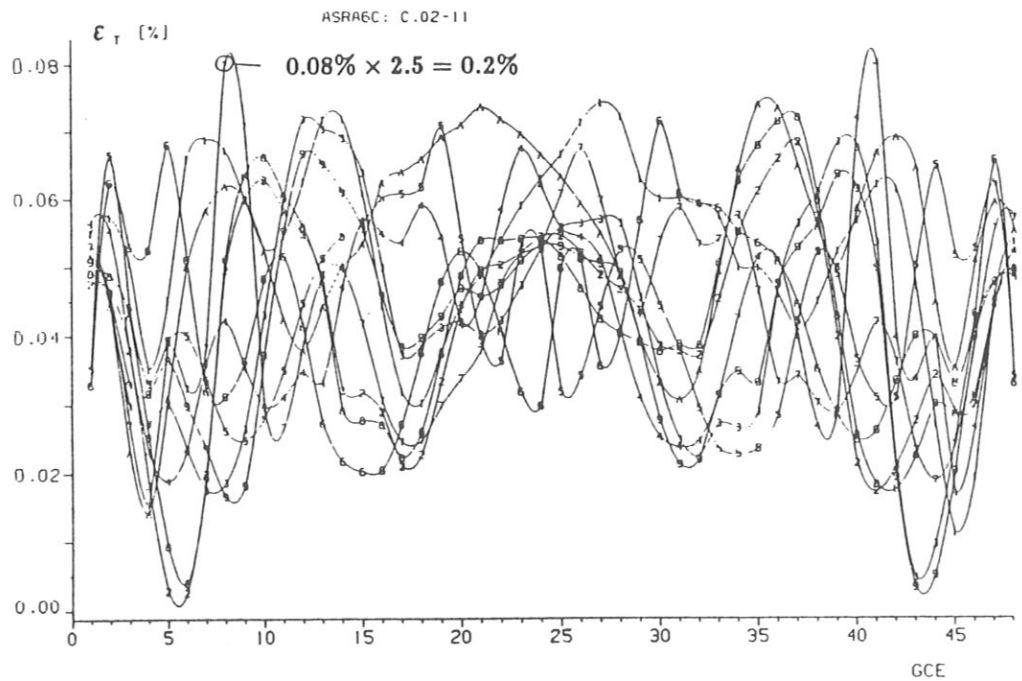

Fig. 7. ASRA6C: tangential strain ϵ_T, orthotropic coil data.

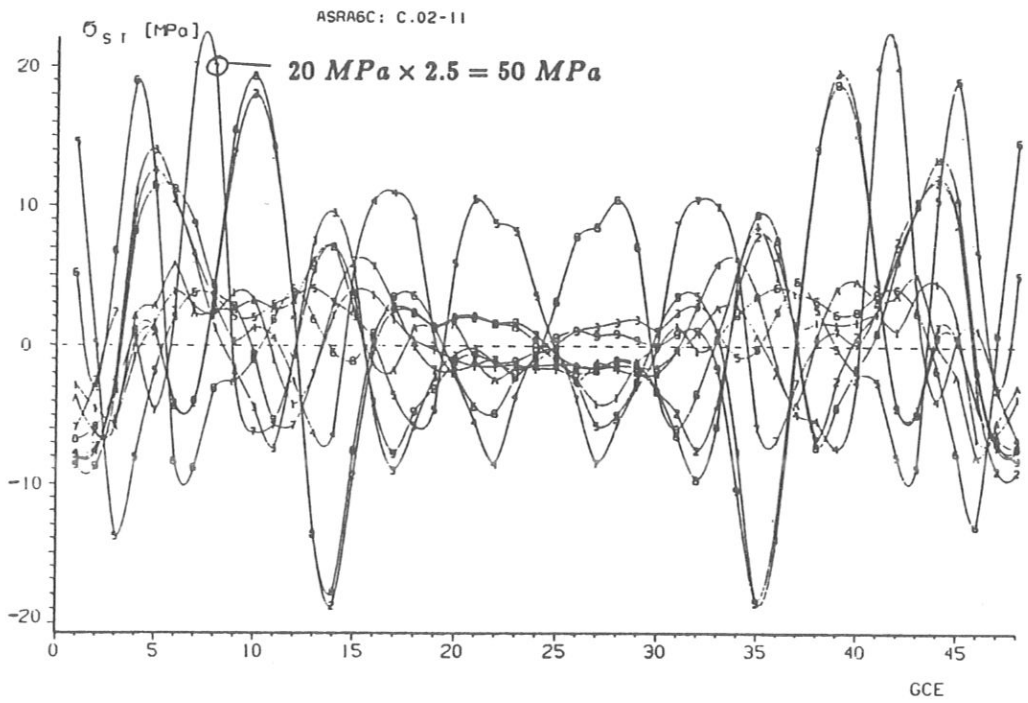

Fig. 8. ASRA6C: shear stress σ_{ST}, orthotropic coil data.

connecting adjacent coils. It is believed that these maxima can be reduced by a smooth shape of the edge support elements, or by introducing a complete housing around each of the coils. Work is underway in that direction for the data set of ASRA6C.

The stress and strain analysis for the coil arrangement of ASRA6B is given in [5]. Using the same support scheme and orthotropic coil data as above, the maximum of the equivalent (von Mises) stress amounts to $180\,MPa$ at a tangential strain of 0.23 %. A maximum of the shear stress of $60\,MPa$ is seen.

The similarity of these results to those of ASRA6C can be understood by a comparison of the 'virial stress', the stored magnetic energy normalized by the total coil volume, $W_m / n V_c$. Here $n = 30$ is the coil number and $V_c = 2\pi r_c wt \cdot f$, where $f > 1$ is a measure of the non-planar coil shape. The quantities w and t are the lateral width and the radial height of the coils, respectively. Inserting the numbers of ASRA6B and ASRA6C, the virial stresses amount to 120 and 100 MPa; the precise numbers are entered in Table I.

5. SUMMARY AND CONCLUSIONS

The Advanced Stellarator Reactor configurations ASRA6B and ASRA6C with major radii of $R_o = 25$ and $20\,m$, minor coil radii of

r_c = 5.3 and 4.6 m, are characterized by distances of Δ = 2.1 and 1.2 m between the plasma edge and the coil bore. This considerable reduction in size is made possible by using a modern approach of a thin blanket.

For the same values of the induction B_o = 5.3 T at the magnetic axis in both cases, the compact system ASRA6C shows a considerably reduced stored magnetic energy, W = 117 GJ, as compared to a value of 193 GJ of the larger system.

Analyzing the distributions of the force densities, with local maxima of around 160 MN/m^3 in both cases, and applying the same support scheme and the same orthotropic material data as in the previously published case of ASRA6B, slightly lower values are obtained in ASRA6C, with a maximum of the equivalent (von Mises) stress of σ_{vM} = 170 MPa, associated with a shear stress of σ_{ST} = 50 MPa. The tangential strain amounts to about 0.2 % for this case.

The similarity of these results can be understood by a comparison of the 'virial stress', the stored magnetic energy normalized by the total coil volume, $W_m / n V_c$. The virial stresses amount to 120 and 100 MPa for ASRA6B and ASRA6C, respectively, although the minimum radii of curvature are smaller in ASRA6C.

From the comparison of stresses we conclude that the coils seem to be feasible for both cases. The shear stresses require some attention in further iterations of the support system. These are directed towards replacing the lateral and radial support rings by a complete coil housing.

In a following step, a more detailed analysis is required, encompassing also the internal stresses by the manufacturing of the coils, and those induced during cooldown. Furthermore, more detailed stress computations are necessary which treat the coils in their details of construction, in the regions of maximum load or stress. Such local models would use the global results of the present or of improved calculations.

REFERENCES

[1] G. Grieger, E. Harmeyer, J. Kisslinger, F. Rau, H. Wobig,
Advanced Stellarator Reactor and Burner Studies,
this conference.

[2] B. Badger, L. A. El-Guelbaly, G. A. Emmert, G. L. Kulcinski,
E. M. Larsen, J. F. Santarius M. E. Sawan, J. E. Scharer,
I. N. Sviatoslavsky, W. F. Vogelsang, P. L. Walstrom,
L. J. Wittenberg,
Annual Report on Contributions to ASRA6C,
a Commercial Stellarator Fusion Reactor,
FPA–85–4 , Madison Wi (1985).

[3] E. Harmeyer, J. Kisslinger, F. Rau, H. Wobig,
A General Winding Law of Modular Stellarator Coils,
IPP Garching Report IPP 2/274 , (1985).

[4] E. Harmeyer, U. Brossmann, H. Gorenflo, J. Kisslinger,
S. Mukherjee, J. Raeder, F. Rau, H. Wobig.
On Modular Coil Systems of the Wendelstein VII-AS Type
with Reactor Dimensions, IPP Garching Report IPP 2/269 , (1983).

[5] E. Harmeyer, J. Kisslinger, F. Rau, H. Wobig,
On Modular Coils of a Stellarator Reactor.
Proc. 11^{th} Sympos. on Fusion Engineering.
Austin, Tx (USA) 1985, in press.

[6] E. Harmeyer, J. Kisslinger, F. Rau, H. Wobig,
On Modular Stellarator Coils of the W VII-AS Type
with Reactor Dimensions,
Proc. 13^{th} Sympos. on Fusion Technology.
Varese, Italy, 1984, Vol. 2, pp.1599-1605.

MAGNETIC FIELD STUDIES FOR ADVANCED STELLARATOR REACTORS

E. HARMEYER, F. HERRNEGGER,
J. KISSLINGER, F. RAU, H. WOBIG
Max-Planck-Institut für Plasmaphysik,
Euratom-IPP Association,
Garching,
Federal Republic of Germany

Abstract

The coil topology of modular non–planar coils of Advanced Stellarator Reactors (ASR) and Burner configurations (ASB) is derived from magnetic vacuum field studies, starting from the fields of the Garching Advanced Stellarator experiment Wendelstein VII–AS, which is characterized by a reduction of the secondary plasma currents as compared to those of a standard stellarator.

Both, numerical and analytic winding laws are used for the contours of the coils. There are 5 field periods. The number of coils is varied between 18 and 4 coils per field period. An optimum is seen at 6 coils per field period, compromising between magnetic field quality (reduction of secondary currents, magnetic well, plasma aspect ratio, field modulation) and requirements of accessibility and maintenance of such coils.

The rotational transform $\iota = 0.4 \ldots 0.6$ at the magnetic axis is determined mainly by the minor coil radius and by the specific coil contours, i.e. the shapes of coil cross section and of the toroidal excursions. The latter also influence the field quality, as does the radial position of the centers of the different coils. Rational ι–values are to be avoided because of the formation of magnetic islands. Both, the presence of such islands near the separatrix, as well as the behaviour of field lines started outside of this last closed surface, lead to the choice of pumped limiters for edge control of the presently considered ASR systems.

Magnetic field calculations at finite plasma pressure are done for the reference configuration ASRA6C up to an average value of $\beta_{eq} = 4.7\,\%$ for the equilibrium–β, yielding a relative shift of the magnetic axis up to about 50 % of the radial distance to the edge, at a considerable deepening of the magnetic well.

1. INTRODUCTION

The distinguishing feature of an Advanced Stellarator is a reduction of the secondary currents, in comparison to those of a standard stellarator, by observing several side conditions. This is detailed in [1] , where the references describing the optimization principle are given. Modular non–planar coils are essential to produce such optimized fields with improved confinement properties.

In Chapter 2 of the present paper the coil geometry for Advanced Stellarator Reactor or Burner systems is discussed, the latter being smaller in size but encompassing a larger induction. Examples of the dependence of field properties on data of the non–planar coils are given. Two reference cases using an analytic winding law for the coils are introduced in Chapter 3. Effects of perturbation fields are briefly mentioned. Chapter 4 summarizes the results of computations of the finite–beta fields for one of these reference configurations, called ASRA6C. In Chapter 5, a short summary lists the main conclusions regarding coil topologies and magnetic fields of Advanced Stellarator Reactors, as studied so far.

2. VACUUM FIELDS OF ADVANCED STELLARATOR REACTOR AND BURNER CONFIGURATIONS

Starting from the magnetic field topology of the Garching Advanced Stellarator experiment Wendelstein VII–AS and enlarging the dimensions and fields to values of a fusion reactor or a burner experiment, several coil sets are derived with average major radii $R_0 \approx 25.5\,m$ for the Advanced Stellarator Reactor (ASR), and about $15\,m$ for the Advanced Stellarator Burner experiment (ASB), respectively. In the present study, the number of coils of each of the 5 field periods (FP) is varied between 18 and 4, as can be seen in Fig. 1, showing the top view of the coil arrangements of three different ASR and of those of one ASB with 18, 9 or 6 coils/FP, drawn in the same scale. As is clearly visible in the figure, the major radii of the coil positions vary in the toroidal direction with fivefold periodicity. The spatial curves describing the coil centers are obtained numerically, using procedures as were developed for the design of the coils for Wendelstein VII–AS, see [2]. The average value of the induction along the magnetic axis is set to $B_0 = 5.3\,T$ for ASR, and to a larger value of $7\,T$ for ASB. In the two systems with 10 coils per FP, the current densities and coil cross sections are matched to keep the maximum value of the magnetic induction at values $B_m < 9\,T$ at the coil surface, such as to stay within the limits of $NbTi$ as superconducting material operating at the temperature of liquid helium.

The case ASR254E with 4 coils/FP offers distinct advantages for assembly and maintenace, but shows a large value for the peak induction of $10.1\,T$ at the coils, in contrast to $8.8\,T$ for ASR2510, as detailed in [3],

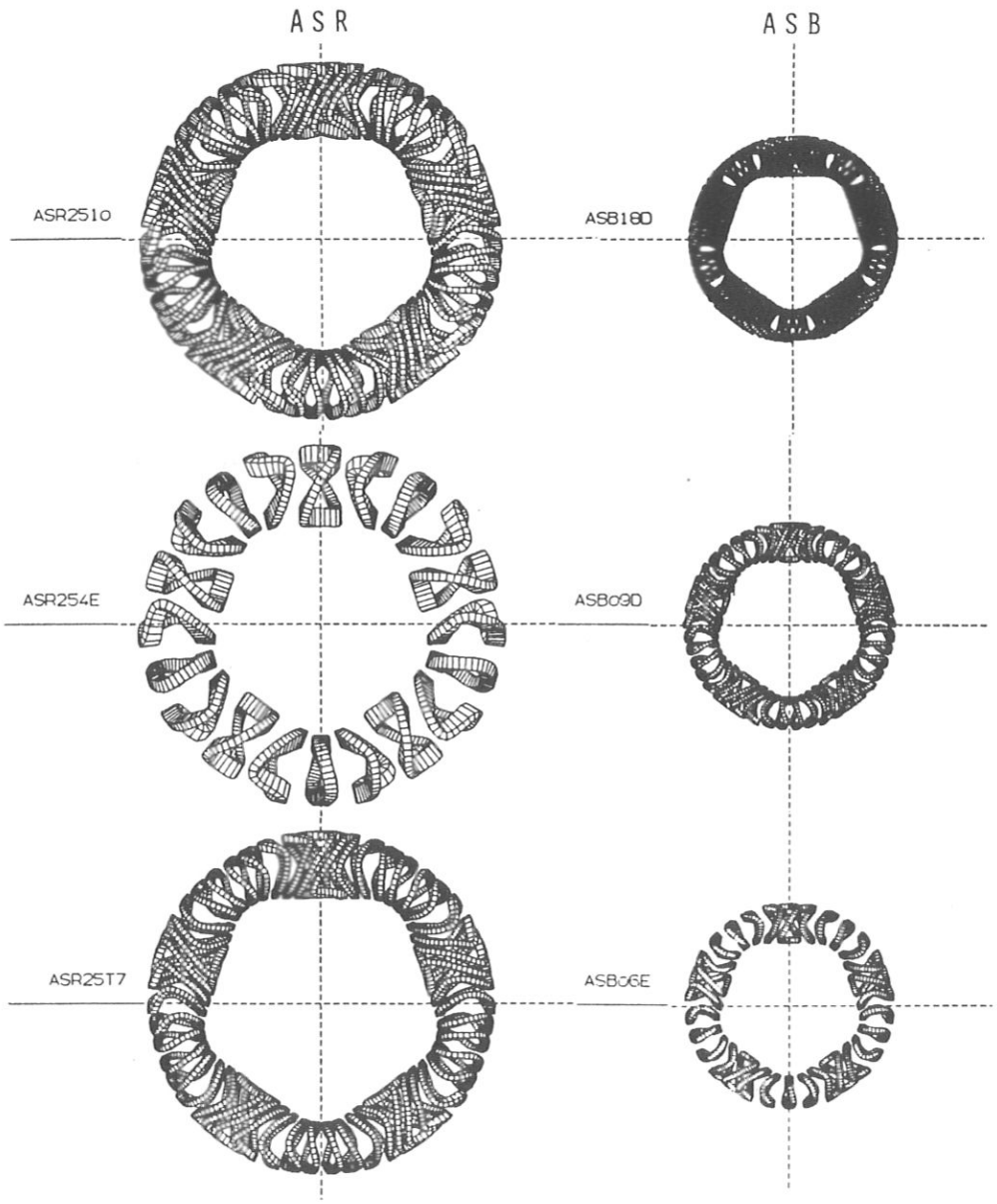

Fig. 1. Coil configurations of Advanced Stellarator Reactor or Burner systems with different numbers of coils per field period, shown in same scale.

although the effective current density is larger in the latter case. Furthermore, the modulation of the induction (magnetic field ripple) between the axis and the last closed surface is considerably increased in ASR254E , see Fig. 2. In the trace of the magnetic induction along the axis (top), a periodicity with each of the $m = 5$ field periods is visible. An increased

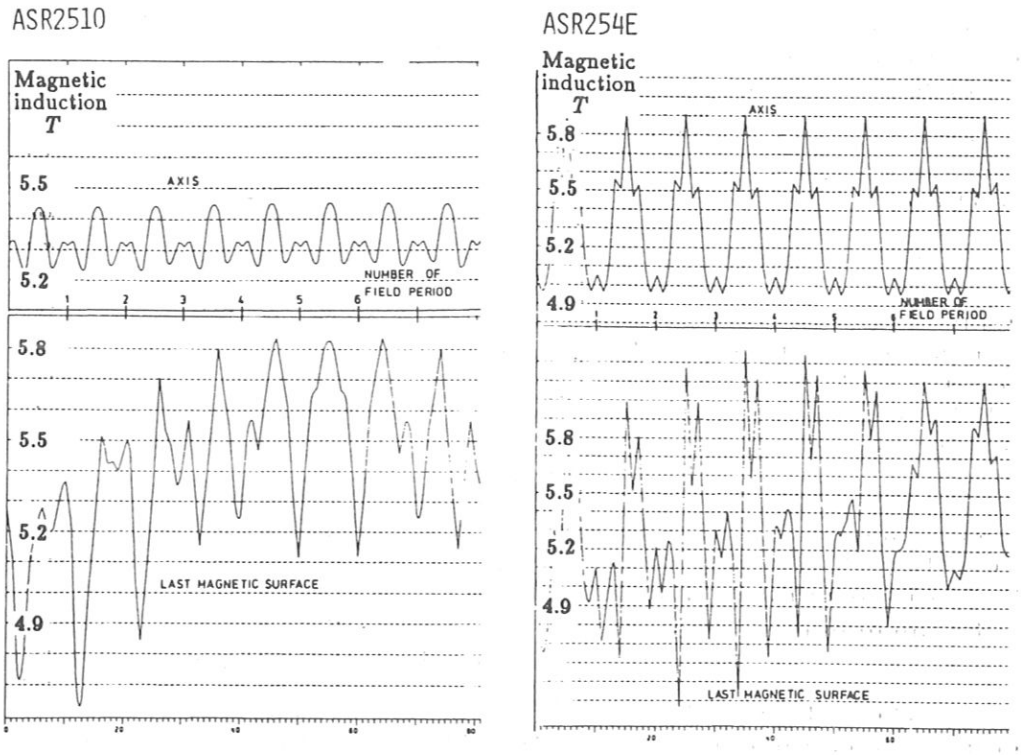

Fig. 2. Magnetic induction along the axis (top)
and for the last closed surface of the vacuum field (bottom)
showing an increased field ripple for ASR254E
with 4 coils per FP (right part),
in comparison to ASR2510 (10 coils / FP)
The curves extend over 8 field periods .

value of this helical ripple is responsible for larger neoclassical energy and particle losses, see [4]. Therefore this data set is rejected.

As shown in the lower left of Fig. 1, a coil configuration ASR25T7 is derived, which produces the same average value of the induction along the magnetic axis, $B_o = 5.3\,T$, using smaller coils at increased current density. Simultaneously, the rotational transform ι is raised to a value of about 0.6, in order to achieve a larger value of the equilibrium–beta. In a standard or 'classical' stellarator, this quantity roughly scales as $\beta_{eq} \approx \iota^2 / A$, where the aspect ratio $A = R_o/r_p$, and $r_p \approx 1.6\,m$ is the plasma radius. Note that for an Advanced Stellarator a larger value of the equilibrium–β applies, due to the reduction of the secondary currents, and the smaller vertical fields which then introduce a smaller Shafranov–shift of the configuration.

The configuration ASR25T7 has about the same value of the magnetic field ripple $\delta B/B = (B_{max} - B_{min}) / (B_{max} + B_{min})$ as the data set ASR2510.

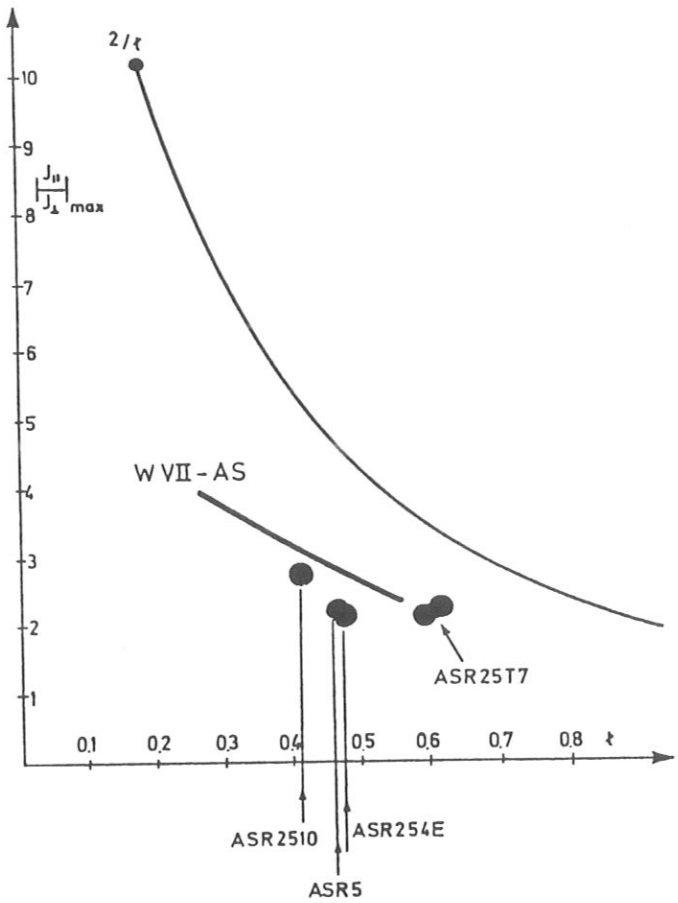

Fig. 3. Dependence of $|j_{||}/j_{\perp}|$ versus the rotational transform ι for several Advanced Stellarator Reactor configurations, in comparison to data for WVII-AS and standard stellarators, the latter being described by the upper curve labelled $2/\iota$.

The quality of these reactor data sets as Advanced Stellarators is demonstrated in Fig. 3, showing the maximum absolute values of $j_{||}/j_{\perp}$ versus the rotational transform ι, where $j_{||}$ and $j_{\perp}$ are the parallel and diamagnetic current densities, respectively. The dots characterize the ASR data sets with values close to those computed for the Garching Advanced Stellarator experiment Wendelstein VII-AS; the upper curve labelled by $2/\iota$ characterizes the behaviour of a standard stellarator. The secondary currents $j_{||}$ are reduced by a factor of about 2 in WVII-AS and in these ASR, compared to those of a standard stellarator.

The coil configurations for ASB (right part of Fig. 1) are derived from the data set ASR25T7 by a reduction of the major radius to a value of $15\,m$, and by doubling the coil current density to $j_{eff} = 18\,MA/m^2$,

TABLE I. Characteristic data of ASR25T7 and of three ASB data sets

System			ASR25T7	ASB18D	ASB09D	ASB06E
Aver. major radius	R_o	$[m]$	25.5	15.2	15.2	15.2
Aver. coil radius	r_c	$[m]$	5.24	3.24	3.24	3.24
Coil number/FP			10	18	9	6
Conductor			NbTi	Nb_3Sn	Nb_3Sn	Nb_3Sn
Effect. current density	j_{eff}	$[MA/m^2]$	9.8	18	18	18
Max. induction at coil	B_m	$[T]$	8.7	10.3	11.0	12.6
Induction on axis	B_o	$[T]$	5.3	7.0	7.0	7.0
Rotat. transf. axis	ι_o		0.58	0.51	0.50	0.53
Rotat. transf. edge	ι_r		0.61	0.52	0.51	0.51
Magn. well depth	V''	%	-0.1	0.1	-0.08	-0.04
Aver. plasma radius	r_p	$[m]$	1.75	0.9	0.9	0.9
Distance to coils	Δ	$[m]$	> 1.8	1.2	1.2	1.2

where this number is the effective value averaged over the whole conducting cross section, i.e. including superconductor, stabilizer, internal structure as well as insulation and helium channels. The induction at the axis is increased to $B_o = 7\,T$ in order to achieve ignition at the comparatively small plasma radius, $r_p = 0.9\,m$, see [4]. Associated with the increased axis induction, a large value of the induction B_m at the coil surface results, calling for Nb_3Sn as superconductor.

The number of coils per field period is changed from 18 to 9 and 6 in the ASB configurations, in order to see the effect on the peak induction at the coils, as well as the influence on the field quality between the magnetic axis and the plasma radius. Some quantitative information is given in Table I, comparing the data sets ASR25T7 with the three ASB cases at 18, 9 and 6 coils per FP. In the three ASB cases the peak values of the induction at the coils increases at a lower coil number, keeping the axis values of the magnetic induction and of the current density unchanged. This is caused by the increased coil size at a low coil number.

Comparing the axis and edge values of the rotational transform, ι_o and ι_a, a negative shear is introduced in the data set with 6 coils per FP, and the depth of the magnetic well is about half the value of the cases with 9 or 18 coils per FP.

The general properties of an Advanced Stellarator are maintained,however. Therefore, data sets with 6 coils per field period are developed to reactor dimensions, since this number of coils / FP is considered as a reasonable compromise between field quality and prospects for assembly and maintenance, as will be described in [5].

The coil shapes for these ASR and ASB data sets vary along the field period. This is visible in Fig. 4, showing the contours of the adjacent coils at toroidal positions of the beginning and 1/2 of the field period, together with the system of nested magnetic surfaces of the vaccum field. Outside of the drawn magnetic surface, a number of 10 dots is visible.

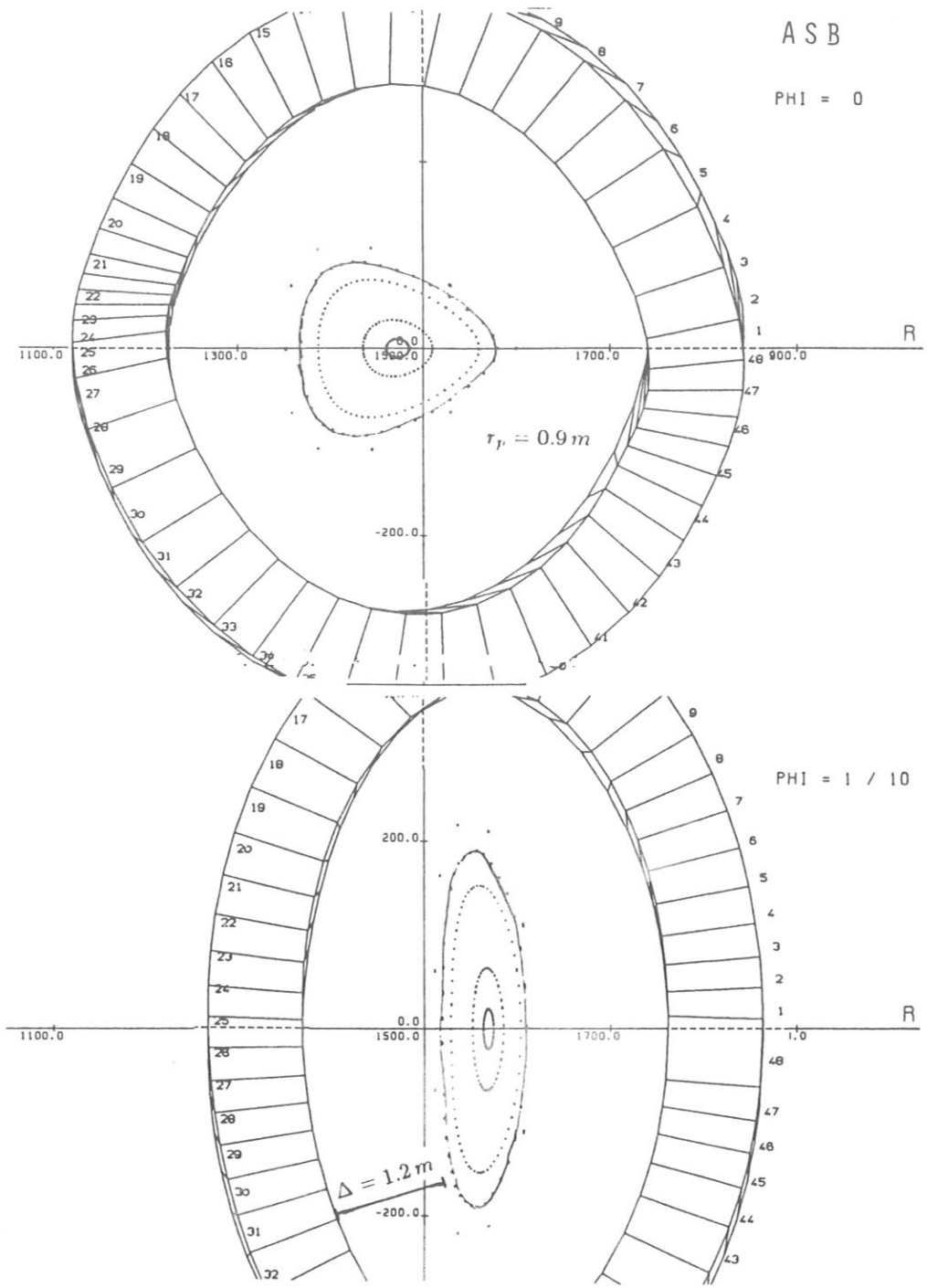

Fig. 4. Coil shape and nested system of magnetic vacuum field for the Advanced Stellarator Burner ASB06E, for toroidal angles 0 and at 1/2 of the field period.

TABLE II. Characteristic data of WVII-AS and ASR25T7, compared to those of the reference data sets ASRA6B and ASRA6C

System			WVII-AS	ASR25T7	ASRA6B	ASRA6C
Aver. major radius	R_o	$[m]$	2.0	25.5	25.0	20.0
Aver. coil radius	r_c	$[m]$	0.48	5.24	5.22	4.57
Conductor			Cu	NbTi	Nb_3Sn	Nb_3Sn
Coils / FP			8+1	10	6	6
Coil current	I_c	$[MA]$	0.6/1.5	13.7	22.5	18
Effect. current density	j_{eff}	$[MA/m^2]$	27	9.8	15	15
Max. induction at coil	B_m	$[T]$	5.2	8.7	11.0	10.4
Stored mag. energy	W_m	$[GJ]$	0.04	170	193	117
Induction on axis	B_o	$[T]$	3.0	5.3	5.3	5.3
Rotat. transform	ι_o		0.39	0.58	0.39	0.47
Aver. plasma radius	r_p	$[m]$	0.2	1.75	1.6	1.6
Distance to coils	Δ	$[m]$		> 1.8	2.1	1.2

Here, the value of the rotational transform $\iota = 5/10 = 1/2$ is a low-valued rational number. As described in detail in [6], such low-valued rational ι-values should be avoided. This can be easily realized in vacuum fields with small shear.

Due to the non-planar shape of the coils there exists a complicated spatial distribution of the magnetic forces. Integrating the magnetic forces over one field period yields the usual net radial force which characterizes a toroidal arrangement of planar coils. Further details of the magnetic forces and their dependence on the large number of parameters describing the coils are given in [7], concerning the presently investigated data sets, labelled ASRA6B and ASRA6C.

3. REFERENCE SYSTEMS ASRA6B AND ASRA6C

Using a flexible system of desribing the spatial curves of the coil centerlines with an analytic "winding law", applicable for arbitrary position and orientation of the modular coils as detailed in [8], the two reference cases ASRA6B and ASRA6C are derived. The abbreviations of these data sets stand for Advanced Stellarator Reactors with coils described by an Analytic winding law and 6 coils per field period, version B and C. The label C indicates a more compact version than the preceding data set ASRA6B. This is made possible by introducing a modern design for blanket and shield, see [5], by reducing the decisive distance Δ between the first wall of the system and the inner contour of the coil winding, from the previous value of about 2 m to 1.2 m. In consequence, the major radii can be changed from $R_o = 25\,m$ in ASRA6B to a value of $20\,m$ in ASRA6C, keeping other parameters unchanged. Other data of this system are entered in Table II, in comparison to those of ASRA6B, as

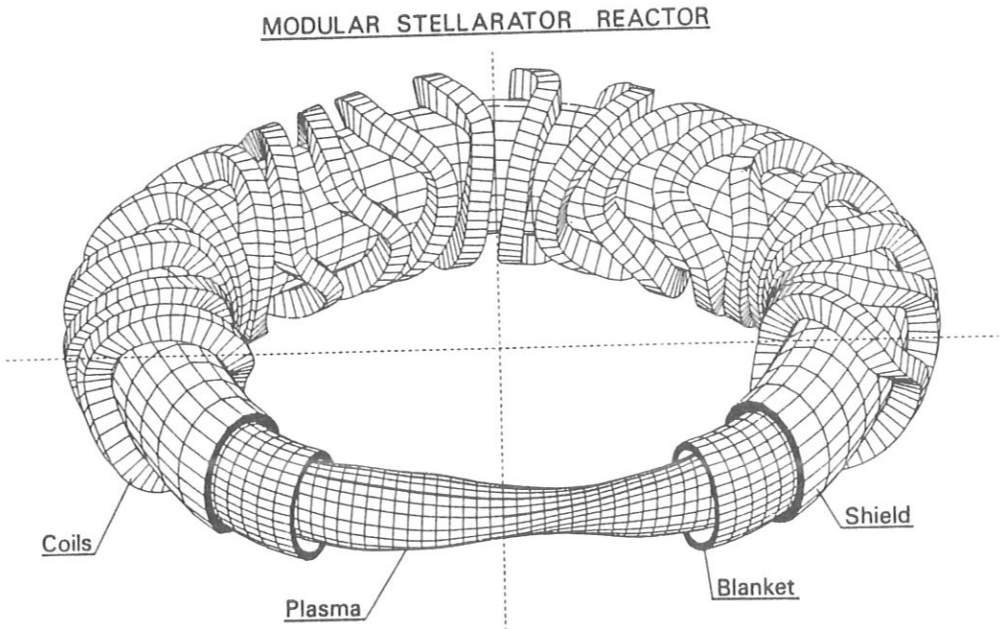

Fig. 5. Schematic view of the contours of plasma, blanket and shield, along with the system of the modular non–planar coils
6 coils in each of the m=5 field periods
provide an axis induction of $B_o = 5.3\,T$.

well as to data of the previous configuration ASR25T7 and of the Garching Advanced Stellarator experiment Wendelstein VII–AS. Note the remarkable decrease in the magnetic energy when reducing the size of ASRA6B to that of the compact system ASRA6C.

The coil geometry of ASRA6 is schematically shown in Fig. 5. A perspective view is given on the non–planar modular coils for three of the 5 field periods, along with nested toroidal volumes representing the shield and the blanket, as well as the last closed magnetic surface of this particular coil system. There are 6 coils per FP and three different coil shapes are present in the complete coil system, if one considers the two-fold mirror symmetry. All coil apertures are of the same elliptic cross section, centered at major radii according to $R(\varphi) = R_o\,(1 - k\,cos(5\varphi)\,)$, where $k = 1.6\,\%$ for both cases, and φ is the toroidal angle.

For the beginning and at $1/2$ of the field period, Fig. 6 shows the contours of the coils, together with the nested system of the magnetic surfaces of the vacuum field. The varying contours for the magnetic surfaces and the radially oscillating axis position are a geometric characteristic of an Advanced Stellarator. Outside of the last closed magnetic surface, the separatrix, an "ergodic" region is seen, with 11 small magnetic islands at a rational value of the rotational transform, $\iota = 5/11$. Inside of the separatrix, no low–numbered rational ι–values are present. The modulation of the induction along a field line is demonstrated in Fig. 7 for the magnetic axis and the last closed surface of ASRA6C.

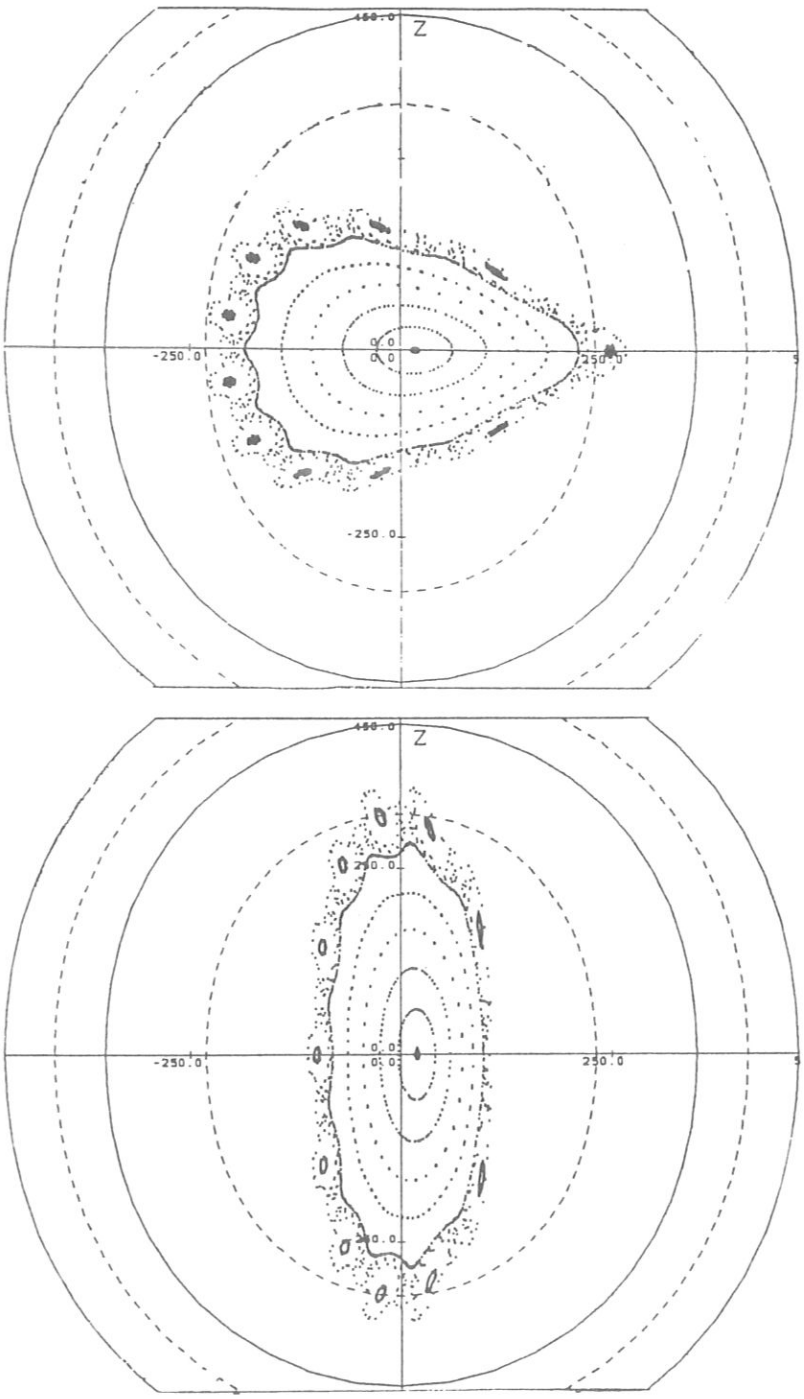

Fig. 6. Coil shape and nested system of magnetic vacuum field
Advanced Stellarator Reactor ASRA6C,
for toroidal angles 0 and at 1/2 of the field period
outside of last closed flux surface an "ergodic" region
is present with magnetic islands at $\iota = 5/11$
inner dashed line at distance $\Delta = 1.2\,m$ from coil bore.

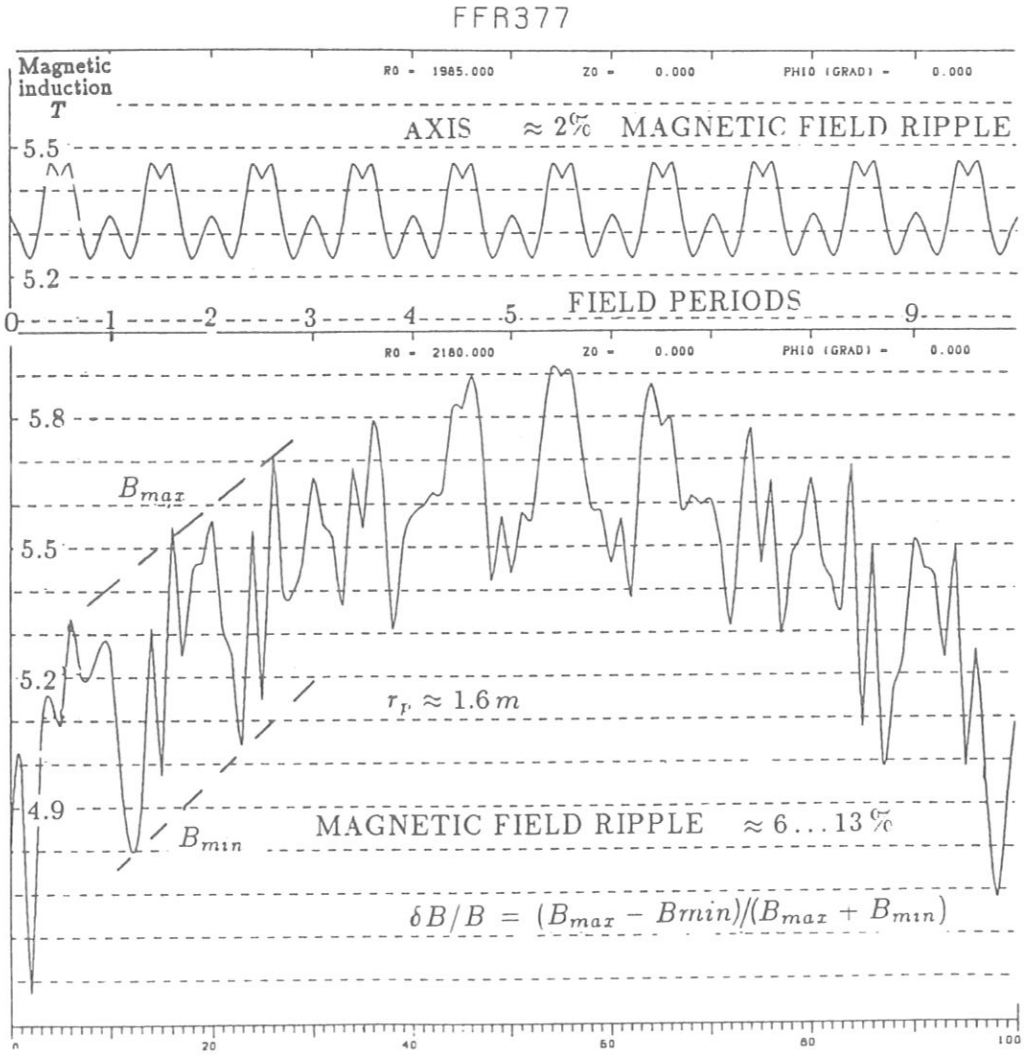

Fig. 7. Magnetic induction along the axis (top)
and for the last closed surface of the vacuum field (bottom)
for ASRA6C, with 6 coils per field period,
showing a magnetic ripple of 2 % near the axis,
which increases to 6 ... 13 % for the last closed surface.

It is easy to adjust the rotational transform to irrational values by a proper choice of the minor coil radii, see top part of Fig. 8, once the shape of the center line of the modular coils is fixed. The amount of toroidal excursion also changes the value of ι, and the higher harmonics present in the winding law of the coil centers influence the degree of reduction of the secondary currents. The amplitudes of these higher harmonics differ for the three coil shapes present in the ASRA6C data sets. As to be seen in the lower half of Fig. 8, the effective radius of the

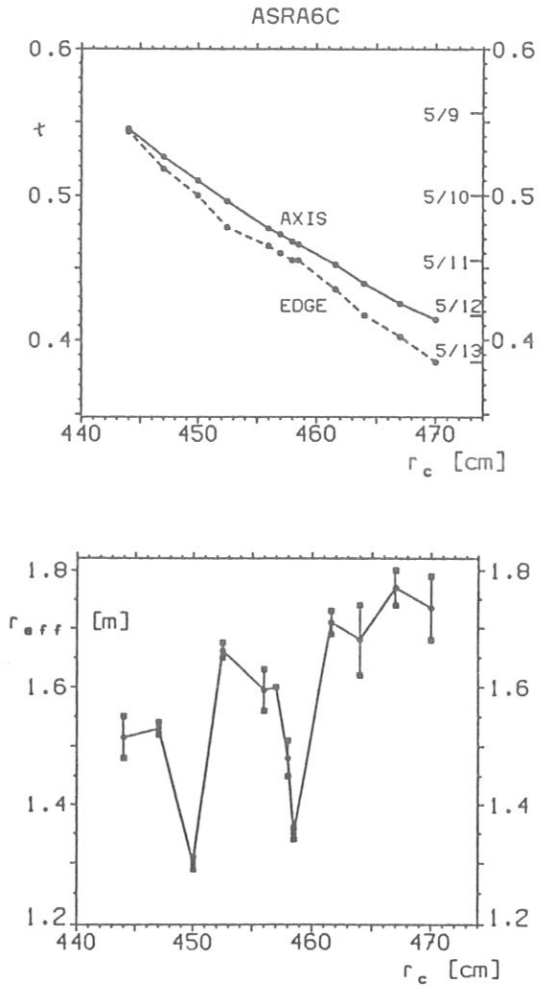

Fig. 8 . Dependence of rotational transform ι on the coil radius for the data set ASRA6C, (top)
and effective radius of the last closed surface .

last closed magnetic surface is smaller at rational ι. This is caused by N "natural" magnetic islands which are found at rational $\iota = m/N$ in such Advanced Stellarators inside and near the separatrix, see also [2] and [6]. In these references, more information on these islands is given, and their sensitivity to external perturbation fields is studied. ASRA6C allows a comparatively large value of such a perturbation, $B_y/B_o = 0.2\,\%$, see Fig. 9. The system of outer islands vanishes and the average radius of the last closed surfaces is reduced by a relatively small amount of about 10 %.

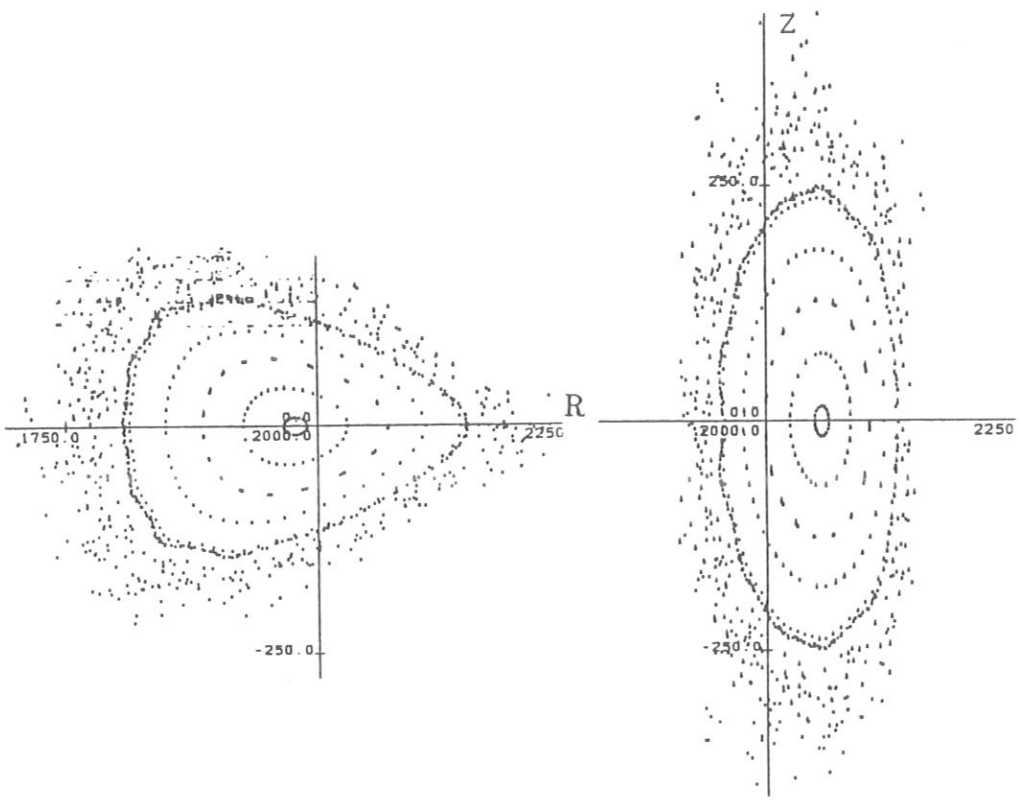

Fig. 9 . ASRA6C with superimposed horizontal perturbation field $B_y/B_o = 0.2\,\%$.

4. FINITE BETA FIELDS IN ASRA6C

Magnetic field computations for a finite value of the plasma pressure are done so far for one of the reference configurations, ASRA6C, up to values of the plasma pressure normalized by the magnetic field energy density, $\beta \approx 5\,\%$. The shapes of the magnetic surfaces of the vacuum field and at $\beta = 4.7\,\%$ are shown in Fig. 10 at the toroidal positions of 0, 1/4 and 1/2 of a field period. The drawn curve of the vacuum field contours is used as a fixed boundary for the computations. At finite β–values, the inner surfaces and especially the magnetic axis are radially shifted. This axis shift (Shafranov–shift) amounts to about 50 % of the average minor radius. Such a value of the axis shift is regarded as determining the upper limit for the equilibrium–β. A parabolic pressure profile is used in the computations presented here.

In addition to the radial Shafranov–shift, a slight helical offset of the magnetic axis is also visible. The magnitude of the axis shift is obtained by varying the number of grid points used in the code and extrapolating

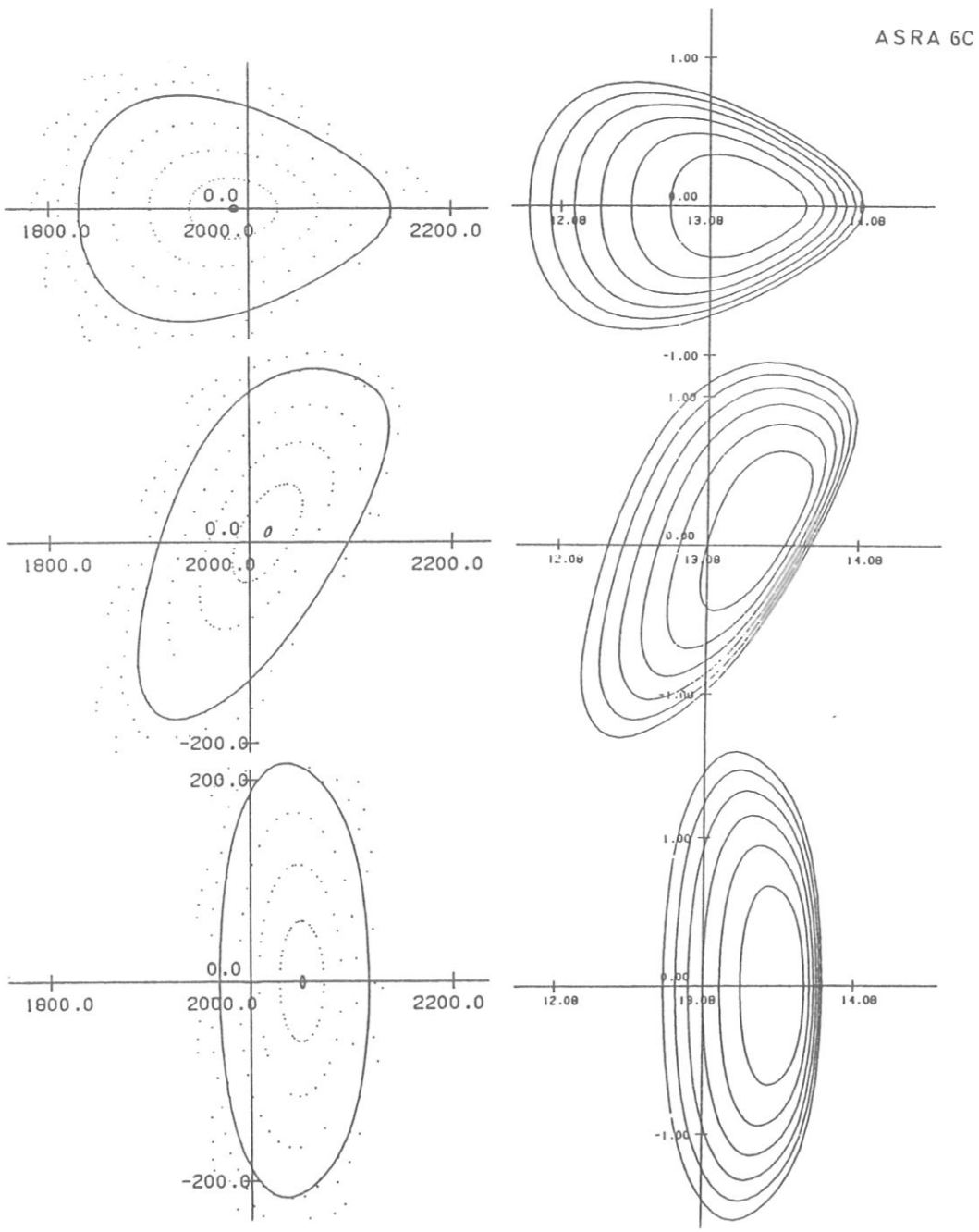

Fig. 10. Magnetic surfaces of ASRA6C
Initial vacuum field (left) with fixed boundary close to separatrix
right half: final configuration at $\beta_{eq} \approx 5\,\%$, showing a value
of about 50 % for the Shafranov shift.

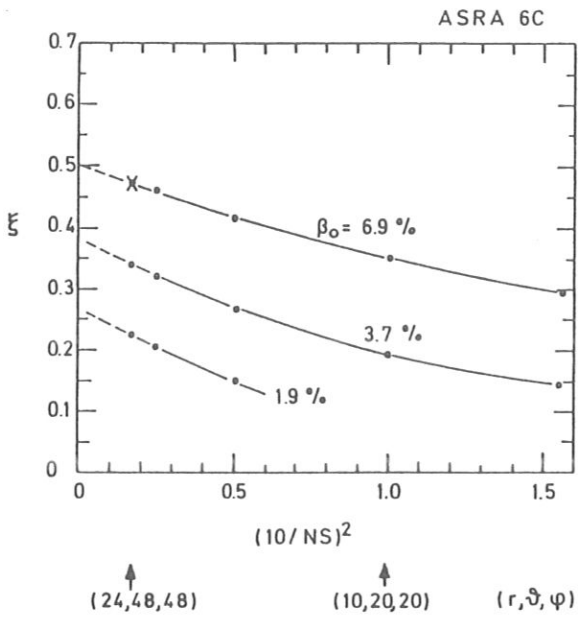

Fig. 11. Dependence of the axis shift on the grid size for different peak values of β_o = 1.9, 3.7, and 6.9 %. The point marked by 'x' corresponds to the result of the previous figure.

to zero mesh size, see Fig. 11. Here, three curves are shown for different peak values of β_o = 1.9, 3.7, and 6.9 %; the point marked by 'x' corresponds to the result of the previous figure.

The upper part of Fig. 12 shows the dependence of this radial shift versus the peak value of β_o. Simultaneously, a considerable deepening of the magnetic well is obtained, see lower part of the figure. The dashed curves give the result of a net current free computation, whereas the drawn curves apply for a flux conserving case, yielding nearly the same results. A certain difference is seen in the radial profile of the rotational transform, $\iota(r)$, as demonstrated in Fig. 13. In the flux conserving case, the initial profile of the rotational transform of the vacuum field with low shear is maintained, whereas the net current free computations show a decrease of the rotational transform in the region of the plasma edge.

5. SUMMARY AND CONCLUSIONS

Magnetic field studies for Advanced Stellarator Reactors and Burner systems are done, using numerical and analytic relations for the positions and contours of the non-planar coils. Starting from topologies similar to

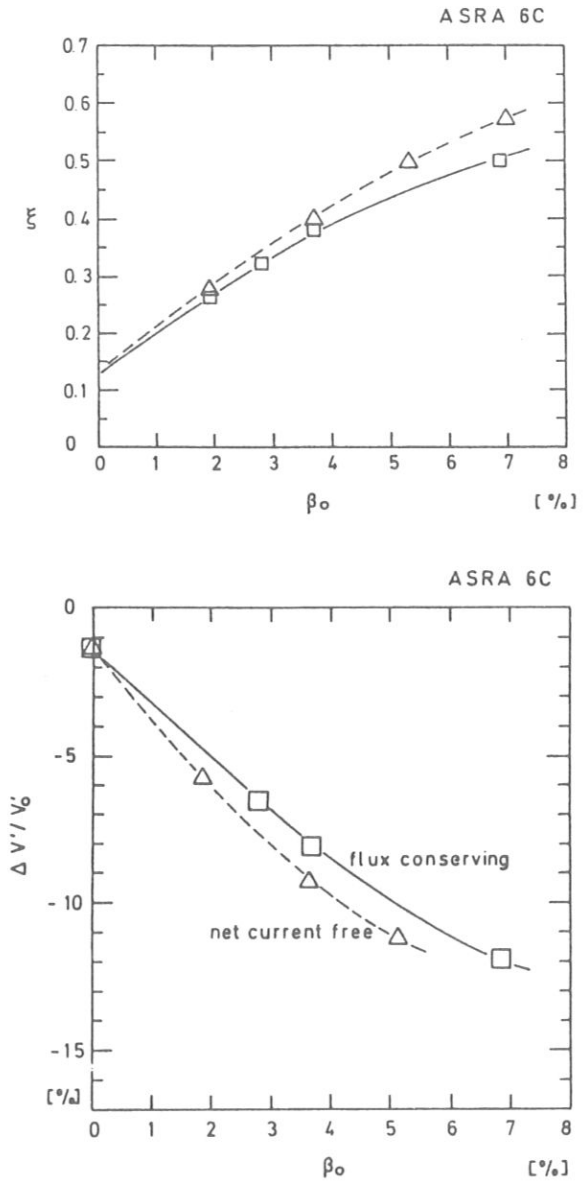

Fig. 12. Dependence of the radial axis shift (upper part) on β_o and considerable deepening of the magnetic well (lower part). Dashed curve: result of a net current free computation, the drawn curve is a flux conserving case with nearly identical results.

those of the Garching Advanced Stellarator experiment Wendelstein VII-AS, considerable progress is made in the two reference data sets ASRA6B and ASRA6C regarding the simplicity of the coil system.

The compact system ASRA6C is obtained by reducing the size of ASRA6B from a value of the major radius from $R_o = 25\,m$ to $20\,m$. This

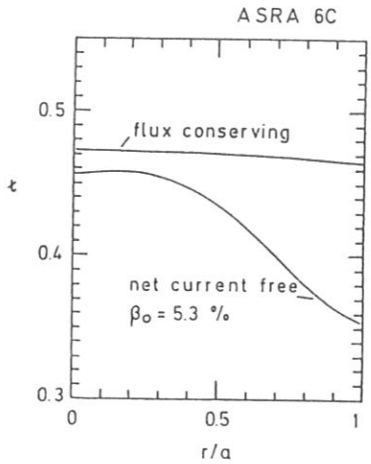

Fig. 13. Radial profile of the rotational transform ι
flux conserving and current free computations,
a is the average minor radius of the fixed boundary.

is correlated with a change of the magnetic energy from $W_m = 193\,GJ$ to a value of $117\,GJ$. Using smaller coils at the same average current density, the peak field at the coils and the average induction at the magnetic axis are kept constant. Also the minor plasma radius remains unchanged. This reduction of system size is made possible by use of a modern approach of a thin blanket with appropriate reflector and shield.

Magnetic field computations at finite plasma pressure are done for ASRA6C up to an average $\beta \approx 5\,\%$, yielding a considerable deepening of the magnetic well and a still tolerable shift of the magnetic surfaces.

REFERENCES

[1] G. Grieger, E. Harmeyer, J. Kisslinger, F. Rau, H. Wobig,
Advanced Stellarator Reactor and Burner Studies,
this conference.

[2] U. Brossmann, W. Dommaschk, F. Herrnegger, G. Grieger,
J. Kisslinger, W. Lotz, J. Nührenberg, F. Rau, H. Renner,
H. Ringler, J. Sapper, A. Schlüter, H. Wobig,
Concept of an Advanced Stellarator,
Proc. Plasma Phys. and Contr. Nucl. Fusion Research
Baltimore 1982, Vol. III, 141, (1983).

[3] E. Harmeyer, U. Brossmann, H. Gorenflo, J. Kisslinger,
S. Mukherjee, J. Raeder, F. Rau, H. Wobig,
On Modular Coil Systems of the Wendelstein VII-AS Type
with Reactor Dimensions, IPP Garching Report IPP 2/269 , (1983).

[4] E. Harmeyer, J. Kisslinger, F. Rau, H. Wobig,
Heating and Burn Scenarios for ASR and ASB,
this conference.

[5] J. Hübener and W. Maurer,
General Design of a Modular Stellarator Reactor,
this conference.

[6] E. Harmeyer, J. Kisslinger, F. Rau, H. Wobig,
Magnetic Field Studies Near Separatrix,
13^{th} Eur. Conf. on Contr. Fusion and Plasma Heating
Schliersee, Germany 1986.

[7] E. Harmeyer, J. Kisslinger, F. Rau, H. Wobig,
Engineering Considerations of Modular Coils for ASRA6C,
an Advanced Stellarator Reactor,
this conference.

[8] E. Harmeyer, J. Kisslinger, F. Rau, H. Wobig,
A General Winding Law of Modular Stellarator Coils,
IPP Garching Report IPP 2/274 , (1985).

HEATING AND BURN SCENARIOS FOR ASR AND ASB

E. HARMEYER, J. KISSLINGER, F. RAU, H. WOBIG
Max-Planck-Institut für Plasmaphysik,
Euratom–IPP Association,
Garching,
Federal Republic of Germany

Abstract

Heating and Burn scenarios for Advanced Stellarator Reactors (ASR) and Burner configurations (ASB) are established as sequences of computed equilibria, using a one–dimensional code to calculate the coupled equations of particle and energy transport (heat conduction and bremsstrahlung) for electrons and ions in the presence of electric fields. The complicated structure of the magnetic fields in ASR and ASB is modelled by an effective ripple ranging from 2 to about 10 % between the magnetic axis and the edge.

For start–up, an effective heating power of 30 to 50 MW is sufficient. By increased refuelling, ASR is brought up to full power, preferentially at a moderate temperature $T = 12 \ldots 15\,keV$ at the plasma center. The fusion power amounts to typically $P_{th} \approx 4\,GW$ for ASR, whereas ASB stays at about 10 % of this value. For ASR6C, central radiation losses up to 300 MW can be tolerated if the fusion power output is increased by an increased refuelling rate. Particle input fluxes of Φ_o of 1.0 to $1.1 \times 10^{23}\,s^{-1}$ are required in the two cases without and with radiation, yielding values of the average β of 5.3 and 6.4 % at a thermal fusion power of 3.8 and 5.6 GW. In a different computation with a radiative power loss of 300 MW near the plasma edge and a refuelling rate of $1.1 \times 10^{23}\,s^{-1}$, a total fusion power of 3.9 GW is obtained at an average β of 5.0 %. The peak temperature is $T \approx 19\,keV$. In this case the ripple losses are reduced by a factor of two, in order to take account of the improved confinement of an Advanced Stellarator, and the field is raised to $5.5\,T$ at the axis.

1. INTRODUCTION

A survey of studies regarding Advanced Stellarator Reactor and Burner Systems, called ASR and ASB, respectively, is given in [1], where some results regarding heating and burn scenarios in such configurations are also mentioned. Stationary systems are assumed in the burn state. The start–up procedure is treated as a sequence of such stationary states, called equilibria, with a preset amount of external heating. The question of thermal stability of such equilibria remains to be studied in detail.

In Chapter 2 of this paper, the transport model and assumptions made in the one-dimensional code calculations are commented. In the third Chapter earlier findings on a comparison of an ASR with an ASB are summarized, as published in [2]. In Chapter 4, results are given as obtained for the presently considered reference data set, ASRA6C. Radiation losses in addition to bremsstrahlung are considered. The influence of the smaller major radius of ASRA6C, $R_o = 20\,m$, as compared to a previous value of $25\,m$ on the required start-up power and the operation regime is also commented. The paper ends with summary and conclusions in Chapter 5.

2. TRANSPORT MODEL AND BOUNDARY CONDITIONS

The computations of the start-up and of the burning conditions in ASR and ASB are done with the use of a one-dimensional transport code, details of which are described in [3]. The coupled equations of particle and energy transport are solved for neoclassical diffusion and heat conduction of electrons and ions. Corrections to account for the varying shape of the magnetic surfaces are neglected. The system of equations is

$$-\frac{1}{r}\frac{\partial}{\partial r} r\, n\, \chi_e \frac{\partial T_e}{\partial r} = Q_e(r) + Q_{e,\alpha} - P_{rad} - P_{ei} \tag{1}$$

$$-\frac{1}{r}\frac{\partial}{\partial r} r n \chi_i \frac{\partial T_i}{\partial r} = Q_i(r) + Q_{i,\alpha} + P_{ei} \tag{2}$$

$$-\frac{1}{r}\frac{\partial}{\partial r} r\, D \frac{\partial n}{\partial r} = Q_D(r) \tag{3}$$

In these equations χ_e and χ_i are the coefficients of thermal conductivity and D is the particle diffusion coefficient. In our model neoclassical transport coefficients as given by Shaing and Houlberg are used. To the neoclassical terms the anomalous electron thermal conductivity as found in ohmically heated plasmas in W VII-A is added, see [4].

The coefficients of thermal conductivity are given in Fig. 1 for ASRA6C at half radius. The abscissa is the inverse collisionality $\lambda\iota/R$, where λ is the mean free path between collisions, $\iota = 1/q$ is the rotational transform, with q being the safety factor of a Tokamak with comparable toroidal and poloidal fields and equal major radius R. Four curves at constant temperatures $T = 8, 10, 13,$ and $16\,keV$ are entered in each of the four parts of the figures, which apply for electrons (ions) in the left (right) part of the figure; the top half is without radial electric field, in the lower half a normalized field equal to the temperature gradient is assumed. The thermal conductivity increases with temperature at all

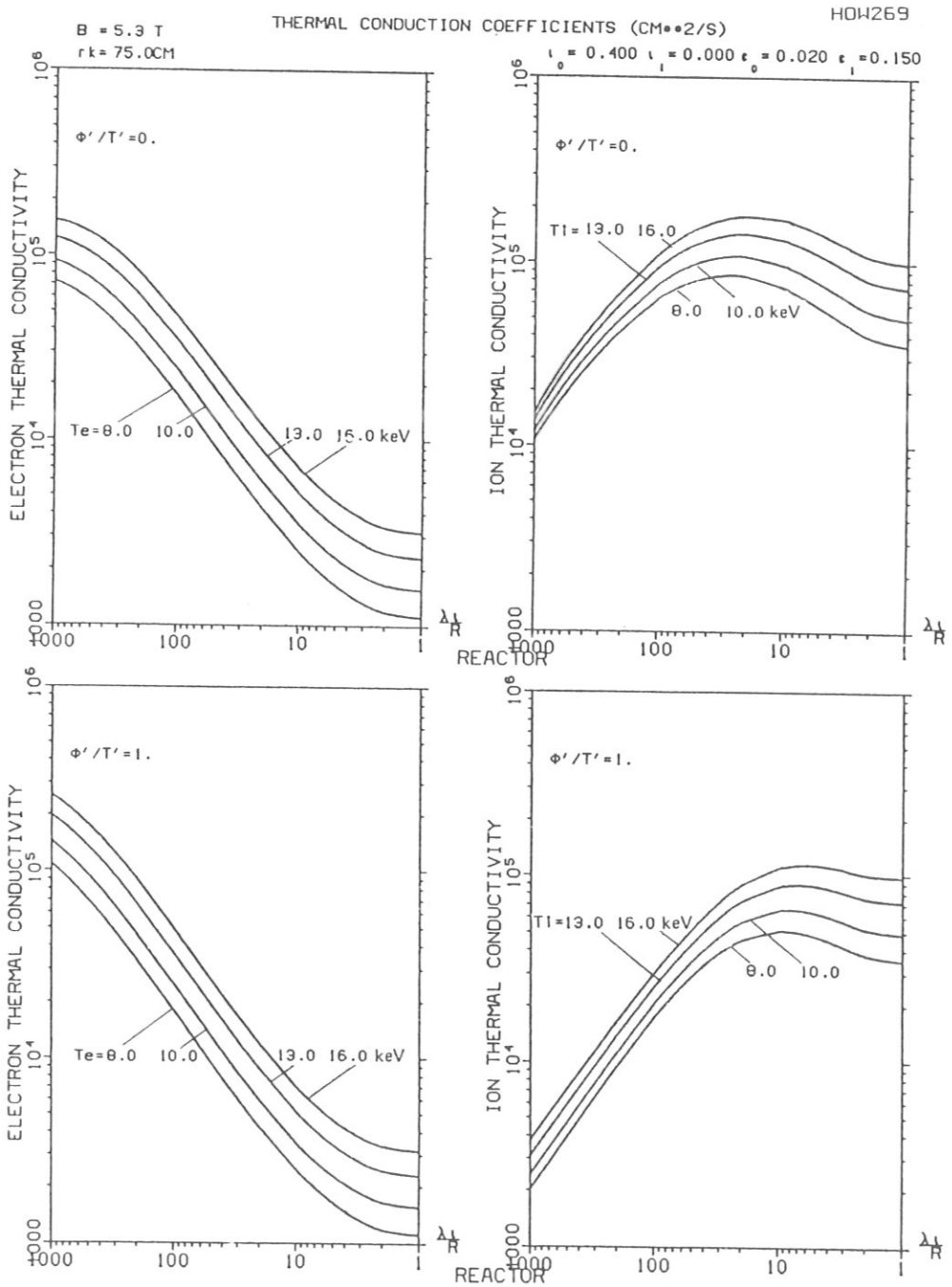

Fig. 1. Thermal conduction coefficients for ASRA6C calculated versus the inverse collisionality $\lambda t/R$ without and with radial electric field (top and bottom parts), for electrons and ions (left and right parts), respectively. For details see text.

collisionalities. For electrons there is a continuous increase in the thermal conduction coefficient with $\lambda t/R$, depending on the amplitude ϵ of the magnetic field modulation. This 'ripple' is about 2 % at the magnetic axis of ASRA6C, and rises to 6 ... 13 % near the plasma edge, see [5]. An edge ripple of $\epsilon_1 = 15\%$ is assumed in the above computation; thus the effect of the trapped particles is overestimated.

The thermal ion conduction coefficient at large values of $\lambda t/R$ decreases again, due to the depletion of the distribution function, since the loss rate of trapped ions is faster than the scattering in velocity space. A loss cone develops in addition to the drift term included in the analytical formula for the ion thermal conduction coefficient.

Note that the radial electric field plays a major role only for the ions in the reactor relevant regime of $\lambda t/R \approx 100 \ldots 1000$, and effectively reduces the conduction coefficient, typically by a factor of about 5. A larger radial field would yield a still larger reduction. So far, a self-consistent radial electric field, depending on the radial position, such as to locally balance the electron and ion particle loss rates is out of scope of our code.

The quantities Q_e, Q_i, and Q_D are external sources, the start-up power applied to electrons and ions, respectively, and the external refuelling rate. The latter also is required during stationary burn. These quantities are given in their radial profiles, peaked either at the center or near the edge. The α-particle heating power to electrons and ions, $Q_{e,\alpha}$ and $Q_{i,\alpha}$, respectively are obtained from the temperature-dependent reaction rate $< \sigma v >$ of the D-T process. In the transport equations, the quantity P_{ei} is the electron-ion Coulomb interaction, entering the electron and ion equations at opposite sign. The term P_{rad} in the electron equation consists of two parts: the first part, the bremsstrahlung, can be increased by an optional radiative loss simulating the effects of impurity radiation within the whole cross section or those of a radiative layer near the plasma edge. This is done by an appropriate radial profile of the additional radiation.

The transport code is operated iteratively, starting from an initial radial density profile. Other boundary conditions are fixed values of electron and ion temperature and density, $T_e(a)$, $T_i(a)$, and $n(a)$, respectively, at the edge radius a. Prompt α-particle losses are neglected. The refuelling rate and its radial profile are essential input data for the stationary burn state. The start-up computations are determined by the applied heating power, in addition to the refuelling.

3. HEATING AND BURN SCENARIOS FOR ASR AND ASB

Computations of the burning conditions for a typical Advanced Stellarator Reactor and an Advanced Stellarator Burner are given in [2]. The results of these considerations are summarized in the following.

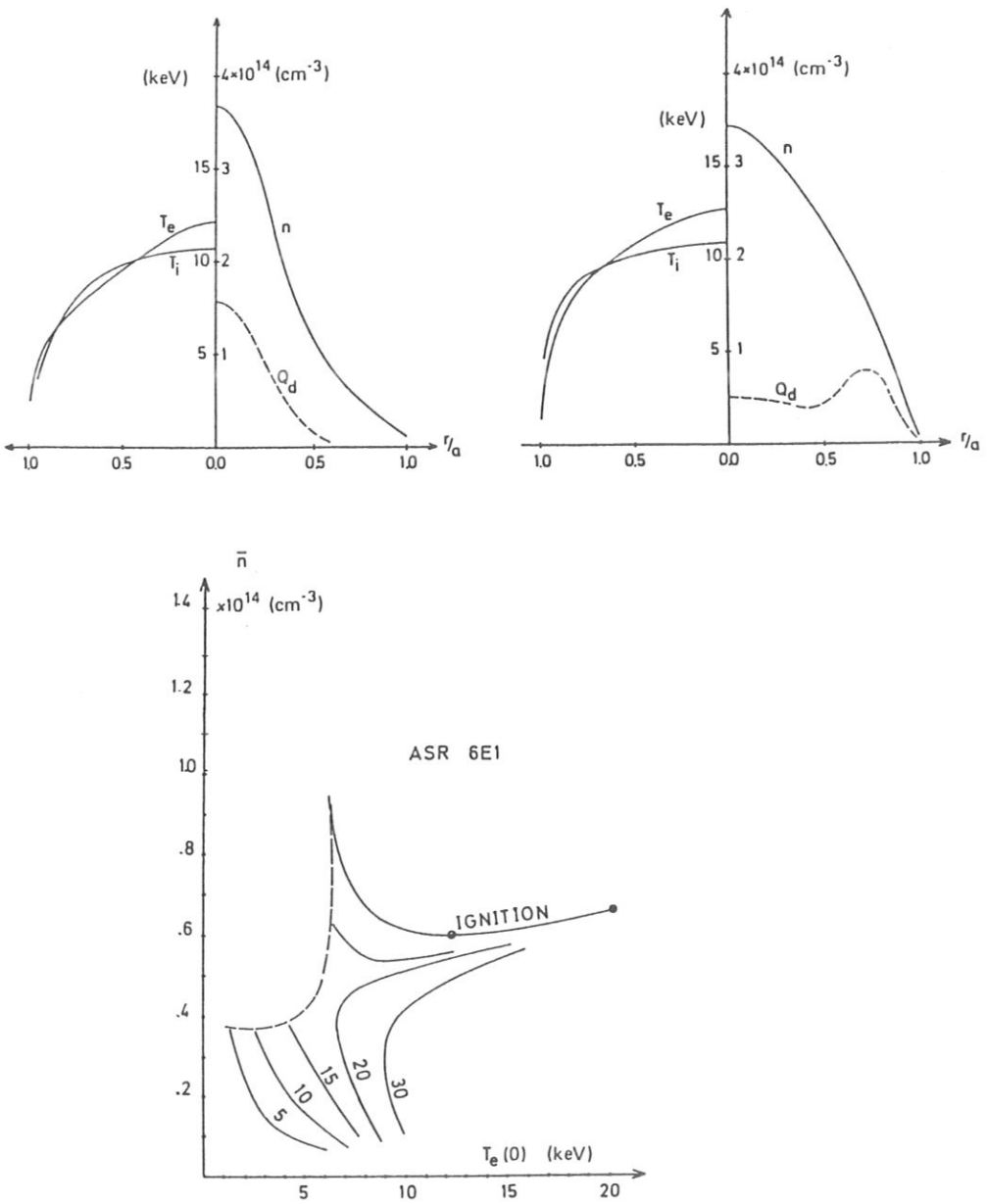

Fig. 2. Profiles of temperatures and density in ASR for different radial refuelling at ignition and burn states (upper left and right parts) and heat scenario (lower part)

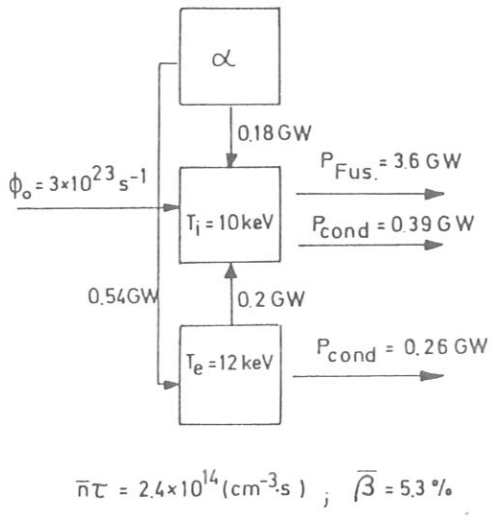

Fig. 3. Power flow diagram for ASR as given in [2].

The system sizes of ASR and of ASB are major radii of R_o = 25 and 15 m, with plasma radii of r_p = 1.6 and 0.9 m, at an average induction of B_o = 5.3 and 7.0 T, respectively.

Using the transport code as mentioned above, with a radial electric field and an effective helical ripple of 2 % amplitude at the axis and 7 % at the plasma edge, a net heating power of 30 MW is found for ASR as well as for ASB to reach ignition. This is shown in the lower part of Fig. 2 for ASR. At ignition, the fusion power amounts to P_{th} = 0.6 and 0.4 GW, in ASR and ASB, respectively, at values of the average β of about 2 and 2.5 %. At these comparatively low β-values the neutron load on the first wall is still moderate. In ASR then the ports for the start-up power can be closed and shielded for neutrons.

The reactor power is increased by raising the input flux of particles, e.g. of injected pellets. Two different scenarios are envisaged, a centered refuelling and a deposition profile which is peaked near the plasma edge.

In the top left part of Fig. 2, radial profiles are given of the electron and ion temperatures T_e and T_i, respectively, as well as of the density n and the refuelling rate. The refuelling is peaked at the plasma center. The curves pertain to the ignited state of ASR. Increasing the refuelling rate at a centered deposition profile raises the temperatures, and thus the fusion output to values above $P_{th} > 3\,GW$.

As demonstrated in the upper right part of Fig. 2, a refuelling profile peaked near the edge of ASR broadens the density profile and allows for a power production of P_{th} = 3.2 GW, at temperatures close to those of

the ignition state at centered refuelling. Increasing the refuelling rate to a value of $\Phi_o = 3 \times 10^{23}\, s^{-1}$, brings the system to full power of $3.6\, GW$, at average temperatures of $T_i = 10$ and $T_e = 12\, keV$ for the ions and electrons, respectively. The average β amounts to 5.3 %. The power flow diagram of this state is given in Fig. 3, at an average density of $1.4 \times 10^{20}\, m^{-3}$.

Thus, a change of the radial deposition of refuelling constitutes a viable option for increasing the power of the reactor after ignition without an essential temperature rise. This keeps the neoclassical heat conduction losses limited.

4. RESULTS FOR THE REFERENCE CASE ASRA6C

The smaller major radius, $R_o = 20\, m$ of the data set ASRA6C, as compared to a major radius of $25\, m$ in the earlier ASR configurations, introduces a more difficult situation regarding start-up and stationary burn of the reactor. In [1], under optimized conditions, heating and burn scenarios of ASRA6C are shortly mentioned, including also the effect of an additional radiative loss. These findings are elaborated in more detail in the following.

In Fig. 4, upper part, the relation between the fusion power output and the peak values of $\beta(0)$ are given for the reference case ASRA6C versus the axis values of density and temperature. The middle and lower parts of the figure show the dependence of these quantities on the external heating power P_i of start-up. In the middle part of the figure, the magnetic field is $B_o = 5.3\, T$, and the ripple losses are as given in [3] and [4], with a magnetic ripple amplitude up to about 10 %, as to be seen in [5]. Under these circumstances, ignition is possible at an effective heating power $P_i \approx 50\, MW$ with center densities of $N(0) \approx 3 \times 10^{14}\, cm^{-3}$, and temperatures of $T_i(0) \approx 10\, keV$, respectively. A full power operation point is found at an input flux $\Phi = 1 \times 10^{23}\, s^{-1}$, characterized by an average β of 5.3 % and a fusion power of $P_{th} = 3.8\, GW$ This data point is labelled '400' in the middle part of the figure. Introducing an additional radiative loss with a broad centered profile and amounting to $P_{rad} = 0.3\, GW$, the fusion power is to be increased to $P_{th} = 5.6\, GW$ at an average $\beta = 6.4$ %, by an increased input flux $\Phi = 1.1 \times 10^{23}\, s^{-1}$, as shown by the point marked '406'. Such radiation losses with a centered broad distribution should be avoided in order to keep the total power output within reasonable limits.

In the lower part of Fig. 4, the improved confinement properties of an Advanced Stellarator are modelled by a reduction of the ripple losses by a factor of 2. The magnetic field is also varied to values of 5.0 and 5.5 T, the larger field being indicated by the dashed curve. In these cases, an effective heating power of 30 MW is sufficient to reach ignition, as is the case with the larger systems at $R_o = 25\, m$. In ASRA6C with reduced

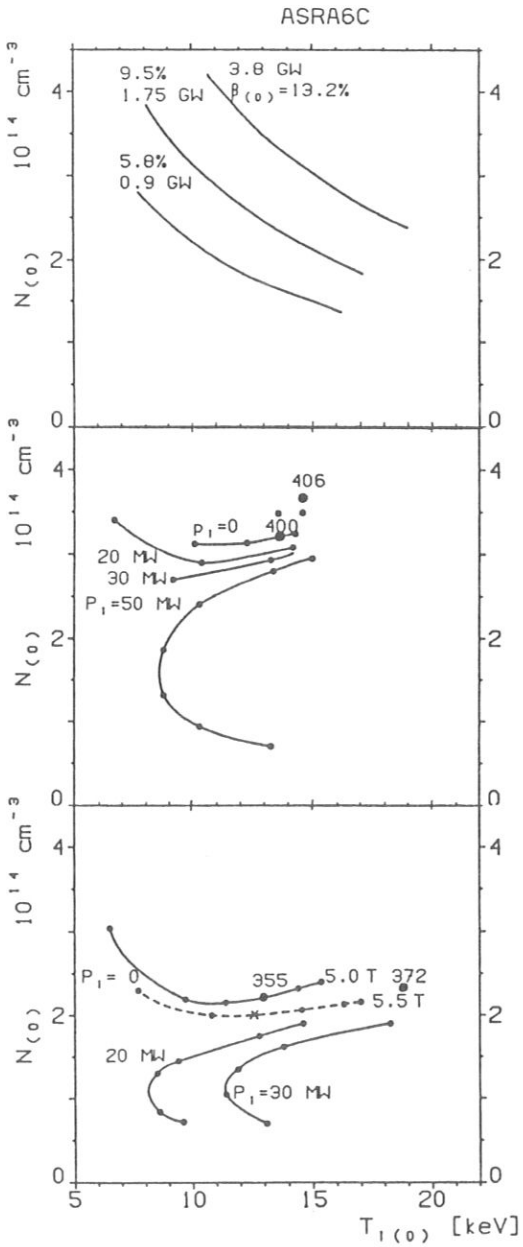

Fig. 4. Heating and burn scenarios for ASRA6C
top part: fusion power and center values $\beta(0)$
middle and lower parts: curves of constant external power P_1 at full and reduced value of the ripple heat conduction coefficient; several operation points indicated, for details see text.

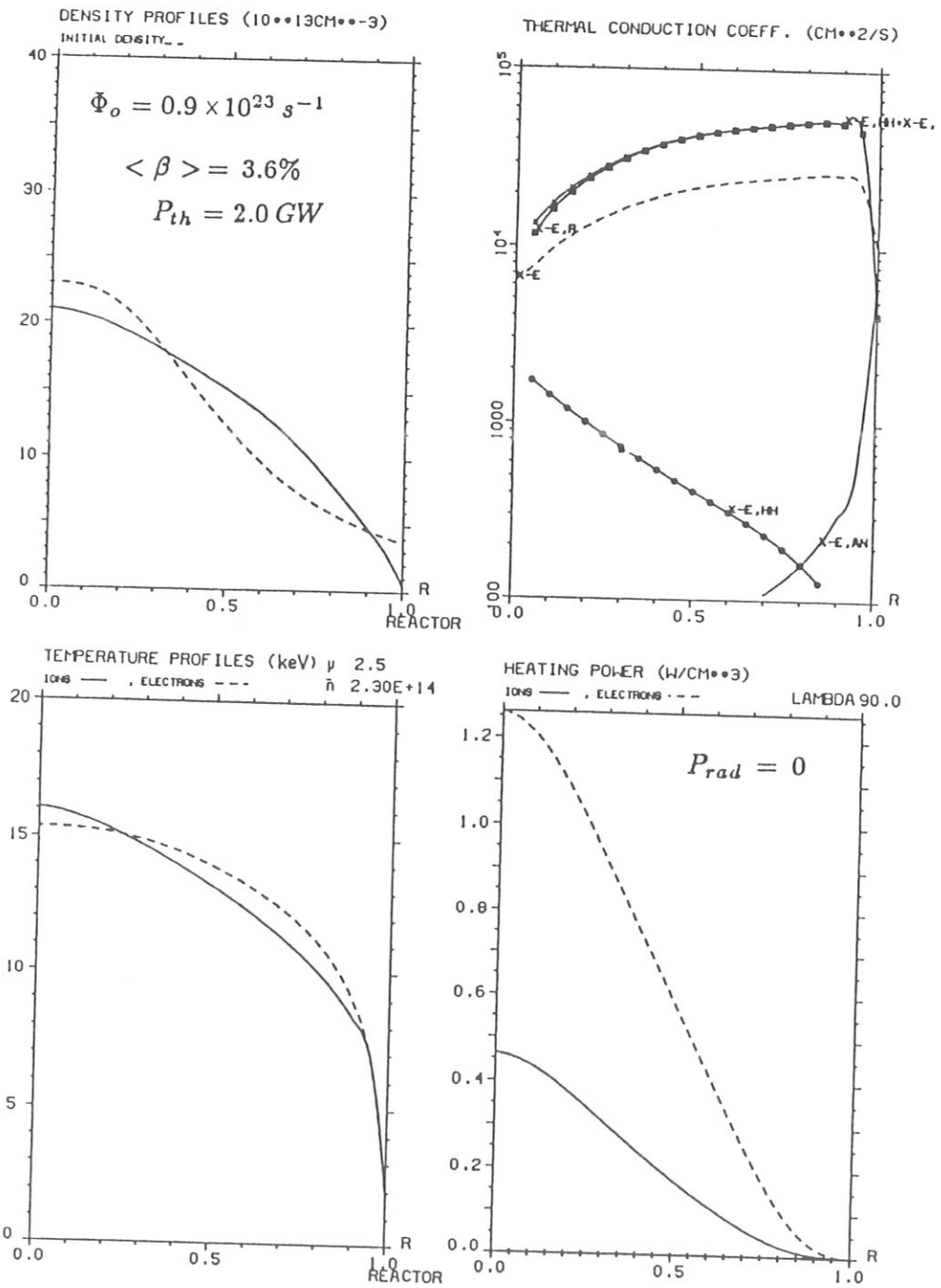

Fig. 5. Radial profiles for ASRA6C, calculated in HOW391
top left: final and (dashed) initial density
lower left: ion and (dashed) electron temperature
top right: thermal conduction coefficients
lower right: ion and (dashed) electron heating power
no radiation included beyond bremsstrahlung.

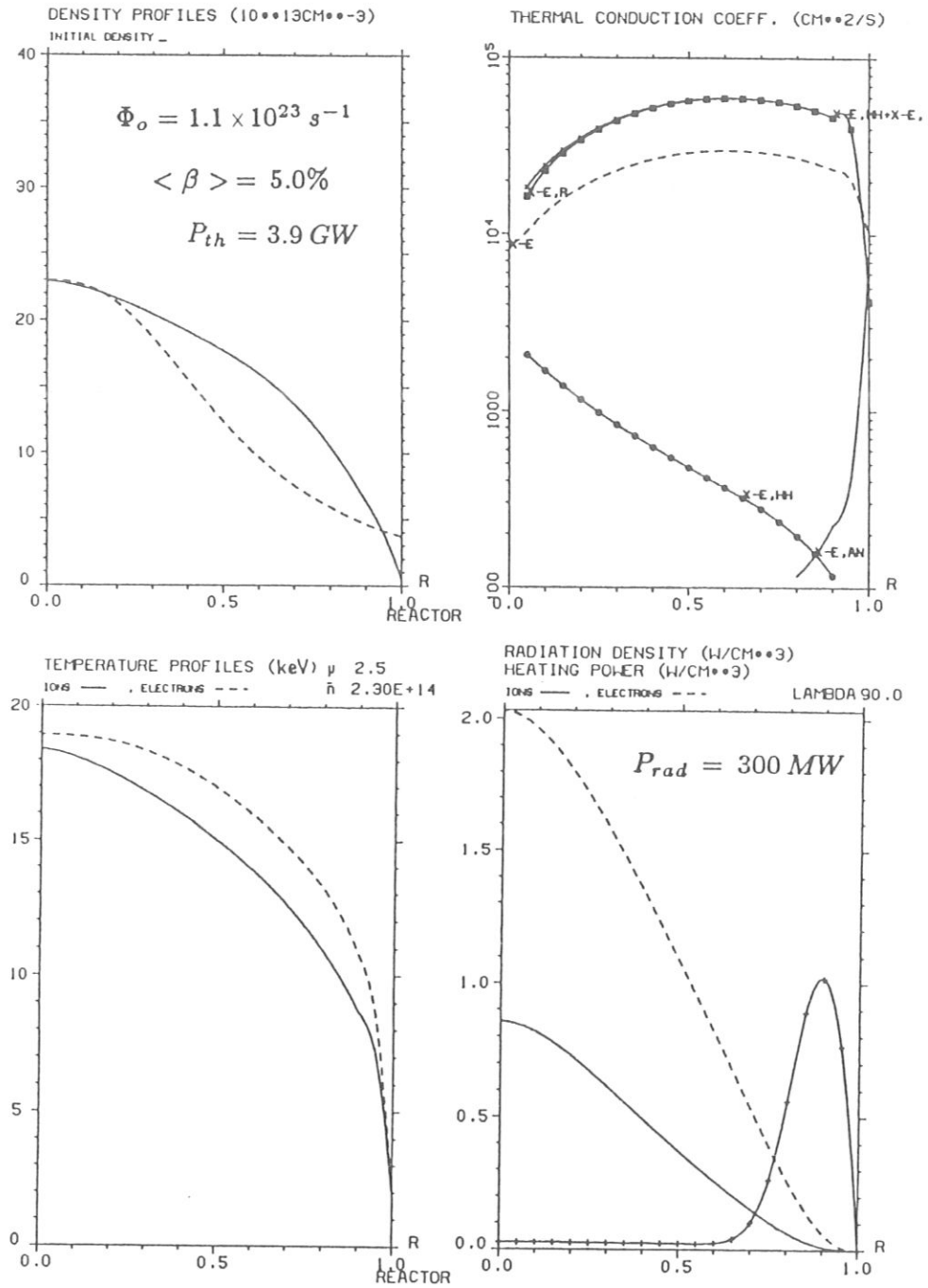

Fig. 6. Radial profiles for ASRA6C, calculated in HOW387 as Fig. 5. 300 *MW* radiation included beyond bremsstrahlung as indicated by the radial profile in the lower right part.

ripple losses, ignition occurs at a peak ion temperature of about $10\,keV$ and central densities around $2.2 \times 10^{14}\,cm^{-3}$, with little dependence on the magnitude of the magnetic field.

Two examples of the various calculations of operation points for ASRA6C are shown in the Figures 5 and 6, using input rates of $\Phi_o = 0.9$ and $1.1 \times 10^{23}\,s^{-1}$, respectively. The first case is without radiation; in Fig. 6 a radiative loss of $300\,MW$ is assumed near the boundary, as to be seen in the lower right of the figure. In the lower right part of Figures 5 and 6, the two other curves indicate the α-particle heating power densities to ions and electrons, respectively. Due to the larger electron heat conduction, $Q_{e,\alpha} > Q_{i,\alpha}$. The radial profiles of the thermal conduction coefficients are given in the upper right part of the figures. The largest contribution is by the ripple term, whereas the anomalous coefficient found in the WVII-A experiments is important only at the very plasma edge.

For the two examples shown in the Figures 5 and 6, the total fusion power amounts to $P_{th} = 2.0$ and $3.9\,GW$ with average β-values of 3.6 and 5 %, respectively.

The density and temperature profiles (upper and lower left part of the figures) are comparatively broad and reveal steep gradients near the plasma edge, set at $r_p = 1.5\,m$. Peak values are 2.1 and $2.3 \times 10^{20}\,m^{-3}$ for the density, and $15 \ldots 19\,keV$ for the temperatures, respectively, as can be seen in the left parts of the figures.

The data point with the radiative loss of 300 MW at a thermal fusion power of 3.9 GW is labelled '372' in the lower part of Fig. 3. The average value of $\beta = 5\,\%$ agrees well with the computed $\beta_{eq} = 4.7\,\%$, see [5]. There, a comment is also made, regarding a comparable value for β_{stab}, and a new interesting configuration with the prospect to attain such stable β-values.

Note that the edge physics in laboratory or fusion reactor plasmas is not described by the equations used in the transport model. If one assumes a pumped limiter system, assisted by an efficient radiative outer layer, similar to that introduced in Fig. 6, other terms are to be included. Furthermore, so far, the electric field is not treated selfconsistently, such as to ensure equal particle loss rates of electrons and ions for all radial positions. The three-dimensional topology of the stellarator fields, changed in addition by the Shafranov-shift at the different finite β-values of the start-up and burning plasma states, introduces further geometrical corrections. Furthermore, the thermal stability of these operation points needs to be analyzed.

5. SUMMARY AND CONCLUSIONS

Although there are several open questions regarding the transport model as described above, especially regarding the very edge region of the

plasma, it can be concluded that essential features of the start–up and burn conditions of an Advanced Stellarator Reactor or Burner system can be described appropriately.

Under neoclassical conditions, the plasma confinement is dominated by the effect of trapped particles and the associated ripple transport. A radial electric field reduces the losses by decreasing the ion heat conduction. The heat conduction coefficients, increasing with temperature, introduce relatively broad temperature and density profiles.

For start–up, an effective heating power of $P_i = 30$ to $50\,MW$ is sufficient for ASB and ASR. Larger major radii, e.g a value of $R_o = 25$ instead of $20\,m$, eases the requirements for start–up and allows a larger difference in the β–values of the ignition and the burn points.

This is of importance, if one takes into account that Stellarators allow in principle the operation at steady state. Thus, after reaching ignition, the start–up power can be turned down, and appropriate shielding be introduced into the respective ports, in order to avoid problems of neutron streaming.

Furthermore, a continuous operation of the reactor is of essential advantage regarding the material stresses and life–times. Due to the absence of cyclic loads a longer operation at full power is possible in a stationary system than in a pulsed reactor.

REFERENCES

[1] G. Grieger, E. Harmeyer, J. Kisslinger, F. Rau, H. Wobig,
Advanced Stellarator Reactor and Burner Studies,
this conference.

[2] E. Harmeyer, J. Kisslinger, F. Rau, H. Wobig,
Some Aspects of Modular Stellarator Reactors,
Proc. Plasma Phys. and Contr. Nucl. Fusion Research,
London 1984, Vol. III, 363, (1985).

[3] H. Wobig,
Ignition Condition in a Stellarator Reactor,
unpublished.

[4] H. Wobig and WVII–A Team,
A Transport Model of ECR–Heated Plasmas in WVII–A,
13^{th} Eur. Conf. on Contr. Fusion and Plasma Heating,
Schliersee, Germany, 1986.

[5] E. Harmeyer, F. Herrnegger, J. Kisslinger, F. Rau, H. Wobig,
MagneticField Studies for Advanced Stellarator Reactors,
this conference.

EVALUATION OF THE LOCAL HEAT CONDUCTIVITY COEFFICIENT BY POWER-MODULATED ELECTRON CYCLOTRON HEATING IN THE WENDELSTEIN VII-A STELLARATOR

H.J. HARTFUSS, H. MAASSBERG, M. TUTTER, W VII-A TEAM* (Max-Planck-Institut für Plasmaphysik, Euratom Association, Garching, Federal Republic of Germany), ECRH GROUP** (Institut für Plasmaforschung der Universität Stuttgart, Stuttgart, Federal Republic of Germany)

ABSTRACT. An upper bound for the local electron heat coefficient $\chi(r)$ in electron cyclotron heated (ECH) discharges is determined experimentally. The method applied uses power modulation of the ECH and measures the time delay of the electron temperature response as a function of radius by means of a multi-channel radiometer for second-harmonic electron cyclotron emission (ECE). The evaluation is restricted to plasma radii between 3 and 6.5 cm, where the pre-conditions of the method are best verified experimentally. The theoretical transport model considers only processes related to the electron temperature gradient and neglects the dependence of χ on T_e.

1. INTRODUCTION

The localized power deposition of electron cyclotron heating (ECH) makes heat transport studies possible if the heating power is modulated at the proper frequency and amplitude and if the resulting temperature modulation of the plasma electrons is measured as a function of time and plasma radius. A temperature change, $\Delta T_e(r_0, t)$, created at time t in the plasma centre (r_0), causes a heat wave to propagate outwards, resulting in a temperature change $\Delta T_e(r_i, t + \Delta t_i)$ at plasma radius r_i with a specific time lag Δt_i due to the finite propagation speed of the heat wave. If $\Delta T_e(r_i, t + \Delta t_i)$ can be measured with sufficient spatial and temporal resolution, the local thermal heat conductivity $\chi(r_i)$ can be derived.

First experiments of this kind were conducted in the Wendelstein VII-A stellarator (R = 2.0 m, a = 0.1 m, ℓ = 2, m = 5) at a main field of 1 T and with one 28 GHz gyrotron for plasma buildup and heating. The radial temperature response was measured with the electron cyclotron emission (ECE) diagnostic [1]. For reasons discussed below, no significant time delay was found on visual inspection of the experimental data, and so no attempt was made to derive the heat conductivity from the modulation experiment.

Recently, successful experiments were reported for the Doublet III tokamak [2], using power-modulated 60 GHz gyrotrons for heating and a soft-X-ray array for monitoring the response. The Wendelstein VII-A programme was resumed after replacement of the 28 GHz gyrotron by a 70 GHz tube, and the earlier experiment was repeated with a toroidal field of 2.5 T on axis and the same experimental arrangement. In this context, the early experiments conducted on the FM-1 spherator device to determine the electron thermal conductivity across magnetic surfaces should be mentioned [3].

2. EXPERIMENTAL SET-UP, PLASMA PARAMETERS, MODE OF OPERATION

The ECH power from the gyrotron is launched from the low-field side of the torus as a highly polarized wave (HE_{11}) in the O-mode direction ($E \parallel B$, $k \perp B$) which is nearly completely absorbed in a single pass through the plasma column. The output power of the gyrotron is 170 kW, the maximum pulse duration is 100 ms. The time sequence of a plasma shot in the series of power modulation experiments is as follows. During a pre-phase of about 40 ms, with the gyrotron operated at maximum output power P_0^{ECH}, quasi-stationary plasma parameters are reached: the output power is then square-wave modulated by periodic reduction by $2\Delta P^{ECH}$. The value of $2\Delta P^{ECH}/P_0^{ECH}$ is 0.3, resulting in an approximately 15% reduction of the time-averaged heating power. As a consequence, the average electron temperature falls by a small amount, but then stays constant until the end of the discharge, at about 100 ms. The results to be reported as an example were obtained with a readily reproducible discharge characterized by the following parameters:

- total energy content 400 J
- electron density on axis 2×10^{19} m^{-3}
- electron temperature on axis 740 eV
- ion temperature about 150 eV.

* G. CATTANEI, D. DORST, A. ELSNER, V. ERCKMANN, G. GRIEGER, P. GRIGULL, H. HACKER, H.J. HARTFUSS, H. JÄCKEL, R. JAENICKE, J. JUNKER, M. KICK, H. KROISS, G. KUEHNER, H. MAASSBERG, C. MAHN, S. MARLIER, G. MÜLLER, W. OHLENDORF, F. RAU, H. RENNER, H. RINGLER, F. SARDEI, M. TUTTER, A. WELLER, H. WOBIG, E. WÜRSCHING, M. ZIPPE.

** W. KASPAREK, G. MÜLLER, K. SCHWÖRER, M. THUMM, R. WILHELM.

To avoid modification of the plasma parameters by the local rotational transform ι in the vicinity of rational numbers, especially $\iota = 0.5$, shear was introduced into the almost shearless W VII-A stellarator by an Ohmic plasma current of −4 kA which was externally controlled and kept constant during the discharge [4, 5]. The heating power due to this plasma current is negligible.

3. ELECTRON TEMPERATURE MEASUREMENTS

The electron temperature is measured with an eight-channel heterodyne radiometer tuned to the second harmonic of the electron cyclotron frequency $f_{ce}(r)$ around 140 GHz. Since the W VII-A stellarator has a large aspect ratio of $R/a = 20$, the relative width $\Delta f/f_{ce}$ of the ECE spectrum is only $0.1 = 2\,a/R$. It is completely free of harmonic overlap. If one restricts observation to half of the emission spectrum, the frequency band to be monitored is small enough to be processed by a fixed tuned heterodyne receiver system. We choose the high-field side of the temperature profile $r < 0$ ($-a \leqslant r \leqslant +a$) because the emission from this region is due to reabsorption that is not significantly distorted by non-thermal electrons [6]. The band between 140.96 and 146.00 GHz, corresponding to small plasma radii r of between +0.4 cm and −6.5 cm, is converted to an intermediate frequency band ranging from 5 to 10.04 GHz. (The best results are obtained with the main field increased by 1%. The radii are calculated for B = 2.525 T.) Eight bandpass filters, each 300 MHz wide, are placed 720 MHz apart in this band [7]. Using this system, the electron temperature $T_e(r_i, t)$ is measured at eight discrete radii r_i within the plasma column. The distance $r_i - r_{i-1}$ is about 1 cm, the spatial resolution due to the finite filter bandwidth is less than 0.5 cm. The temporal resolution defined by the sampling rate of the data processing unit is 13.6 kHz.

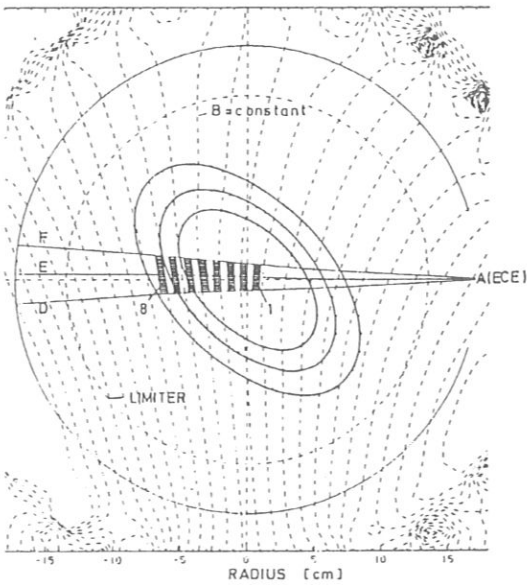

FIG. 1a. Observation geometry: rays D, E, F, central ray and rays at the −3 dB level of the ECE receiving horn antenna A (ECE). The hatched areas indicate the eight emission zones as monitored by the ECE diagnostic.

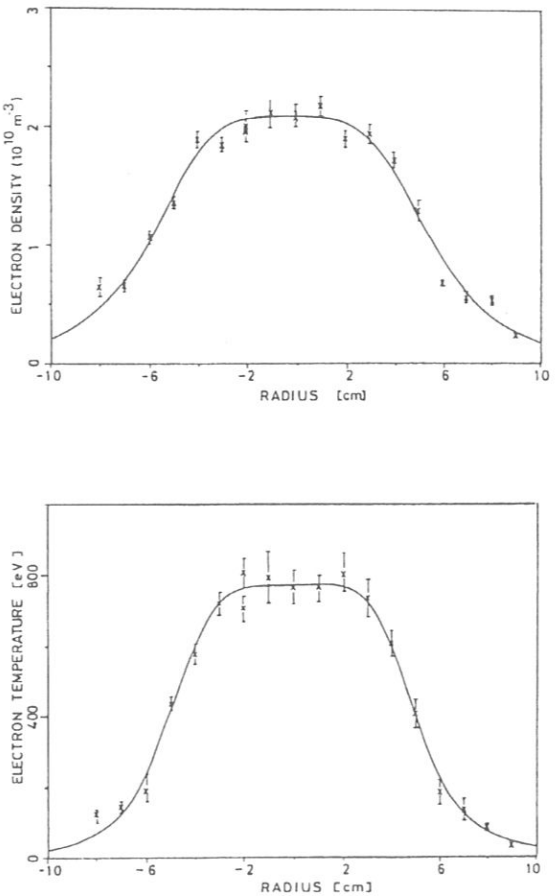

FIG. 1b. Electron temperature and density profiles as measured by Thomson scattering.

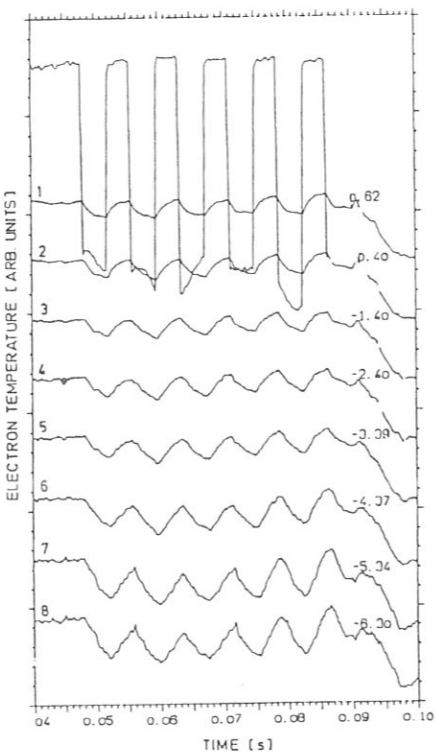

FIG. 2. Normalized electron temperature as a function of time during modulated ECH. The figures at the left and right indicate channel numbers and radial positions, respectively.

Figure 1 shows the observation geometry. Three rays (D, E, F) characterize the receiving horn (A(ECE)) aperture. The dashed areas indicate the position of the eight radiometer channels. The profile information gained with this instrument is in good agreement with the Thomson scattering diagnostic.

Figure 2 gives an example of the transient electron temperature $T_e(r_i, t)$, i = 1...8, as measured by the eight-channel radiometer during a series of shots with power-modulated ECH. The modulation frequency is 130 Hz. Though evaluation of the time delay Δt_i is possible for a single shot, a series of about 20 shots were amplitude-averaged to improve the statistics. The central radiometer channel (channel 1, $r_1 = 0.4$ cm) is well within the ECH power deposition zone, and so the modulation of this channel has fixed phase relation to the ECH power modulation. We take this channel as the reference and measure the time delay of the other channels relative to this one.

4. EVALUATION OF THE HEAT WAVE BY THE CROSS-CORRELATION TECHNIQUE

The cross-correlation technique was applied to determine the phases $\varphi(r_i) = 2\pi f_m \cdot \Delta t_i$ between the transient electron temperature $T_e(r_i, t)$ and the reference temperature $T_e(r_1, t)$.

The Fourier transform

$$G_{1i} = F\{R_{1i}(\tau)\} \qquad i = 2...8 \tag{1}$$

of the cross-correlation function

$$R_{1i}(\tau) = (1/T)\int_0^T T_e(r_1, t) \cdot T_e(r_i, t+\tau)\,dt \tag{2}$$

(T is the observation interval, T ≈ 60 ms) is a complex function of the frequency

$$G_{1i} = C_{1i}(f) + iQ_{1i}(f) \tag{3}$$

and yields directly the phase angle

$$\varphi(r_i) = \tan^{-1}(Q_{1i}(f)/C_{1i}(f)) \tag{4}$$

at the modulation frequency $f = f_m$ [8] (only the first harmonic of the modulation frequency was evaluated in these experiments).

Figures 3(a, b, c) give the experimental results for three different modulation frequencies, 130 Hz, 230 Hz and 370 Hz. Each of the figures gives the measured time delay, Δt_i, the absolute modulation amplitude, $\Delta T_e(r_i)$, and the modulation depth, $\Delta T_e(r_i)/\langle T_e(r_i, t)\rangle$.

A monotonic increase of the time delay with increasing distance |r| from the plasma centre is found. The absolute modulation amplitude decreases as expected, but the relative modulation amplitude increases slightly with |r|. This observation, which is obvious from Fig. 2 as well, might be an indication of additional absorption of direct or stray ECH waves in the boundary layers of the plasma (see below). (In numerous discharges a decrease of time delay with increasing |r| for |r| > 4 cm has been observed, which is a still stronger argument for power deposition in the boundary layers.) This observation is valid for each of the three modulation frequencies. In addition, a correlation is found between the maximum

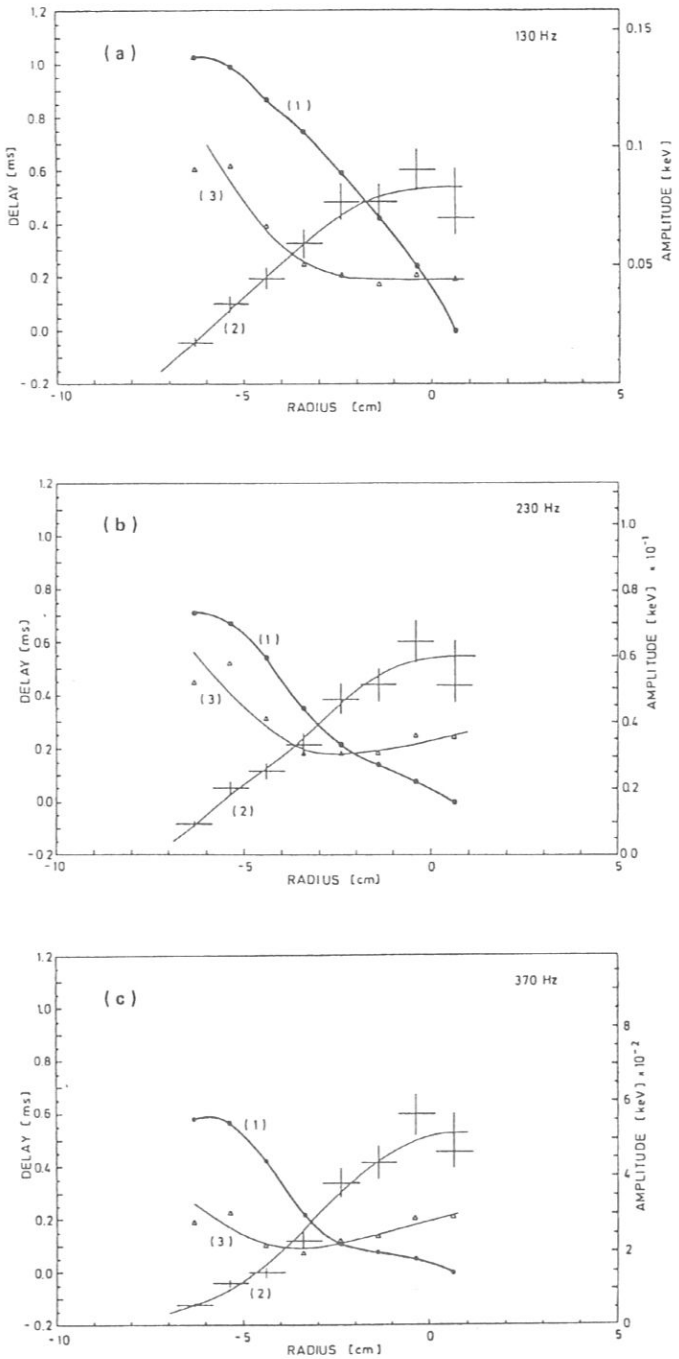

FIG. 3. Time shift (1), modulation amplitude (2), and modulation depth (3) as measured during power-modulated ECH at modulation frequencies of 130 Hz (a), 230 Hz (b) and 370 Hz (c). The quantities are defined in Section 4. Curve (3) has no separate scale; it is included to demonstrate the increase of modulation depth with |r|.

time delay Δt_s, as observed at $r = -6.3$ cm, and the modulation frequency. This observation, which is in agreement with the theoretical model as given below, means faster propagation of a heat wave of higher frequency.

5. THEORETICAL MODEL

We use the electron energy balance in a relatively simple form to estimate the local values of the electron heat conductivity coefficient $\chi(r)$. In an axisymmetric model we neglect all transport processes not related to the electron temperature gradient:

$$\frac{3}{2}\frac{\partial}{\partial t}(nT_e) = \frac{1}{r}\frac{\partial}{\partial r}\left(rn\chi\frac{\partial T_e}{\partial r}\right) + P^{ECH} - P^{L} \qquad (5)$$

where P^{ECH} is the deposited power and P^{L} is the power loss (see below). For simplicity, we neglect higher harmonics of the angular modulation frequency $\omega = 2\pi \cdot f_m$:

$$P^{ECH} = P_0^{ECH}(r) + \Delta P^{ECH}(r) \cdot e^{i\omega t} \qquad (6)$$

Consequently, for the electron temperature, we make the ansatz

$$T_e(r, t) = T_{e0}(r) + \Delta T_e(r) \cdot e^{i\omega t} \qquad (7)$$

where ΔT_e is a complex quantity including phase shift effects. The electron density $n(r)$ is assumed to be time-independent. With Taylor expansion in time, the heat conductivity coefficient χ and the total electron power loss P^{L} are given by

$$\chi(r, t) = \chi_0(r) + \frac{\partial \chi}{\partial T_{e0}} \cdot \Delta T_e(r) \cdot e^{i\omega t} \qquad (8)$$

$$P^{L}(r, t) = P_0^{L}(r) + \frac{\partial P^{L}}{\partial T_{e0}} \cdot \Delta T_e(r) \cdot e^{i\omega t} \qquad (9)$$

Since the temperature modulations are small, $\Delta T_e \ll T_{e0}$ (experimentally, $(2...9) \times 10^{-2}$), the electron balance equation is expanded in zeroth order (stationary balance):

$$0 = (1/r)\,(rn\chi_0 T_{e0}')' + P_0^{ECH} - P_0^{L} \qquad (10)$$

and in first order:

$$0 = (\Delta T_e)'' + \frac{(rn\chi_0)'}{rn\chi_0}(\Delta T_e)' + \frac{P^{ECH}}{n\chi_0} + \left\{\frac{\left(rn\,T_{e0}'\,\dfrac{\partial \chi_0}{\partial T_{e0}}\right)'}{rn\chi_0} - \frac{1}{n\chi_0}\frac{\partial P^{L}}{\partial T_{e0}} - \frac{3}{2}\,i\,\frac{\omega}{\chi_0}\right\}\Delta T_e \qquad (11)$$

The energy loss term P^{L} consists of two parts:

$$P^{L} = P^{ei} + P^{rad}$$

P^{ei} is the collisional energy transfer to the background ions and P^{rad} is the radiative energy loss term.

Since the power deposition profile is not known in detail, we restrict the evaluation of the electron heat conductivity coefficient to the outer regions ($|r| \geq 3$ cm), where in this experiment the deposition is negligible, P^{ECH} ($|r| \geq 3$ cm) = 0 (Eq. (11)). Caution is necessary because even small contributions of P^{ECH} will have a great influence on the time shift at greater radii.

6. RESULTS AND DISCUSSION

The amplitude and the phase shift of ΔT_e can be calculated numerically by means of Eq. (11) as a function of χ_0 and $\partial\chi_0/\partial T_e$. In order to fit ΔT_e to the measured ECE data and to estimate χ_0 and $\partial\chi_0/\partial T_e$, a very good database with high radial resolution is necessary. For simplicity, we neglect the time dependence of χ in a first step, $\partial\chi_0/\partial T_e = 0$, in Eq. (11). (Work is also being done to evaluate $\partial\chi_0/\partial T_e$ from the experimental data. The results will be presented, together with $\chi(r)$ results obtained with different types of discharges, in a later publication.)

Figures 4(a, b) give as an example the results obtained at a modulation frequency of 230 Hz. The best fit to the experimental data (dashed curves) is plotted together with the best fit obtained via Eq. (11) which determines $\chi(r)$ within 3.5 cm and 6 cm (full line). If $\chi(r)$ determined in this way is put into Eq. (10),

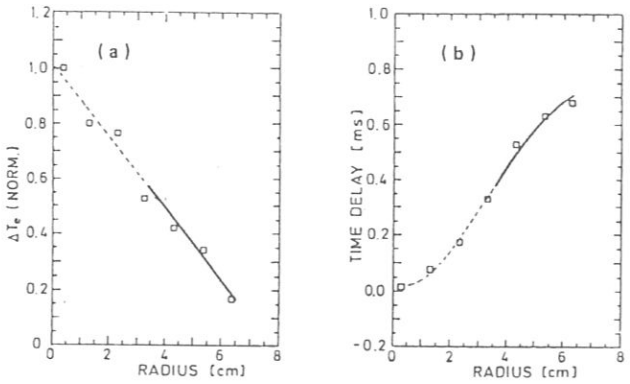

FIG. 4. Modulation amplitude (a) and time shift (b) from the 230 Hz modulation experiment (dashed curve) together with the best fit (solid line) of the transient energy balance (Eq. (11)) for $3 \leqslant r \leqslant 6$ cm.

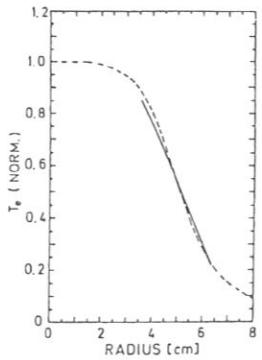

FIG. 5. Normalized electron temperature profile as measured by Thomson scattering (dashed line). The solid line gives the temperature profile which results if the $\chi(r)$ value determined from the modulation experiment (Fig. 6) is applied to the stationary balance (Eq. (10)).

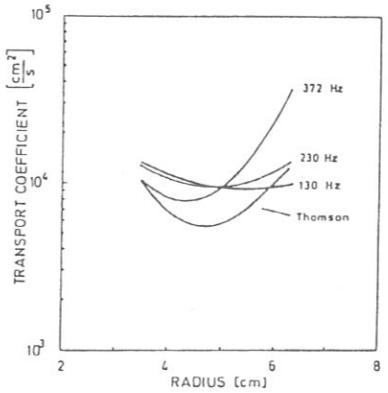

FIG. 6. Heat transport coefficient as a function of radius, as evaluated from the modulation experiment, for modulation frequencies of 130 Hz, 230 Hz and 370 Hz. The curve labelled Thomson was derived from the stationary balance.

$T_e(r)$ can be calculated. Figure 5 demonstrates that the resulting temperature gradient is slightly smaller than that of the temperature profile measured with the Thomson diagnostic (dashed line).

Figure 6 summarizes the $\chi(r)$ results for the three modulation frequencies on the basis of the experimental data given in Figs 3(a, b, c). Included in Fig 6 is the $\chi(r)$ dependence (labelled Thomson) derived by means of the stationary balance equation (10) on the basis of the electron temperature and density profiles measured by Thomson scattering. The relatively good agreement demonstrates the usefulness of the modulation-correlation technique.

The accuracy of the method is mainly determined by the degree to which the ideal experimental condition, namely clear separation between the power deposition zone and the zone of observation, can be realized. Ray refraction and incomplete single-pass absorption of the ECH wave followed by wall reflection causes power deposition in the boundary region of the plasma column, resulting in partial or complete compensation of the phase delay.

Since power deposition within the observation zone cannot be completely excluded, the $\chi(r)$ profiles evaluated may only give an upper bound to the real $\chi(r)$ as one gets closer to the plasma boundary. Inverting the problem, the power deposition profile in the boundary region might be evaluated by comparing the assumed $\chi(r)$ profile with the profiles experimentally determined by the modulation–correlation technique.

Two observations should be mentioned. Firstly, a correlation seems to exist between the modulation frequency and the $\chi(r)$ evaluated (Fig. 6). Secondly, the relative modulation amplitude or modulation depth (Figs 3, curves 3), $\Delta T_e(r_i, t)/\langle T_e(r_i, t)\rangle$, increases with $|r|$ for $r > 5$ cm. It is most pronounced at the lowest modulation frequency.

The first observation might be explained by boundary layer deposition because the highest modulation frequency leads to the smallest modulation amplitude (Figs 3, curves 2), which is therefore most sensitive to direct superposition.

The reason for the second observation is related to $\partial\chi/\partial T_e$. If the modulation of the heating power is not really a small perturbation, $\Delta P_0^{ECH} \ll P_0^{ECH}$, and the modulation period is comparable to the internal time constants, e.g. the energy confinement time, then the electron temperature profile changes periodically in shape because of the increasing transport rate at the plasma boundary with decreasing electron temperature (anomalous transport $1/nT_e^{2/3}$ [5]), resulting in the enhanced modulation depth observed at the plasma boundary.

Concerning the earlier 1 T experiment, there was no chance to detect phase shifts by visual inspection. If neoclassical transport is the dominant term within the radius range of observation and with additional contributions from anomalous transport, the total heat transport coefficient is up to an order of magnitude larger than the values obtained in the 2.5 T experiment. In addition, interference by suprathermal electrons could not be completely excluded in the 1 T experiment. Therefore, in this case, one had to rely on quasi-static measurements [1]. So the transition from 28 GHz to 70 GHz and the corresponding increases in field and cutoff density were essential to obtain useful experimental data by the modulation–correlation method.

REFERENCES

[1] ERCKMANN, V., JANZEN, G., KASPAREK, W., MÜLLER, G., RÄUCHLE, E., et al., in Plasma Physics and Controlled Nuclear Fusion Research 1984 (Proc. 10th Int. Conf. London, 1984), Vol.2, IAEA, Vienna (1985) 419.

[2] JAHNS, G.L., WONG, S.K., PRATER, R., LIN, S.H., EJIMA, S., Nucl. Fusion 26 (1986) 226.

[3] EJIMA, S., OKABAYASHI, M., SCHMIDT, J., Phys. Rev. Lett. 32 (1974) 872.

[4] W VII-A TEAM, NI TEAM, ECRH GROUP, in Controlled Fusion and Plasma Physics (Proc. 12th Europ. Conf. Budapest, 1985), Vol. 95, Part I (1985) 393.

[5] GRIEGER, G., W VII-A TEAM, NI TEAM, ECRH GROUP, ibid., Vol. 28, Part IA (1985).

[6] HARTFUSS, H.J., TUTTER, M., W VII-A TEAM, ECRH GROUP, in Electron Cyclotron Emission and Electron Cyclotron Resonance Heating (Proc. 5th Int. Workshop San Diego, CA, 1985).

[7] HARTFUSS, H.J., TUTTER, M., Rev. Sci. Instrum. 56 (1985) 1703.

[8] BENDAT, J.S., PIERSOL, A.G., Measurement and Analysis of Random Data, Wiley, New York (1966).

(Manuscript received 18 December 1985
Final manuscript received 19 February 1986)

PLASMA CONFINEMENT IN THE WENDELSTEIN VII-A STELLARATOR

H. Wobig, H. Maaßberg, H. Renner, W VII-A Team
ECRH Group, NI Group

Max-Planck-Institut für Plasmaphysik
Association EURATOM-IPP
Garching bei München
Federal Republic of Germany

Abstract

The confinement behaviour of the W VII-A stellarator depends on the magnetic field structure, the heating method as well as the plasma properties. At low (m, n) rational numbers of the rotational transform, $\iota = \frac{m}{n}$, strongly deteriorated confinement is observed which is explained by island formation and ergodization of magnetic surfaces. Only in the close vicinity of these fundamental resonances, $\iota = \frac{1}{2}$ and $\frac{1}{3}$, where the most stable magnetic surfaces are expected, optimum confinement was found. It was sensitively dependent on both the edge value of ι and on small additional shear. Only for these optimum confinement conditions, the particle and energy transport is analysed in this paper.

The ion energy transport in W VII-A is found in rather good agreement with neoclassical theory. In detail, in case of NBI heating, large radial electric fields are built up by the fast ions strongly improving the confinement of thermal ions. Collisional slowing down of the ions originating from the NBI was found. For ECF heated discharges, the observed radial electric fields are comparable with neoclassical estimates (by means of the ambipolarity condition). For the central part of the plasma, the particle fluxes are explained in terms of neoclassical transport; at outer radii, strongly enhanced particle transport must be concluded. ECF heated discharges, especially with low density, indicate neoclassical electron heat conduction in the central part; in the edge region, however, the electron energy confinement must be described by anomalous transport.

I. Introduction

Experiments in the low shear stellarator W VII-A exhibit a critical dependence of the plasma confinement on the structure of the magnetic field. At particular values of the external rotational transform ($\iota_0 = \frac{1}{2}$ and $\frac{1}{3}$), the confinement is deteriorated whereas in the close neighbourhood of these values confinement time and energy content are maximum (Figure 1). Both energy and particle balance at optimum confinement have been studied in "currentless" plasmas generated by NBI and ECRH and will be discussed in the subsequent sections. The residual current (1-2 kA) observed under these conditions does not contribute to the heating power.

In NBI heated plasmas (Section II), the main topics are ion energy balance, the role of the radial electric field and the heating mechanism, where in contrast to earlier assumptions /1/ the classical slowing down mechanism could be verified. Paricle transport is discussed in Section III. ECR heated plasmas offer a better chance to analyse the electron energy balance (Section IV) than NBI heated plasmas. In ECR heated plasmas, the electron transport in the bulk of the plasma can be explained by neoclassical effects, in the boundary regions, however, anomalous transport has to be assumed. In the minima of confinement ($\iota_0 = \frac{1}{2}$ and $\frac{1}{3}$), the most plausible explanation for the enhanced losses is island formation in the magnetic field structure and stochasticity caused by external perturbations. This effect will be discussed in Section V.

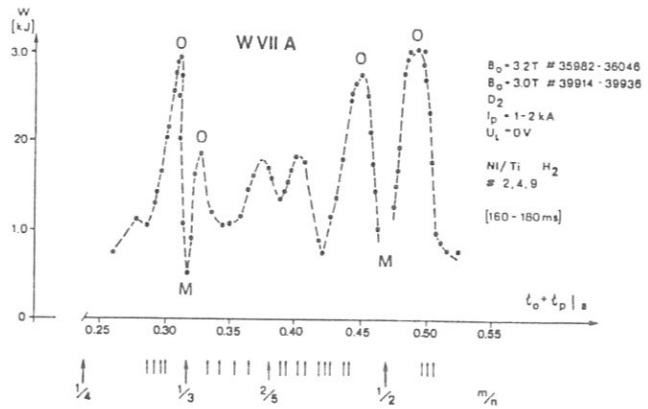

Fig. 1:
Total plasma energy in W VII-A as a function of the rotational transform at plasma edge, $\iota_a = \iota_0 + \iota_p|_a$. Heating by neutral beam injection. O indicates regions of optimum confinement, M are the states of minimum confinement.

II. NBI heating

The slowing down of the fast ions originating from the nearly perpendicular (84°) neutral beam injection had been experimentally proofed to be collisional both for stationary conditions and after switching off the injectors /2/. This was demonstrated by neutron flux measurements of D-D reactions in case of D^0 injection into a D^+ target plasma as well as by the charge exchange diagnostic. Both the absolute value of the stationary neutron production as well as the transient neutron flux after the D^0 injection switched off were found to be in rather good agreement with simplified Fokker-Planck estimates based on the assumption of only collisional interaction (Coulomb scattering) /3/. Additionally, the measured time decay of high energetic CX neutrals after switching off the NBI could be reproduced by Monte Carlo simulation on the basis of only collisional slowing down (see Figure 2). The ion distributions were estimated to be highly anisotropic /4/ due to the high power NBI. By means of linear stability analysis /5/, these ion distributions were found to be stable against low harmonic ion cyclotron instabilities (ion Bernstein modes) for stationary conditions. Unstable lower hybrid modes are expected to smooth the ion distribution function near the injection velocities but having negligible effect on the energy transfer.

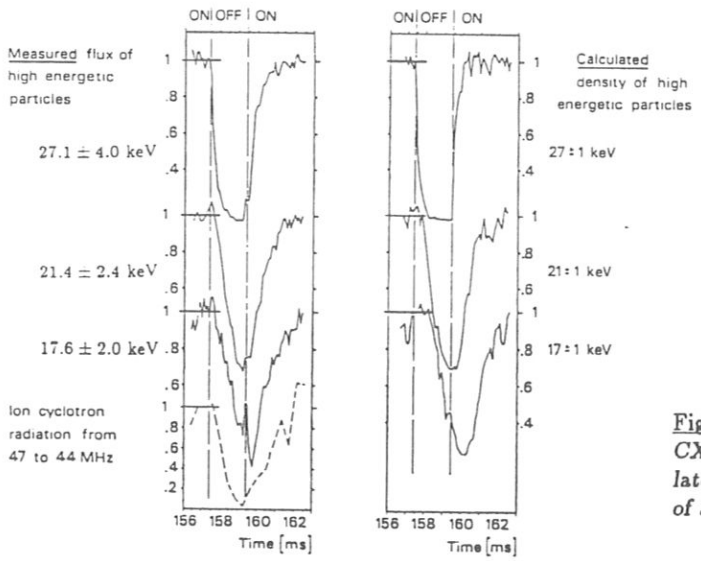

Fig. 2:
CX-fluxes measured (on the left) and simulated (on the right) vs time for the phase of all neutral beam injectors switched off.

Only in the transient phase after switching on the injectors, the radiation close to the low ion cyclotron harmonics (ICE) measured by a probe in the limiter shadow was strongly increased. From the stability analysis of the transient ion distributions after switching on the NBI, low harmonic ion Bernstein modes were found to be strongly unstable. Although these distributions were calculated on the basis of collisional slowing down, strong instability is expected leading to preferential ion heating. This prediction is consistent both with a measured delay of the neutron flux increase and with the strong increase of the ion temperature immediately after switch on of an additional beam. This temperature increase, ΔT_i (see Figure 3), is in rather good agreement with the assumption that the absorbed NBI power of the additional beam given by the diamagnetic signal is only transfered to the ions, direct electron heating is rather small ($\Delta T_e \ll \Delta T_i$). For collisional slowing down, however, preferential electron heating should be expected for the initial phase since high energetic ions are mainly slowed down by electrons.

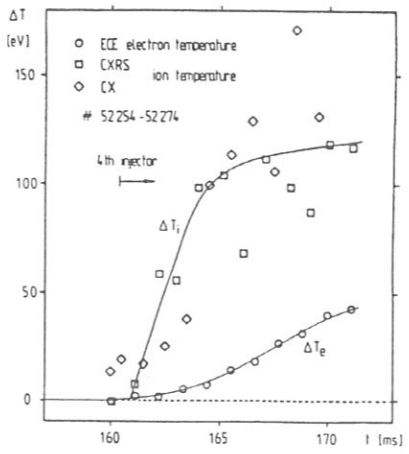

Fig. 3: *Ion and electron temperature increase, ΔT, vs time after a 4th neutral beam injector is switched on ($T_i \approx 650\ eV$ and $T_e \approx 500\ eV$).*

From the measured Doppler shift of impurity lines connected with poloidal plasma rotation, radial electric fields up to 1 kV/cm were deduced. The toroidal plasma rotation, v_ϕ, was found to be not larger than the poloidal one: $v_\theta \gg \iota v_\phi / A$ where A is the aspect ratio ($A = 20$ for W VII-A); this result is quite different to tokamak cases /6, 7/. Without radial electric fields, the fast ion loss rate is quite high due to the nearly perpendicular injection and the small plasma radius in W VII-A ($r_a \leq 10$ cm) leading to only poor heating efficiency. It was clearly shown by Monte Carlo calculations (ODIN code, /8/) that the fraction of fast ion losses can be significantly reduced by radial electric fields which, on the other hand, are built up by the loss of such fast ions /9/. Due to the strong radial electric fields deduced from the measured poloidal plasma rotation the heating efficiencies for both co- and counter-injection (which are analogously defined with respect to the rotational transform ι) are strongly improved. For both injection cases which are experimentally realized by changing all magnetic field directions, similar confinement properties were found. However, in case of counter-injection, higher electric fields, E_r, were observed than for co-injection. This is consistent with the condition $E_r + \iota v_\parallel Br/R \simeq const$ which can be derived for strong radial electric fields from the kinetic equation (poloidal component of $(\underline{v}_\parallel + \underline{v}_D) \cdot \underline{\nabla} f \simeq const$) describing the partial compensation of the ∇B-drift effects.

The connection of fast ion losses with the global confinement properties was demonstrated by measuring the Fe sputtering by means of laser induced fluorescence (LIF). By Monte Carlo calculations with electric fields included, the fast ion flux distribution onto the stainless steel vacuum vessel was estimated leading to Fe densities which are within a factor of 2 in agreement with the LIF measurements. Figure 4 shows the time behaviour of the Fe sputtering (upper plot) which is equivalent to the orbit loss rate for a discharge in which the rotational transform was transiently shifted over the deteriorated confinement regime from the optimum confinement below to the one above $\iota \simeq \frac{1}{2}$. This shift of the external rotational transform leads to a strong decrease in the energy content, W (middle plot), within the deteriorated confinement regime. The corresponding decrease of line density, $\int n\, dl$ (lower plot), is partially compensated by higher neutral gas influx due to the increased recycling. The stronger neutral gas production is confirmed by an increase of the H_α signal. Then, both the energy as well as the particle confinement times are significantly reduced close to the rational value $\iota = \frac{1}{2}$ which is connected with an increase of fast ion losses leading to a reduced NBI heating efficiency and the strong decrease of the energy content. For degraded confinement properties,

this flux of fast ions onto the vacuum vessel is up to 20% of the total influx of NBI neutrals (the fraction of transmitted neutrals is typically between 30% and 60% depending on line density). Consequently, fast ion losses can contribute significantly to the particle transport. Furthermore, the poloidal plasma rotation was found to be smaller within the ι-range of deteriorated confinement. These experimental findings confirm the correlation between radial electric fields and the confinement properties of the fast ions. Although the fraction of fast ions is relative small (typically <10%), the fast ion loss contributes significantly to the particle fluxes. Consequently, the radial electric fields are mainly determined by the fast ion loss rate to satisfy the ambipolarity condition of the particle fluxes.

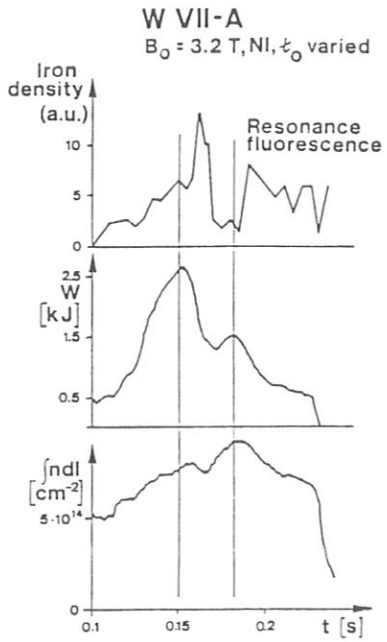

Fig. 4: *Fe sputtering, total energy content and line density vs time. For these discharges, the external rotational transform was shifted from the optimum confinement below (line on the left) to the one above* $\iota \simeq \frac{1}{2}$ *(line on the right).*

III. Particle transport

Since in general detailed information about the particle sources is not available (especially the neutral gas distribution within the torus is largely unknown), the analysis of particle transport has to be based on some reasonable assumptions. This situation is different to the energy analysis where profiles of heating power deposition and radiated power are known, at least to some extent. However, both particle transport and heat conduction are strongly correlated in all transport theories of interest.

In the early phase of W VII-A operation with only ohmic heating, detailed energy transport studies were carried out leading to the electron thermal conductivity /9/: $\chi_e^{\mathrm{OH}} \propto n_e^{-1} \cdot T_e^{-2/3}$ (see Section IV). Only for the case of ohmically heated helium discharges the particle diffusion coefficient could be derived from the measured ionization rates /10/. The radial behaviour was found to be similar to the electron thermal conductivity, but the absolute value was about one order of magnitude smaller: $D^{\mathrm{OH}} \simeq 0.1 \cdot \chi_e^{\mathrm{OH}}$. The flattening of the density profiles at outer radii which is typical for all discharges in W VII-A and the increased particle sources due to neutral gas ionization lead to strongly enhanced particle transport as it is described by the n and T dependence of the *anomalous* diffusion coefficient D^{OH}. Contrary to the electron heat conduction, the *anomalous* flux, $\Gamma^{\mathrm{AN}} \simeq -D^{\mathrm{OH}} \cdot n_e'$, is less than or of the same order of magnitude as the neoclassical particle flux in the central part of the plasma. The transport coefficients of the thermal ions are mainly determined by the values of the plateau collisionality regime which without radial electric fields strongly exceed the electron transport coefficients.

In case of the strong neutral beam heating in W VII-A, the beam particle deposition is the main particle source in the central region of the plasma column leading to the nearly linear density increase during the duration of the NBI heating ($\leq$ 200 ms) for good confinement conditions. The beam particle deposition, however, is not known accurately enough since the ionization profiles of the charge exchange generated thermal neutrals cannot be determined up to now; the transport of these neutrals is mainly determined by CX collisions quite similar to the problem of neutral gas influx. Assuming that all these neutrals are ionized, a lower limit of the particle confinement time can be estimated. In doing this, particle confinement times of typically more than 100 ms were found for the central plasma region. These very good confinement properties were confirmed by pellet injection experiments where all the additional particles were confined for the rest of the discharge duration ($\leq$ 100 ms). Only in the case of an additional ECF pulse, theses particle confinement properties seem to be degraded /11/. For the other cases, the experimentally deduced particle fluxes are

of the same order of magnitude as the neoclassical electron transport in the bulk part of the plasma within the uncertainty of the particle sources. However, already in the maximum gradient region the *anomalous* transport becomes dominant.

ECF sustained discharges at higher densities where the ions are effectively heated by electron collisions can be analyzed on the basis of the neoclassical formalism since the ion distribution functions are close to Maxwellians. As the ions are in the plateau collisonality regime, their transport coefficients are reduced by a suitable radial electric field in order to satisfy the ambipolarity condition. On the basis of measured profiles of density and temperatures, the local radial electric field is calculated by means of the ambipolarity condition of only the neoclassical fluxes $\Gamma_i^{NC} = \Gamma_e^{NC}$ consisting of Pfirsch-Schlüter and plateau regime contributions /12/. The calculated radial electric fields are in good agreement with the values deduced from the Doppler shift of impurity lines for the case of ECF heated discharges (s. Figure 5a); however, it must be mentioned that the measured values are obtained at radii where the *anomalous* transport is dominant. Furthermore, on the basis of measured profiles it is impossible to satisfy the continuity equation with only neoclassical fluxes at outer radii.

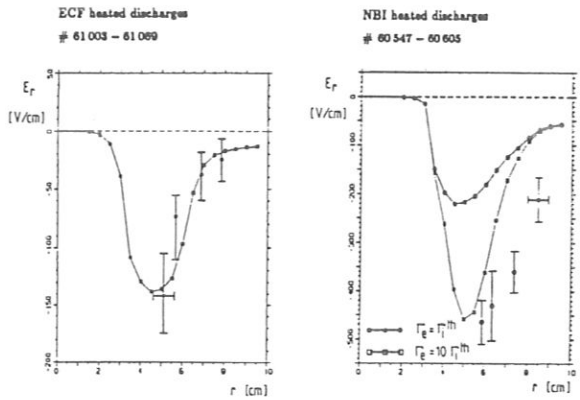

Fig. 5:
Radial electric fields measured (dots) and calculated vs plasma radius for ECF and NBI heated discharges, plots (a) and (b), respectively.

In order to get a consistent description, the total particle flux density is modeled by: $\Gamma = \Gamma^{NC} + \Gamma^{AN}$ where Γ^{NC} is the neoclassical term consisting of Pfirsch-Schlüter and plateau regime contributions and Γ^{AN} the *anomalous* term derived from the ohmically heated discharges ($\Gamma^{AN} \simeq -D^{OH} \cdot n_e'$). In the plasma boundary region, the *anomalous* term exceeds the neoclassical term by orders of magnitude. Up to now, no proven picture exists for these *anomalous* fluxes, however, it is believed that both the *anomalous* particle transport and the *anomalous* electron heat conduction are caused by convective transport. This hypothesis of convective transport based on **E×B**-drift is in agreement with the experimental experience. Then, the *anomalous* transport of electrons and ions is ambipolar on their own: $\Gamma_i^{AN} = \Gamma_e^{AN}$. With this assumption, the radial electric fields have to be determined by the balance of the neoclassical fluxes (mainly of the plateau regime contributions) with the fast ion losses included in case of neutral beam heating. Then, neoclassical theory may be used to estimate the radial electric fields and the ion heat conduction. The basis of the neoclassical formalism is the expansion of the distribution functions starting from Maxwellians. For estimating the radial electric fields, experimental values of density and temperature have to be used to define the local Maxwellians. On this basis, the analysis of the ECF heated discharges supports the hypothesis of the ambipolarity of the *anomalous* fluxes.

In case of strong neutral beam heating, however, the highly anisotropic ion distributions violate the basic assumption of distribution functions being close to Maxwellians. For this case, the observed radial electric fields are much larger than those estimated with the assumption of only thermal ions (s. Figure 5b) supporting the conclusion that the radial electric fields are mainly generated by the fast ions. The thermal ion heat conduction is strongly reduced by the electric fields in both cases. Only with this reduction of the ion heat conductivity coefficients, the ion energy balance could be satisfied for both the high density ECF as well as the NBI heated discharges /13/. However, as the neutral gas density and thus the CX losses are largely unknown, the ion energy balance is not conclusive at outer radii.

Finally, the influence of the *anomalous* particle transport on the ion energy balance is discussed shortly. At outer radii, the dominant *anomalous* flux is related to the ionization of neutral gas: $div\ \Gamma_i^{AN} \approx \langle\sigma v\rangle_e n_e n_0$ where $\langle\sigma v\rangle_e$ is the ionisation rate due to electron collisions. The contribution to the ion heat conduction Q_i is given by $\frac{3}{2} T_i \Gamma_i^{AN}$ and less than the charge exchange ion energy loss by the factor $\langle\sigma v\rangle_e / \langle\sigma v\rangle_{CX}$ where $\langle\sigma v\rangle_{CX}$ is the charge exchange rate coefficient; this factor is typically of the order of 0.3 at outer radii. Consequently, *anomalous* transport is of minor importance for the ion energy balance which may be significantly influenced by CX losses at outer radii.

IV. Electron heat conduction

Local analysis of electron thermal conduction was made for OH- discharges, NBI-heated discharges and ECRH-discharges. The transport coefficient was obtained from the measured profiles with the power deposition profile taken from the current density profile (OH) or from numerical calculations (NBI).

In the analysis of ohmically heated discharges one has to avoid strong effects of current driven MHD instabilities which significantly deteriorate the confinement. In the region outside the $q = 1$ surface, when strong tearing modes are absent, the local thermal conductivity, χ_e, has been evaluated from local measurements of density, temperature and radiative power. Within the main field range $B_0 = 2.5 - 3.5\ T$, an experimental thermal conductivity $\chi_e^{OH} \simeq 3.8 \cdot 10^{18} \cdot n_e^{-1} \cdot T_e^{-2/3}\ [cm^2/s]$ was found depending on the density $n_e\ [cm^{-3}]$ and $T_e\ [eV]$, see /9/.

The analysis of electron heat losses during currentless operation with NBI was more difficult since the separation of electron heat conduction is hampered by the uncertainties of the heating power deposition, the strong coupling of electrons and ions at densities $n_e \sim 10^{14}\ cm^{-3}$, the radiative losses, and the nonstationary conditions due to the strong particle input flux. However, there are strong indications that neoclassical thermal conductivity alone is not sufficient to model the discharge.

ECF sustained discharges seem to be more suited for analysing the electron energy transport. The wave energy is transfered directly to the electrons. Other loss channels such as electron ion coupling and radiation play a minor role. Consequently, the dependence of the heat conduction on various parameters (B, n_e, ι, T_e) could be studied. Launching the rf power with different modes of irradiation (TE02, HE11 at o-mode or x-mode) and for off-axis resonance conditions, strong variation of the power deposition profiles and the electron temperature profiles have been obtained /14/. Furthermore, a power modulation technique has been applied. Analysing the generated heat waves across the plasma, the local conductivity coefficients could be derived from the time dependent temperature profiles /15/.

A coupled system of equations for the energy balance of electrons and ions was solved to fit the experimental density and temperature profiles /16/. The steady state TEMPL code models the electron thermal conductivity by a sum of the axisymmetric neoclassical part, the magnetic ripple dependent neoclassical part and the anomalous part. Especially in the boundary, enhanced electron energy transport seems to be necessary to fit the flat temperature profiles. The anomalous transport coefficient was assumed to follow the same scaling as in ohmically heated discharges.

So far, at ι-values with optimum confinement good agreement of experimental data with the neoclassical model is concluded for the central part of the plasma. Especially at higher temperature (low collisionality) and large magnetic ripple at higher ι, ripple effects become dominant. In the boundary region where the density and temperature are small, enhanced losses have to be assumed. Atomic processes, perturbations of the magnetic surfaces or drift instabilities may be responsible for the enhanced loss. However, the dependence of the anomalous heat conduction $\chi_e^{OH} \sim C \cdot n_e^{-1} \cdot T_e^{-2/3}$ restricts its influence more and more to the boundary the higher the energy density of the plasma grows. The anomalous transport used to fit the currentless ECF heated discharges is following the empirical scaling for OH discharges assuming the coefficient C to be proportional to B. If in both cases the same loss process occurs, this suggests that current driven instabilities are not responsible for the anomaly.

V. Destruction of magnetic surfaces

At particular values of the rotational transform, $\iota = \frac{1}{2}, \frac{1}{3}, \frac{2}{5}, \ldots$, confinement is deteriorated, which indicates that around these low-order rational values of ι magnetic surfaces may be destroyed by symmetry breaking perturbation fields. This effect occurs in currentless operation obtained by various heating methods (NBI, ECRH) and seems to appear independently on the plasma pressure. The experimental results suggest that the perturbation breaks the five fold symmetry of the configuration and therefore can be explained by field errors coming from the coil system. Numerical calculations have indeed shown that current leads to the helix create a local perturbation field of $10 - 20$ G, which gives rise to island formation on rational surfaces. The largest islands occur at $\iota = \frac{1}{2}$, three smaller islands at $\iota = \frac{1}{3}$ and five islands at $\iota = \frac{2}{5}$. Islands are also found at $\iota = \frac{3}{7}$ and $\iota = \frac{3}{8}$. Other perturbations which are caused by misalignment of the coils and magnetic material may also exist and lead to larger islands as calculated above.

The plasma confinement shows pronounced minima around $\iota = \frac{1}{2}, \frac{1}{3}, \frac{2}{5}$ and $\frac{2}{3}$; in close proximity of $\iota = \frac{1}{2}$ and $\iota = \frac{1}{3}$, however, the confinement is maximum (Figure 1). This effect can be understood on the basis of island formation by a general external, time independent field $\mathbf{B_1}$. The Fourier spectrum of this field may contain several harmonics with decreasing amplitude. Then, every harmonic generates a chain of primary islands on a rational surface with $\iota = \frac{m}{n}$ (n = toroidal mode number, m = poloidal mode number). In the neighbourhood $\iota = \frac{1}{2}$ or $\frac{1}{3}$ or any other low (m, n) rational surface only large (m, n) rational surfaces exist, which is a general result of number theory. Therefore only high harmonics of $\mathbf{B_1}$, or nonlinear interaction of low harmonics can create islands in the vicinity of $\iota = \frac{1}{2}$ or $\frac{1}{3}$. The size of these islands, in general, will be small.

In order to study the behaviour of small shear stellarators under the influence of an external perturbation $\mathbf{B_1}$, the mapping technique developed by J. Greene /17/ was applied /18/. In general the perturbation $\mathbf{B_1}$ leads to a perturbed twist map T of the poloidal plane onto itself. Written in the magnetic coordinates ψ, θ of the unperturbed field $\mathbf{B_0}$ the twist map can be derived from a generating function

$$S(\psi_1, \theta_0) = \psi_1 \theta_0 + 2\pi \int^{\psi_1} \iota(\psi)\, d\psi + h(\psi_1, \theta_0)$$

and yields $T : (\psi_0, \theta_0) \longrightarrow (\psi_1, \theta_1)$. Iteration of T generates the desired Poincaré plot. The effect of the perturbation field $\mathbf{B_1}$ is described by the function $h(\psi_1, \theta_0)$ and various analytical perturbation functions $h(\psi_1, \theta_0)$ have been investigated. Variation of the rotational transform $\iota_0 + \iota_1 \psi$ with a fixed perturbation $h(\psi_1, \theta_0)$ always shows the same pattern : The vicinity of $\iota = \frac{1}{2}$ or $\frac{1}{3}$ ((O) in Fig. 1) is the most stable against island formation and destruction. The feature is independent of the particular choice of $h(\psi_1, \theta_0)$. With increasing amplitude of h the neighbourhood of $\iota = \frac{1}{2}$ or $\frac{1}{3}$ is the last one to be destroyed. Figure 6 compares the region at $\iota = 0.47 - 0.49$ with $\iota = 0.45 - 0.47$ under the same perturbation.

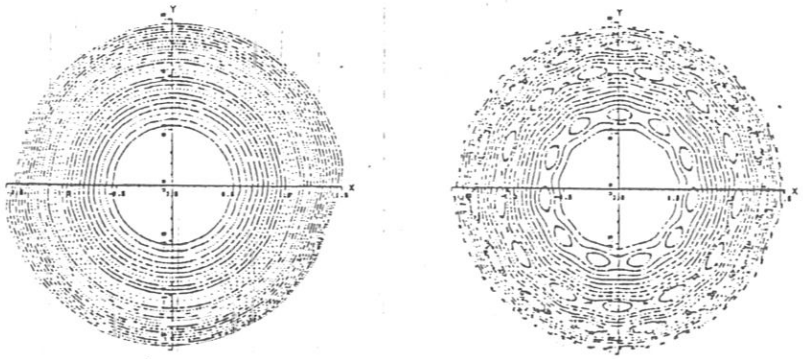

Fig. 6: *Poincaré plots of magnetic surfaces for the same perturbation function with nearly undisturbed magnetic surfaces ($0.47 < \iota < 0.49$, on the left) and island formation ($0.45 < \iota < 0.47$, on the right).*

The size of the islands has been computed /18/ from the residues and the sum of all island widths was subtracted from the plasma radius a, thus defining an effective plasma radius, Δ. This effective plasma radius is plotted vs $\iota(a)$ in Figure 7. One sees that the effective plasma radius vs $\iota(a)$ exhibits a similar pattern as the measured plasma energy.

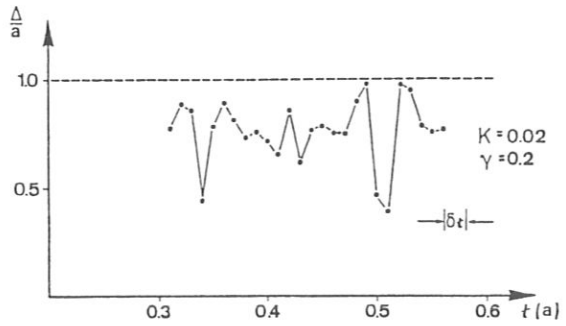

Fig. 7:
Effective plasma radius, Δ, as function of the external rotational transform, $\iota(a)$. K and γ are parameters describing the perturbation.

These considerations are of pure geometric nature, the plasma may react in different ways on the presence of islands. Plasma currents and electric fields will be modified by islands leading to enhanced convective losses. But also neoclassical particle losses will be enhanced as has been shown by Boozer and White /19/ for tokamaks. It has to be expected that due to islands and field ergodization also the energy transport of electrons will be strongly enhanced, therefore, the confinement in W VII-A based on neoclassical effects will exhibit a similar dependence on ι_0 as the effective plasma radius, Δ. A Monte Carlo code addressing this effect is in preparation.

VI. The effect of shear

Experimentally the influence of shear on confinement was extensively studied starting from a nearly shearless magnetic configuration /20/ with $\delta\iota/\iota \simeq 10^{-2}$ and varying the shear up to $\delta\iota/\iota = \pm 0.2$. Shear was introduced externally by operating the 2 sets of the helical windings with unbalanced currents (Torsatron mode /21/) and internally by a small induced toroidal current and the inhomogeneous distribution of the residual plasma current including effects of the plasma pressure. Mainly around $\iota = \frac{1}{2}$ the effect of shear was investigated.

In the ECR-heated plasmas ($B = 2.5$ T, $n \approx 10^{13}\ cm^{-3}$) the negative shear resulting from 4 kA induced toroidal current improves the confinement at $\iota = \frac{1}{2}$ but leads to no further improvement in the region of optimum confinement (O). At higher plasma density ($n = 2 - 4 \cdot 10^{13}\ cm^{-3}$), however, 2 kA plasma current provides optimum conditions, whereas 4 kA reduce the confinement everywhere to the level of $\iota = \frac{1}{2}$. At this density the bootstrap current may already modify the ι-profile, therefore the exact shear is not known. Numerical studies indicate that strong shear reduces the island widths but due to islands overlapping ergodization of the region in between islands occurs. Consequently moderate shear may reduce the influence of a single island at the fundamental resonance but a strong shear deteriorates confinement by island overlapping.

A small positive external shear seems to be more favourable for high β plasmas ($\beta(0) \leq 1\%$). The residual plasma current which roughly grows proportional with plasma pressure and which probably is related to the bootstrap current leads to further positive shear. Starting from negative external shear the current density profile of the residual current which in case of the bootstrap current is peaked in the maximum gradient region may compensate the shear locally to zero, which could lead to large islands. After a rapid loss of plasma the build-up of the plasma pressure and the pressure driven current would start again and thus lead to relaxation oscillations. Consistent with this idea, strongly unstable conditions were observed for the negative external shear case during increase of the plasma energy. These experiments support the picture of island formation and ergodization of the magnetic surfaces as the reason for deteriorating the confinement.

VII. Summary and conclusions

As demonstrated, plasma confinement in W VII-A depends very sensitively on the structure of the magnetic field which is determined by the particular value of the rotational transform and the magnitude of the shear. The effect appears with all heating methods if the shear is small enough. The strong dependence of the confinement on the values of ι_0 and shear can be understood on the basis of magnetic surface destruction by external symmetry breaking field errors among which some helix joints could be identified. Close to the fundamental resonance $\iota = \frac{1}{2}$ and $\iota = \frac{1}{3}$ only high Fourier harmonics of the perturbation field may create small islands. This explains why this region is the most stable against any kind of external perturbations. Since external perturbations are maximum at the plasma boundary, this also explains the experimental finding that confinement is deteriorated in particular if the resonant $\iota = \frac{1}{2}$ - surface is close to the plasma boundary. Small variations of the ι-profile during the discharge, either caused by pressure effects or by small induced currents, may shift the plasma from optimum confinement (O) to minimum confinement (M). Therefore in the experiment a careful control of the edge values of the rotational transform and the shear is necessary to achieve optimum plasma parameters. The conclusion for future stellarator experiments with low shear is that modifications of the ι-profile with increasing plasma pressure be as small as possible and external symmetry breaking field errors be avoided or minimized.

For optimum conditions of ECR-heated currentless plasmas the electron thermal conductivity in the central part of the plasma column can be described by neoclassical theory including effects of helical ripple. In the edge region an anomalous transport coefficient, assumed to be the same as in ohmically heated discharges, is necessary to fit the experimental data. Because of the uncertainties of the exact power deposition profile, this hypothesis has to be considered with caution; so far, however, no contradiction did arise. A conclusion from these results is that the anomalous thermal conductivity, which exists in all tokamaks, is not caused by the ohmic heating current. Due to the $T_e^{-2/3}$- scaling of the anomalous conductivity its influence in future high temperature experiments is expected to be small. The effect of the anomaly will be shifted more and more towards the plasma boundary. A temperature independent thermal conductivity $\chi_e \sim 1/n$ did not provide a good fit to the experimental data.

In ECR-heated plasmas neoclassical ambipolarity condition explains the measured E-field. Anomalous particle transport - if ambipolar - does not change this result. In NBI-heated plasmas high energetic particle losses drive the observed radial electric field which improves the confinement of the thermal ions in the plateau regime. This beneficial effect is predicted by neoclassical theory and it is particularly effective in large aspect ratio devices as W VII-A ($A = 20$).

Particle transport in the plasma center is comparable with neoclassical predictions, if one takes into accout the uncertainties of the particles sources. In the boundary region, however, strongly enhanced particle losses (possibly by convective mechanisms) have to be concluded.

References

/ 1/ W VII-A Team and NI Group, Plasma Phys. and Contr. Nucl. Fusion Research, Brussels (1980), IAEA, **1**, 185

/ 2/ W VII-A Team and NI Group, Plasma Phys. and Contr. Nucl. Fusion Research, London (1984), IAEA, **2**, 371

/ 3/ A. Weller and H. Maaßberg, Report IPP 2/278 (1985)

/ 4/ H. Maaßberg, Report IPP 2/281 (1986)

/ 5/ H. Maaßberg and M.A. Hellberg, Report IPP 2/282 (1986)

/ 6/ R.C. Isler et al., Nucl. Fusion **26**, (1986), 391

/ 7/ W.M. Stacey, Jr. and D.J. Sigmar, Phys. Fluids **27**, (1984), 2076

/ 8/ F.P. Penningsfeld, W. Ott and E. Speth, Contr. Fusion and Plasma Phys., Budapest (1985), ECA **9F 1**, 397

/ 9/ G. Grieger et al., Plasma Phys. and Contr. Fusion **28**, (1986), 43

/10/ W VII-A Team, Proc. 9th Europ. Conf., Oxford (1979), **A2.4**

/11/ H. Ringler et al., these proceedings, Kyoto (1986)

/12/ H. Maaßberg et al., Contr. Fusion and Plasma Phys., Budapest (1985), ECA **9F 1**, 389

/13/ W VII-A Team and NI Team, 5th Int. Workshop on Stellarators, Proc. of the IAEA Technical Committee Meeting on Plasma Confinement and Heating in Stellarators, ECSC-EEC-EAEC, EUR 9618 EN, **1** (1984), 219

/14/ V. Erckmann et al., Plasma Phys. and Contr. Fusion **28**, (1986), 1277

/15/ J. Hartfuß et al., Nucl. Fusion **26** (1986), 678

/16/ H. Wobig and W VII-A Team, Contr. Fusion and Plasma Phys., Schliersee (1986), ECA **10C 1**, 291

/17/ J. Greene, J. Math. Phys. **20** (1973), 1183

/18/ H. Wobig, Report IPP 2/283 (1986)

/19/ A.H. Boozer, R.B. White, Phys. Rev. Lett. **49** (1982), 786

/20/ H. Renner and W VII-A Team, Contr. Fusion and Plasma Phys., Schliersee (1986), ECA **10C 1**, 287

/21/ E. Harmeyer et al., Report IPP 2/275 (1985)

IMPURITY BEHAVIOUR IN THE WENDELSTEIN VII-A STELLARATOR

Abstract

Plasma build-up and heating of net-current-free plasmas by ECRH (70 GHz) and further heating by NBI was successfully demonstrated at B_o = 2.5 T. Impurity transport studies were carried out. In NBI-sustained discharges neoclassical behaviour was found for impurities, similar as in discharges starting from OH target plasmas reported earlier. During combined application of ECRH and NBI heating Al introduced by laser ablation was lost much faster than neoclassically expected. The electron line density, which increased linearly with time during NBI, levelled off during the additional ECRH pulse and remained constant.

A similar degradation of impurity confinement was observed in pure ECRH discharges.

Impurity Confinement

In the W VII-A stellarator high radiation losses due to impurity accumulation were observed for NBI-heated, "currentless" plasma discharges created by ohmic heating /1/. The impurity transport study presented here refers to "currentless" plasmas created by ECRH with a 70 GHz gyrotron at B_o = 2.5 T with $\iota_o \lesssim 0.5$. Three main types of discharges were investigated:

a) NBI-sustained discharges at an input power level of 750 kW, $\bar{n}_e \simeq 3.7 - 5.5 \times 10^{13}$ cm^{-3}, $T_e(o) \simeq 400$ eV, $T_i(o) \simeq 600$ eV.

b) EC-sustained discharges at 70 GHz with a power of 150 kW, $\bar{n}_e \simeq 1.7 - 2.7 \times 10^{13}$ cm^{-3}, $T_e(o) \simeq 900 - 1400$ eV, $T_i(o) \simeq 100 - 300$ eV.

c) NBI-sustained discharges with additional ECR heating during part of the discharge, $\bar{n}_e \simeq 4 \times 10^{13}$ cm^{-3}, ($n_e(o)$ close to the cutoff density), $T_e(o) \simeq 500$ eV, $T_i(o) \simeq 600$ eV.

As in previous transport studies, both Al trace impurities injected by the laser blow-off technique and intrinsic impurities were considered. The simulations were done with the SITAR code /1/.

a) For NBI-sustained discharges starting from an ECRH target plasma, the measured Al radiation is reproduced reasonably well by neoclassical transport simulations using experimental profiles for n_e and T_e. In particular, good agreement is found for the time evolution and the absolute intensity of the central Al XII + Al XIII radiation from soft X-ray measurements and of line-averaged intensities from six Al ionization states. According to neoclassical expectations, the measurements show Al accumulation at the plasma center and no evidence of appreciable losses during the time of the discharge.

   For the intrinsic impurities (predominantly oxygen in W VII-A) good agreement of soft X-ray measurements and neoclassical calculations was obtained by assuming in the calculations, in addition to a 1 % oxygen contamination of the neutral beam, which constitutes an oxygen deposition of $\simeq 2 \times 10^{18}$ s^{-1}, an oxygen influx from the walls increasing from 1×10^{18} to 7×10^{18} s^{-1} during the discharge.

b) In contrast to the NBI-sustained discharges, for pure ECRH discharges the Al XII + Al XIII radiation from soft X-ray measurements (Fig. 1a) and the single line radiation from six ionization states Al VIII - Al XIII could not be reproduced by the neoclassical model (Fig. 1b). The main discrepancy concerns the fast loss of Al from the plasma center after 80 ms as indicated by the decrease of the central Al XII + Al XIII radiation and of the corresponding line radiation, which cannot be explained by atomic processes (n_e, $T_e \simeq$ constant in time). Furthermore, the time scale for the Al penetration into the plasma center is much shorter than in the neoclassical simulations. The fast loss of Al could be simulated, however, by an additional diffusivity $D_{anom} = 3 \times 10^3$ cm^2 s^{-1}, constant in space and time. An additional inward velocity $v_{anom} = 3 \times 10^3 \times r/a$ cm s^{-1}, linearly decreasing to zero during the ECRH pulse, was used to accelerate the Al penetration and to fit the absolute level of the central radiation approximately (Fig. 1c).

c) The discharges heated jointly by NBI and ECR differ from the purely NBI-heated discharges in that for the former an additional 150 kW ECRH pulse was switched on for $\simeq$ 50 ms during the discharge. During this time interval a flattening of the density evolution is typically observed (see Fig. 5). This flattening may be explained by a deterioration of the particle confinement during the ECRH pulse or by a reduced penetration of recycled neutrals due to edge deposition of ECRH power, which is discussed later in this paper. The interpretation of reduced particle confinement is supported by the observed evolution of the Al radiation from soft X and single-line radiation measurements, which indicate a fast loss of Al from the plasma center, in contradiction with neoclassical theory. The time scale for the decay of the radiation and the values of D_{anom} required to simulate it with the code were about the same as for pure ECRH discharges, with the anomalous impurity behaviour extending throughout the gradient region.

The soft X-radiation from the intrinsic impurities for this discharge type is shown in Fig.2a. In a previous paper /2/ it was shown that the increase of the central radiation could be reproduced reasonably well by pure neoclassical transport with oxygen impurities from 1 % beam contamination and from wall influx rising from 2×10^{18} to 5×10^{18} s^{-1} during the discharge. However, if the same anomalous behaviour is assumed for the intrinsic impurities as for the ablated Al during its escaping phase from the plasma center, i.e. if the same D_{anom} is added while keeping the wall influx unaltered, then the central oxygen radiation drops to unacceptably small intensities. In this case, the measured radiation could only be reproduced if the oxygen influx at the plasma edge was raised by almost an order of magnitude with respect to the values assumed for the neoclassical simulations. However, only about 10 % of this impurity influx contributes to the increase of the central oxygen density. The remaining 90 % circulates, after ionization, back to the wall, thus keeping the impurity gradients at the plasma edge higher than in the neoclassical case.

In this picture of enhanced transport the typical neoclassical impurity accumulation is strongly reduced. That is, for a given central radiation level the impurity density at the edge can be maintained at a substantially higher level than in the neoclassical picture. This may facilitate impurity removal from the plasma edge. A further consequence of this model is that the plasma particle outflux to the walls, which is linearly related to the oxygen desorption rate, would also have to be increased by about an order of magnitude with respect to the neoclassical transport case.

Unfortunately, the experimental informations available on the edge plasma of these discharges was not sufficient to decide whether the high oxygen influx is a reasonable assumption. On the other hand, the code calculations show that the higher oxygen density at the plasma edge resulting from the increased oxygen influx would still be too small to give an observable increase of the bolometer signal. Uncertainties would also arise in checking the simulations with spectroscopic measurements of the lower oxygen ionization states. In fact, the enhanced transport would lead to an outward shift of the higher ionization states, thus decreasing the density of the lower states with respect to their values at coronal equilibrium. This would compensate to a large extent the density increase due to the higher fluxes at the edge.

Concerning the possibility of an impurity flow reversal mechanism associated with the ECR heating process /3/, it is not yet clear at present whether or not the required additional poloidal electric field was sufficiently high for the W VII-A discharges discussed here to create outward drift contributions compensating to a large extent the neoclassical inward drift. However, even if this was the case, the outward drift would have essentially the same consequences as the assumed enhanced diffusion with respect to the high impurity sources required to maintain the central radiation level.

The evolution of the OVII + OVIII radiation resulting from the code calculations discussed is shown in Fig. 2b. At the late stage of the discharge, a drop of the measured soft X-radiation is observed (Fig. 2a), in evident contrast to the simulation, which shows a steep increase of the OVII + OVIII radiation. Such an increase of oxygen radiation is essentially a consequence of the T_e drop (ΔT_e = 140 eV within 10 ms) observed after switching off the ECRH pulse. In order to reduce the discrepancy, additional high-Z material was included in the simulations for this discharge type (Fig. 2c). Such impurities could originate from, for example, sputtering of plasma ions at the vacuum vessel (Fe, Cr) and sputtering at the limiter and NI beam dump plates (Mo)/4,5,6/. By assuming a Fe wall influx of 4 % of the oxygen influx, the measured central radiation could be qualitatively reproduced.

For the same discharge type, the evolution of the O^{8+} density has been measured by CX recombination spectroscopy (active signal) /2/. On the other hand, the passive signal, obtained with the diagnostic beam off, yields a flux which is proportional to the O^{7+} density /2/. The time histories of both signals are reproduced reasonably well by the simulations (Figs. 3,4). In particular, the decrease of the O^{8+} density related to the T_e drop observed after switching off the ECRH pulse is clearly confirmed by the CX recombination measurements.

Electron Confinement

As shown above, Al introduced by laser ablation into a combined NBI and ECRH discharge is lost faster than neoclassically. (Similar results are reported for Si from the Heliotron E experiment /7/.) Using the same transport coefficients for the oxygen transport to model the total radiation requires an increased oxygen influx from the walls.

In this section the confinement behaviour of the background plasma, protons and electrons during this phase will be discussed.

Starting from ECRH target plasmas NBI leads to density increases of $\dot{N}_e \simeq 0.5 - 2 \times 10^{20}\ s^{-1}$, as in NBI discharges starting from OH target plasmas, which can be explained by the total particle influx from the neutral beams (ECRH switched off after transition phase). There is no saturation of the density increase during the injection phase, which leads to particle confinement times in the $\tau_p \simeq 100$ ms range. Impurity transport and particle confinement show no difference from those measured earlier /1/.

With an additional ECRH pulse during NBI, however, the line density increase levels off and stays constant, with a significant increase in the H_α signal. An influence of ECRH on the time evolution of the density has also been observed in tokamaks /8,9/. At electron densities n_{eo} well below $n_{e,crit.}$, core heating is observed, while for n_{eo} approaching $n_{e,crit.}$, edge heating is seen from ECE /10/, but even for $n_{eo} > n_{e,crit.}$ during ECRH $\int n_e dl$ stays constant. Two possible explanations for this behaviour have been given /8/:

a) In addition to impurity confinement, the electron confinement is also decreased, or

b) the gas flux from the walls is ionized by ECRH power outside the last closed flux surface, reducing the gas flux penetrating through the scrape off layer and thus allowing constant density with electron confinement still unchanged.

So far no clear-cut experimental proof for either one of these explanations can be given. In this position a discussion of both possibilities in a more or less phenomenological way seems appropriate.

a) - Looking at the time history of the H_α signal there is increased recycling (or loss of particles) even in the early ECRH target phase, when NBI starts and external fluxes are switched off (Fig. 5), with no density increase. After ECRH shut-off the density increases strongly with a sharp drop in the H_α signal. With the second ECRH pulse applied later in the discharge $\int n_e dl$ stays constant and H_α increases, this being followed by a drop and a corresponding density increase after the ECRH is switched off again.

- At the line density under consideration (5.7×10^{14} cm^{-2}) a large fraction of the beam particles 20×10^{19} s^{-1} (63 % of the NB power) hit the molybdenum beam dump. Owing to a surface temperature of $\simeq$ 400°C all beam particles are expected to be released from the beam dump during the 100 ms interval of injection /11/ and used to refuel the plasma.

  The source of fast ions, produced mainly by CX, amounts to 12×10^{19} s^{-1}. Only a source of $S_{electrons} \simeq 7 \times 10^{19}$ s^{-1} is estimated to lead to particle production, with 1/3 of the halo neutrals assumed to be reionized in addition to 1/3 of the flux of fast ions which is created by proton and electron collision rather than by charge exchange.

  A flux of 10×10^{19} s^{-1} fast ions is lost via orbit losses (ODIN code calculations, including electric fields), is deposited in the SS wall of the vacuum vessel and is not released during the injection interval /9/. The reflux from the wall and limiter due to plasma losses with an expected particle confinement time of $\tau_p \simeq 100$ ms during the pure NBI phase and a recycling coefficient of 0.7 ($N_{e,total} = 8.4 \times 10^{18}$) is also small compared with the flux from the beam dump, which thus appears to be the main particle source.

- Now, if during the $\dot{N}_e \simeq 0$ phase with ECRH applied a particle confinement time of $\tau_p \simeq 100$ ms were to be maintained, a flux of 2.5×10^{19} s^{-1} particles would be sufficient, which is of the order of the flux of particles directly produced by the beam.

  The ECRH - power would therefore have to decouple the large hydrogen flux out of the beam dump from the plasma almost completely.

  Density profiles during and after ECRH, however, show little change and thus do not support this explanation. In addition, the ionization length by electron collisions for thermal hydrogen atoms released at the beam dump is long enough to penetrate into the non-ergodic region, where particles are confined on flux surfaces. This would hold even for electron densities up to 10^{12} cm^{-3} within the ergodic region, because $\langle \sigma v \rangle$ is only weakly dependent on temperature.

It is therefore not very likely that the neutral flux from the outside is strongly reduced by ECRH.

b) - Poloidal plasma rotation shows no change during the ECRH pulse, so radial electric fields which are associated with the rotation still indicate good confinement.

- By application of an additional external gas flux $\int n_e dl$ can be made to increase again during ECRH, which, however, would also be true with reduced particle confinement.

Conclusion

The technique of an additional ECRH pulse applied to a NBI-sustained discharge has some very interesting aspects:

- Stationary discharges can be maintained with good energy confinement at tolerable radiation levels, whereas without additional ECRH pulse the density increases linearly with time along with high radiation losses due to impurity accumulation.

- There is experimental evidence that the electron particle confinement is also deteriorated.

- For the ablated Al a faster loss of impurities from the central region is observed.

References

/1/ W VII-A Team, NI Group, Nuclear Fusion 25 (1985) 1593.

/2/ M. Kick, H. Ringler, F. Sardei, A. Weller et.al.,13th Europ. Conf. Contr. Fusion and Plasma Heating (1986), TU58.

/3/ W.M. Stacey, The Effect of Poloidal Electric Fields on Impurity Asymmetries and Transport in Tokamaks, GTFR 63 (1986).

/4/ W VII-A Team, NI Group, 5th Int. Workshop on Stellarators, Vol . 1, CEC Brussels (1984) 259.

/5/ P. Bogen and B. Schweer, H. Ringler and W. Ott, J. Nucl. Mat. 111 + 112 (1982) 67-70.

/6/ A. Weller, Measurements of the Radiation Energy Distribution in the Soft X-Ray Region in the Wendelstein VII-A Stellarator, IPP 2/277 (1985).

/7/ O.M. Motojima, paper D-I-1 this conference.

/8/ V.V. Alikaev et.al. Proc. 10th Int. Conf. on Plasma Phys. and Contr. Nucl. Fus. Res. London (1984) Vol. 1, p 419

/9/ FOM ECRH Team and TFR Group, 12th ECCFPP, Budapest EPS Vol. 12, 60 (1985)

/10/ V. Erckmann, et.al. Plasma Phys. 28 (1986) 1277.

/11/ W. Moeller, B. Scherzer, priv. communication.

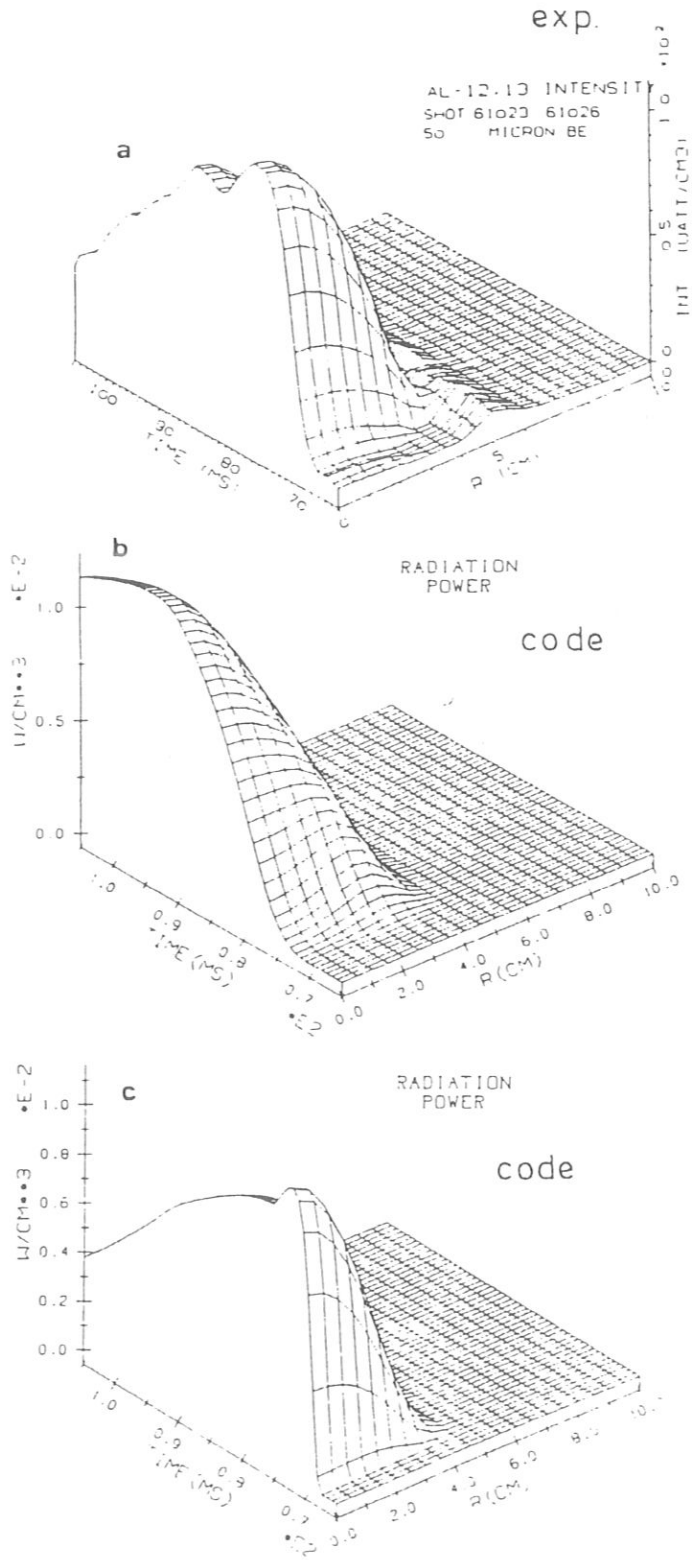

Fig. 1: a) Evolution of Al XII + Al XIII radiation power from soft-X ray measurements after Al injection into an EC-sustained discharge.
b) Code simulation with neoclassical transport fluxes.
c) Code simulation with additional anomalous diffusivity and inward velocity.

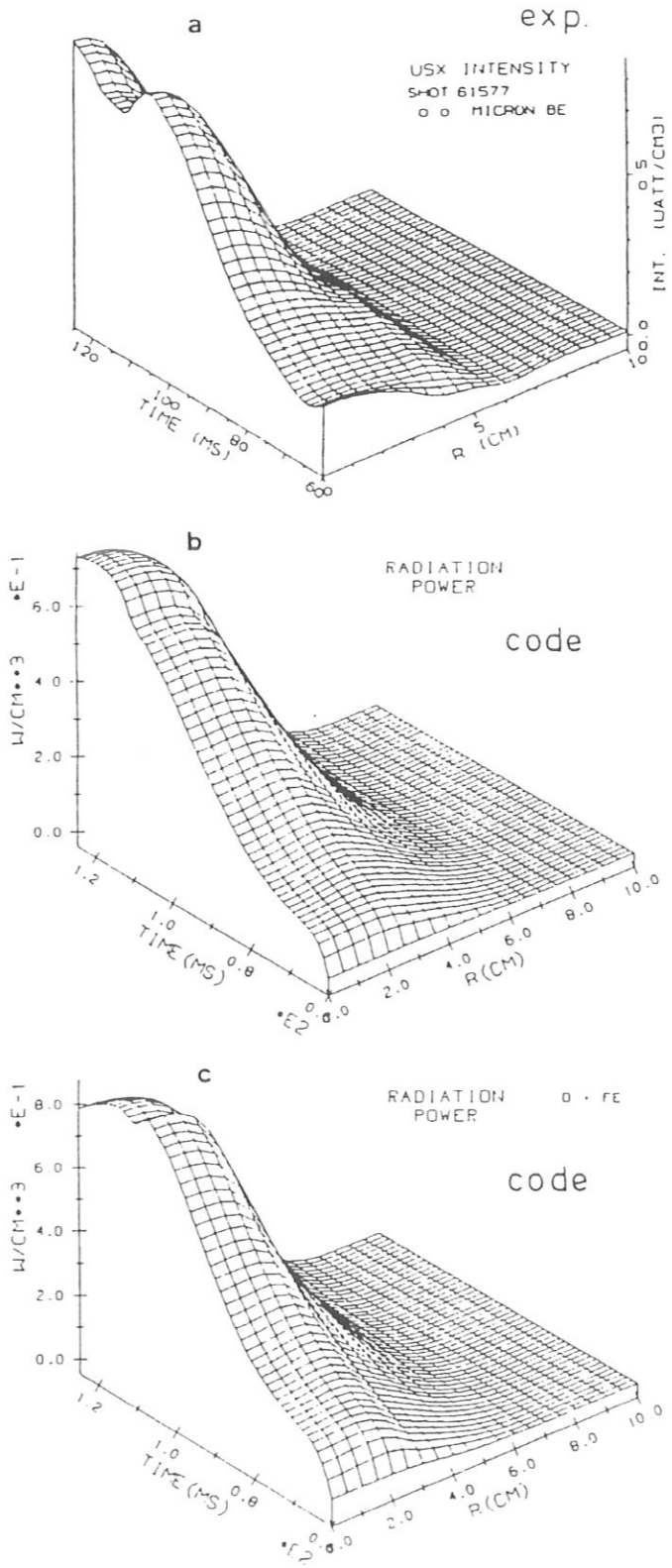

Fig. 2: a) Evolution of soft X-radiation for a NBI + EC heated discharge.
b) Code simulation with oxygen impurities and neoclassical + anomalous transport.
c) Same as b) but with additional Fe impurities.

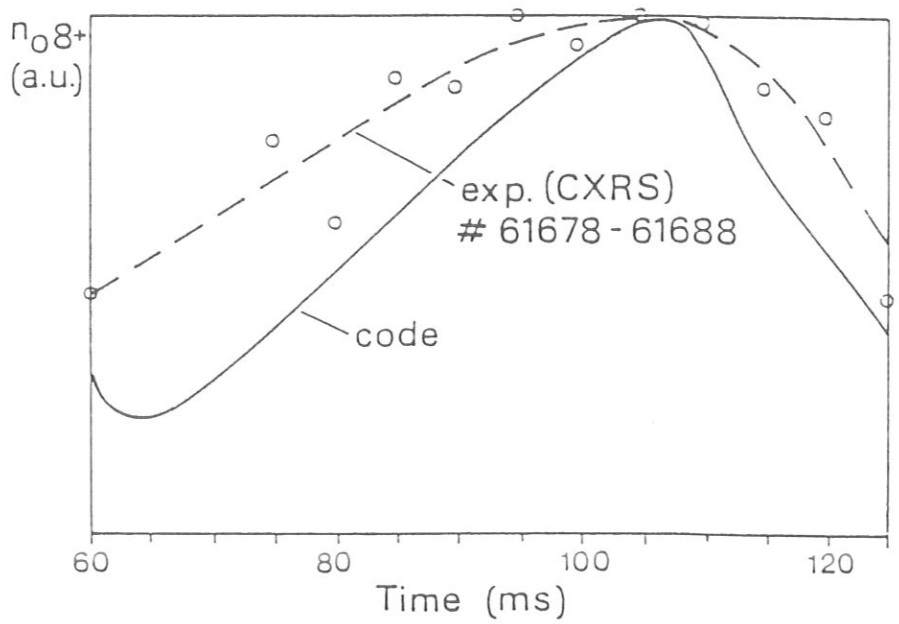

Fig. 3: Central O^{8+} density (a.u.) vs. time from active CXRS measurements in comparison with code calculations.

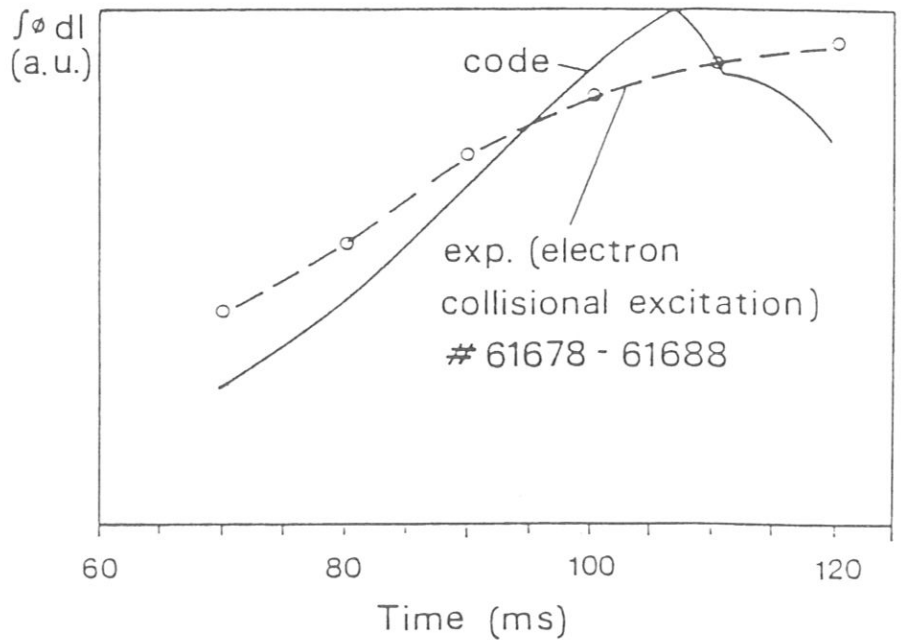

Fig. 4: Flux of OVIII (2976 Å) line intensity (a.u.) vs. time from electron excitation in comparison with code calculations.

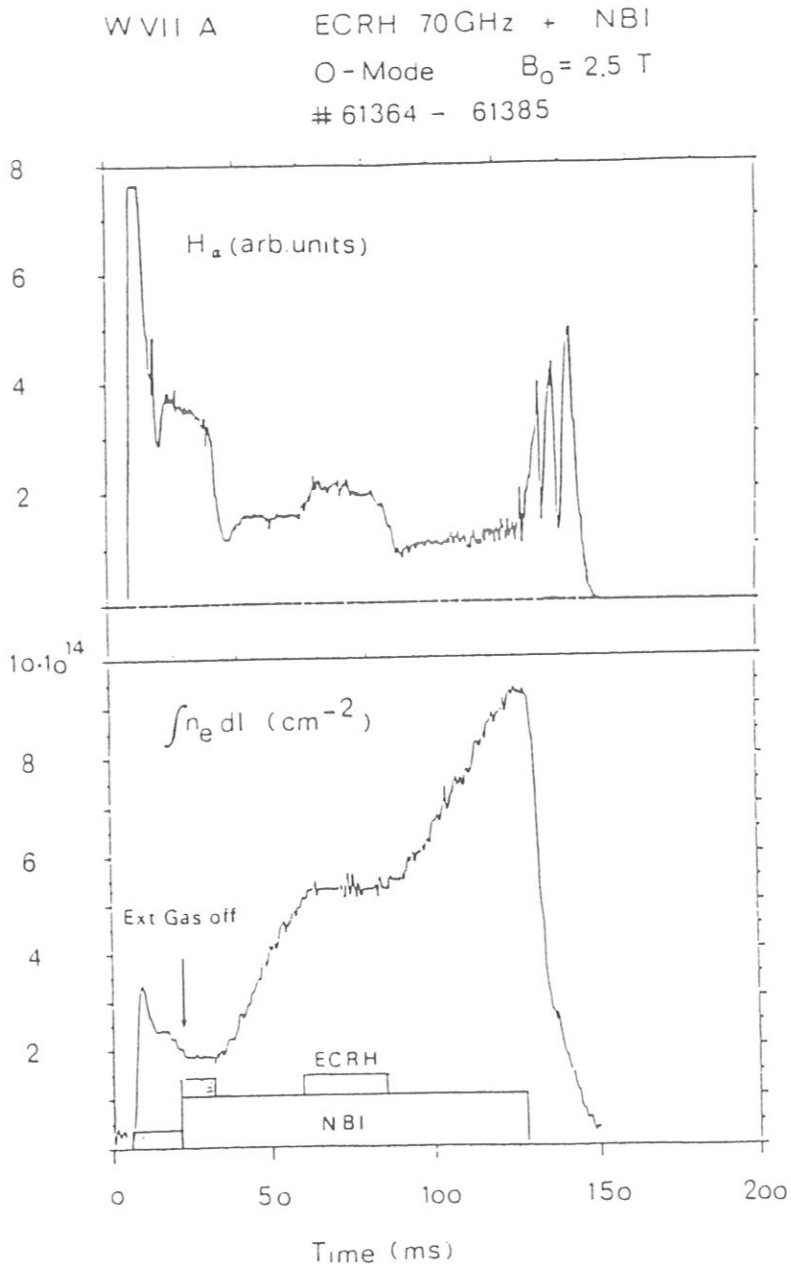

Fig. 5: H_α signal and line integrated electron density vs. time. H_α signal taken at the position of the ICRH antenna.

STELLARATOR RESEARCH - STATUS AND TRENDS

H. Wobig

Max-Planck-Institut für Plasmaphysik
EURATOM-Assc., D-8044 Garching, FRG

ABSTRACT

The paper describes the main results of currentless operation in stellarator/heliotron experiments. Various heating methods (ECRH, ICRH and NBI) with a power up to 4MW have been applied in Wendelstein VII-A, Heliotron E, L-2 and Uragan 3. Strong increase of impurity radiation terminates the discharge in NBI-heated plasmas. Toroidal currents, driven either by the plasma pressure or the heating mechanism, have been observed in several experiments. New experiments, ATF and Wendelstein VII-AS will start operation in 1987. Main aim of theoretical efforts is to increase β-limits of equilibrium and MHD-stability. This led to the Heliac concept and the concept of the Advanced Stellarator. Both in the field of torsatrons/heliotrons and advanced stellarators activity has started to plan the next generation of major experiments.

KEYWORDS

Stellarator; heliotron; torsatron; Advanced Stellarator; currentless operation; bootstrap current; helical windings; modular coils.

I. INTRODUCTION

In the last years stellarator research has made remarkable progress both in experiment and theory. Existing experiments (Heliotron E, Wendelstein VII-A, L-2, Uragan 3) have extended their capability in heating methods and heating power and new experiments (Wendelstein VII-AS and ATF) will start operation before the end of 1987. Furthermore, a new line, the Heliac, has started with a small scale experiment, Sheila, in Canberra, another one (H-I) is under construction, and a third Heliac, TJ-II in Madrid, is in its design phase. Smaller devices (Heliotron DR, IMS (Madison), Auburn Torsatron) have continued to investigate basic problems of stellarator physics and to contribute to better understanding of confinement in stellarators. Newly designed torsatrons, L2-M in Moscow and U2-M in Kharkov, have been approved and a compact helical system (CHS) is under construction in Nagoya. In this paper the generic term "stellarator" is used for all the various systems: stellarators, heliotrons, torsatrons and Heliacs.

With respect to the next generation of large stellarator experiments, two activities exist to design experiments which are at least twice as large as the existing ones. A joint team of IPP Nagoya and University Kyoto with collaboration from other universities is planning a large helical system (LHS) following the heliotron/torsatron line, whereas at the IPP Garching a modular stellarator is being planned, based on the "Advanced Stellarator" principle. In both cases the aim is to demonstrate the reactor capability of the stellarator and to investigate critical issues of its physics. In order to allow for quasi-steady state operation the magnetic field will be generated by superconducting coils.

The parameters of existing and future stellarators are summarized in table I.

Table I

	Type	l/m	B	R	$\bar{a}$	$\iota(0)/\iota(\bar{a})$
URAGAN III	Torsatron	3/9	2.5	1.0	0.135	0/0.6
L-2	Stellarator	2/14	1.5	1.0	0.115	0.2/0.7
W VII-A*	Stellarator	2/5	3.5	2.0	0.1	0.23, $\iota'=0$
HELIOTRON E	Heliotron	2/19	2.0	2.2	0.2	0.5/2.5
HELIOTRON DR	Heliotron	2/15	1.0	0.9	0.07	0.82/2.2
IMS	Mod. Stell.	3/7	0.6	0.4	0.05	0/0.6
PROTO-CLEO	Torsatron	3/7	0.3	0.4	0.05	0/0.6
AUBURN TORSATRON	Torsatron	2/	0.1-0.3	0.58	0.1	
SHEILA	Heliac	/3	0.4	0.19	0.03	1.18/1.35
CLEO**	Stell.	3/7	2.0	0.9	0.13	0/0.6
SHATLET-M	Mod.Torsatr.	2/12	0.15	0.4	0.03	0.55/0.8
	Begin of Experiment 1987					
W VII-AS	Mod. Stell.	l=1,2,3 m = 5	3.5	2.0	0.2	0.4, $\iota'\geq 0$
ATF	Torsatron	2/12	2.0	2.1	0.3	0.3/0.9
	Construction, Design, Planning					
CHS	Helical sys.	2/8	1.5	1.0	0.2	0.1/0.6
L-2M	Torsatron	2/8	2.5	1.12	0.19	0.25/0.75
U-2M	Torsatron	2/4	2.4	1.7	0.22	0.57/0.75
TJ-II	Heliac	/4	1	1.5		1.52
H-1	Heliac	/3	1	1.0	0.2	1.1/1.18
LHS	Helical sys.	2/	4	4-5	0.5-0.6	
W VII-X	Adv. Stell.		4	≥5	≥0.4	

l = number of poloidal field periods
m = number of toroidal periods,
B = magnetic field in Tesla
Mod. = Modular
R = major radius in m
$\bar{a}$ = plasma radius in m
ι = rotational transform

* no longer in operation
** stellarator-tokamak hybrid

One of the main aims of stellarator theory is to calculate 3-dimensional equilibria and to study the MHD-stability. For this purpose several numerical codes have been developed during the last years. Also transport properties of stellarator configurations have been investigated using elaborate numerical codes. In the present paper only a short overview about the main results of stellarator research will be given, a more detailed description of the present status of stellarator experiments and theory can be found in "Progress in Stellarator/Heliotron research 1981-1986" (Carreras, et al., 1987).

II. EXPERIMENTAL RESULTS

Over the last years most stellarator experiments have concentrated on the study of plasmas without net toroidal current. This state can be achieved by various methods and the procedure is well established now. The first method was to begin with an ohmically heated target plasma and to maintain the discharge either by neutral beam heating (NBI) or electron cyclotron heating (ECRH). Most frequently, however, an ECRH-generated plasma serves as a target for neutral beam heating. Besides its principal importance for stellarator research this currentless state is well suited to investigate plasma confinement without tearing modes, sawtooth oscillations and disruptions. Also small pressure driven currents (bootstrap current) or currents excited by the heating mechanism can be detected.

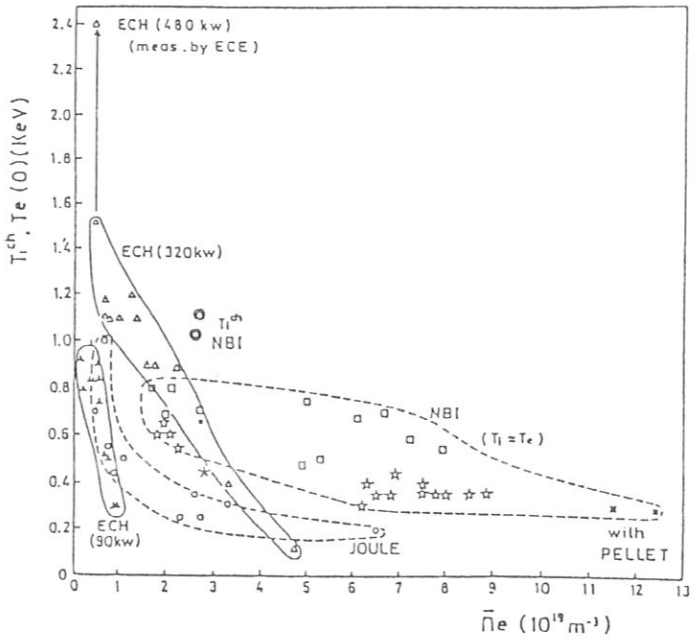

Fig. 1 Electron/ion temperature and density regime in Heliotron E, obtained by various heating methods. (Iiyoshi, 1985)

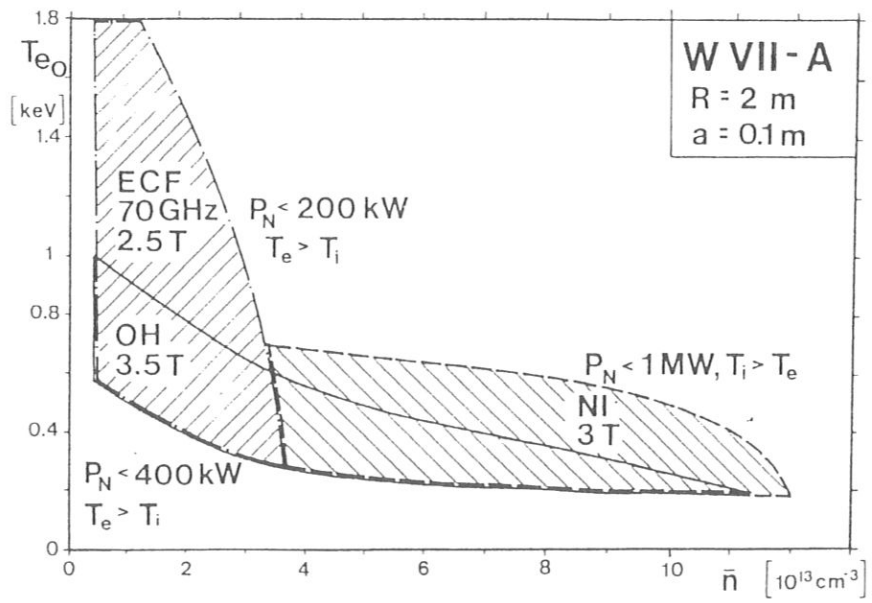

Fig. 2 Electron temperature and density regime in Wendelstein VII-A.

The following table II summarizes the various methods and scenerios which have led to currentless operation in stellarators.

Table II

ECRH	Heliotron E Heliotron DR Wendelstein VII-A IMS, L-2
ICRH	Heliotron E Uragan 3
OH + NBI	Wendelstein VII-A
OH + ECRH	L-2
ECRH + NBI	Heliotron E Wendelstein VII-A
ECRH + ICRH	Heliotron E

The term "currentless operation" needs some further explanation, since in many cases a small residual current $I \leq 3$ kA was observed without a loop voltage being applied. The maximum current of about 3 kA was measured in W VII-A in NBI-heated plasmas, and it could be verified, that the almost perpendicular injection is not responsible for this current. A similar result was found in Heliotron E (Besshou, 1984). Even in HF-heated plasmas a current smaller or equal to 2 kA was observed (Wendelstein VII-A: 1 kA, L-2: 0.7 kA, Uragan 3: 2 kA (Velikhov, 1987)). In Wendelstein VII-A only a small fraction of the current could be attributed to the ECR-heating mechanism, the main part is pressure driven (Gasparino, 1987).

The toroidal currents observed in stellarators are in the range of the neoclassical bootstrap current, the predicted dependence on plasma parameters, however, still needs to be verified. Identifying the neoclassical bootstrap current is important, because in a high-beta plasma it changes the rotational transform and may cause instabilities. So far, bootstrap current driven instabilities have not yet been observed.

In non-ohmically heated plasmas higher plasma parameters could be obtained than with ohmic heating alone. This is mainly due to larger heating power available with ICRF and NBI, and to high density attainable with pellet injection. The absence of tearing modes in this high density regime also improves the confinement. Impurity radiation, however, terminates the discharge and several methods are being studied to cope with this problem. In Heliotron E wall carbonization led to a reduction of metallic impurities and thus to a quasi steady state with neutral beam heating. In Figs. 1 and 2 the plasma parameters achieved by various heating methods are shown in the n-T-diagram. The maximum parameters reached so far in Wendelstein VII-A and Heliotron E are:

Table III

Highest value	$\bar{n}_e$ ($10^{20}m^{-3}$)	$T_i(0)$ (keV)	$T_e(0)$ (keV)	$\langle\beta\rangle$(%) at B_o(T)	$\bar{n}_e\tau_E \times 10^{18}$ ($m^{-3}\cdot s$)	P_{abs}(MW) type[a]	Device[b]
T_e	0.1	0.11	2.4	0.1 (2.5T)	0.04	0.11, ECH	W VII-A
T_i	0.26	1.6	0.66	0.3 (1.9T)	0.26	3.5, NBI	H-E
Pressure	1.2	1.0	0.7	0.45 (3.2T)	2.5	0.46, NBI	W VII-A
$\langle\beta\rangle$	0.9	0.41	0.41	2.0 (0.94T)	0.63	1.8, NBI	H-E
$\bar{n}_e\tau_E$	1.4	0.3	0.3	0.47 (1.9T)	5.0	2, NBI	H-E

τ_E = net energy replacement time, radiation losses corrected.
[a] ECH = electron cyclotron heating, ICH = ion cyclotron heating, NBI = neutral beam injection.
[b] W VII-A = Wendelstein VII-A, H-E = Heliotron E.

Experimental energy confinement times stay below 30 ms. Compared with those of present tokamaks these temperatures are small, however, considering the small plasma radius of $\leq$ 20 cm and a maximum power of 4 MW (NBI in Heliotron E) no higher parameters are expected. The highest densities ($\bar{n} \approx 10^{20}$ m^{-3} in Wendelstein VII-A and $1.8 \cdot 10^{20}$ m^{-3} in Heliotron E) are well above the density limit of ohmically heated discharges.

Currentless operation in stellarators is characterized by the absence of tearing modes and disruptive instabilities. This facilitates to study transport processes of plasma and impurities. ECR-heated plasmas, in particular, are well suited to investigate electron energy transport, because in the energy balance ions play a minor role and radiation losses remain small. In both experiments, W VII-A and Heliotron E, the electron temperature follows roughly the scaling law as predicted by neoclassical confinement, however, the profile analysis of $T_e(r)$ requires an anomalous electron thermal conductivity in the outer plasma region, whereas in the central region the temperature profile can be explained by neoclassical transport including the effect of helical ripple (Wobig, 1986; Zushi, 1984). A similar conclusion has been drawn for ECR-heated plasmas in L-2 (Dyabilin, 1985). A detailed comparison of energy confinement in stellarators and tokamaks is given in a recent paper (Lackner, 1987). Since the observed anomaly of electron thermal conduction exists in currentless plasmas, and - as is suggested from Wendelstein VII-A results (Wobig, 1986) - follows the same scaling law as in ohmically heated discharges, the underlying mechanism must be independent of the toroidal current.

One reason for the anomaly could be destruction of magnetic surfaces in the boundary region, but also density fluctuations, as have been observed in Wendelstein VII-A in the range of 50-3000 kHz (Müller, 1984), could be responsible for these anomalous losses.

In NBI-heated plasmas large radiative losses aggravate the electron energy balance. This regime of stellarator research is more appropriate for the analysis of ion energy balance. There is agreement between both experiments, Wendelstein VII-A and Heliotron E, that the slowing-down process of injected ions is the result of Coulomb collisions. The analysis of ion energy balance has to rely on the computed power deposition profile, which, because of the essential role of the mostly unknown radial electric field, is only known with error bars. Nonetheless, the analysis shows, that the ion thermal conductivity agrees roughly with neoclassical coefficients, where the beneficial effect of the radial E-field has to be taken into account (Wobig, 1986). The dominant effect of a radial electric field is to reduce the radial excursions of ripple trapped particles and thus leading to a smaller radial transport. In a device with large aspect ratio like Wendelstein VII-A, however, also those circulating particles in the boundary layer between circulating and trapped particles are affected by the electric field, which results in reduced transport coefficients even in the plateau regime.

Currentless plasmas without sawtooth oscillations or minor disruptions offer a good chance to study transport of impurities. In Heliotron E, W VII-A and L-2 inward diffusion of impurities released from the wall have been analysed and compared with theory. Furthermore silicon and titanium have been introduced by laser blow-off technique and the time evolution has been compared with computer simulation. There is agreement that transport of impurities can be described by the neoclassical process and an inward convective term. $D \approx 1000 - 3000$ cm^2/s, and $v \approx 1000$ cm/s are typical values of these quantities in W VII-A (Ringler, 1986). This inward flow of impurities, predominantly oxygen in W VII-A and iron in Heliotron, causes a strong increase of radiative power loss and thus a termination of NBI-heated discharges. Wall carbonization in Heliotron E could reduce the iron content by more than a factor of ten and a quasi steady state discharge became possible (Uo, 1986). Another interesting effect is the influence of an ECR-pulse on inpurity accumulation. As observed in Wendelstein VII-A, the ERC-pulse in a NBI-heated discharge stops further increase of density and radiative power. In Heliotron E the confinement time of impurities (Si) was diminished. No explanation for these results exists so far. In purely ECR-heated plasmas impurity radiation only plays a minor role and does not seriously limit the discharges.

Degradation of confinement with increasing auxiliary heating power is a phenomenon observed in many tokamaks. In stellarators results on this problem are not unique and differ from experiment to experiment. In Wendelstein VII-A auxiliary heating at moderate power leads to higher confinement times than in ohmically heating discharges. This result was observed with NBI-heating and with ECR-heating. In purely currentless plasma such a clear result could not be obtained, more or less the confinement time stays independent of the heating power. From Heliotron E (Uo, 1986) a degradation of confinement time in NBI-heated plasmas is reported. It should be noticed, however, that neoclassical confinement time in stellarators degradates with growing temperature, which is caused by locally trapped particle losses. Replacing the temperature by heating power yields a confinement time which decreases with heating power. Therefore any deviation from neoclassical confinement has to be found from a careful analysis of the experimental scaling laws or the temperature profiles.

The different scaling between Heliotron E and Wendelstein VII-A may be understood from the differences in aspect ratio, iota-profile, heating power and beta-regime, however, further

...in an extended parameter regime are needed to clarify this important issue. In this respect valuable contributions are expected from the new experiments under construction.

Beta limits in stellarator have always been in the focal point of interest. In currentless operation pressure driven instabilities are expected to limit the maximum plasma pressure. For Wendelstein VII-A no information on this subject is available, since even at the highest beta-value of $\beta(o) \approx 1$ % no macroscopic instability was observed. This number is close to the value expected from the onset of the resistive interchange instability. In Uragan 3 (Pavlichenko, 1986) the plasma became unstable at an average beta of 0.6 %, a similar result is reported from Heliotron DR (Morimoto, 1986). The most elaborate analysis of beta-limits has been done in Heliotron E (Uo, 1986) where a maximum averge beta of 2 % could be obtained. Depending on the peakedness of the pressure profile sawtooth oscillations and 1/1-modes and 3/2-modes were observed (socalled S-mode). With a broad pressure profile a quiescent phase (Q-mode) could be achieved, however, recent results (Takeiri, 1987) indicated that plasma fluctuations occur when higher beta-values with a broad pressure profile are attempted to be reached. These experimental results are in good agreement with a theoretical analysis of Wakatani, Ichiguchi (Wakatani, 1986) and Johnson, Rewoldt (Johnson, 1986). According to the theory of Wakatani, the plasma pressure in Heliotron E is limited by the occurence of the resistive interchange instability on the rational surface with $\iota = 2/3$, which leads to internal disruptions. These results demonstrate the importance of resistive interchange modes in determining the maximum beta in stellarators. There remains the open question, whether the resistive interchange mode sets a hard limit, or whether it only results in an enhanced plasma loss, which can be compensated by more heating power thus raising the plasma pressure beyond the stability limit. Such an effect of resistive pressure-gradient driven turbulence on plasma transport has been calculated by Carreras et al. (Carreras, 1986).

For good plasma confinement in stellarators the existence of undestroyed magnetic surfaces is of great importance. As is well-known, small error fields can generate magnetic islands on rational magnetic surfaces. In small shear systems these islands are larger than in high shear systems, however, in high shear systems islands overlapping and onset of stochasticity may occur. Recently in several devices (Uragan 3 (Gutarev, 1986), Heliotron E (Takahashi, 1986), Auburn torsatron (Swanson, 1986)) magnetic islands and stochastic areas could be detected, and in the low-shear stellarator Wega (Heiler, 1987) large islands caused by a small displacement of the helical windings relative to the toroidal field coils could be found.

Such kind of island formation is now believed to be the reason, why low-shear systems like Wendelstein VII-A exhibit a strong dependence on the external rotational transform (Wobig, 1986). The presence of islands modifies the plasma equilibrium and leads to enhanced collisional and convective losses. In the close vicinity of low order rational surfaces ($\iota = 1/3, 1/2$), however, only high order rational surfaces exist. On these surfaces negligibly small islands may arise which have little or no effect on plasma confinement. This feature qualitatively explains the Wendelstein VII-A results, where close to low order rational values of the rotational transform optimum confinement was found.

Concluding from these results low-shear stellarators must be carefully designed to avoid low order rational surfaces in the vacuum field and to prevent a modification of the rotational transform by finite beta effects or by the bootstrap current.

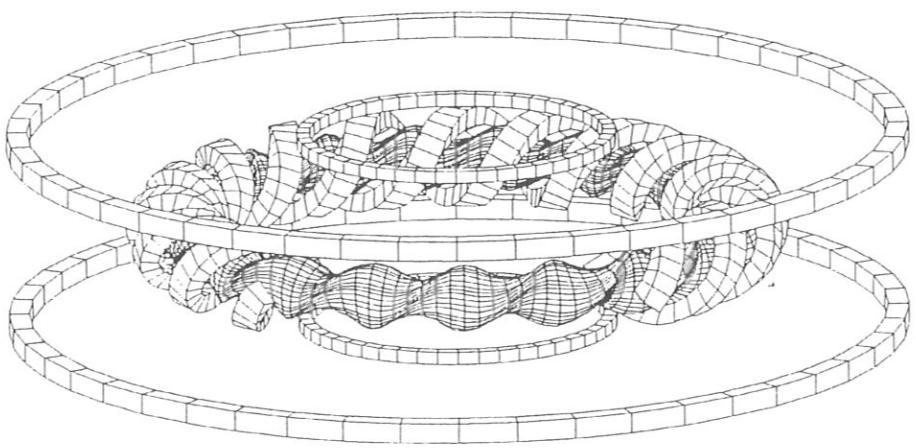

Fig. 3 Coil system and magnetic surface of a heliotron/torsatron experiment.
l = 2 helical windings, 19 field periods.

III. FUTURE EXPERIMENTS AND REACTOR STUDIES

Besides Heliotron E (see Fig. 3), which will continue to operate in the next years, two more major devices will contribute to stellarator research and extend the parameter regime beyond its present limits. These are ATF in Oak Ridge and Wendelstein VII-AS in Garching, both are finishing construction phase and are scheduled to start operation still in 1987. The geometrical data are given in table I. In both devices there will be sufficient power available to test the beta-limits and to extend the collisionality into the long-mean-free-path regime, where localized trapped particles dominate neoclassical confinement. ATF is a 12-period, $l = 2$ torsatron with a rotational transform of 0.3 on the axis and 0.9 at the boundary, the shear is moderate and occupies the intermediate regime between the very low shear of Wendelstein VII-AS and a high shear system like Heliotron E. A major aim of the ATF-experiment is to test MHD-stability in the second stability regime where the m=1/n=1 internal mode should be stable up to $\langle\beta\rangle=8\%$. The path to the second stability regime requires a control of the ι-profile during the rise phase of beta, which will be provided by the flexibility of the poloidal field. Furthermore ATF is capable of steady state operation at $B = 1T$ thus allowing investigation of long term plasma confinement.

Wendelstein VII-AS, a stellarator with modular twisted coils instead of helical windings, will aim at testing the effect of reducing Pfirsch-Schlüter currents and Shafranov shift. This has also a favorable effect on the beta limit defined by the resistive interchange criterion. In Wendelstein VII-AS this limit is expected around $\langle\beta\rangle = 2\%$, which should be achievable with the available heating power. For reactor purposes, however, such a low beta limit is too small and therefore reduction of Pfirsch-Schlüter currents and deepening of the magnetic wall has to be continued with the aim of higher stability limits. The results of these theoretical efforts will be described later in this paper.

In Canberra a 3-period Heliac device H-1 is under construction and will start in 1988. This will be the first major experiment to test the potential of this line. The objective of the experiment is to investigate a low beta plasma, its confinement properties as a function of the magnetic field. As already indicated by the small experiment Sheila, rational magnetic surfaces show degradation of confinement. H-1 has as small shear and a similar critical dependence on the rotational transform as found in Wendelstein VII-A has to be expected. Another Heliac experiment, TJ-II in Madrid, is in its design phase and may start operation in 1990. With a major radius of $R = 1.5$ m it is larger than the Australian experiment, the magnetic field is the same ($B \approx 1T$). Instead of 3 field periods in TJ-II there are 4 field periods (see Fig. 4). This difference in the number of field periods should also raise the beta limit against resistive interchange modes, which is expected to

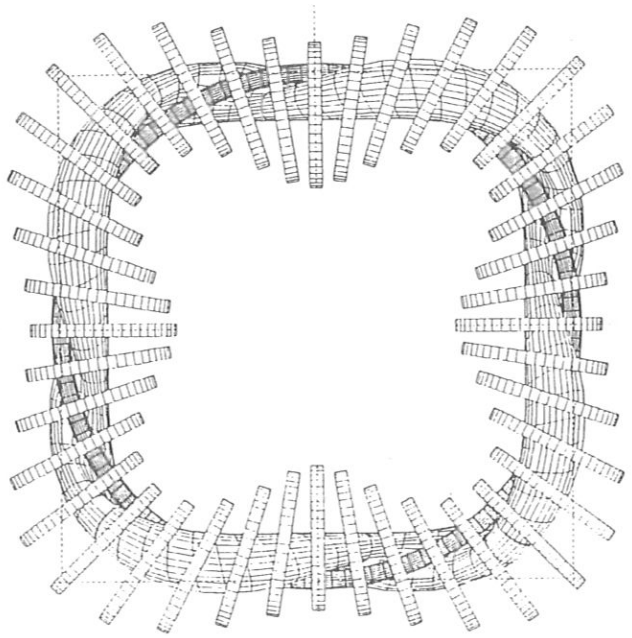

Fig. 4 Coil arrangement and magnetic surface of a 4-period heliac experiment. Field lines on the magnetic surface are shown.

be rather high (20-30%) in a system close to straigth helical symmetry. In a Heliac typical values of the rotational transform are larger than one, therefore Pfirsch-Schlüter currents are small and so is the Shafranov shift. Consequently, equilibrium limits resulting from a large Shafranov shift are no matter of concern in Heliacs.

In a recent paper by NÜhrenberg, Zille and Hirshman (NÜhrenberg, 1987) the resistive interchange stability limit of Heliac with different number of field periods was calculated. For TJ-II a critical beta of 2% was found, in a 8-period configuration already $\langle\beta\rangle_{crit.} \sim 5\%$ may be expected. In its first phase the TJ-II experiment is equipped with 400 kW ECR-heating power. This is not enough to achieve beta close to the stability limit, therefore in this phase confinement in the long-mean free path regime is one of the main issues. Another important objective is, as in H-1, to vary the magnetic field (rotational transform, shear, magnetic well) and investigate the effect on confinement. The device is equipped with various systems of independent currents to modify the magnetic field in a wide parameter regime.

Along the heliotron/torsatron line several new experiments are being planned. One of these is the low-aspect ratio device CHS (Compared Helical System) in Nagoya. This configuration is an 8-period $l = 2$ - torsatron with helical windings. For the data see table I. From the reactor point of view a small aspect ratio ($A = 5$) is attractive, since it reduces the weight of the reactor core. However, the main motivation of selecting a low number of field periods is the reduction of the helical ripple and its effect on trapped particle losses, improvement of MHD-stabilities by a magnetic well and access to the second stability regime. Recent theoretical studies by Carreras et al. (Carreras, 1986) showed that in low-aspect ratio torsatrons ($m = 6$) the equilibrium limit can be raised to $\langle\beta\rangle = 5\text{-}7\%$ by making use of the Cary-Hanson technique to prevent stochasticity of the outer magnetic surface by appropriate shape of the helical windings.

In the CHS-experiment several heating scenarios are foreseen (NBI(2MW), ECRF(200kW), ICRF(500kW)), so that many aspects of this configuration can be investigated.

In the Soviet Union two new torsatron experiments are being planned, Uragan 2-M in Kharkov and L-2M in Moscow. Uragan 2-M has 4 field periods only, therefore the shear is moderate and MHD-stability depends very much on the magnetic well. Flexibility of the experiment is provided by additional toroidal field coils and a vertical field. The main heating method will be ICRH. The L-2M device planned in Moscow also is an $l = 2$ torsatron with similar objectives as Uragan 2M.

The trend with torsatrons is to abandon $l = 3$ systems because small or zero transform in the plasma center makes the configuration susceptible to island formation and large Shafranov shift with finite beta. In all new devices under construction the rotational transform on the axis is finite.

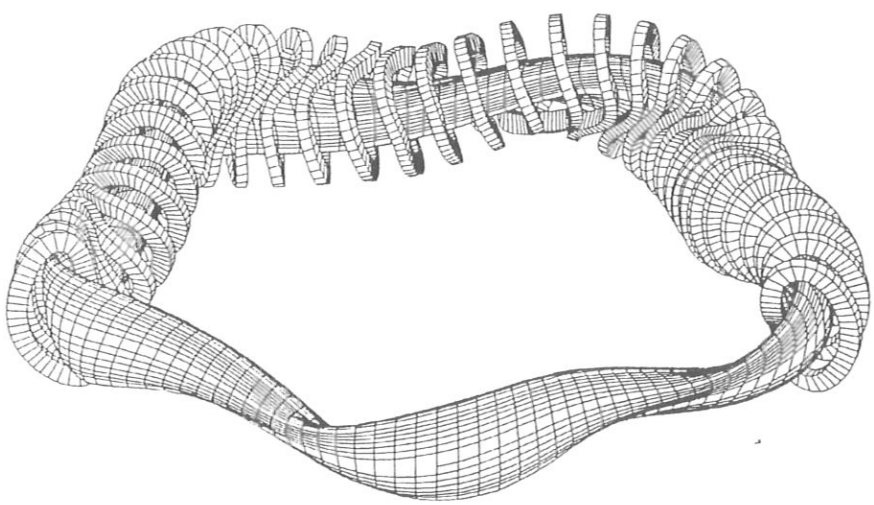

Fig. 5 Coil system and magnetic surface of a 5-period Helias configuration (HS-5-3).

In Garching future planning has concentrated on a modular Advanced Stellarator with higher β-limits than in Wendelstein VII-AS. As a synthesis of a Heliac with helical axis and modular Advanced Stellarator with reduced Pfirsch-Schlüter currents the Helias concept was developed (Nührenberg, 1986). Helias stands for helical Advanced Stellarator. By proper shaping of the magnetic surfaces Pfirsch-Schlüter currents $J_{\parallel}$ can be made smaller than the diamagnetic currents $J_{\perp}$ resulting in a very small Shafranov shift even at an average beta of 9% (Dommaschk, 1986). Stability against resistive interchange modes is provided by the magnetic well and the small Pfirsch-Schlüter currents which occur in the denominator of the critical beta. It is believed that besides the good equilibrium and the stability properties also the transport can be optimized: not only in the plateau region but also in the long mean free path regime. This especially means to employ the idea of the so-called σ-optimized stellarator by Mynick et al. (Mynick, 1982) where localized particles have small radial drift, thus leading to small losses in the long mean free path regime. Finite β-effects may even improve this effect. In a recent paper (Rau, 1987) an example of a 4-period Helias vacuum field (HS-4-8) is given, where strong reduction of Pfirsch-Schlüter currents and σ-optimisation of trapped particle orbits is simultaneously achieved.

Another important aim is to reduce the neoclassical bootstrap current. According the theory of Shaing, Callen, Hirshman (Shaing, 1986) and Shaing, Solano (Rodriguez-Solano, 1987), the neoclassical bootstrap current depends on all helical harmonics of the stellarator field, it even may change sign compared to its axisymmetric tokamak limit. In the above mentioned Helias HS-4-8 a neglibly small bootstrap current has been calculated. It is believed that the parameter space of stable Helias equilibria with $\langle\beta\rangle$ = 5-9% is large enough to allow reduction of all neoclassical effects in the long mean free path regime including the bootstrap current. As a successor of the Wendelstein VII-AS a large experiment Wendelstein VII-X is being planned following the Helias concept. The aim of this experiment is to demonstrate the reactor capability of a modular stellarator, especially the quasisteady state, stable beta above 5% and sufficient confinement in the long mean free path regime.

The dimensions of the experiment are not yet fixed. In order to allow sufficient heating power (P ≈ 20-30 MW), to drive the plasma parameters to a reactor relevant regime, the device has to be at least 2 to 3 times larger than the Wendelstein VII-AS experiment.

In Japan a similar planning activity is under way to design a larger experiment along the heliotron/torsatron line. A joint design team of the universities of Kyoto, Hiroshima, Tokyo and the IPP Nagoya has been established in order to develop the concept of a large proof-of-principle experiment (Large Helical System, LHS). Also the exact size of this experiment is not yet fixed, it will at least be twice the size of Heliotron E. The aims are very similar to those of Wendelstein VII-X, however, due to the difference in their magnetic field configurations also different plasma behavior has to be expected.

Because in both experiments quasi-steady state is one of the main aims, a stationary magnetic field produced by superconducting coils is seriously deliberated. This poses different technical issues to both experiments. The modular coils of Wendelstein VII-X are smaller components than the helical windings of an equal-size torsatron. For this reason superconducting joints are a main technical issue in a large torsatron experiment or reactor. Deuterium-Tritium operation is not foreseen in both experiments, this would introduce further problems and technical difficulties concerning shielding and safety. Since α-particle heating is expected to be same in stellarators and tokamaks there is also no need to duplicate experiments which are scheduled already in tokamaks.

It cannot be said in advance which of the four lines, Advanced Stellarators, heliotrons, torsatrons and Heliacs will be the most successful. In the world wide stellarator programme all four lines are being investigated, they are largely complementary in the selected properties of their magnetic field configurations. The next generation of experiments will certainly provide an essential step in selecting the optimum stellarator concept.

Compared with tokamak reactor studies only a small number of papers on stellarator reactor issues have been published. A good survey of current literature can be found in "Progress in Stellarator/Heliotron research: 1981-1986 (Carreras 1987). Critical issues of an Advanced Stellarator reactor have been studied in a joint paper of IPP Garching, KfK Karlsruhe and Fusion Power Assoc. Madison (Böhme, 1987). In this paper only some aspects of stellarator reactors will be discussed for further details the reactor is referred to current literature. The aspect ratio of stellarators usually is larger than 10, only in a torsatron reactor with a low number of field periods the aspect ratio can be made smaller than 10 (Houlberg, 1986). For this reason stellarator reactors tend to be comparatively large devices with a major radius of 15 m to 25 m. On one hand this affects the economics of the reactor negatively, on the other hand wall loading is smaller ($P \approx 2\ MW/m^2$) than in compact devices like low-aspect ratio tokamaks. These circumstances together with the envisaged steady-state operation may lead to longer life time of first wall and blanket.

Because the geometry of the various stellarator configurations is so different, the problem of maintenance and repair, exchange of first wall and blanket modules has to be solved separately for each configuration. In a torsatron reactor the superconducting helical winding are considered as permanent components, any modularization requires demountable superconducting joints. In the Advanced Stellarator reactor or in modular torsatrons this problem is circumvented by dividing the coil set in different modules which are withdrawn to give access to first wall and blanket. This solution has been studied for UWTOR-M (Sviatovslavsky, 1981) and ASRA 6C (Böhme, 1987). Heliac or Helias configurations have not yet been investigated in this respect. Before the optimum configuration from the physics point of view is not known, any detailed study of these technical issues would be premature.

Ignition of the stellarator reactor requires a sufficient long confinement time, however, prediction of confinement time in a reactor is only relevant on the basis of neoclassical transport processes, since anomalous losses are not understood and reliable scaling laws are not available. Anomalous losses, as found in Wendelstein VII-A, would not endanger confinement in the reactor, because of their favourable temperature dependence. Present reactor studies assume neoclassical loss mechanisms and they demonstrate that in a reactor with minor radius between 1.5 m and 2 m ignition is possible. Thereby it is of particlular importance, that localized ion losses are reduced by a radial electric field. Therefore, to clarify the behaviour of this electric field is one of the principal tasks of future experiments and theory.In order to provide sufficient fusion power output, a reactor should not operate with an average beta below 5 %. In all reactor studies, so far, this value or higher ones were anticipated, since, as has been described above, experiments have reached a beta of 2 %, and only future experiments will push beta into the reactor regime. Theoretical progress in the last years, however, demonstrated the existence of MHD-stable stellarator equilibria with beta above 5 %, and the question remains, which other effects may lead to smaller MHD-beta limit.

Impurity radiation is a threat to steady state operation of a stellarator reactor. In a torsatron/ heliotron there exists a seperatrix-like structure outside the last magnetic surface, which could be used for divertor action, the same is true for Heliacs. In Advanced Stellarators with stronger deviation from axisymmetry the surroundings of the last magnetic is more or less ergodic with inbedded islands. Any active or passive means of impurity control has to take into account this magnetic field topology. From present experiments only little experience exists about control of impurity inflow, main interest sofar was in understanding the transport of impurities. Impurity accumulation is a common problem of stellarators and tokamaks, and any method to reduce impurity contents in the plasma may be applicable in both devices.
These few remarks may be sufficient to illuminate present knowledge of a stellarator reactor.

SUMMARY AND CONCLUSIONS

The present article gives a short outline of major results in stellarator research and describes new trends and future development. During the last years in existing experiments great progress has been made in

- successful application and understanding of various heating mechanisms
- achieving currentless operation by various heating mechanisms
- sustaining quasi-steady state at high density without disruption
- achieving plasma parameters higher than with ohmic heating
- analysing and understanding transport of plasma and impurities
- exploring the beta limits
- developing three-dimensional codes for computing equilibrium and stability
- improving neoclassical transport theory and developing numerical codes

New ideas, concepts and methods have been worked out

- how to improve beta-limits of equilibrium and stability
- how to reduce neoclassical losses and the bootstrap current
- how to find modular coils or helical windings for optimized vacuum fields

However it should be noticed, that in spite of these successes the distance from the present generation of experiments and the achieved parameter regime to the reactor regime is still large and extrapolations to the reactor regime have to be made with caution. There are still several critical issues which might endanger the very existence of a steady state stellarator reactor. In particular these are:

- Insufficient control of impurities which prevents steady state operation.
- Degradation of confinement at high beta.
- Destruction of magnetic surfaces at high beta.
- Occurrence of drift instabilities and trapped particles instabilities resulting in enhanced electron losses.
- Insufficient control of the bootstrap current and modification of the ι-profile.
- Anomalous losses of α-particles.

The new generation of experiments (ATF, Wendelstein VII-AS) will certainly extend the parameter regime and yield new results on stability and confinement. Further experiments including the Heliac are under construction and the next large steps, ATF-II, LHS and Wendelstein VII-X, are being planned.

The field of stellarators is characterized by a large variety of configurations, everyone with its own merits, advantages and disadvantages. On one hand this large spectrum offers the chance to find a configuration with many optimized properties, on the other hand it is impossible to explore all alternatives appropriately with a limited budget, personal and time.

International collaboration has made it possible that the four major lines are investigated in parallel and are being further developed. At least three of them offer good prospects for a steady-state fusion reactor.

REFERENCES

Besshou, S., et al., (1984). Plasma Phys. 26, 565.

Böhme, G., et al., (1987). Studies of a Modular Advanced Stellarator Reactor ASRA &C, Report IPP 2/285, KfK 4268, FPA-87-2.

Carreras, B.A., et al., Progress in Stellarator/Heliotron research: 1981-1986, to be published in Nuclear Fusion.

Carreras, B.A., L. Garcia, L.H. Charlton, J.A. Holmes, V.E. Lynch, P.H. Diamond, (1986). 11th Int. Conf. on Phys. and Contr. Thermonucl. Fus., Kyoto, Nov. 13-20 1986, IAEA-CN-47/D-V-2.

Carreras, B.A., et al., (1986). Proc. Int Stellarator/Heliotron Workshop, Kyoto, Nov. 25-28 1986, Japan PPLK-6, Vol. II, p.319.

Dommaschk, W., F. Herrneggger, W. Lotz, P. Merkel, J. Nührenberg, A. Schlüter, U. Schwenn, R. Zille, (1986). 11th Int. Conf. on Phys. and Contr. Thermonucl. Fus., Kyoto, Nov. 13-20 1986, IAEA-CN-47/D-I-3.

Dyabilin, K.S., L.M. Kovrizhnykh, (1985). Plasma Physics and Contr. Fusion Research, Proc. 10th Int. Conf. London 1984, Vol. II, IAEA, Vienna 1985.

Gasparino, U., H. Maassberg, H. Tutter, M. Räuchle, et al., (1987). 14th European Conf. on Contr. Fusion and Plasma Phys., Madrid, 22-26 June 1987, Europhys. Conf. Abstracts, 11D, Part 1, 818.

Gutarev, Ju.V., et al., (1986). Proc. Int. Stellarator/Heliotron Workshop, Nov. 25-28 1986, Kyoto, Japan PPLK-6, Vol.I, p.233.

Heiler, H., J. Massig, F. Schuler, K. Schwörer, H. Zwicker, (1987). 14th European Conf. on Contr. Fusion and Plasma Phys., Madrid, 22-26 June 1987, Europhys. Conf. Abstracts, 11D, Part 1, 818.

Houlberg, W.A., J.T. Lacatski, N.A. Uckan, (1986). Fusion Technology, Vol. 10 (1986), 227.

Iiyoshi, A., (1985). Basic Physical Processes of Toroidal Fusion Plasmas, Aug. 26 - Sept. 3 1985, Varenna, EUR 10418 EN, Vol. II, p. 451.

Johnson J.L., G. Rewoldt, (1986). Proc.Int.Stellarator/Heliotron Workshop, Kyoto, Nov. 25-28 1986, Japan PPLK-6, Vol. I, p.233.

Lackner, K., H. Wobig, (1987). 14th European Conf.on Contr.Fusion and Plasma Phys., Madrid, 22-26 June 1987, invited paper.

Morimoto, S., et al., (1986). Proc.Int.Stellarator/Heliotron Workshop, Nov. 25-28 1986, Kyoto, Japan PPLK-6, Vol.I, p.197.

Müller, G., W VII-A Team, (1984). Proc.Int.Workshop on Stellarators, Sept. 24-28 1984, Ringberg, EUR 9618 EN VOL. II, 437.

Mynick, H.E., T.K. Chu, A.H. Boozer, (1982). Phys.Rev.Lett. 48, 322.
Nührenberg, J., R. Zille, S.P. Hirshman, (1987). 14th European Conf. on Contr. Fusion and Plasma Phys., Madrid, 22-26 June 1987, Europhys. Conf. Abstracts, 11D, Part 1, 415.
Nührenberg, J., R. Zille, (1986). Phys.Rev.Lett. 114A, 129.
Pavlichenko, O.S., (1986). Proc. Int. Stellarator/Heliotron Workshop, Nov. 25-28 1986, Kyoto, Japan PPLK-6, Vol.II, p.398.
Rau, F., e. Harmeyer, F. Herrnegger, J. Kisslinger, A. Montvai, H. Wobig, (1987). 14th European Conf. on Contr. Fusion and Plasma Phys., Madrid, 22-26 June 1987, Europhys. Conf. Abstracts, 11D, Part 1, 411.
Ringler, H., F. Sardei, A. Weller, W VII-A Team (1986). 11th Int.Conf. on Phys.and Contr. Thermonucl.Fus., Kyoto, Nov. 13-20 1986, IAEA-CN-47/D-V-1.
Rodriguez-Solano, E., K.C. Shaing, (1987). Phys.Fluids 30 (1987), 462.
Shaing, K.C., S.P. Hirshman, J.D. Callen, (1986). Phys.Fluids 29, 520.
Sviatovslavsky, I., et al., (1981). IEEE Trans.on Plasma Science 4, 163.
Swanson, D.G., R.F. Gandy, G.J. Hartwell, M. Henderson, (1986). Proc. Int. Stellarator/Heliotron Workshop, Nov. 25-28 1986, Kyoto, Japan PPLK-6, Vol.I, p.238.
Takahashi, R., et al., (1986). Proc. Int. Stellarator/Heliotron Workshop, Nov. 25-28 1986, Kyoto, Japan PPLK-6, Vol.I, p.220.
Takeiri, V., F. Sano, O. Motojima, M. Sato, S. Sudo, et al., (1987). 14th European Conf. on Contr. Fusion and Plasma Phys., Madrid, 22-26 June 1987, Europhys. Conf. Abstracts, 11D, Part 1, 349.
Uo, K., et al., (1986). 11th Conf.on Phys.and Contr.Thermonucl.Fus., Kyoto, Nov. 13-20 1986, IAEA-CN-47/D-I-1.
Velikhov, E.P., K.B. Kartashev, V.D. Ryutov, N.S. Cheverev, (1987). Woprosü Atomnoi Nauki i Techniki. Termojadernüi Sqntez, WÜp.1, 3.
Wakatani, M., K. Ichiguchi, (1986). Proc. Int. Stellarator/Heliotron Workshop, Nov. 25-28 1986, Kyoto, Japan PPLK-6, Vol.I, p.310.
Wobig, H., W VII-A Team, (1986). 13th European Conf. on Contr. Fusion and Plasma Phys., Schliersee, 22-26 June 1986, Europhys. Conf. Abstracts, 11D, Part 1, 818.
Wobig, H., H. Maassberg, H. Renner, W VII-A Team, (1986). 11th Conf.on Phys.and Contr.Thermonucl.Fus., Kyoto, Nov. 13-20 1986, IAEA-CN-47/D-I.
Zushi, H., et al., (1984). Nucl.Fusion 24, 305.

PHYSICS STUDIES FOR HELICAL-AXIS ADVANCED STELLARATORS

G. GRIEGER, C. BEIDLER, E. HARMEYER, J. JUNKER,
J. KISSLINGER, W. LOTZ, P. MERKEL, A. MONTVAI*,
J. NÜHRENBERG, F. RAU, A. SCHLÜTER,
H. WOBIG, R. ZILLE

Max-Planck-Institut für Plasmaphysik, IPP-EURATOM Association
D-8046 Garching near Munich, FRG
* Central Research Institute for Physics, H-1525 Budapest, Hungary

Abstract

– Various HELIAS configurations (= HELIcal Advanced Stellarator) are known with $M = 4$ to 6 field periods. Wendelstein VII-X , the future large Garching stellarator experiment, will employ a Helias configuration with $M = 5$. – Helias systems can be typified between the two limiting cases, linked-mirror configurations and quasi-helical configurations, according to their different structure of $mod\, B$ on the magnetic surfaces. Stability calculations have shown that resistive interchange and ideal ballooning modes are stable up to $\langle\beta\rangle \approx 5\%$ in Helias configurations with 5 field periods and aspect ratio $A \approx 10$. – Monte Carlo computations of neoclassical transport have been developed to the stage that confinement times of a finite-β lmfp quasi-neutral Maxwellian plasma with an assumed radial electric field can be estimated. The studies show that Helias stellarators may be found which are characterized by an equivalent ripple smaller than 2% at half the plasma radius. Monte Carlo simulations have also been used to obtain a preliminary assessment of the bootstrap current in the lmfp regime. Other transport studies are concerned with the solution of the bounce-averaged Fokker-Planck equation for Helias configurations and with heating scenarios obtained in a simple 1D transport code which allows for additional radiative losses. For neoclassical losses and anomalous ones at the edge, typical values of $\langle\beta\rangle = 5$ % are attained with a power of 20 MW at $B = 2$ to 2.5 T , at densities of about 10^{20} m^{-3}, and peak temperatures around 5 keV. – Applications of the Neumann problem for vacuum magnetic fields of stellarators have led to improvements in the structure of magnetic surfaces, of the structure of island chains bounding the confinement region, in computing free-boundary equilibria, and in the search for modular coils. These are then slightly modified according

to additional constraints. – Engineering studies of superconducting coil systems for Helias configurations have shown that the lateral force components can reach the magnitude of meridional force components which exhibit helicity in accordance with the helix-like magnetic axis. In a case with 4 periods, 12 coils per period, $R_0 = 5$ m, $B_0 = 4$ T, current density in the coils $j_c = 40$ MA/m^2, the maximum net coil force amounts to approximately 4 MN. Studies of mechanical stresses show that all components of the stress tensor are important and amount to a maximum von-Mises stress of about $\sigma_{vM} \approx 110$ MPa , and a maximum shear stress of about 1/3 of this value inside the coils.

1. Introduction

Optimization of advanced stellarators towards the definition of the future large Garching stellarator experiment WENDELSTEIN VII-X is being performed according to the strategy and the principles described in the following.

The plasma behaviour in the confinement region can be optimized by noting that the geometry of the confinement boundary within the last closed flux surface completely determines the properties of the confinement region since this boundary yields a Neumann problem for the magnetic field inside of this boundary. Thus, boundary value problems may be solved during an optimization, the parameters of the boundary being the optimization variables. In a second step, after optimization of the confinement region, optimization of the coils necessary to produce this confinement region can be done, again by solving boundary value problems at the boundary of the confinement region. The coil geometry is then further improved by local amendments according to requirements which have not yet been included in the numerical procedure. Nevertheless, boundary value problems are the basic steps of the optimization procedure employed here which allows large steps to be taken in the stellarator configurational space. The boundary representation used for Helias equilibria [1] appears to provide a suitable configuration space.

The following principles of optimization have been taken into account.

I. High quality of vacuum field magnetic surfaces
A regular boundary of the confinement region will guarantee good magnetic surfaces. If low-order rational transform values are avoided, then small error fields are harmless [2] . If medium-order values of rotational transform per period are avoided, then effects of the natural islands will be harmless. Another possibility is the use of significant shear ($\Delta\iota/\iota \approx 0.2$) to render resonant MHD effects [3, 4] harmless. A regular boundary also allows controlled positioning of an island chain at the boundary which can be envisioned as a resonant divertor.

II. Good finite-β equilibrium properties
A small Shafranov-shift and a small change of rotational transform and shear with β for vanishing net toroidal current will yield a high equilibrium-β limit. This is obtained with $\langle j_{||}^2/j_{\perp}^2\rangle \lesssim 1$, which is primarily achieved by a suitable combination of helical curvature and elliptical flux surface cross-section, see for example [1, 3].

III. Good MHD stability properties
The stability of small-shear equilibria is governed by three aspects. Stability is provided by magnetic well stabilization. A vacuum field magnetic well of approximately 2 % can be created by exploiting the helical curvature and suitably chosen indentation and triangularity of the flux surfaces. Magnetic well stabilization at sufficiently high β-values requires sufficiently reduced parallel current density, see II. Side conditions on the geometry of the magnetic surfaces (aspect ratio, local curvature, local flux surface spacing) have to be observed to avoid local ballooning instabilities becoming more restrictive than Mercier instabilities.

IV. Good neoclassical transport properties in the $\frac{1}{\nu}$-regime
A lower theoretical limit is given by isodynamic configurations [4] for which the magnetic field $B = B(s, \phi)$ in magnetic coordinates s (flux label), θ, and ϕ (poloidal and toroidal angle-like coordinates). These configurations would have $j_{||} \equiv 0$ and classical instead of neoclassical transport, but apparently cannot be closely approximated at finite aspect ratio because it is impossible to eliminate all poloidal variation from B in a curved system. Some approximation is achieved in linked mirror type Helias configurations [5, 6]. A lower limit analogous to neoclassical transport in axisymmetric systems is given by quasi-helically symmetric configurations [6] in which the field strength is given by $B(s, \theta - \phi)$. In this situation neoclassical banana-transport –without appearence of the $\frac{1}{\nu}$-regime – is obtained as in true helical symmetry. The general nonsymmetric case can be characterized by a normalized ripple transport coefficient $D_R^* = 1.65\delta_e^{\frac{3}{2}} L^*$ (L^* normalized mean free path) with an equivalent ripple δ_e determined by Monte Carlo simulation of electron transport in the lmfp regime. This ripple must be kept small, typically smaller than or about 2 % at half of the minor radius, to guarantee sufficiently good neoclassical energy confinement.

V. Small bootstrap current in the lmfp regime
While axisymmetric configurations exhibit a bootstrap current which increases the rotational transform, quasi-helically symmetric configurations show a reverse bootstrap current, i.e. one which decreases the rotational transform. Since the radial behaviour of the associated field strength component is of the same type in these two cases continuity suggests that nonsymmetric configurations with a bootstrap current vanishing on each magnetic surface should exist.

VI. Good modular coil feasibility
Generally, strong geometrical shaping of the plasma boundary will yield better results while it adversely affects coil feasibility. So, side conditions on the shaping parameters of the plasma boundary will have to be used to qualitatively ensure coil feasibility. Some of them remain to be incorporated in the numerical procedure. A necessary prerequisite for application to an experimental device is a sufficiently broad accessible range of variable magnetic field parameters, like field strength, rotational transform, axis position.

2. Helias Stability Calculations

In the Helias class of stellarators the stably accessible ranges of rotational transform, aspect ratio, and number of field periods M were investigated [7]. Configurations with $0.7 \lesssim \iota_0 \lesssim 1.1$, $0.8 \lesssim \iota_1 \lesssim 1.2$, $8 \lesssim A \lesssim 12$, $4 \leq M \leq 6$, $0.03 \lesssim \langle\beta\rangle \lesssim 0.09$, were found which are stable with respect to resistive interchanges. The examples, see Table I, show the flexibility of Helias stellarators with respect to the selection of the rotational transform, shear, and aspect ratio.

Smaller $\langle\beta\rangle$ -values are found for 4 periods than for 5 periods if optimizations are done with $0.8 \lesssim \iota \lesssim 1$, see the cases 4081 and 5081 as well as 4099 and 5099. The relevant resonances up to order 10 in this range of the rotational transform are for 4 periods $\frac{1}{5}$, $\frac{2}{9}$, $\frac{1}{4}$ per period, while for 5 periods the corresponding values are $\frac{1}{6}$ and $\frac{1}{5}$. In addition, the $\langle j_{||}^2/j_{\perp}^2\rangle$-values tend to be somewhat larger for 4 periods than for 5 periods; profiles of these quantities and pressure profiles obtained by iteration towards marginal stability with respect to the resistive interchange criterion are shown in Fig. 1.

Evaluations of selected local ideal ballooning modes, see Table II, support the conclusion that a higher critical β-value can be achieved with 5 periods than with 4 periods. Most of the configurations shown in Tables I and II were obtained by optimization towards a vacuum field magnetic well and quasi-helical symmetry, while some contain a significant mirror field (for example case 5281, the configuration studied in [3]) and toroidal curvature (for example case 4978, HS4-12).

	4889	4978	4881	4081	4099	5081	5099	5281	5912	6081	6281
M	4	4	4	4	4	5	5	5	5	6	6
$A \approx$	8	9.5	8	10	10	10	10	12	10	10	12
ι_o	0.8	0.7	0.8	0.8	0.8	0.8	0.8	0.8	1.1	0.8	0.8
ι_a	0.9	0.8	1.0	1.0	0.9	1.0	0.9	1.0	1.2	1.0	1.0
$\langle\beta\rangle$	0.045	0.05	0.04	0.03	0.05	0.075	0.07	0.09	0.05	0.06	0.075

Table I: Various Helias configurations characterized by their number of periods M, rotational transform or twist, ι, and shear, average-β-value $\langle\beta\rangle$ (stable with respect to the resistive interchange criterion), aspect ratio A. The configuration label designates the number of periods (first digit), approximate aspect ratio (second digit), $\iota(0)$ (third digit) in the vacuum field, $\iota(1)$ (fourth digit) in the vacuum field.

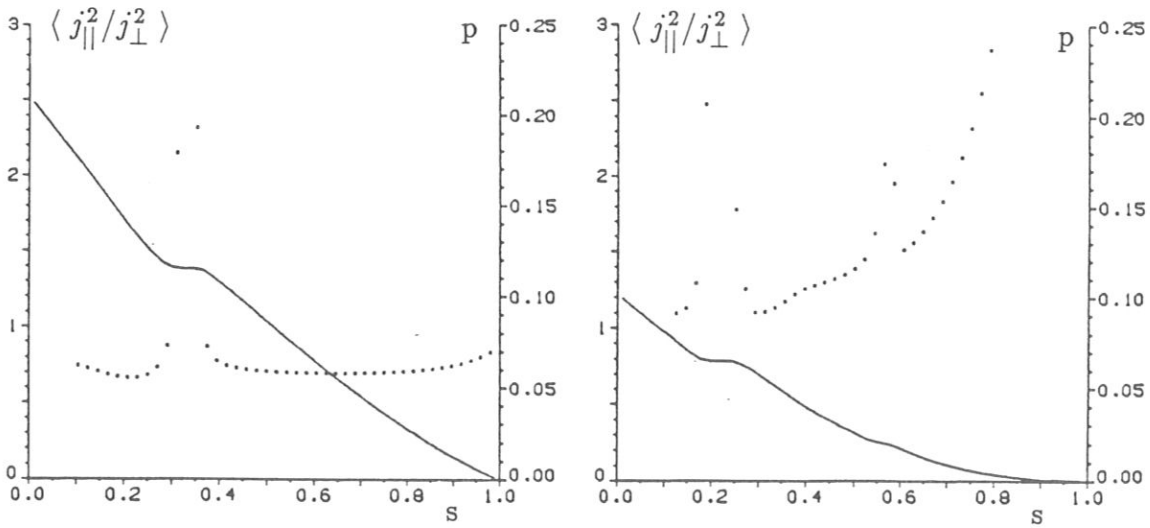

Fig. 1 : Profiles of $p(s)$ (—) flattened around $\iota_p = \frac{1}{6}$, and of $\langle j_{||}^2/j_{\perp}^2 \rangle$ (. . .) for the case 5081 (left part); the right part shows the corresponding results for the case 4081 with the resonances $\frac{1}{5}$, $\frac{2}{9}$, and $\frac{1}{4}$.

	5281	HS4V12	4881	4081	5081	5099	6081	6281
$\frac{n}{m}$	$\frac{7}{8}$	$\frac{5}{6}$	$\frac{7}{8}$	$\frac{7}{8}$	$\frac{7}{8}$	$\frac{7}{8}$	$\frac{7}{8}$	$\frac{7}{8}$
$\langle\beta\rangle$	0.05	0.03	0.023	0.02	0.047	0.047	0.03	0.047

Table II: Ballooning mode numbers and $\langle\beta\rangle$ -values for marginal stability of the ballooning mode investigated.

3. Types of Helias Fields

In general, toroidal stellarators involve the risk that neoclassical energy confinement may turn out to be characterized by losses exceeding the plateau level in the long mean free path regime. Helias stellarators can be found which combine small Pfirsch-Schlüter current density and small equivalent ripple so that the requirements of good neoclassical transport and good MHD behaviour do not conflict. Two limiting types of Helias fields can be distinguished according to their differing structure of $mod\,B$ on the magnetic surfaces. Linked mirror configurations tend towards poloidally closed contour lines, whereas quasi helical configurations exhibit a nearly helical invariance, see Fig. 2. Besides the low Pfirsch-Schlüter currents these quasi helical configuration have the favourable property of confining trapped particle which in particular will reduce α-particle losses in a stellarator reactor. Other Helias configurations are of an intermediate type. An example of a linked mirror configuration is studied in [5], quasi-helical Helias configurations were first published in [6], modular Heliac configurations with nearly helically invariant structure of $mod\,B$ and improved transport properties in [8].

Quasi helical equilibria seem to be rather resistent against finite beta effects or the superposition of a toroidal current. Figure 3 shows results for finite-β calculations without and with a significant amount of toroidal (bootstrap) current. These equilibrium calculations are for fixed boundary, the effect of free boundary remains to be studied.

In both types of Helias configurations collisionless guiding center orbits are well confined. Circulating particles stay close to magnetic surfaces. Deeply trapped particles with nearly vanishing parallel velocity are lost in local field minima (modular ripple) between two of the modular coils. Moderately trapped particles show reduced drift velocities and small radial banana widths, they can perform nearly closed orbits for a longer time, unless they are lost in a modular ripple. These orbits deviate from

magnetic surfaces. Nearly circulating particles can perform many transits around the torus in one direction, before getting reflected close to the local maxima of the field; these occasional reflections lead to stochastic orbits and a slow diffusion of these intermediate particles. Quantitatively the behaviour of trapped particles depends on the details of the configuration and of the particles, e.g. magnetic field structure, starting point, energy, pitch angle, a classification of trapped particles is difficult because of frequent trapping and detrapping processes.

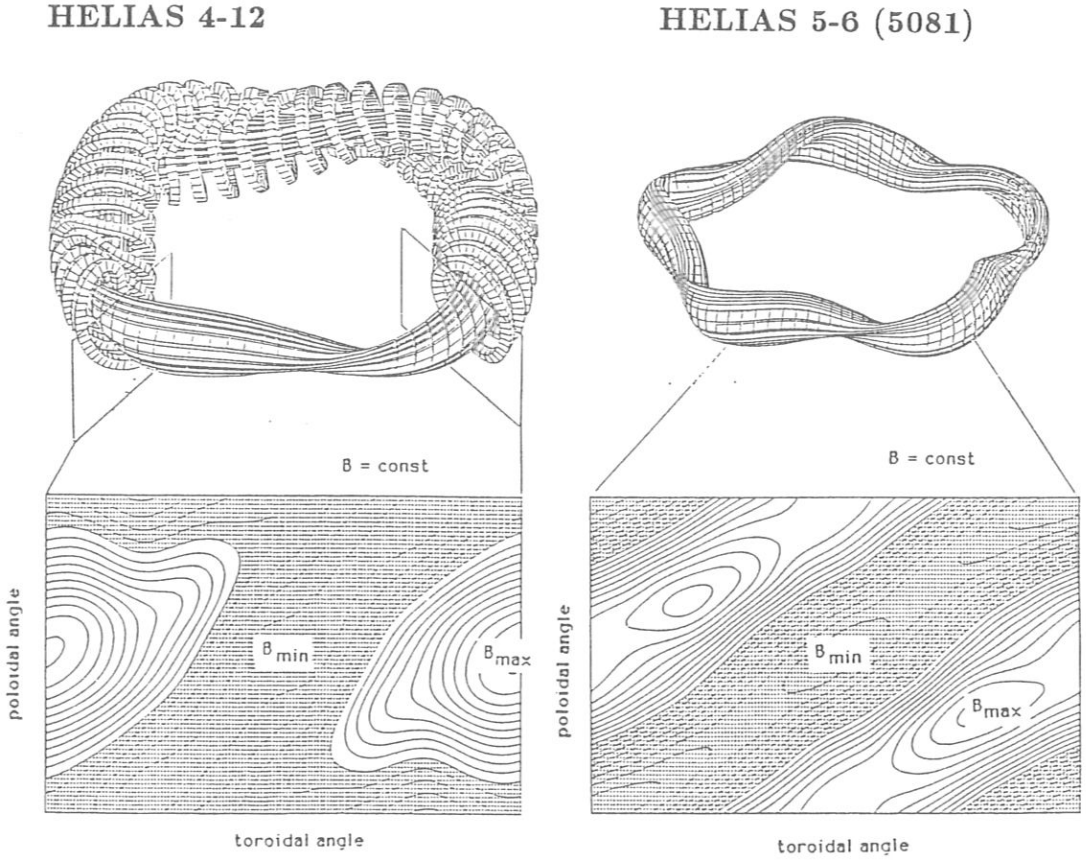

Fig. 2 : Left part: Perspective view on the coils and a magnetic surface of HS4-12, a 4 period Helias system and *mod B* of one field period with localized maxima at the radial inside, typical for linked mirror configurations.
Right part: Magnetic surface of HS5-6, a 5 period configuration similar to 5081, showing a nearly helical invariance of *mod B* .

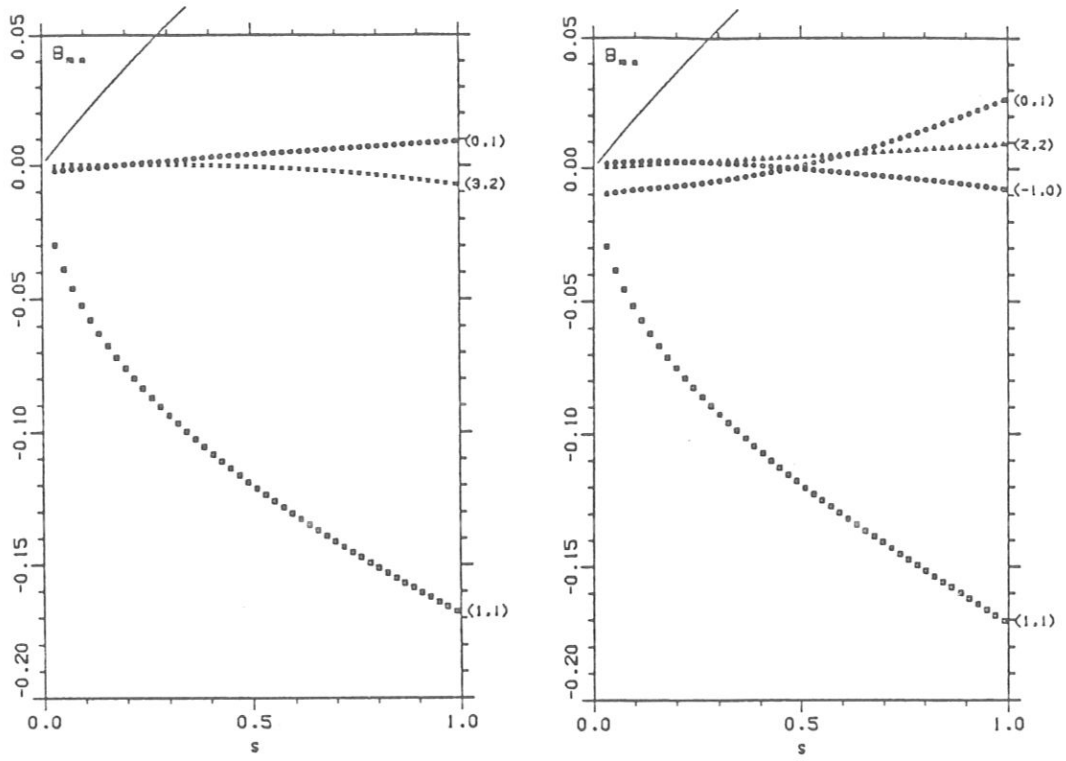

Fig. 3 : Fourier coefficients $B_{m,n}$ versus normalized flux surface label s; for example, $-[B_{0,0} - B_{0,0}(s=0)]$, $\times$ $B_{3,2}$, $\square$ $B_{1,1}$; $B = \sum B_{m,n} \cos 2\pi(m\theta - n\phi)$. Fourier coefficients smaller than 0.0065 are not shown. The left part shows a $\langle\beta\rangle = 0.05$ result without toroidal current, the right part the result for a current which changes the boundary value of the rotational transform by approximately a factor of two.

4. Bootstrap Current

Bootstrap currents in Helias configurations have been calculated following the theory of Shaing, Solano [9] and Shaing, Callen [10]. As a figure of merit the geometrical factor C_b has been evaluated for various Helias configurations with the equivalent axisymmetric configuration serving as the reference case. In quasi-helical configurations a simple relation between bootstrap current I', neoclassical diffusion flux Γ_{neo} and electron thermal flux $q_{e,neo}$

$$< B^2 > \eta\, I'(\psi) \;\propto\; (\iota - \gamma)\,\{\frac{\Gamma_{neo}}{n} + 0.32\frac{q_{e,neo}}{nT_e}\}$$

can be derived which holds for all regimes of collisionality. The quantity η is the Spitzer resistivity, γ is the slope of $mod\,B = const$-lines on a magnetic surface, $\gamma = 0$ in axisymmetric tokamaks. This equation predicts a non-vanishing bootstrap current for quasi-helical configurations flowing opposite to the bootstrap current in axisymmetric ones.

In non-symmetric Helias configurations, exemplified by linked-mirror systems, the proportionality factor between bootstrap current and neoclassical fluxes depends on the details of $mod\,B$ on the magnetic surface and can be made very small or even close to zero by modelling the Fourier spectrum of $mod\,B$ appropriately. An example of a configuration with very small bootstrap current is HS4-12, shown in Fig. 2. The configurations HS5-7 and HS5-8 are of the intermediate type between linked-mirror configurations and quasi-helical ones, and show reduced bootstrap currents in the plateau regime.

It is not so much the modification of the plasma equilibrium or the potential source of kink instabilities which makes the bootstrap current a matter of concern, it is the uncontrolled variation of the ι-profile in low-shear stellarators during the rise phase of the discharge, which - as experiments in Wendelstein VII-A have shown - can lead to a collapse of confinement whenever the rotational transform crosses a low order rational number. It is for this reason that the bootstrap current will be minimised in a future low-shear stellarators.

5. Neoclassical Transport

5.1 Monte Carlo Computations of Neoclassical Transport

A code [11] was developed which uses monoenergetic Monte Carlo simulations of neoclassical transport coefficients as a basis for estimates of confinement times in the long mean free path regime for plasmas in stellarators of general geometry with Maxwellian energy distribution. Three diffusion coefficients relating to density-gradient-driven particle flux (D_1), temperature-gradient-driven particle flux (D_2), and temperature-gradient-driven energy flux (D_3) are then obtained by convoluting the monoenergetic results with a Maxwellian energy distribution and appropriate energy weighting factors. Fig. 4 shows such results for the case 5081 for an assumed radial electric field. With formal definitions of confinement times τ_i relating to D_i , approximate particle and energy confinement times are given by $\tau_P \approx \tau_2$ and $\tau_E \approx \tau_3$, respectively. The confinement times τ_k were taken from those D values where $D_{ke} = D_{ki}$ for $k = 1, 2, 3$. This procedure is suggested by the condition of quasineutrality $(\tau_{2e} \approx \tau_{2i})$, which is thus incorporated in a consistent though primitive way compatible with the lmfp regime. It is instructive to obtain results for various devices scaled to $R_0 = 5$ m, $B_0 = 4$ T, $kT(r_0) = 6.4$ keV, see Table III .

Case 5099G is characterized by $B_{1,0} \approx \frac{1}{2} B_{1,1}$ which yields a small bootstrap current in the lmfp regime according to Monte Carlo simulations of the distribution function [12].

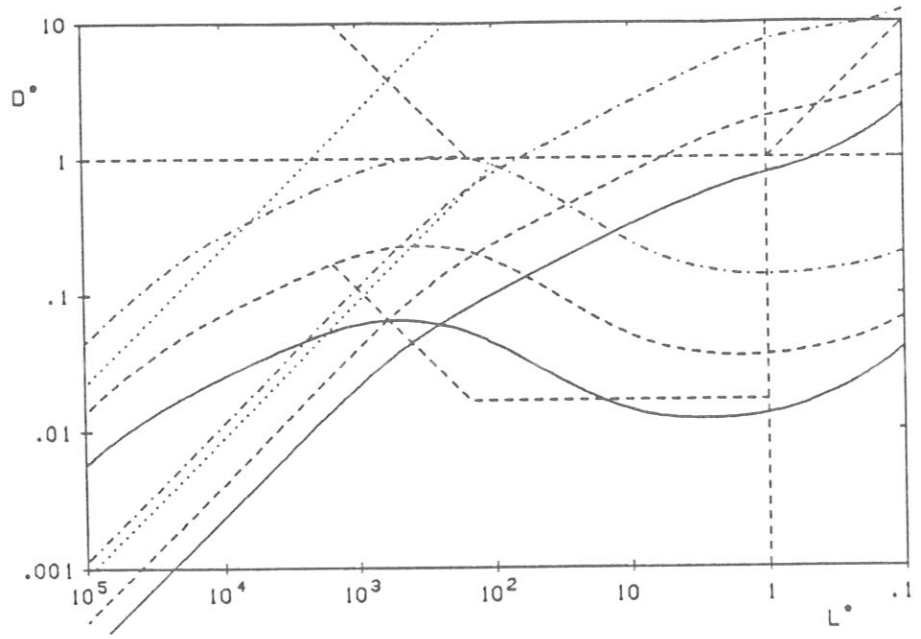

Fig. 4 : Transport coefficients D_1^* (—), D_2^* (- - -), and D_3^* (- · -) obtained for the case 5081 at $A = 20$ with $Q_{o\rho}^+ = 100$ (deuterons), $Q_{o\rho}^- = 6{\cdot}10^3$ (electrons), and $e\phi_o/E_o = 1$. Dotted lines represent $D_{\mathrm{B}}^* = A^{\frac{3}{2}}/L^*$ and $D_{\nu\mathrm{c}}^* = H_{\mathrm{c}}^2\,\nu^*$, which, in turn, corresponds to $S_\nu = \nu$. The transport coefficients are normalized to the tokamak plateau value ($D^* = 1$) , and the mean free path is normalized to half the connection length ($L^* = 1$) .

5.2 Bounce-Averaged Fokker-Planck Code

Recently, a power series solution of the bounce-averaged kinetic equation has been found which is valid for the whole range of low collision frequencies, and for both, classical stellarators or torsatrons with standard or transport-optimized ripple profiles [13] . Using only the lowest Fourier components of the magnetic field a simple analytical model for the magnetic field is given by

$$B = B_o(1+C_{o,1}\cos\theta - C_{1,o}\cos M\phi - C_{1,1}\cos\theta\cos M\phi - S_{1,1}\sin\theta\sin M\phi),$$

where M is the number of field periods. This model is extended to also incorporate higher harmonics. It is applied to cases of various Helias coil systems.

		W VII-AS	W VII-AS	HS-49	HS-5081	HS-5099G	HS-61
R_o	[m]	2.0	5.0	5.0	5.0	5.0	5.0
a	[m]	0.20	0.50	0.50	0.50	0.50	0.50
$\iota(r_o)$		0.389	0.389	0.746	0.882	0.844	1.531
B_o	[T]	3.0	4.0	4.0	4.0	4.0	4.0
$kT(r_o)$	[keV]	2.0	6.4	6.4	6.4	6.4	6.4
$n_e(r_o)$	$[10^{19}\,\mathrm{m}^{-3}]$	2.8	6.2	6.2	15.5	6.2	9.3
$\beta(r_o)$	[%]	0.5	2.0	2.0	5.0	2.0	3.0
τ_c	[ms]	3.6	9.2	9.2	3.7	9.2	6.2
τ_o	[ms]	3.6	17	33	40	38	69
τ_1	[ms]	55	160	490	640	870	12000
τ_2	[ms]	19	60	190	240	320	3800
τ_3	[ms]	8	27	80	100	140	1500

Table III : Calculated plasma parameters and confinement times for W VII-AS and for various Helias systems at aspect ratio $A = 20$, i.e. at about half of minor radius a .

τ_c is the effective collision time, τ_o is the plateau confinement time, τ_1 is the density-gradient-driven confinement time of monoenergetic particles, $\tau_2 \approx \tau_P$ and $\tau_3 \approx \tau_E$ are the particle and the energy confinement times, respectively, of a Maxwellian plasma, with electric potential $q\phi_o/E_o(r_o) = 1$, where E_o is the average Maxwellian energy.

An example is shown in Fig. 5 for the case of the linked-mirror type configuration HS4-8 which was increased to reactor size. Parameters of interest in standard notation are $R_o = 25$ m, $a = 2.5$ m, $B_o = 8$ T, $\iota = 0.55\,, \phi = T = 5000$ V. The poloidally averaged ripple amplitude at half of the minor radius is $\epsilon = 4.7$ % . Numerical Monte-Carlo results for ions ($*$) and electrons ($\circ$), obtained for the model field, are found to

agree very well with analytic estimates, shown as dashed lines in Fig. 5. Monoenergetic test particles are used with pitch angle scattering. The collision frequency is varied by changing the background density. The numerically observed losses for the full ripple spectrum for ions are increased by a factor of about two for ν_{eff}/Ω_E between 0.1 and about 3, and stay always considerably below the axisymmetrix plateau value, $D^* = 1$. Similar results are obtained for the quasi-helical configuration HS5-6.

These results clearly demonstrate the improved confinement of the Helias concept; the expected ripple transport rate in an equivalent classical stellarator is much larger.

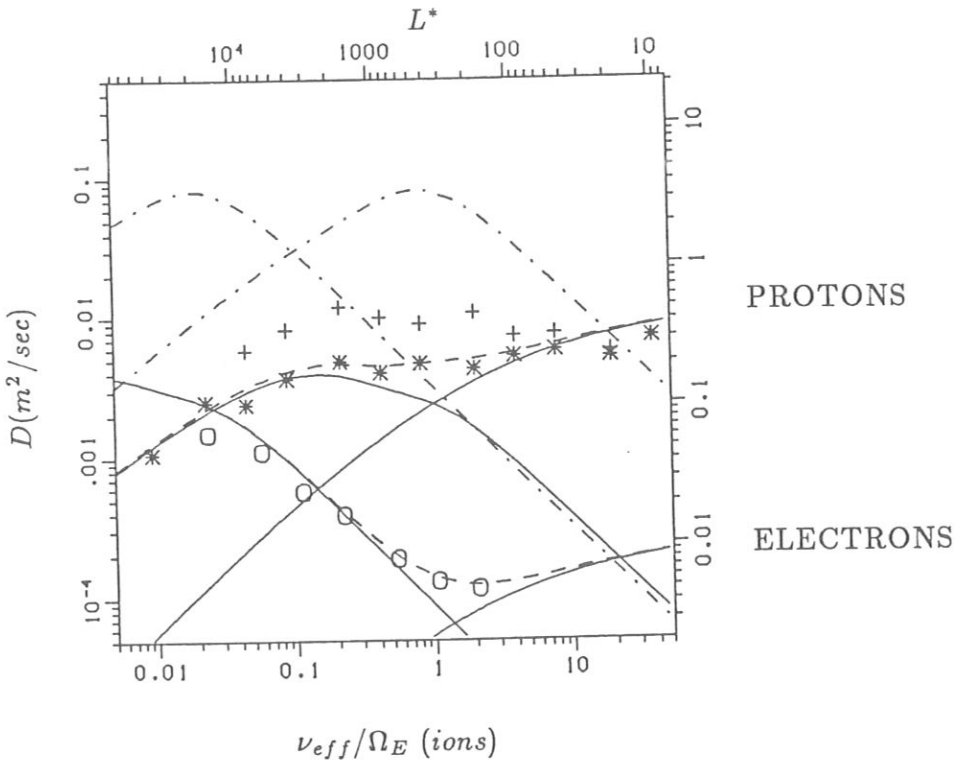

Fig. 5 : Transport coefficients for protons and electrons, obtained for HS4-8 in reactor size. Solid lines are the power series estimates according to the model field given in the text and the expected axisymmetric contribution; the dashed lines are the sum of the solid lines. The dot-dashed lines indicate the expected ripple transport rate in an equivalent classical stellarator. Numerical Monte-Carlo results are shown, for monoenergetic ions (∗) and electrons (○), obtained for the model field, and for ions(+) for the full ripple spectrum.

5.3 Projection of Plasma Parameters

Plasma parameters in a Helias system are estimated by application of a simple 1D transport code. This code solves the combined equations of particle and energy transport of ions and electrons for given radial profiles of energy and particle input. Radiative losses with given profile are optional. Neoclassical transport coefficients $(\chi, D)_{neo} = (\chi, D)_{HH} + (\chi, D)_{ripple}$ are used, with the Hazeltine-Hinton formula for the plateau regime, and the Shaing-Houlberg formula for the ripple regime, with an equivalent ripple amplitude δ_e adjusted to the result of Monte Carlo calculations and analytic theory. In addition, anomalous losses are assumed with $(\chi, D)_{an} \propto n^{-1} T^{-\frac{2}{3}}$.

Preliminary parameters for this investigation are: Major and minor radii $R_o = 5$ m and $a = 0.45$ m, respectively and a magnetic field of $B = 2.5$ T. A radial electric field with potential $e\phi = kT$ and radiative losses near the edge of 10 MW are assumed. With a net heating power of 20 MW and densities around 10^{20} m^{-3} peak temperatures between 4 and 6 keV were calculated. The goal of an average value of $\langle\beta\rangle = 5$ % is also attained at other distributions of the absorbed power of 20 MW at $B = 2$ to 2.5 T at densities of about 10^{20} m^{-3} and peak temperatures around 5 keV. To achieve these parameters a low recycling coefficient has to be assumed, in particular with respect to a gas influx connected with neutral beam heating.

6. Vacuum Fields and Coils

The NESCOIL code as application of the vacuum field Neumann problem has mainly been used in systematic optimizations of the coils with respect to their distance from the plasma and their curvature. The contours of the center filaments of the coils are obtained on an outer surface which is chosen with considerable flexibility, preferably similar to the geometry of a magnetic surface inside of, and near the outermost magnetic surface. Preparatory studies with NESCOIL of a resonant divertor concept have identified a variety of possibly promising situations with different topologies and localizations of diverting field lines [14]. A case in which the structure of the islands looks quite optimal, because it favours the tips of the indented cross-section and the tip of the triangular cross-section as divertor regions is shown in Fig. 6, and one field period of the corresponding coil set in Fig. 7. The result of a free-boundary calculation with NEMEC [14] are presented in Fig. 8, which indicates that the positions of the O-points of the islands vary little with β.

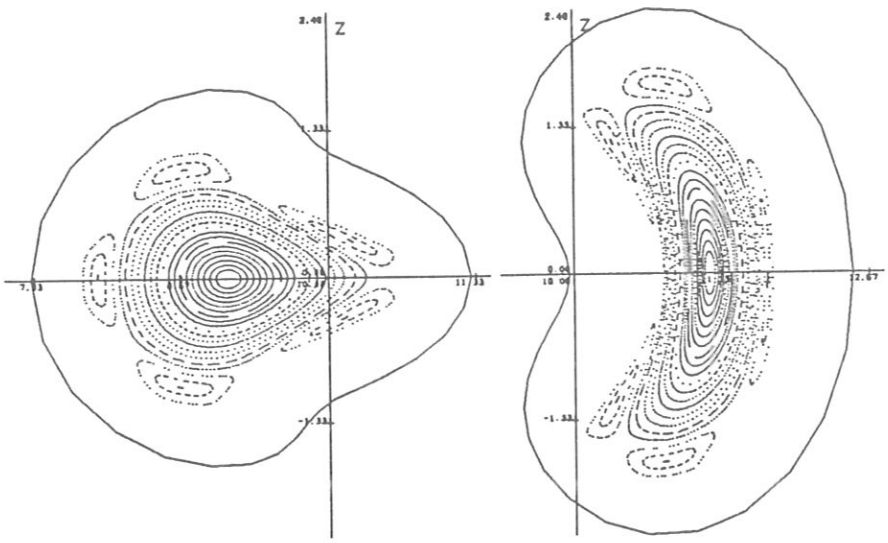

Fig. 6 : Poincaré plots of the 5081 Helias stellarator and contours of the current carrying surface.

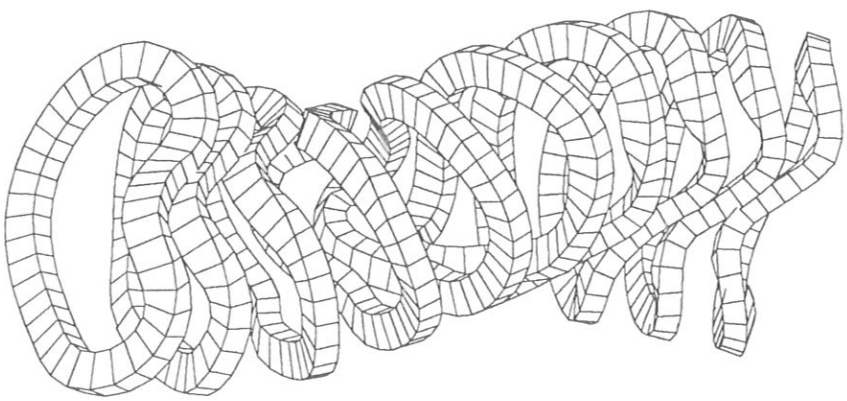

Fig. 7 : One period of the coils for the 5081 Helias stellarator.

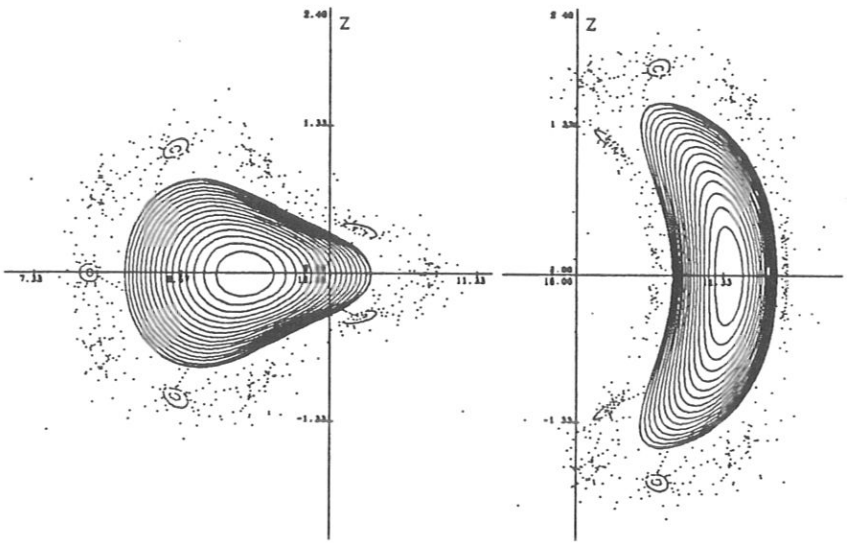

Fig. 8 : Flux surfaces of a 5081 free-boundary equilibrium with $\langle\beta\rangle \approx 0.06$. The Poincaré plots of the surrounding vacuum field show the influence of β on the size and position of the five magnetic islands with $\iota = 1$.

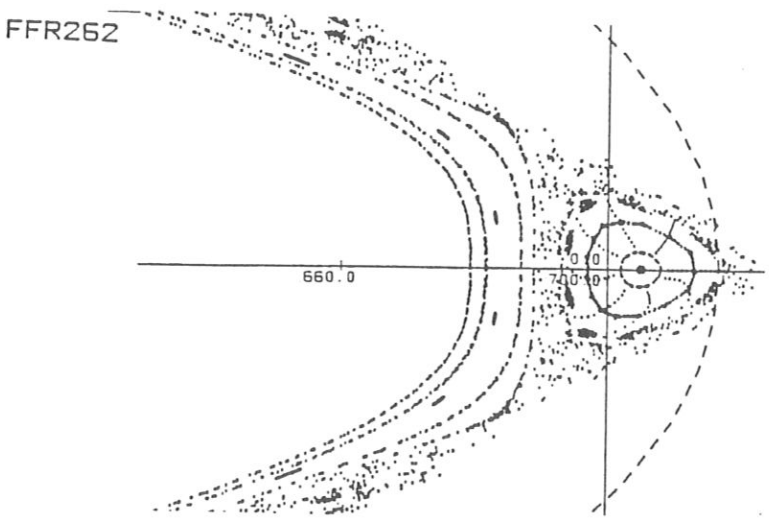

Fig. 9 : Details of outer magnetic surfaces for HS5-7 with $\iota = 1$ at the edge.